Investigation of chemical noise propagation and its consequence in simple regulatory motifs and complex networks

A Thesis Submitted for the Degree of Doctor of Philosophy

by

Soutrick Das 16CHPH28



School of Chemistry
University of Hyderabad
Hyderabad-500046, INDIA
December, 2022

DEDICATED TO MY FAMILY & FRIENDS

Content

Decl	laration	i
Cert	tificate	iii
Ack	nowledgments	vii
Char	oter 1. Introduction	1-23
1.1	Chemical noise	1
1.1	1.1.1 Intrinsic noise	6
	1.1.2 Extrinsic noise	6
1.2	Complexity in biological networks	6
1.3	Systems biology and mathematical modeling.	8
1.4	Network Motifs	9
	1.4.1 Feedback loops	10
	1.4.2 Feed-forward loops	11
1.5	Performance of reaction networks under chemical noise	12
1.6	Objective of the thesis	13
	1.6.1 Previous works	13
	1.6.2 Layout of the thesis	14
1.7	References	16
Cha	pter 2. Methodology	25-34
2.1	Chemical Master Equation	25
2.2	Linear noise Approximation	26
2.3	Gillespie's Stochastic Simulation Algorithm	29
2.4	Pseudo Potential based bifurcation analysis method	31
2.5	References	33
	pter 3. Chemical Noise propagation in reversible multisite sphorylation-dephosphorylation chain	35-50
3.1	Introduction	35
3.2	Model .	36
3.3	Results	41
3.4	Conclusion	47

3.5	References	48

	_	. Pulse c noise	processing of bistable network motifs in presence	51-73
4.	l Ir	ntroducti	ion	51
4.2	2 N	Iodel		53
4.3	3 R	esults		57
4.4	4 C	onclusio	on	67
4.5	5 R	eference	es	69
	pter 5		of extrinsic noise on the heterogeneity of bistable	75-100
5.1	l Ir	ıtroducti	ion	75
5.2	2 N	Iodel		76
5.3	3 R	esults		79
5.4	4 C	onclusio	on	94
5.5	5 R	eference	es	97
Cha	pter 6	. Contr	ol of chemical noise in general network topology	101-140
6.1	Intro	duction		101
	6.A		ical noise propagation in democratic rk topology	103
		6.A1	Model	104
		6.A2	Results	106
		6.A3	Conclusion	118
	6.B		ical noise propagation in autocratic rk topology	120
		6.B1	Model	121
		6.B2	Results	124
		6.B3	Conclusion	136
6.2	Refe	rences		137
Cha	pter 7	. Futur	e Scope	141-142
App	endix			143-174
Plag	giarisn	n Repor	t	

Declaration

I, Soutrick Das, hereby declare that the matter embodied in this thesis entitled,

'Investigation of chemical noise propagation and its consequence in simple

regulatory motifs and complex networks' is the result of investigations carried out by

me in the School of Chemistry, University of Hyderabad, Hyderabad, under the

supervision of Dr. Debashis Barik.

In keeping with the general practice of reporting scientific investigations, due

acknowledgments have been made whenever the work described is based on the finding

of other investigations. Any omission or error that might have crept is regretted. This

research work is free from plagiarism. I hereby agree that my thesis can be deposited in

Shodhganga/INFLIBNET. A report on plagiarism statistics from the University library

is enclosed.

University of Hyderabad December, 2022 Soutrick Das Reg No. 16CHPH28

TOF HOLD AND ADDRESS OF THE PARTY OF THE PAR

School of Chemistry

University of Hyderabad Hyderabad-500046 Telangana, India

Certificate

This is to certify that the thesis entitled 'Investigation of chemical noise propagation and its consequence in simple regulatory motifs and complex networks' submitted by Soutrick Das bearing the registration number 16CHPH28 in partial fulfilment of the requirements for the award of Doctor of Philosophy in Chemistry is a bonafide work carried out by him under my supervision and guidance.

This thesis is free from plagiarism and has not been submitted previously in part or in full to this University or any other University or Institution for award of any degree or diploma.

Parts of this thesis have been published in the following publications:

- 1. Das, S. & Barik, D. Pulsatile signaling of bistable switches reveal the distinct nature of pulse processing by mutual activation and mutual inhibition loop. *J. Theor. Biol.* **540**, 111075 (2022). (Chapter 4)
- 2. Das, S. & Barik, D. Scaling of intrinsic noise in an autocratic reaction network. *Phys. Rev. E* **103**, 042403 (2021). (Chapter 6A)
- 3. Das, S. & Barik, D. Qualitative and quantitative nature of mutual interactions dictate chemical noise in a democratic reaction network. *Phys. Rev. E* **101**, 042407 (2020). (Chapter 6B)
- 4. Das, S. & Barik, D. Investigation of chemical noise in multisite phosphorylation chain using linear noise approximation. *Phys. Rev. E* **100** 042407, (2019). (Chapter 3)
- 5. Das, S. & Barik, D. Origin, robustness and interoperability of heterogeneous atypical switches in bistable network motifs with dual signalling. (Chapter 5) Manuscript under communication.

He also participated in oral/poster presentations in the following conferences:

1. Chemfest 2021, 19-20th March 2022

Oral: 'Investigation of stochasticity in generalised biochemical reaction network' School of Chemistry, University of Hyderabad

2. Conference on 'Cellular lineage and development from single cell to landscapes, 1-4th November, 2022

Poster: 'Origin, robustness and interoperability of heterogeneous atypical bistable switches in bistable network motifs with dual signalling'

Simons NCBS, TIFR, Bangalore

3. Conference on 'Nonlinear Dynamics in Chemistry and Biology (NLDCB)', 7-9th April, 2019

Poster: 'Investigation of chemical noise in multisite phosphorylation chain using linear noise approximation'

S.N. Bose National Centre for Basic Sciences, Kolkata

4. Conference on 'Electronic Structure, Spectroscopy and Dynamics (IACS-CESSD)', 22-25th February, 2018

Poster: 'Stochastic quusi steady state approximation in multistep reversible reactions'

Indian Association for the Cultivation of Science, Kolkata

5. National Meeting of Synthetic and Theoretical Chemists (NMSTC), 13-14th October, 2017

Poster: 'Stochasticity in multistep reversibly chemical reactions at steady state' School of Chemistry, University of Hyderabad

Further the student has passed the following courses towards the fulfilment of course work requirement for PhD:

Sl. No.	Course No.	Title of the Course	No. of Credits	Grade
1	CY801	Research Proposal	3	Pass
2	CY802	Chemistry Pedagogy	3	Pass
3	CY805	Instrumental Methods-A	3	Pass
4	CY806	Instrumental Methods-B	3	Pass

Dr. Debashis Barik Supervisor

Dr. Debashis Barik Associate Professor School of Chemistry University of Hyderabad Hyderabad-500 046, India.

Dean (I/2) of Chemieter School of Chemistry

Dean

SCHOOL OF CHEMISTRY University of Hyderabad Hyderabad-500 046.

Acknowledgements

During my PhD tenure, many people have helped, inspired and contributed at different stages. The thesis would not be completed without acknowledging them.

First and foremost, I would like to express my heartfelt gratitude to my PhD supervisor, *Dr. Debashis Barik* for his constant guidance and enormous support. Without his valuable involvement in both my research and my personal life, these few years would been difficult. He has been always very approachable, and ready to solve any doubts and discussion. Apart, from research work I really enjoyed the many informal discussions over tea or food about his past experiences of research and global news. I always look up to him always for his sincerity and disciplined lifestyle. Thank you, sir, for encouraging me throughout my PhD tenure and help me becoming better version of myself.

I would also like to thank my DRC members *Prof Susanta Mahapatra* and *Prof Tushar Jana* for their cooperation and guidance. I extend my gratitude to the present and former Dean of School of Chemistry for providing this wonderful environment to work.

Next are my family members, first of all my parents, my maa, *Mrs Ila Das* and my father, *Mr. Narayan Chandra Das*. Without their blessing and constant hardship throughout their life, it would have been impossible for me to come this far. Coming from a small town like Gangarampur, West Bengal, studying and working in the elite institutions needed a lot of mental support and backing from the family, which I was never deprived of. I would like to mentioned my *bara mesho*, *Mr Ranjit Kumar Saha*, who encouraged and helped me throughout my life and inspired me to become whatever I am today. He is the person we all in our family always look up to for any situation ever. I will always be indebted to him. I would to thank you my bara mana, *Late Kana Saha* and my choto mana, *Mrs. Baby Saha* who treated me as their child and had a great contribution in my upbringing.

I would like to specially mention *Dr. Sudipta Ghosh*, my friend. Thank you for standing beside me at every moment of my life. Next are my school friends who are still in touch and helped me to overcome the work pressure: *Rahul Basak, Sharif Khan, Sambow Das, Indranil Bhadra, Ananya Saha, Sanchita Saha, Nabanita Mazumder, Debashis Saha, Mainak Majumder*.

Next, I would like to say a big thank you to my labmates, *Dr Anupam Dey*, our in person google map and telugu translator; *Archana GR*, our Malayalam teacher and dry fruit provider; *Hafijur Rahman*, our tea and news specialist and *Suchana Chakravarty*, the Biswa Bharati phenomenon, the singer. I would also like to thank the project students I worked with *Amruta, Rakesh, Samyukta, Theinmozhi, Shakira, Rabiul, Bijit, Meghna, Pratyush*. Thank you all for a friendly environment in the lab.

I would also like to convey my regards to *Dr. Durba Roy*. Thank you, mam, for your blessings and constant support and all the delicious home cooked food. I would also like to thank *pupu (Trinabh Barik)*, our youngest lab member. I will always remember our discussions on latest tech-news.

I also did my masters here at University of Hyderabad. So, within this past 8 years I was very fortunate to come in contact with many seniors, juniors and batchmates. I would like to express my gratitude to our large Bengali community. I was lucky enough to be the part of organising many events in the campus by our Bengali community, in this regard I would like to thank all for their contribution and making every event a grand success. Throughout my journey, I was guided by two seniors Dr. Rudraditya Sarkar and Dr. Sugata Goswami. Thank you for your support. I was helped and inspired by many seniors at various stages in my journey. I would extend my thanks to Dr. Suman Ghosh, Dr Navendu Mondal, Olivia Neogi, Dr. Kousik Ghosh, Dr. Raja Rit, Dr Sneha Paul, Dr Sabari Ghosh, Dr. Subhabrata Mukhopadhay, Dr. Mehboob Elahi, Rajib Mondal, Arup Dalal, Deepan Chowdhury, Dr Suranjan Paul. Next, I would like to mention my immediate seniors and juniors, with whom I worked more closely, Dr Apurba De, Dr Arijit Mukherjee, Dr Sk Saddam Hossain, Bappaditya Sankhari, Kuntal Bhattacharya, Devika Debnath, Sourav, Sayantan, Imran. I would like to thank my batchmates and juniors for countless Saturday night celebrations: Shubham Debnath, Nilanjan Mukherjee, Suman Mandal, Somnath Das, Anupam Das, Saradamoni Mondal, Md Alamgir. Special thanks to my relatively new hostel mates and friends: Soumen Nayak, Suman Kumar Panja, Abhisekh Saha, Supratik and Subhashree, Munna Sannaki, Debonath, Mahadeb for celebrating each and every event and creating a fruitful atmosphere inside the hostel. I thank my Masters' and bachelors' batchmates who are still in touch and helped me in many ways they can.

Next, I would like to mention *Dr. N Tanmaya Kumar*, my supporting pillar during my phd tenure inside the campus. The journey would not been like this without him. This campus

has gifted me an elder brother for life. I look up to him for everything. Because of him, I was introduced to the lovely origa community in the campus, now I can say, I became a part of them. I would like to thank, *Dr. Sameeta Sahoo and Dr. Shipra Sahoo, Suman Kr Choudhury, Shailendra, Pradipta, Jaykrushna Sahoo, Satya B Satapathy, Swayam Sikha Srichandan, Subhashree Sabnam, Ruturaj Barik, Dillip Kr Muduli, Dhirendra Sahoo, Raj.*

My deepest apologies to the names I am missing out but I wish to express my heartful gratitude to everyone who has played a role in my life in some way or other.

Finally, I acknowledge DST-INSPIRE, Govt. of India for the fellowship. Thank you, University of Hyderabad.

Soutrick Das

CHAPTER 1

Introduction:

1.1 Chemical noise

The main objectives of a living cell are to survive, respond to external conditions and passing its DNA to its progenies. How a tiny cell performs numerous functions has been a central question in biological sciences. The mechanism of gene expression, by which information encoded inside DNA translates into a specific protein, is a key process in maintaining various cellular functions. The change in the expression level and subsequent post-translational modifications of proteins allow the cell to carry out different physiological processes. Physiological processes are often triggered by external cues and membrane bound receptors transmits the extracellular signals to the nucleus via intra cellular signalling pathways leading to change in the expression level of the target genes. The complex process of gene expression and subsequent post-translational modifications are well coordinated by the machinery of gene and protein regulatory networks of biochemical reactions. Steps of information flow from cell surface to nucleus is tightly regulated by regulatory proteins. Numerous numbers of transcripts and proteins are being produced inside a cell in every moment. Network of biochemical reactions are responsible for orchestrating the production and post production regulation of the macromolecular species. In a particular living organism, evolution has defined the network of chemical reactions. Thus, expectedly the physiological response of a population of cell of a particular organism under uniform environment must be identical as they are genetically identical.

Quantification of promoter activity and as well as protein abundance during gene expression by fluorescent probes allowed researchers to measure gene expression at the single cell level^{1,2,3,4}. The findings from these experiments were strikingly different from the expectation. In a population of genetically identical cell grown in a homogeneous environment, gene expression was found to be variable leading to population heterogeneity. Consequently, the probability distribution of the expressed protein showed a significant width^{2,5}. The variable protein production in a population of genetically identical cells was

termed as gene expression noise. Certainly, the observed cell-to-cell variation of the expressed gene was not due to the variation of the genetic background of these cells or due to the environmental factors. These experiments posed a serious question on the conventional understanding of kinetics of chemical reaction where the outcome of the reaction in a macroscopic scale is deterministic. However, in a tiny cell volume, the abundance of various reactants is finite and thus the macroscopic laws of chemical reactions may not be applicable in the context of chemical reactions inside a living cell⁶. The fluctuations of finite number of chemical species during the gene expression cannot be ruled out due to the microscopic to mesoscopic range of abundance of the molecular species. For example, in a typical gene there are an only a few numbers of promoter initiation sites available and typically the average abundance of mRNA ranges in between 1-100 molecules per cell. Thus, any fluctuations of these finite numbers would result a consequential fluctuation in the downstream processes. In order to explain these new experimental findings mathematical models were proposed taking into consideration of the probabilistic nature of chemical reactions involving finite number of chemical species.

Simple model of gene expression was proposed to explain the variability in protein abundance in prokaryotic cells such as Escherichia coli⁷ (Figure 1.1). In the model transcripts are produced from constitutively active gene, mRNAs are translated into protein and both mRNA and protein are degraded. While the transcription rate or the production rate of mRNA is constant and the translation rate or the production rate of protein is directly proportional to the abundance of mRNA. The decay of mRNA and protein were assumed to be first order process.

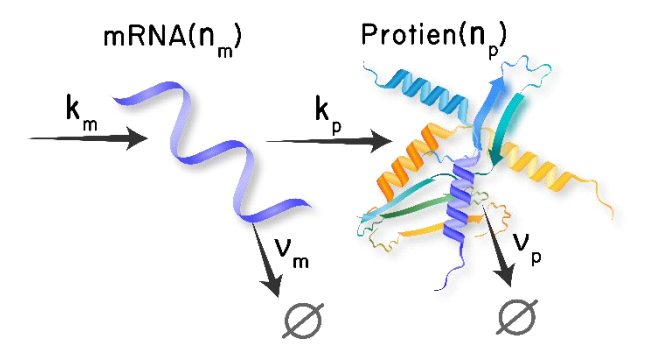


Figure 1.1. Schematic diagram for gene expression model for E. coli. The rate constants of various reactions are indicated accordingly.

Inherent randomness of the chemical reactions involving finite number of molecular species makes the reaction events stochastic. Therefore, the accurate modelling of the gene

expression requires probabilistic description of the model. The chemical master equation (CME) of the simple model of gene expression (See Chapter 2) is given as,

$$\frac{dP(n_m, n_p; t)}{dt} = k_m P(n_m - 1, n_p; t) - k_m P(n_m, n_p; t)
+ \gamma_m (n_m + 1) P(n_m + 1, n_p; t) - \gamma_m n_m (n_m, n_p; t)
+ k_p n_m P(n_m, n_p - 1; t) - k_p n_m P(n_m, n_p; t)
+ \gamma_p (n_p + 1) P(n_m, n_p + 1; t) - \gamma_p n_p P(n_m, n_p; t)$$
1.1

For the purpose of calculating steady state gene expression noise in the protein, the chemical master equation for the model was transformed into linear Fokker-Planck equation and with the help of fluctuation-dissipation theorem the steady state noise in the protein was calculated. The squared coefficient of variation (CV) of protein abundance at steady state is given by⁷

$$CV_p^2 = \left(\frac{\sigma_p}{\langle n_p \rangle}\right)^2 = \underbrace{\frac{1}{\langle n_p \rangle}}_{\substack{Poisson \ noise \ from \\ birth-death \ process}} + \underbrace{\frac{1}{\langle n_m \rangle} \cdot \frac{\gamma_m^{-1}}{\gamma_m^{-1} + \gamma_p^{-1}}}_{\substack{Noise \ from \ mRNA \\ to \ protein}}$$
1.2

 σ_p is the standard deviation of protein. $\langle n_p \rangle (=k_p \gamma_p^{-1} \langle n_m \rangle)$ and $\langle n_m \rangle (=k_m \gamma_m^{-1})$ are the average abundances of protein and mRNA, respectively and are same as the steady state solution of the deterministic rate equations. The first term on the right-hand side of the above equation is due to the individual birth and death processes of protein alone and expectedly it follows Poisson statistics. The second term is due to the noise originating from the transcription process and the transcriptional noise critically depends on the average abundance of mRNA and the relative lifetimes of protein and mRNA.

Several important conclusions emerged from the theoretical model: (1) the variability in protein is mostly due to the mRNA; (2) protein is produced from mRNA in a burst like manner, known as translational bursts, causing major variability in protein; and (3) protein noise strength $(\eta = \sigma_p^2/\langle n_p \rangle = 1 + k_p \gamma_p^{-1} (\gamma_m^{-1}/(\gamma_m^{-1} + \gamma_p^{-1})))$ depends linearly on the translational rate (k_p) not the transcription rate (k_m) consequently the noise strength increases linearly with the average protein abundance $(\langle n_p \rangle)$ when k_p is varied and is very weakly dependent on $\langle n_p \rangle$ when k_m is varied to increase protein abundance.

The predictions of the model were verified experimentally by single-cell quantification of protein using fluorescent reporter assays in prokaryotic bacteria Bacillus subtilis by Ozbudak et al² and also in Escherichia coli by Elowitz et al⁸. These experiments found the linear dependence of η with the $\langle n_p \rangle$ when k_p is increased therefore supporting translational bursting mechanism of protein production. Translational bursting hypothesis was later verified directly by real-time counting of protein molecules in individual E. Coli cell⁹. But experiments on eukaryotic systems, e.g., in yeast cells, found that η behaves differently with $\langle n_p \rangle$ when k_m is varied⁴. This challenged the gene expression model proposed by Thattai et al. To account for the experimental observations on eukaryotic systems, several authors proposed that mRNA could also be produced in a burst like manner, terms as transcriptional bursts.

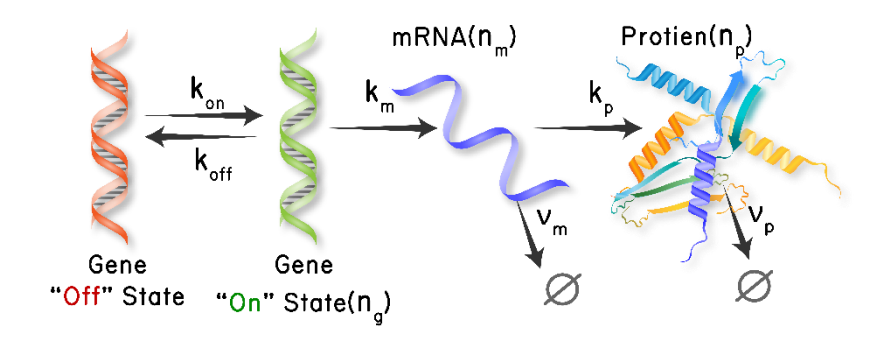


Figure 1.2. Schematic diagram for gene expression model with transcriptional noise. Gene switches between 'on' and 'off' state. From 'on' state it transcribes into mRNA which translates to from protein. The rate constants of various reactions are indicated accordingly.

Transcription of gene to mRNA needs access of DNA by several different types of molecules, e.g., transcription factor etc. and due to the higher order packing of the DNA molecule in higher organisms, it is highly unlikely that the gene will be easily accessible and thus will be constitutively active. Therefore, one assumes that gene can randomly switch back and forth between inactive and active states (Figure 1.2) and while only in the active state it produces mRNA molecules leading to random production kinetics of mRNA called transcriptional bursting. Raser and O'Shea and Paulsson separately determined the variability in protein in the gene expression model with transcriptional bursts^{4,10}. They applied the linear noise approximation, also known as van Kampen's Ω -expansion, to get the moments at the steady state. The protein noise is given by

$$CV_p^2 = \underbrace{\frac{1}{\langle n_p \rangle}}_{\text{Intrinsic noise:}} + \underbrace{\frac{1}{\langle n_m \rangle} \cdot \frac{\gamma_m^{-1}}{\gamma_m^{-1} + \gamma_p^{-1}}}_{\text{Extrinsic noise from mRNA}}$$

$$+ \underbrace{\frac{1 - P_{on}}{\langle n_g \rangle} \cdot \frac{\gamma_m^{-1}}{\gamma_m^{-1} + \gamma_p^{-1}} \cdot \frac{\gamma_g^{-1}}{\gamma_g^{-1} + \gamma_p^{-1}} \cdot \frac{\gamma_g^{-1} + \gamma_p^{-1} + \gamma_g^{-1} \gamma_p^{-1} / \gamma_m^{-1}}{\gamma_g^{-1} + \gamma_m^{-1}}}_{\text{Extrinsic noise from gene activation-deactivation}}$$
1.3

The $\langle n_g \rangle$ indicates the average number of active gene. P_{on} is the probability of the gene to be in the active state and given by $k_{on}/(k_{on}+k_{off})$. Whereas, γ_g (= $k_{on}+k_{off}$) is the average lifetime of the active gene. The different sources of noise contributions are mentioned at the bottom of the equation. The mRNA noise is given by,

$$CV_m^2 = \frac{1}{\langle n_m \rangle} + \frac{1 - P_{on}}{\langle n_g \rangle} \cdot \frac{\tau_g}{\tau_g + \tau_m}$$
 1.4

which is very similar to the protein noise expression without the gene activation-deactivation steps (Figure 1.1). The model predicts that depending on the relative magnitude of activation and deactivation rates there are different types of behavior of noise strength with the average protein noise possible as transcription rate is varied. The transcriptional bursts were observed experimentally by directly counting the number of mRNA molecules over time in living amoeba Dictyostelium cells and in mammalian cells^{11–13}. As predicted by stochastic simulations, these bursts in mRNA causes positively-skewed non-Poissonian statistics, of mRNA. Although simple on-off model of gene provides some light on noise in gene expression but the mechanism through which gene becomes active or active is still unknown. Due to the transcriptional bursting, even with average bigger size protein noise in eukaryotic cells is larger than the noise in eukaryotic cells. In fact, the cells from higher organism show more protein variability compared to lower organism due to higher transcriptional noise arises from complex packing of DNA. The analytical calculation of CME for protein reveals that protein distribution follows a Gamma distribution¹⁴.

The stochastic trajectories of gene expression and consequent cellular heterogeneity was found due to both intrinsic and extrinsic sources of noise inside a living cell. Collectively these two sources of noise are called as 'chemical noise', 15–17.

Introduction

1.1.1 Intrinsic noise

Low copy number of reacting species inside the tiny volume of a living cell leads to discrete firing of reactions events leading to irregular outcome of chemical reactions leading to stochastic trajectories. Such noisy outcome is purely due to the involvement of finite number of molecular species and therefore it is often termed as 'finite number effect'. The finite number effect is purely intrinsic to a particular chemical reaction and thus the noisy behavior is said to be due to the intrinsic noise of the chemical system. Based on the $CV \propto 1/\sqrt{N}$ scaling law of noise with N number of molecular species, the magnitude of intrinsic noise increases with decreasing molecular abundance.

1.1.2 Extrinsic noise

In addition to the intrinsic stochasticity, cell to cell variation of external factors also contribute to the stochasticity of chemical reactions. The extrinsic noise includes global variations in the factors that do not directly correspond to a specific chemical reaction. Such factors can be the variations in cellular volume, copy number variations of transcription factors, ribosome and organelle contents etc. Swain et al. proposed and Elowitz et al. developed a sophisticated method to measure the origins of gene expression noise. In this dual-reporter approach, the transcription of two genes is driven by identical promoters, resulting in the production of two distinct but otherwise nearly similar proteins. In the absence of intrinsic noise, the amount of both gene products, proteins in a cell would always be the same if extrinsic sources of noise affect both promoters in a same manner. This expressly assumes that both genes are translated and transcribed with the same efficiency under the same extrinsic conditions and that both proteins degrade at the same pace. As a result, the intrinsic noise is quantified by the size of the variation in protein levels across a large population of cells, whereas the sum of intrinsic and extrinsic noise characterises the size of the overall fluctuations.

1.2 Complexity in biological networks

Biological complexity arises at different levels of regulation. For example the information flow from DNA to proteins which govern the process of metabolism for *E.coli* is presented in the Figure 1.3. Around 4,000 genes are encoded into proteins or enzymes that catalyse

approximately 1,000 biochemical reactions. Each step of protein production is controlled by multiple and overlapping regulation loops of activator or repressor. These biochemical reactions dictate different cellular functions. Thus, the overall molecular networks look remarkably similar to the wired diagram of any modern electronic circuits. Instead of resistor, capacitors and transistor hooked together by wire, here genes, proteins, metabolites interacting with each other through chemical reactions.

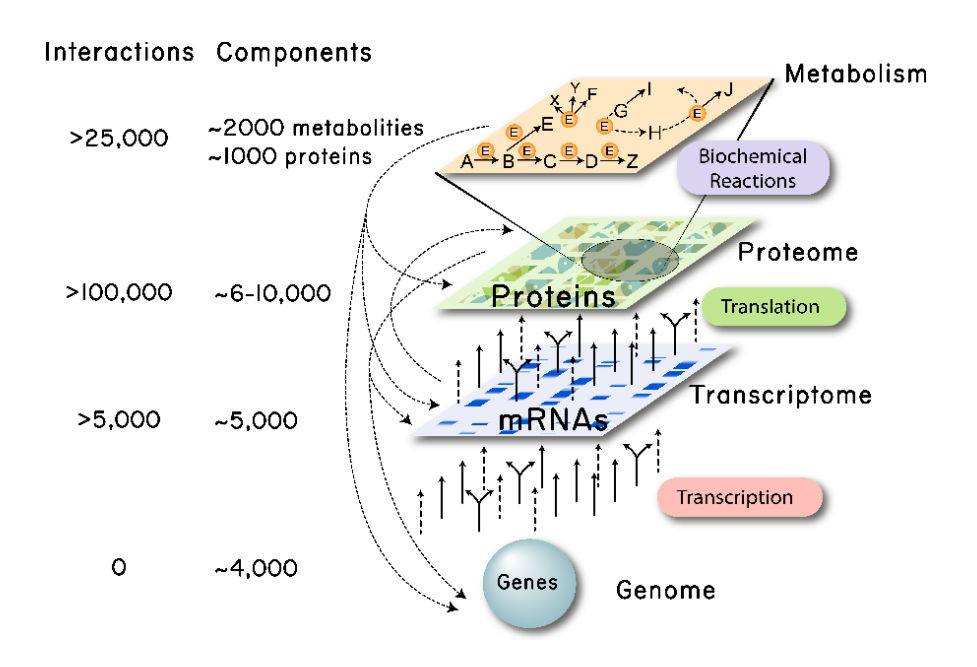


Figure 1.3. Complex cellular networks for metabolism in *E. Coli*. Dashed line indicates the regulatory interactions.

Apart from network complexity each biochemical processes are precisely modelled to work under specific set of physio-chemical conditions. Like slight change in the temperature, pH or the concentration would impact largely in the reaction outcome affecting the target functions. As an example, in case of the cellular differentiation during the cell cycle, a change in the experiment conditions, e.g., initial conditions, stimulus, can be resulted in a different cell, even can show counter-intuitive patterns. This is due to the dynamic characteristics and non-linearity of this process. There is additional level of complexity like organisation of different cell types which form tissues and leading to an organ.

Recent advancement in molecular biology have been undoubtably taken our knowledge of biological systems to the next level. However, as mentioned above only genes, protein and

Introduction

their interconnections alone are not sufficient to describe all the complexities in physiological process. Thus, a system level analysis of biological systems is needed to provide a deeper insight into these biological phenomena.

1.3 Systems biology and mathematical modeling.

The increasing amount of data collected on individual cellular components and a better understanding of these interactions has led to the emergence of systems biology as a new interdisciplinary field that regards biological processes as dynamic networks. In general, this investigates the complex relationships within such systems using mathematical techniques and computer simulations, with the ultimate goal of developing new, improved biological systems for practical uses like the efficient prevention or treatment of diseases^{19–21}. Here the biological networks are abstracted as a 'model'. The model basically translates the information of the temporal evolution of its state in some formal form. It allows to visualize and predict the cause and effect of the biological system with time through different computer simulations. With the help of modeling, one can rapidly analyse the effect of different experimental conditions without performing complex and costly experiments. These models can be tweaked accordingly to prior known experimental facts. Further analysing of the model helps to understand with specific part of system which contribute the most for the desired properties of interest. Therefore, the goal of biological network modelling is to accurately encode the knowledge of biological systems.

To study biological systems, several modeling and simulation techniques are used. The deterministic approach, which considers the concentration of molecular species, has the capacity to forecast the dynamic behaviour of biochemical systems. The law of mass action, which asserts that the rate of a reaction is directly proportional to the concentration of reactant molecules, is frequently applied in deterministic approaches. A set of ordinary differential equations (ODEs), sometimes known as reaction rate equations, thoroughly describes the time evolution of a biochemical network (RREs). As a result, an analytical or numerical method can be used to generate the system's full dynamic image given an initial condition. Further, the behaviour of ODE can also be studied using a variety of well-developed methods, including as stability and bifurcation analysis²².

1.4 Network motifs

As already mentioned in the Section 1.2, a living cell is basically a miniature biochemical machinery which responds towards its environment in a sophisticated manner in order to sustain and reproduce. The cell membrane is densely packed with different cellular receptors which are sensitive to various external ques like temperature, pressure, osmotic stress. A cell's capacity for information processing is carried out via complex networks of interconnected proteins and genes, an illustration is portrayed in Tyson et al. paper²³. Now the study of overall information processing unit is a tedious task to perform due to large number of components which result in different reaction time scales, abundances. Thus, one can look in to different alternatives, apart from studying the such reaction networks at whole. If these networks are looked closely one can find several repeating sub units, these are termed as 'network motifs' 24,25. Each of these sub-units, defined by a certain arrangement of interactions between nodes connected with edges, may represent a structure that effectively performs a specific function. These network motifs received a lot of attention recently as a practical idea for identifying the structural design principles of complicated networks. Though these network motifs can give a thorough understanding of the overall network's functional capabilities, but detecting them computationally is challenging.

Holland and Leinhardt first in 1970 introduced the theory of network motifs by introducing the idea of a triad census of networks²⁶. They proposed techniques for counting alternative subgraph configurations and determining if the subgraph counts deviate statistically from what is predicted in random networks. Uri Alon and his team in 2002^{24} , first generalised the idea when network motifs were found in the gene regulatory networks of *E. coli*. Numerous research projects on the topic have been carried out since then. While some works are concentrated on the computational theory of network motifs, other studies concentrate on their biological applications.

A network motif often consists of nodes, which generally represent macromolecules like genes, proteins, transcription factors, etc and vertices termed as 'edges', which describe the nature of interactions between different nodes. Depending upon the type of interactions and the arrangement of nodes these network motifs show different functional capabilities.

Introduction

1.4.1 Feedback loops

The most common interactions between these systems are the feedback loops. As the name suggest, in these motifs the output data is fed back to the system's input. Positive feedback occurs when output speeds up the transformation input and thus intensify its own production, i.e.; input and output both helping each other. In negative feedback motif, the output counters the input (Figure 1.4).

Negative feedback systems make up the majority of biological feedback systems. When a system's output reduces or dampens the processes that result in its output, the system produces less output. Thus, negative feedback loops (NFL) typically enable systems to self-stabilize. A crucial regulating mechanism for maintaining the body's homeostasis is negative feedback²⁷. NFL can also generate oscillatory responses^{28,29}. Various core regulatory network motifs in circadian clock systems³⁰, cAMP signalling³¹, NF-KB signalling^{32,33}, In general, NFL attenuates noisy input signals by suppressing the signal amplitudes. Whereas, positive feedback loops (PFL) amplify signals^{27,34}, thus causes instability. Another aspect of PFL is multistability. System with a PFL and ultrasensitive response architecture has the capacity to generate digital switch responses, which is termed as 'bistability'^{35–38}. Upon increasing the number of PFLs these responses can show tristability^{39–41} or even multistability. With this switch like phenomena, cell regulates crucial decision-making process for example is cellular differentiation^{42–44}, cell cycle^{45–48} cellular memory^{49,50}.

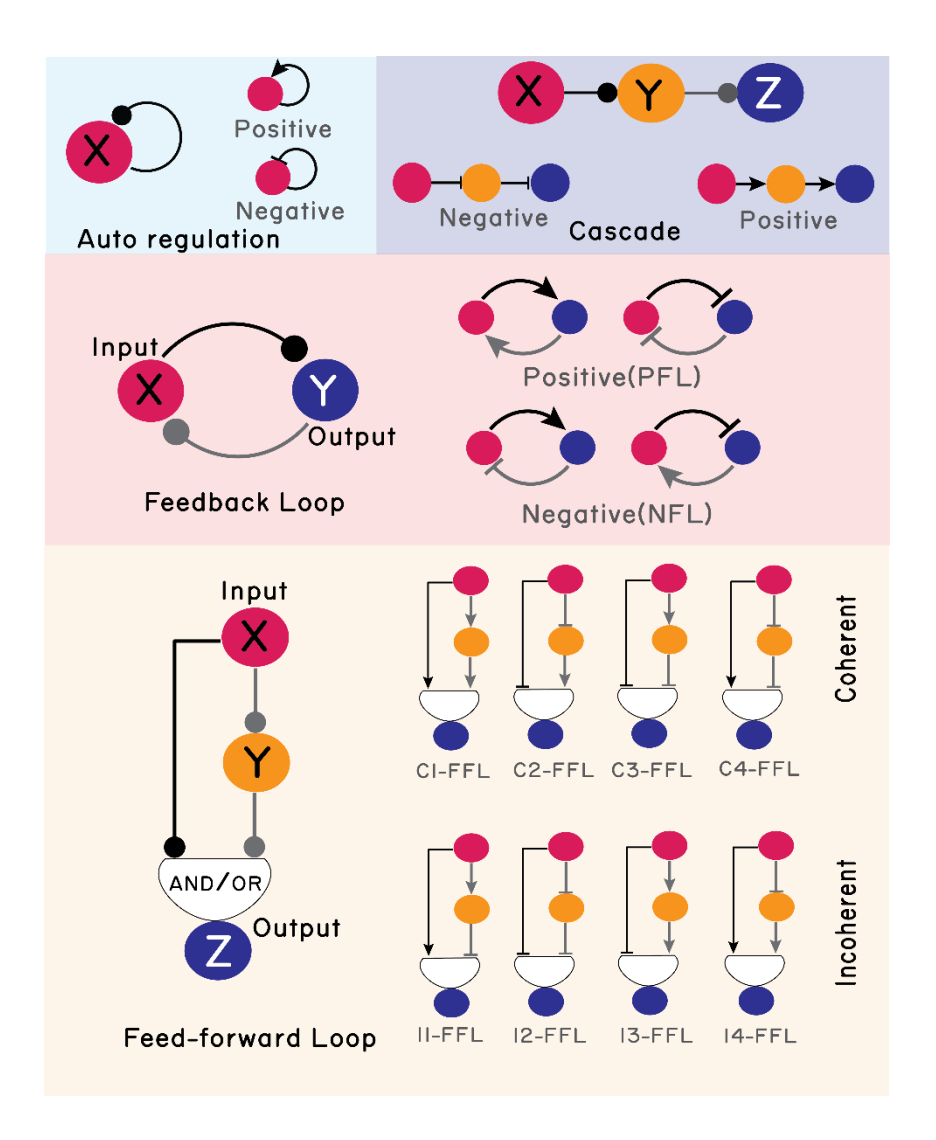


Figure 1.4. Schematic diagram of recurrently found network motifs. Different colored circles denotes different nodes and vertices with different arrow heads represents different interactions. The normal arrow represents activation, the 'T' shaped arrow head represents inhibition and the rounded arrowhead can be either activation or inhibition.

1.4.2 Feed-forward loops

The feed-forward loop (FFL) is one of the recurrently found network motifs. In FFL network motif, a regulator, X (input node), controls Z (output node) in two ways, one directly and other indirectly by controlling Y which in turn controls Z. These FFLs have eight different structural forms since each of the three interactions in the FFL can either be an activation or a repression. Network topologies where both the direct arm and the indirect arm (via Y) from X have similar function of acting activator or repressor on Z are labelled as 'Coherent' and topologies with two dissimilar arms are labelled as 'Incoherent' feed-

Introduction

forward loops. In many cases, X and Y work together as roughly AND or OR gates to control Z. The coherent type 1 FFL (C1-FFL) and the incoherent type 1 FFL (I1-FFL) are the two most prevalent FFLs. The C1-FFL with an AND gate functions as both a persistence detector and a 'sign-sensitive delay' element. I1-FFL can work as a pulse generator and response accelerator. The I1-FFL has the capability to work as a fold-change detector for a specific range of parameters, where response dynamics strictly depend only on the fold-change of the input signal rather than the absolute change⁵¹. Examples of other network motifs are autoregulations⁵², cascades, interlinked PFLs and NFLs, and integrated FFLs⁵³.

1.5 Performance of reaction networks under chemical noise

Now the discussion lies on how the inherent cellular noise affects the function of different gene regulatory networks. A living cell is programmed in such a way that it can adapt to any changes in its environment by gathering and processing the information. The same set of genes are present in all the cells in the human body, yet they code for a wide variety of cell types. The most accepted conclusion regarding this is that distinctively different stable states of the underlying gene regulation network typically result in qualitatively different cell morphologies (Citation). Cells are forced to differentiate into these different phenotypic states by the developmental programme. This switching can occasionally be hampered by the random intrinsic and extrinsic fluctuations^{54–56}. These inherent fluctuations can also force the system to make binary cellular decisions⁵⁷. For example, a simple signalling network with fused positive and negative feedback loops produces a bimodal distributed downstream signalling product instead of an anticipated intermediate value. Another example, where noise has an impact on cellular dynamics is genetic oscillators, i.e., the circadian clock. Even when deterministic rate equations predict a stable steady state, genetic oscillator networks can produce oscillations in the presence of cellular noise⁵⁸. This shows how noise can cause a system to leave a stable fixed point and begin a new cycle, which is a manifestation of the 'stochastic resonance' phenomena. By adjusting the level of noise, the incidence of oscillations can also be controlled.

1.6 Objective of the thesis

A living cell must be dependable and robust in order to respond appropriately to diverse internal and external cues and to ensure their long-term survival. These two crucial characteristics of biological systems are hindered by the stochasticity of chemical reactions emanating from both intrinsic and external sources. Typically, this results in a population heterogeneity of many cellular features that is of little consequence, such as desynchronization in oscillatory response⁵⁹ and variability in important signalling events during the cell cycle⁶⁰. However, the heterogeneity has occasionally been discovered to be advantageous for living things^{61,62}. For instance, under stress, the gene expression noise enables single-cell organisms to quickly adapt to the new environment. Ultimately, this enables the organisms to survive and even thrive in an adverse environment through phenotypic diversity^{63,64}. Thus, apart from already well investigated gene expression noise, it is interesting to study the noise propagation in other regulatory reactions which are equally essential in maintaining proper cellular functions. This thesis work mainly focused on the study of chemical noise propagation and its effect on the functional properties of such regulatory reaction networks.

1.6.1 Previous work

Theoretical and computational models of gene expression noise were able to quantitatively explain many experimental observations on protein noise by using probabilistic descriptions of chemical events. These models have emphasised the importance of differences in the average protein and mRNA lifetimes, as well as translational and transcriptional bursts in the noise of gene expression as discussed in Section 1.1. Further research was carried out to understand how feedback regulations affect the attenuation or amplification of biochemical noise. Early research showed that whereas positive feedback amplifies noise, negative feedback has the potential to reduce noise. Later calculations, however, showed that PFL also has the capacity to do so with maintaining higher sensitivity toward the incoming signal as compared to NFL ⁶⁵. This study further extended to analysis of role of different network topology in noise propagation (Citation). Like many gene regulatory networks found to have multiple positive or negative feedback loop and both PFL/NFL interlinked as core regulatory motif. Parallel arrangements of interconnected positive feedback loops are found to be better topology to efficiently reduce chemical noise

Introduction

as compared to its serial analogue⁶⁶. More recent study also includes the epigenetic controls of gene expression noise, where effect of nucleosome positioning, TATA box binding affinity and transcription factor binding sites have all been further investigated in prokaryotic and eukaryotic systems^{67,68}.

1.6.2 Layout of thesis

In chapter 2, the methodologies were briefly explained that were used to study the stochasticity in chemical reaction networks. The intrinsic stochasticity in a chemical reaction network was quantified by determining the steady state variance or covariance of the chemical species of interest. Thus, both analytical and numerical routes to determine various statistical quantities of chemical species was used. In this chapter, the analytical method of system size expansion of the chemical master equation was first outlined that allows to quantify statistical quantities. Next, the numerical method of Gillespie's stochastic simulation algorithm was summarised that has been used extensively in various chapters. Finally, recently developed pseudo-potential energy based bifurcation analysis method was explained which was further tweaked to determine the effect of extrinsic noise on the heterogeneity of bistable response.

The quantitative and qualitative nature of chemical noise propagation in biochemical reaction networks depends crucially on the topology of the networks. Multisite reversible phosphorylation-dephosphorylation of target proteins is one such recurrently found topology that regulates a host of key functions in living cells. In chapter 3, the stochasticity in multistep reversible phosphorylation /dephosphorylation reactions were analytically calculated. Using linear noise approximation, the steady state variance of phosphorylated species in order to investigate the effect of mass action and Michaelis-Menten kinetics on the noise of phosphorylated species were determined. The dependence of noise on the number of phosphorylation sites and the equilibrium constants of the reaction equilibria was further probed to investigate the chemical noise propagation in the multisite phosphorylation chain.

Cells often encounter a plethora of external and internal signals in a non-sustained pulsatile manner with varying amplitude, duration and residual value. However, the effect of signal pulse on the regulatory networks is poorly understood. In chapter 4, pulse induced population inversion kinetics was investigated in bistable switches generated either by

mutual activation or by mutual inhibition motifs to gain a quantitative understating of pulse processing by noisy chemical reactions involved. Population inversion and its maintenance required a proper tuning of all three signal parameters. From the investigation it was concluded that a bistable switch originating from mutual activation loop is found to be less susceptible to spurious signals as compared to the mutual inhibition loop.

Due to the extrinsic source of heterogeneity in isogenic cell populations, the strength of regulatory interactions in similar regulatory motifs may vary from one cell to another. This variability in the strength of regulatory interactions may result in different qualitative behaviors. In chapter 5, the robustness of such network topologies attaining bistable responses in presence of extrinsic noise was investigated. Here, total 14 different twocomponent positive feedback loop (PFL) networks were worked out, where the PFL was achieved either by a mutual activation or a mutual inhibition loop topology and both the components(genes/proteins) are regulated by a common regulator. Using pseudo potential energy based high-throughput bifurcation analysis, by sampling millions of random parameter combinations, we found out that these PFL networks with dual signing arms are capable of generating a variety of noncanonical bistable switches. These noncanonical switches may consist of one or multiple bistable regions that originate from the fusion of multiple canonical bistable switches in different orientations. We found that the mutual inhibition network with coherent signaling and mutual activation network with incoherent signaling generated both canonical and noncanonical responses. Whereas, other network topologies were more robust towards any variability in their regulatory interactions, resulting in only canonical responses. The occurrence probabilities showed that noncanonical switches such as isola and mushroom are highly probable in randomized parameter conditions. The phase diagrams of these switches unveiled that the feedback strengths of the PFL dictated the transition from one switch to another.

The functions of a living cell rely on a complex network of biochemical reactions that allow it to respond against various internal and external cues. The global network topology of these gene regulation networks is an intriguing feature. Although the propagation of chemical noise in biological reaction networks involved in small regulatory motifs has been extensively studied in the literature, but investigation of stochasticity in a generalised network is sparse. In the chapter 6, chemical noise was computationally investigated in these global reaction networks with democratic (Chapter 6a) and autocratic (Chapter 6b) architecture. The effects of the qualitative and quantitative nature of interactions between

nodes(genes/proteins) on the propagation of intrinsic noise in the network were extensively studied. In the case of democratic network, an ultrasensitive switching of average was found with an increased number of inhibitory signals. This led to a sharp transition of intrinsic noise and the intrinsic noise exhibits a biphasic power-law scaling with the average. Whereas in autocratic network architecture, an unconventional scaling of noise with average abundance was found. Here the noise passed through a minimum, suggested that the network may be noisy at both low and high abundance. The bursty kinetics of the trajectories at a higher number of activatory interactions were found to be responsible for this scaling.

In last chapter, the future scope of the research work was discussed. A pulsatile signal was used investigate the difference between the transition kinetics for a bistable system originating two different network topologies. This work can be extended further with other types of input signals and network topologies with noncanonical responses. The work on the effect of extrinsic noise on the heterogeneity of bistable switches can be extended to tristable switches for suitable network motifs with additional feedback loops using our automated method. Further, the mass action rate law of chemical reactions was used to model the generalized networks to accurately capture the effect of intrinsic noise using Gillespie's SSA. In the future, it will be worthwhile to investigate the propagation of noise in networks with nonlinear rate laws using approximate simulation methods such as the chemical Langevin equation.

1.7 References

- (1) Michael B. Elowitz; Stanislas Leibler. A Synthetic Oscillatory Networkof Transcriptional Regulators. *Nature* **2000**, *403*, 335–338.
- Ozbudak, E. M.; Thattai, M.; Kurtser, I.; Grossman, A. D.; Van Oudenaarden, A. Regulation of Noise in the Expression of a Single Gene. *Nat. Genet.* **2002**, *31* (1), 69–73. https://doi.org/10.1038/ng869.
- (3) Blake, W. J.; Kærn, M.; Cantor, C. R.; Collins, J. J. Noise in Eukaryotic Gene Expression. *Nat.* 2003 4226932 **2003**, 422 (6932), 633–637. https://doi.org/10.1038/nature01546.
- (4) Raser, J. M.; O'Shea, E. K. Control of Stochasticity in Eukaryotic Gene Expression.

- *Science* (80-.). **2004**, 304 (5678), 1811–1814. https://doi.org/10.1126/SCIENCE.1098641/SUPPL_FILE/RASER.SOM.PDF.
- (5) Cai, L.; Friedman, N.; Xie, X. S. Stochastic Protein Expression in Individual Cells at the Single Molecule Level. *Nature* **2006**, *440* (7082), 358–362. https://doi.org/10.1038/nature04599.
- (6) Kampen, V. N. G. Stochastic Processes in Physics and Chemistry. *Stoch. Process. Phys. Chem.* **2007**. https://doi.org/10.1016/B978-0-444-52965-7.X5000-4.
- (7) Thattai, M.; Van Oudenaarden, A. Intrinsic Noise in Gene Regulatory Networks. *Proc. Natl. Acad. Sci. U. S. A.* **2001**, 98 (15), 8614–8619.
 https://doi.org/10.1073/PNAS.151588598/ASSET/296583DD-83EE-408D-8B96-34237EE6E852/ASSETS/GRAPHIC/PQ1515885005.JPEG.
- (8) Elowitz, M. B.; Leibler, S. A Synthetic Oscillatory Network of Transcriptional Regulators. *Nature* **2000**, *403*, 335. https://doi.org/10.1038/35002125.
- (9) Swain, P. S.; Elowitz, M. B.; Siggia, E. D. Intrinsic and Extrinsic Contributions to Stochasticity in Gene Expression. *Proc. Natl. Acad. Sci. U. S. A.* 2002, 99 (20), 12795–12800. https://doi.org/10.1073/PNAS.162041399/SUPPL_FILE/0413SUPPTEXT.PDF.
- (10) Paulsson, J. Summing up the Noise in Gene Networks. *Nat. 2004 4276973* 2004,427 (6973), 415–418. https://doi.org/10.1038/nature02257.
- (11) Chubb, J. R.; Trcek, T.; Shenoy, S. M.; Singer, R. H. Transcriptional Pulsing of a Developmental Gene. *Curr. Biol.* **2006**, *16* (10), 1018–1025. https://doi.org/10.1016/j.cub.2006.03.092.
- (12) Raj, A.; Peskin, C. S.; Tranchina, D.; Vargas, D. Y.; Tyagi, S. Stochastic MRNA Synthesis in Mammalian Cells. *PLoS Biol.* **2006**, *4* (10), 1707–1719. https://doi.org/10.1371/journal.pbio.0040309.
- (13) Suter, D. M.; Molina, N.; Gatfield, D.; Schneider, K.; Schibler, U.; Naef, F. Mammalian Genes Are Transcribed with Widely Different Bursting Kinetics. *Science* 2011, 332 (6028), 472–474. https://doi.org/10.1126/science.1198817.
- (14) Shahrezaei, V.; Swain, P. S. Analytical Distributions for Stochastic Gene Expression. *Proc. Natl. Acad. Sci. U. S. A.* **2008**, *105* (45), 17256–17261.

- https://doi.org/10.1073/PNAS.0803850105/SUPPL_FILE/APPENDIX_PDF.PDF.
- (15) Kærn, M.; Elston, T. C.; Blake, W. J.; Collins, J. J. Stochasticity in Gene Expression: From Theories to Phenotypes. *Nat. Rev. Genet.* 2005, 6 (6), 451–464. https://doi.org/10.1038/nrg1615.
- (16) Paulsson, J. Models of Stochastic Gene Expression. *Phys. Life Rev.* 2005, 2 (2), 157–175. https://doi.org/10.1016/j.plrev.2005.03.003.
- (17) Coulon, A.; Chow, C. C.; Singer, R. H.; Larson, D. R. Eukaryotic Transcriptional Dynamics: From Single Molecules to Cell Populations. *Nat. Rev. Genet.* **2013**, *14* (8), 572–584. https://doi.org/10.1038/nrg3484.
- (18) Elowitz, M. B.; Levine, A. J.; Siggia, E. D.; Swain, P. S. Stochastic Gene Expression in a Single Cell. *Science* (80-.). **2002**, 297 (5584), 1183–1186. https://doi.org/10.1126/SCIENCE.1070919/SUPPL_FILE/ELOWITZSOM.PDF.
- (19) Kitano, H. Foundations of Systems Biology. 2001, 297.
- (20) Kitano, H. Computational Systems Biology. *Nat. 2002 4206912* **2002**, *420* (6912), 206–210. https://doi.org/10.1038/nature01254.
- (21) Kitano, H. Systems Biology: A Brief Overview. *Science* (80-.). 2002, 295 (5560), 1662–1664. https://doi.org/10.1126/SCIENCE.1069492/ASSET/2746D838-E2BC-495A-AE68-95E58A86D09A/ASSETS/GRAPHIC/SE0820239001.JPEG.
- (22) Stumpf, M. P. H. (Michael P. H. .; Balding, D. J.; Girolami, M. Handbook of Statistical Systems Biology. **2011**, 508.
- (23) Tyson, J. J.; Novák, B. Functional Motifs in Biochemical Reaction Networks. http://dx.doi.org/10.1146/annurev.physchem.012809.103457 **2010**, 61, 219–240. https://doi.org/10.1146/ANNUREV.PHYSCHEM.012809.103457.
- (24) Alon, U. Network Motifs: Theory and Experimental Approaches. *Nat. Rev. Genet.* **2007**, 8 (6), 450–461. https://doi.org/10.1038/nrg2102.
- (25) Shen-Orr, S. S.; Milo, R.; Mangan, S.; Alon, U. Network Motifs in the Transcriptional Regulation Network of Escherichia Coli. *Nat. Genet.* 2002 311 **2002**, 31 (1), 64–68. https://doi.org/10.1038/ng881.
- (26) Holland, P.; Leinhardt, S. The Statistical Analysis of Local Structure in Social

- Networks. Sociol. Methodol. 1974, 45.
- (27) Kim, J. R.; Yoon, Y.; Cho, K. H. Coupled Feedback Loops Form Dynamic Motifs of Cellular Networks. *Biophys. J.* **2008**, *94* (2), 359–365. https://doi.org/10.1529/BIOPHYSJ.107.105106/ATTACHMENT/14A1E198-95F9-44BD-BD1C-B80D52485A02/MMC1.PDF.
- (28) Jensen, M. H.; Sneppen, K.; Tiana, G. Sustained Oscillations and Time Delays in Gene Expression of Protein Hes1. *FEBS Lett.* **2003**, *541* (1–3), 176–177. https://doi.org/10.1016/S0014-5793(03)00279-5.
- (29) Pigolotti, S.; Krishna, S.; Jensen, M. H. Oscillation Patterns in Negative Feedback Loops. *Proc. Natl. Acad. Sci. U. S. A.* **2007**, *104* (16), 6533–6537. https://doi.org/10.1073/pnas.0610759104.
- (30) Duong, H. A.; Robles, M. S.; Knutti, D.; Weitz, C. J. A Molecular Mechanism for Circadian Clock Negative Feedback. *Science* (80-.). 2011, 332 (6036), 1436–1439. https://doi.org/10.1126/SCIENCE.1196766/SUPPL_FILE/1196766.DUONG.SOM .PDF.
- (31) Mika, D.; Richter, W.; Conti, M. A CaMKII/PDE4D Negative Feedback Regulates Camp Signaling. *Proc. Natl. Acad. Sci. U. S. A.* 2015, 112 (7), 2023–2028. https://doi.org/10.1073/PNAS.1419992112/SUPPL_FILE/PNAS.1419992112.SAP P.PDF.
- (32) Hoffmann, A.; Levchenko, A.; Scott Martin, L.; Baltimore, D. The IκB-NF-KB Signaling Module: Temporal Control and Selective Gene Activation. *Science* (80-.). 2002, 298 (5596), 1241–1245. https://doi.org/10.1126/science.1071914.
- (33) Krishna, S.; Jensen, M. H.; Sneppen, K. Minimal Model of Spiky Oscillations in NF-KappaB Signaling. *Proc. Natl. Acad. Sci. U. S. A.* 2006, 103 (29), 10840–10845. https://doi.org/10.1073/PNAS.0604085103.
- (34) Brandman, O.; Meyer, T. Feedback Loops Shape Cellular Signals in Space and Time. *Science* (80-.). **2008**, 322 (5900), 390–395. https://doi.org/10.1126/SCIENCE.1160617/SUPPL_FILE/SIMULATEFEEDBAC KSYSTEMS.ZIP.
- (35) Ferrell, J. E.; Xiong, W. Bistability in Cell Signaling: How to Make Continuous

- Processes Discontinuous, and Reversible Processes Irreversible. *Chaos* **2001**, *11* (1), 227–236. https://doi.org/doi.http://dx.doi.org/10.1063/1.1349894.
- (36) Angeli, D.; Ferrell, J. E.; Sontag, E. D. Detection of Multistability, Bifurcations, and Hysteresis in a Large Class of Biological Positive-Feedback Systems. *Proc. Natl. Acad. Sci.* **2004**, *101* (7), 1822–1827. https://doi.org/10.1073/pnas.0308265100.
- (37) Ingolia, N. T.; Murray, A. W. Positive-Feedback Loops as a Flexible Biological Module. *Curr. Biol.* **2007**, *17* (8), 668–677. https://doi.org/10.1016/J.CUB.2007.03.016.
- (38) Leite, M. C. A.; Wang, Y.; Leite, M. C. A.; Wang, Y. Multistability, Oscillations and Bifurcations in Feedback Loops. *Math. Biosci. Eng. 2010 183* **2010**, *7* (1), 83–97. https://doi.org/10.3934/MBE.2010.7.83.
- (39) Huang, B.; Xia, Y.; Liu, F.; Wang, W. Realization of Tristability in a Multiplicatively Coupled Dual-Loop Genetic Network. *Sci. Reports* 2016 61 **2016**, 6 (1), 1–12. https://doi.org/10.1038/srep28096.
- (40) Qi, H.; Li, Z. C.; Wang, S. M.; Wu, L.; Xu, F.; Liu, Z. L.; Li, X.; Wang, J. Z. Tristability in Mitochondrial Permeability Transition Pore Opening. *Chaos An Interdiscip. J. Nonlinear Sci.* 2021, 31 (12), 123108. https://doi.org/10.1063/5.0065400.
- (41) Dey, A.; Barik, D. Potential Landscapes, Bifurcations, and Robustness of Tristable Networks. *ACS Synth. Biol.* **2021**, *10* (2), 391–401. https://doi.org/10.1021/ACSSYNBIO.0C00570/SUPPL_FILE/SB0C00570_SI_001.PDF.
- (42) Park, B. O.; Ahrends, R.; Teruel, M. N. Consecutive Positive Feedback Loops Create a Bistable Switch That Controls Preadipocyte-to-Adipocyte Conversion. *Cell Rep.* **2012**, *2* (4), 976–990. https://doi.org/10.1016/J.CELREP.2012.08.038.
- (43) Zhang, J.; Tian, X. J.; Zhang, H.; Teng, Y.; Li, R.; Bai, F.; Elankumaran, S.; Xing, J. TGF-β-Induced Epithelial-to-Mesenchymal Transition Proceeds through Stepwise Activation of Multiple Feedback Loops. *Sci. Signal.* **2014**, 7 (345), ra91. https://doi.org/10.1126/SCISIGNAL.2005304/SUPPL_FILE/7_RA91_SM.PDF.
- (44) Hong, T.; Watanabe, K.; Ta, C. H.; Villarreal-Ponce, A.; Nie, Q.; Dai, X. An Ovol2-

- Zeb1 Mutual Inhibitory Circuit Governs Bidirectional and Multi-Step Transition between Epithelial and Mesenchymal States. *PLOS Comput. Biol.* **2015**, *11* (11), e1004569. https://doi.org/10.1371/JOURNAL.PCBI.1004569.
- (45) Pomerening, J. R.; Sontag, E. D.; Ferrell, J. E. Building a Cell Cycle Oscillator: Hysteresis and Bistability in the Activation of Cdc2. *Nat. Cell Biol.* 2003 54 **2003**, 5 (4), 346–351. https://doi.org/10.1038/ncb954.
- (46) Skotheim, J. M.; Di Talia, S.; Siggia, E. D.; Cross, F. R. Positive Feedback of G1 Cyclins Ensures Coherent Cell Cycle Entry. *Nat.* 2008 4547202 2008, 454 (7202), 291–296. https://doi.org/10.1038/nature07118.
- (47) Yao, G.; Tan, C.; West, M.; Nevins, J. R.; You, L. Origin of Bistability Underlying Mammalian Cell Cycle Entry. *Mol. Syst. Biol.* **2011**, *7* (1), 485. https://doi.org/10.1038/MSB.2011.19.
- (48) Yang, X.; Lau, K.-Y.; Sevim, V.; Tang, C. Design Principles of the Yeast G1/S Switch. *PLOS Biol.* **2013**, *11* (10), e1001673. https://doi.org/10.1371/journal.pbio.1001673.
- (49) Chang, D. E.; Leung, S.; Atkinson, M. R.; Reifler, A.; Forger, D.; Ninfa, A. J. Building Biological Memory by Linking Positive Feedback Loops. *Proc. Natl. Acad. Sci. U. S. A.* **2010**, *107* (1), 175–180. https://doi.org/10.1073/PNAS.0908314107.
- (50) Xiong, W.; Ferrell, J. E. A Positive-Feedback-Based Bistable "memory Module" That Governs a Cell Fate Decision. *Nature* **2003**, *426* (6965), 460–465. https://doi.org/10.1038/NATURE02089.
- (51) Mangan, S.; Alon, U. Structure and Function of the Feed-Forward Loop Network Motif. Proc. Natl. Acad. Sci. U. S. A. 2003, 100 (21), 11980–11985. https://doi.org/10.1073/PNAS.2133841100/SUPPL_FILE/3841TABLE5.XLS.
- (52) Becskel, A.; Serrano, L. Engineering Stability in Gene Networks by Autoregulation. *Nat.* 2000 4056786 **2000**, 405 (6786), 590–593. https://doi.org/10.1038/35014651.
- (53) Shoval, O.; Alon, U. SnapShot: Network Motifs. Cell 2010, 143 (2), 326-326.e1. https://doi.org/10.1016/J.CELL.2010.09.050.
- (54) Arkin, A.; Ross, J.; McAdams, H. H. Stochastic Kinetic Analysis of Developmental Pathway Bifurcation in Phage λ-Infected Escherichia Coli Cells. *Genetics* **1998**, *149*

- (4), 1633–1648. https://doi.org/10.1093/GENETICS/149.4.1633.
- (55) Schultz, D.; Wolynes, P. G.; Jacob, E. Ben; Onuchic, J. N. Deciding Fate in Adverse Times: Sporulation and Competence in *Bacillus Subtilis. Proc. Natl. Acad. Sci.*2009, 106 (50), 21027–21034. https://doi.org/10.1073/PNAS.0912185106.
- (56) Ahrends, R.; Ota, A.; Kovary, K. M.; Kudo, T.; Park, B. O.; Teruel, M. N. Controlling Low Rates of Cell Differentiation through Noise and Ultrahigh Feedback. *Science* (80-.). 2014, 344 (6190), 1384–1389. https://doi.org/10.1126/SCIENCE.1252079/SUPPL_FILE/AHRENDS.SM.PDF.
- (57) Artyomov, M. N.; Das, J.; Kardar, M.; Chakraborty, A. K. Purely Stochastic Binary Decisions in Cell Signaling Models without Underlying Deterministic Bistabilities. *Proc. Natl. Acad. Sci. U. S. A.* **2007**, *104* (48), 18958–18963. https://doi.org/10.1073/PNAS.0706110104/SUPPL_FILE/06110FIG14.PDF.
- (58) Vilar, J. M. G.; Kueh, H. Y.; Barkai, N.; Leibler, S. Mechanisms of Noise-Resistance in Genetic Oscillators. *Proc. Natl. Acad. Sci. U. S. A.* 2002, 99 (9), 5988–5992. https://doi.org/10.1073/PNAS.092133899/ASSET/56ABB4CA-CCD6-4C4F-94F1-C3C9817EB971/ASSETS/GRAPHIC/PQ0921338007.JPEG.
- (59) Geva-Zatorsky, N.; Rosenfeld, N.; Itzkovitz, S.; Milo, R.; Sigal, A.; Dekel, E.; Yarnitzky, T.; Liron, Y.; Polak, P.; Lahav, G.; Alon, U. Oscillations and Variability in the P53 System. *Mol. Syst. Biol.* **2006**, 2, 2006.0033. https://doi.org/10.1038/MSB4100068.
- (60) Talia, S. Di; Skotheim, J. M.; Bean, J. M.; Siggia, E. D.; Cross, F. R. The Effects of Molecular Noise and Size Control on Variability in the Budding Yeast Cell Cycle. Nat. 2007 4487156 2007, 448 (7156), 947–951. https://doi.org/10.1038/nature06072.
- (61) Balázsi, G.; Van Oudenaarden, A.; Collins, J. J. Cellular Decision Making and Biological Noise: From Microbes to Mammals. *Cell* 2011, 144 (6), 910–925. https://doi.org/10.1016/j.cell.2011.01.030.
- (62) Eldar, A.; Elowitz, M. B. Functional Roles for Noise in Genetic Circuits. *Nat. 2010* 4677312 **2010**, 467 (7312), 167–173. https://doi.org/10.1038/nature09326.
- (63) Weinberger, L. S.; Burnett, J. C.; Toettcher, J. E.; Arkin, A. P.; Schaffer, D. V.

- Stochastic Gene Expression in a Lentiviral Positive-Feedback Loop: HIV-1 Tat Fluctuations Drive Phenotypic Diversity. *Cell* **2005**, *122* (2), 169–182. https://doi.org/10.1016/j.cell.2005.06.006.
- (64) Raj, A.; van Oudenaarden, A. Nature, Nurture, or Chance: Stochastic Gene Expression and Its Consequences. *Cell* **2008**, *135* (2), 216–226. https://doi.org/10.1016/J.CELL.2008.09.050.
- (65) Hornung, G.; Barkai, N. Noise Propagation and Signaling Sensitivity in Biological Networks: A Role for Positive Feedback. *PLOS Comput. Biol.* **2008**, *4* (1), e8. https://doi.org/10.1371/JOURNAL.PCBI.0040008.
- (66) Dey, A.; Barik, D. Parallel Arrangements of Positive Feedback Loops Limit Cell-to-Cell Variability in Differentiation. *PLoS One* 2017, 12 (11), e0188623. https://doi.org/10.1371/JOURNAL.PONE.0188623.
- (67) Huh, I.; Zeng, J.; Park, T.; Yi, S. V. DNA Methylation and Transcriptional Noise. *Epigenetics and Chromatin* **2013**, *6* (1), 1–10. https://doi.org/10.1186/1756-8935-6-9.
- (68) Gibney, E. R.; Nolan, C. M. Epigenetics and Gene Expression. *Heredity (Edinb)*.2010, 105 (1), 4–13. https://doi.org/10.1038/hdy.2010.54.

CHAPTER 2

Methodology

2.1 Chemical Master Equation (CME)

A realistic strategy to describe the random and discrete nature of biological chemical reaction is stochastic kinetics, which provides a probabilistic description of chemical reactions. In stochastic kinetics, the state of a system is represented by a population vector which contains the information about the abundance of each species involved a coupled chemical reaction system. A reaction event leads to change in the state of the population vector according to the stoichiometry of the chemical reaction. The foundation of stochastic kinetics lies on the propensity function for each reaction, which indicates the likelihood of a specific reaction occurring in the upcoming infinitesimal time period. This can be derived based on the Markov property of biochemical reactions. The Chemical Master Equation (CME) is a full mathematical formulation for expressing the time evolution of the system state. The CME describes the time evolution of probability of a system having a specific number of molecular species.

Consider, a homogeneous chemical system in a volume, Ω , consisting N and R number of different chemical species and chemical reactions, respectively. The state of the system at a time t is defined by the state vector $\mathbf{X}(=[n_1,n_2,\ldots,n_i,\ldots,n_i,\ldots,n_{i_{max}}])$. Here, $n_i(t)$ is the molecular abundance of species i at time t. Considering v_j corresponds to the change in the state vector for the jth reaction, the time evolution of the probability density function, $P(\mathbf{X};t)$, can be given by the CME below:

$$\frac{dP(\mathbf{X},t)}{dt} = \sum_{j=1}^{R} \left[a_j (\mathbf{X} - v_j) P(\mathbf{X} - v_j, t) - a_j(\mathbf{X}) P(\mathbf{X}, t) \right]$$
 2.1

The summation over the first term on the right-side accounts for the probability of arriving to a state X during an infinitesimal time interval and this probability is basically the sum of

probabilities of leaving from $(X - v_j)$ state to X state. The second term in the CME represents the probability of leaving the state X.

Alternatively, the CME can be represented by the use of step operator as

$$\frac{dP(X,t)}{dt} = \Omega \sum_{j=1}^{R} \left(\prod_{i=1}^{N} \mathbb{E}^{-S_{ij}} - 1 \right) f_j(X,\Omega) P(X,t)$$
 2.2

Where, f_j is the transition rate of the j-th reaction. The macroscopic concentration vector is represented by $x = X/\Omega$. S_{ij} is the element of the stoichiometric matrix in which the element S_{ij} gives the <u>stoichiometric coefficient</u> for species i in the jth reaction. $\mathbb{E}^{-S_{ij}}$ is a step operator which removes S_{ij} from the ith species in the jth reaction. For example,

$$\mathbb{E}^{-S_{23}}f(x_1, x_2, x_3) = f(x_1, x_2 - S_{23}, x_3)$$
2.3

Now, the direct application of CME, is constrained by the fact that the complete probability distribution of a biological system over time can only be determined for a simple chemical system. Furthermore, analytical solution to the master equation may not be possible for reactions with nonlinear rates. Thus, the exact solution of CME is affected by the 'curse of dimensionality', which means that the number of degrees of freedom required for an accurate approximation grows exponentially with any increase in the number of components of the biological system. For instance, if we restrict the copy numbers to a maximum of 10 molecules per species in a relatively modest system with only three species, there will be 10^3 states, which results in 10^3 ODEs that must be solved in order to get the answer. Nevertheless, several approximations on CME have been established to obtain approximate analytical statistical description of the system. Further, there are simulation-based algorithms which mimics the stochastic kinetics.

2.2 van Kampen's system size expansion

In chapter 3, we used van Kampen's system size expansion on the CME in order to calculate steady state fluctuations in the phosphorylated species in multisite phosphorylation-dephosphorylation chains. This method have been extensively used to calculate the gene expression noise and noise in other biochemical reactions^{1–3}.

The main ansatz behind the van Kampen's system size expansion⁴ is that the variance of the steady-state probability distribution of the individual population scales with the system size. Copy number of the i^{th} species can be written as a sum of its 'deterministic' value with concentration, ϕ_i , and a random variable ξ with a scaling factor $\Omega^{1/2}$.

$$X_i = \Omega \Phi_i(t) + \Omega^{1/2} \xi_i$$
 2.4

That is, P(X, t) will have a sharp peak location at $\Omega \Phi$ and with a width of $\Omega^{1/2}$. So, the $\Omega \Phi$ is the 'macroscopic' part and $\Omega^{1/2} \xi$ is the fluctuating part of X. Accordingly, the probability distribution of X now became the probability distribution, Π of ξ .

$$P(X, t) = P(\Omega \Phi + \Omega^{1/2} \xi, t) = \Pi(\xi, t)$$
 2.5

Now following the transformation rules,

$$\frac{\partial \Pi}{\partial \xi} = \Omega^{1/2} \frac{\partial P}{\partial X} \qquad \frac{\partial P}{\partial t} = \frac{\partial \Pi}{\partial t} - \Omega^{1/2} \frac{d\Phi}{dt} \frac{\partial \Pi}{\partial t} \qquad 2.6$$

Using the Taylor series expansion, the transition rate in terms of random variable ξ is written as

$$f_j(x) = f_j(\Phi_i + \Omega^{-1/2}\xi_i) = f_j(\Phi) + \Omega^{-1/2} \sum_{i=1}^{N} \frac{\partial f_j(\Phi)}{\partial \Phi_i} \xi_i + O(\Omega^{-1}).$$
 2.7

As the step operation leads to $\mathbb{E}f_{(n)}=f_{(n+1)}$, the step operator in terms of random variable ξ is given by $\mathbb{E}f(\xi)=f(\xi+\Omega^{-1/2})$. Thus, for all chemical species

$$\prod_{i=1}^{N} \mathbb{E}^{-S_{ij}} \cong 1 - \Omega^{-1/2} \sum_{i} S_{ij} \frac{\partial}{\partial \xi_{i}} + \frac{\Omega^{-1}}{2} \sum_{i} \sum_{k} S_{ij} S_{kj} \frac{\partial^{2}}{\partial \xi_{i} \partial \xi_{k}} + O(\Omega^{-3/2})$$
 2.8

Recasting in the CME (2.2) in terms of the new variable leads to

Methodology

$$\frac{\partial \Pi(\xi,t)}{\partial t} - \Omega^{1/2} \sum_{i} \frac{d\Phi_{i}}{dt} \frac{\partial \Pi}{\partial t}$$

$$= \Omega \sum_{j=1}^{R} \left(-\Omega^{-1/2} \sum_{i} S_{ij} \frac{\partial}{\partial \xi_{i}} + \Omega^{-1} \sum_{i} \sum_{k} S_{ij} S_{kj} \frac{\partial^{2}}{\partial \xi_{i} \partial \xi_{k}} \right) \left(f_{j}(\Phi) \right)$$

$$+ \Omega^{-1/2} \sum_{i=1}^{N} \frac{\partial f_{j}(\Phi)}{\partial \Phi_{i}} \xi_{i} \right) \Pi(\xi,t)$$
2.9

When terms are gathered in various powers of Ω , this expression results in more sensible outcome. $\Omega^{1/2}$ terms give the macroscopic rate equation. The Ω^0 terms result in

$$\frac{\partial \Pi(\xi,t)}{\partial t} = \sum_{j=1}^{R} \left(\sum_{ik} -S_{ij} \frac{\partial f_j(\Phi)}{\partial \Phi_k} \frac{\partial (\xi_k \Pi(\xi,t))}{\partial \xi_i} + \frac{1}{2} f_j(\Phi) \sum_{ik} S_{ij} S_{kj} \frac{\partial^2 \Pi(\xi,t)}{\partial \xi_i \partial \xi_k} \right) \quad 2.10$$

Which can be written as,

$$\frac{\partial \Pi(\xi,t)}{\partial t} = -\sum_{ik} A_{ik} \frac{\partial (\xi_k \Pi)}{\partial \xi_i} + \frac{1}{2} \sum_{ik} B_{ik} \frac{\partial^2 \Pi(\xi,t)}{\partial \xi_i \partial \xi_k}$$
 2.11

Where,
$$A_{ik} = \sum_{j=1}^{R} \left(S_{ij} \frac{\partial f_j(\Phi)}{\partial \Phi_k} \right)$$
 and $B_{ik} = \sum_{j=1}^{R} \left(S_{ij} S_{kj} f_j(\Phi) \right)$

The equation (2.11) resembles with the linear multivariate Fokker-Plank equation where A_{ik} and B_{ik} are the constant matrices and termed as Linear Noise Approximation (LNA). The solution of the linear Fokker-Plank equation is known out to be Gaussian, which is fully determined by calculating the first order (mean) and second order moment (variance). Solving for the equation of the moments, the equation for time evolution of covariances is given as,

$$\frac{\partial \sigma_{ik}}{\partial t} = A_{ik}\sigma_{ik} + \sigma_{ik}A_{ik}^{T} + B_{ik}$$
 2.12

The equation (2.13) provides the information about the steady state variances of each species involved, which is equation (2.12) at steady state, $\frac{\partial \sigma_{ik}}{\partial t} = 0$,

$$A_{ik}\sigma_{ik} + \sigma_{ik} A_{ik}^{T} = -B_{ik}$$
 2.13

Where, σ is the matrix for covariances, σ_{ii} provides the variance of i^{th} species. A is the Jacobian or drift matrix and B is the diffusion matrix.

However, number of studies provides the insufficiency of the linear noise approximation as this fails to adequately account for noise in biological contexts^{5,6}. This prompted researchers to look into higher order system size expansion terms that go beyond linear approximation. With the help of these terms, moment estimates for the variances of the concentration fluctuations in intracellular pathways as well as the mean concentrations and concentrations have been more precisely calculated^{7,8}.

2.3. Gillespie's Stochastic Simulation Algorithm

Due to the limitations of analytical methods, numerical simulations have proven to a useful tool in investigation of noise in the biochemical reaction networks. The primary method for simulating and accurately estimating noise in reaction networks has been Gillespie's stochastic simulation algorithm (SSA)^{9,10}. The SSA provides an exact solution of CME for the coupled chemical reactions whose rates are represented by mass action kinetics. A flowchart for the algorithm is described in the Figure 2.1. The simulation technique is based on determination of the next time point for a chemical reaction and finding out the specific reaction that occurs at the time point. Here, the time interval (τ) of next reaction is chosen from an exponentially distributed random variable. This random variable is based on the sum of all reaction propensities $(a_0 = \sum_j a_j)$ and uniformly distributed random number (r_1) in the range [0,1] and given by,

$$\tau = \left(\frac{1}{a_0}\right) \ln\left(\frac{1}{r_1}\right) \tag{2.14}$$

The choice of next reaction (j) which will occur in the infinitesimal time interval $[t, t + \tau]$ is decided based on the inequality (2.15), basically the reaction probability is calculated by dividing its propensity by sum of propensities of all the reactions $(a_0 = \sum_j a_j)$ involved, and thereafter the species involved in the reaction will be updated according to the reaction stoichiometry.

$$\frac{\sum_{j=1}^{j'} a_j}{a_0} > r_2 \tag{2.15}$$

Based on the smallest j value satisfying the inequality, given j^{th} reaction will fire.

Hereby, a realization for a stochastic process is built by iteratively computing the next time step at which a reaction happens and sampling which reaction occurs. Letting this iterative process to run for a fairly long time, expecting the system has reached their steady state, we can get a single stochastic trajectory.

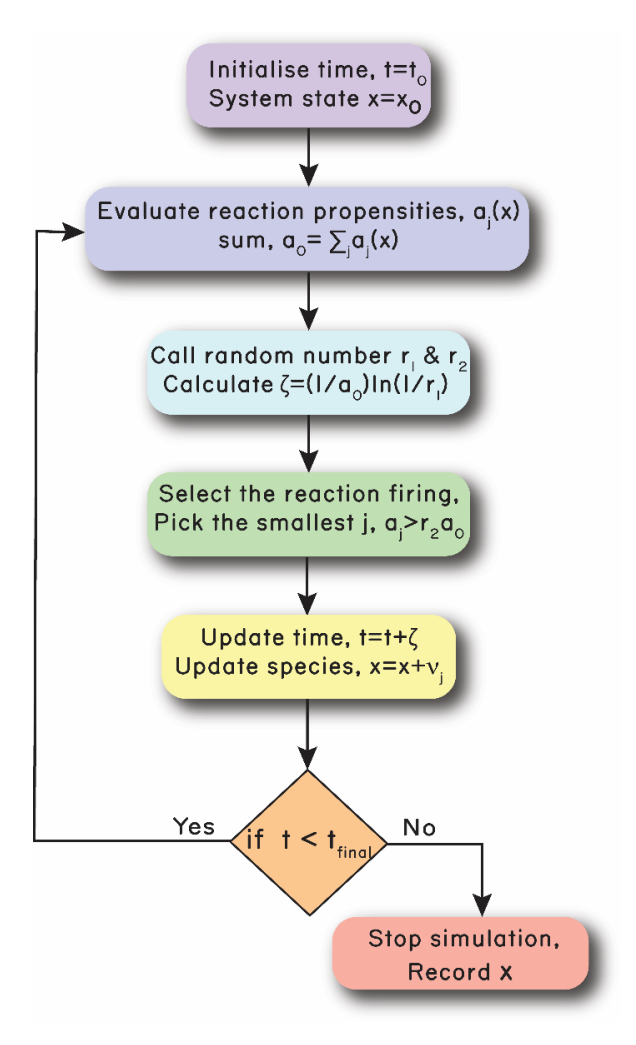


Figure 2.1. Flow chart of Gillespie's Stochastic Simulation Algorithm.

High computational cost is the major drawback of SSA. The SSA mimics each and every reaction event, therefore it becomes sluggish for systems that have a large number of these events. In this scenario, when there is a very big rate constant and a sizable number of molecules, Gillespie's algorithm spends a significant portion of its time choosing for updating that extremely fast reaction¹¹. This makes the computation ineffective. This has spurred research into algorithms that trade off part of the SSA's precision for faster simulation times. The suggested methods, such as the τ -leap method¹² and the Langevin method¹³, allow more than one reaction event per step which leads to faster simulation.

2.3 Pseudo Potential Energy Based Bifurcation Analysis Method

As, discussed in the introduction (Chapter 1), biochemical networks may often yield in distinct steady state and dynamical behaviors such as multistability, temporal pulses and oscillations etc. A part of thesis work is primarily based on the multistability which is found to be involved in many cellular decision processes and processing graded input signals into all or none responses. The signal response curve describes the steady state response of the system with the variation of signal. Mathematically, the qualitative change of the steady state behavior of the system with the change of a parameter is represented by 1-parameter bifurcation diagram. For example, Figure 2.2a shows the 1-parameter bifurcation diagram for a bistable switch. Conventional methods of generating such bifurcation diagrams in based on the concept of 'linear stability analysis' of the steady state of the system. This provides the information of change in stability of the system at the bifurcation point by measuring the eigen value of the Jacobian matrix. As a result, the eigenvalues of the steady states are tracked while the bifurcation parameter is changed in order to produce a bifurcation diagram. XPP-AUT is the widely used tool for running bifurcation analysis of nonlinear dynamical systems and typically bifurcation analysis is carried out by manually tweaking various control parameters in the numerical continuation method of bifurcation analysis.

However, in the Chapter 5, large scale bifurcation analysis needed to be performed under random variation of parameter space. Therefore, the conventional tool of bifurcation analysis cannot be used due to requirement of manual intervention for each bifurcation run. Hence, we developed and implemented a new bifurcation analysis method using the pseudo potential energy of the dynamical system^{14,15}. The theory underlying potential-based bifurcation analysis is based on the fact that for nonlinear dynamical systems, the steady states values correspond to the extrema of potential landscape of the system. The stable and unstable steady state of a system follows the location of minima and maxima of the potential, respectively. As a result, bifurcation diagrams can be generated by keeping an eye on how the extrema changes in and out of the potential landscape. However, the multidimensional dynamical systems pose the biggest challenge in calculating the potential landscape. Potential energy for dynamical systems with more than one dimension cannot be quantified generically because of their non-Newtonian nature. We solved this issue by applying the transfer function method to transform the multivariate system into a univariate

system. For example, two-dimensional equation of a mutual inhibition (MI) network model (2.16) can be written as:

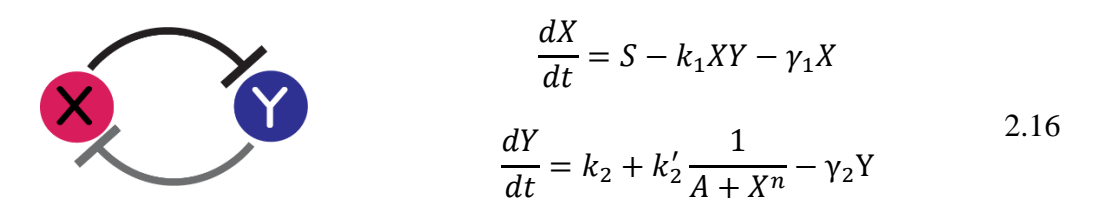


Figure 2.2 Schematic for MI network

At steady state (dY/dt = 0), Y can be written as a function of X and signal S as

$$Y = \mathcal{L}(S, X) = \frac{k_2 + k_2' \frac{1}{A + X^n}}{\gamma_2}$$
 2.17

Substituting the expression of Y at steady state into the equation of X, the dynamics of the system in reduced dimension can be written as,

$$\frac{dX}{dt} = S - k_1 X \mathcal{L}(S, X) - \gamma_1 X$$
 2.18

Thus, the right-hand side of the equation is now basically a function of X and signal, S which is in this case represents the bifurcation parameter. The effective force of the system now becomes

$$F(X,S) = S - k_1 X \mathcal{L}(S,X) - \gamma_1 X$$
 2.19

Now, the effective potential can be calculated by integrating the force term,

$$V(X,S) = -\int_{0}^{X} [S - k_{1}x\mathcal{L}(S,x) - \gamma_{1}x] dx$$
 2.20

It is important to note that the effective energy here is not in true sense of energy because of non-Newtonian nature of the dynamical system, rather it can be termed as a pseudo potential energy of the system. Using (2.20) the potential energy for a range of X values can be determined at different values of S. The local extrema values provide the information about the stable and unstable steady states (Figure 2.2 b-d) of the dynamical system. The whole 1-parameter bifurcation diagram can be generated by determining the steady states from the extrema in the potential energy landscape. Implementing this algorithmic approach in MATLAB, we performed 1-parameter bifurcation analysis in an automated high throughput manner without any manual intervention.

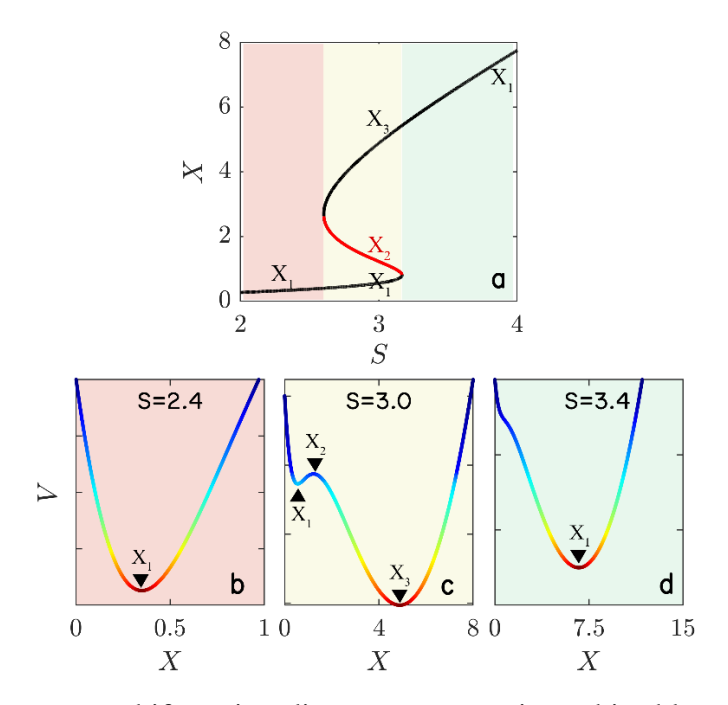


Figure 2.2. 1-parameter bifurcation diagram representing a bistable switch generated by mutual inhibition loop between two regulatory species (a). The black and red lines represent the stable and unstable steady states, respectively. The point where the stable and unstable branches annihilate each other is denoted as saddle-node bifurcation point. Different colored region represents low, bistable and high expressions. Pseudo potential energy diagram corresponding to different signal values indicated the plot (b-c). The indicated location of extrema values in the energy plots (b-d) provides the mentioned steady state value for the bifurcation diagram (a).

2.4 References

- (1) Paulsson, J. Models of Stochastic Gene Expression. *Phys. Life Rev.* **2005**, *2* (2), 157–175. https://doi.org/10.1016/J.PLREV.2005.03.003.
- (2) Elf, J.; Ehrenberg, M. Fast Evaluation of Fluctuations in Biochemical Networks With the Linear Noise Approximation. *Genome Res.* **2003**, *13* (11), 2475–2484. https://doi.org/10.1101/GR.1196503.
- (3) Hayot, F.; Jayaprakash, C. The Linear Noise Approximation for Molecular Fluctuations within Cells. *Phys. Biol.* **2004**, *1* (4), 205. https://doi.org/10.1088/1478-3967/1/4/002.
- (4) Kampen, V. N. G. Stochastic Processes in Physics and Chemistry. *Stoch. Process. Phys. Chem.* **2007**. https://doi.org/10.1016/B978-0-444-52965-7.X5000-4.
- (5) Hayot, F.; Jayaprakash, C. The Linear Noise Approximation for Molecular

- Fluctuations within Cells. *Phys. Biol.* **2004**, *1* (4), 205. https://doi.org/10.1088/1478-3967/1/4/002.
- (6) Ferm, L.; Lötstedt, P.; Hellander, A. A Hierarchy of Approximations of the Master Equation Scaled by a Size Parameter. *J. Sci. Comput.* **2008**, *34* (2), 127–151. https://doi.org/10.1007/s10915-007-9179-z.
- (7) Grima, R.; Thomas, P.; Straube, A. V. How Accurate Are the Nonlinear Chemical Fokker-Planck and Chemical Langevin Equations? *J. Chem. Phys.* **2011**, *135* (8). https://doi.org/10.1063/1.3625958.
- (8) Grima, R. A Study of the Accuracy of Moment-Closure Approximations for Stochastic Chemical Kinetics. *J. Chem. Phys.* **2012**, *136* (15). https://doi.org/10.1063/1.3702848.
- (9) Gillespie, D. T. A General Method for Numerically Simulating the Stochastic Time Evolution of Coupled Chemical Reactions. *J. Comput. Phys.* **1976**, 22 (4), 403–434. https://doi.org/10.1016/0021-9991(76)90041-3.
- (10) Gillespie, D. T. Exact Stochastic Simulation of Coupled Chemical Reactions. *J. Phys. Chem.* **1977**, *81* (25), 2340–2361. https://doi.org/10.1021/J100540A008/ASSET/J100540A008.FP.PNG_V03.
- (11) Bundschuh, R.; Hayot, F.; Jayaprakash, C. Fluctuations and Slow Variables in Genetic Networks. *Biophys. J.* **2003**, *84* (3), 1606–1615. https://doi.org/10.1016/S0006-3495(03)74970-4.
- (12) Gillespie, D. T. Approximate Accelerated Stochastic Simulation of Chemically Reacting Systems. *J. Chem. Phys.* **2001**, *115* (4), 1716. https://doi.org/10.1063/1.1378322.
- (13) Gillespie, D. T. The Chemical Langevin Equation. *J. Chem. Phys.* **2000**, *113* (1), 297. https://doi.org/10.1063/1.481811.
- (14) Dey, A.; Barik, D. Potential Landscapes, Bifurcations, and Robustness of Tristable Networks. *ACS Synth. Biol.* **2021**, *10* (2), 391–401. https://doi.org/10.1021/ACSSYNBIO.0C00570/SUPPL_FILE/SB0C00570_SI_001.PDF.
- (15) Dey, A.; Barik, D. Emergent Bistable Switches from the Incoherent Feed-Forward Signaling of a Positive Feedback Loop. *ACS Synth. Biol.* **2021**, *10* (11), 3117–3128. https://doi.org/10.1021/ACSSYNBIO.1C00373/ASSET/IMAGES/LARGE/SB1C0 0373_0008.JPEG.

CHAPTER 3

Chemical noise propagation in reversible multisite phosphorylation-dephosphorylation chain.

3.1 Introduction

Chemical reaction networks incorporating multiple genes control diverse biological processes. These networks frequently consist of small regulatory network motifs with unique steady-state and dynamical characteristics¹. Therefore, additional research was done to comprehend how network topologies such as signalling cascades, feedback loops, and feed-forward loops affect the propagation of chemical noise²⁻⁷. One such network motif that controls the catalytic activity, binding, transport, and degradation of target proteins is multisite reversible phosphorylation-dephosphorylation of proteins^{8,9}. For instance, cyclin-dependent kinase phosphorylates a number of important proteins several times to control important processes in the eukaryotic cell cycle¹⁰. Phosphorylation-dephosphorylation of protein can take place either by processive or distributive manner. In a processive mechanism, the substrate attaches mutliple phosphate groups after just one interaction between the enzyme and the substrate. In contrast, a single interaction leads to a single enzymatic event in the distributive mechanism. An ultrasensitive signal response is produced when a single enzyme catalyses many phosphorylations in a distributive fashion, which is necessary for producing nonlinear responses in biochemical reaction networks^{11,12,13}. Due to this, bistability and oscillations have been mathematically and computationally modelled extensively using multisite phosphorylation mechanisms^{9,14–17}. While considering its deterministic dynamics, numerous aspects of multisite phosphorylation have been explored^{8,11,13,16,17}. However, systematic research into stochasticity in multiphosphorylation is limited. Therefore, the characteristics of chemical noise propagation in multisite phosphorylation chains must be thoroughly studied. It is important to look into how the rate laws of chemical reactions, kinetic factors, and the overall number of phosphorylation sites affect the intrinsic noise in multiphosphorylation chains.

Noise propagation in multiphosphorylation chain

This chapter discussed how intrinsic noise propagated in multisite phosphorylation chains with varying "chain lengths," or with different total numbers of phosphorylation sites on the target protein. In order to understand the impact of non-linearity on noise propagation, investigation was performed with the mass action (MA) and Michaelis-Menten (MM) rate laws for phosphorylation and dephosphorylation activities. Linear noise approximation (LNA) to the chemical master equation, popularly known as the van Kampen's system size expansion approach was used to examine the quantitative and qualitative nature of variability in phosphorylated species¹⁸. Additionally, stochastic simulations were carried out for the chemical reactions in the chain using Gillespie's stochastic simulation algorithm(SSA)¹⁹ technique to benchmark the analytical calculations.

3.2. Model

An ordered distributive multisite phosphorylation was studied, where each enzyme-substrate interaction results in a single phosphorylation or dephosphorylation of the target protein, and enzymatic processes take place in a predefined order. Figure 3.1 represents the reaction scheme for a three component, distributive, reversible multisite phosphorylation-dephosphorylation network. The assumption is that one enzyme is responsible for all phosphorylation reactions, and that a different enzyme is responsible for all dephosphorylation reactions.

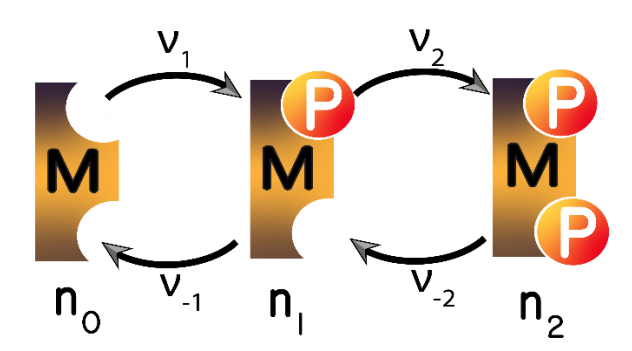


Figure 3.1: Schematic diagram for multi-phospho chain for protein with two phosphorylation sites. MP_i's are the different phosphorylated states of protein M, i.e., species with subscripts 0 (M), 1 (MP) and 2 (MP₂) refers to unphosphorylated, monophosphorylated and bisphosphorylated forms. v_i and v_{-i} are the macroscopic reaction rates for phosphorylation and dephosphorylation.

The chemical master equation corresponding to the three-component reaction system can be represented as,

$$\begin{split} \frac{dP(n_0,n_1,n_2;t)}{dt} \\ &= a_1(n_0+1,n_1-1,n_2)P(n_0+1,n_1-1,n_2;t) \\ &+ a_2(n_0,n_1+1,n_2-1)P(n_0,n_1+1,n_2-1;t) + a_{-2}(n_0,n_1-1,n_2-1;t) \\ &+ 1)P(n_0,n_1-1,n_2+1;t) + a_{-1}(n_0-1,n_1-1,n_2+1;t) + a_{-1}(n_0,n_1,n_2) + a_{-1}(n_0,n_1,n_2) + a_{-2}(n_0,n_1,n_2)P(n_0,n_1,n_2;t) \end{split}$$

Where, $P(n_o, n_1, n_2; t)$ represents the joint probability density for n_0 , n_1 and n_2 number of molecules for the species MP₀, MP₁ and MP₂ respectively at time t. The total number of molecules of, n_T (= $n_o + n_1 + n_2$), is fixed and holds a mass conservation. The a_i 's are the reaction propensities for phosphorylation (a_1 , a_2) and dephosphorylation (a_{-1} , a_{-2}) reaction steps in the chain. As, mass conservation law holds in the chain, chemical master equation can also be written as a function of any two variables of the phospho chain²⁰ as the total number, n_T is fixed all the time.

The system was studied with two different reaction kinetics. In the first case, it was assumed that the enzymes which catalyzed the forward and backward (i.e., phosphorylation and dephosphorylation) reactions are in much excess concentrations compared to their substrates consequently the reactions can be represented by pseudo-first order mass action rate laws. And in the second case, where each reaction rate follows Michaelis-Menten kinetics. The mean field dynamical equations of the system are given by

$$\frac{\partial \bar{n}_1}{\partial t} = (\nu_1 + \nu_{-2}) - (\nu_2 + \nu_{-1})$$

$$\frac{\partial \bar{n}_2}{\partial t} = (\nu_2 - \nu_{-2})$$
3.2

Where \bar{n}_i s are the average values of phosphorylated species. The average for unphosphorylated species population can be calculated by applying mass conservation. In order to simulate the dynamics of multisite phosphorylation events, MM rate laws have been widely used. Particularly since the study of Markevich et al¹², in the context of the mitogen-activated protein kinase pathway, the applicability of the MM rate laws in multisite phosphorylation has grown rather substantially. Their research has demonstrated that, under specific circumstances, bistability can be produced solely by a three-component phosphorylation-dephosphorylation

cycle, without the need for an external positive feedback loop in the reaction network. However, an ultrasensitive switch can also be produced via a two-component phosphorylation-dephosphorylation cycle with MM kinetics²¹. Further investigations for various aspects of multisite phosphorylation with MM kinetics for ultrasensitive switches have been conducted¹¹. However, a robust and tunable ultrasensitivity was also found to be generated from MA based multisite phosphorylation in addition to the MM kinetics¹³. The reaction rates for two different kinetics, ν_i 's are listed in the table below,

Table 3.1

Mass-action kinetics	Michaelis-Menten kinetics
$v_1 = k_1(n_T - \overline{n}_1 - \overline{n}_2)$	$v_1 = \frac{k_1 E_1 (n_T - \bar{n}_1 - \bar{n}_2) / K_{M1}}{1 + (n_T - \bar{n}_1 - \bar{n}_2) / K_{M1} + \bar{n}_1 / K_{M2}}$
$ u_2=k_2\overline{n}_1$	$v_2 = \frac{k_2 E_1 \bar{n}_1 / K_{M2}}{1 + (n_T - \bar{n}_1 - \bar{n}_2) / K_{M1} + \bar{n}_1 / K_{M2}}$
$\nu_{-2}=k_{-2}\overline{n}_2$	$v_{-2} = \frac{k_{-2}E'\bar{n}_2/K_{-M2}}{1 + \bar{n}_2/K_{-M2} + \bar{n}_1/K_{-M1}}$
$\nu_{-1}=k_{-1}\overline{n}_1$	$v_{-1} = \frac{k_{-1}E'\bar{n}_1/K_{M4}}{1+\bar{n}_2/K_{-M2}+\bar{n}_1/K_{-M1}}$

In the above set of equations, for the MA kinetics, k_i and k_{-i} are the catalytic conversion rate constants for phosphorylation (k_1, k_2) and dephosphorylation (k_{-1}, k_{-2}) respectively. The abundances of enzymes were kept constant in the entire calculations. Therefore, they are not mentioned explicitly as they were absorbed in the rate constants k_i . In case of MM kinetics the rate expressions are similar to the expressions as given by Markevich et al.¹² in the context of phosphorylation of mitogen-activated protein kinase cascade. E_1 and E' are the kinase and phosphatase abundances, respectively and those abundances were kept constant throughout out calculations. The K_{Mi} 's are the Michaelis constants for phosphorylation (K_{M1}, K_{M2}) and dephosphorylation (K_{-M1}, K_{-M2}) reactions.

Now in order to calculate the steady-state noise in the phospho species, Linear Noise approximation (LNA)(See Chapter 2 Methodology) was used on the chemical master equation. At the steady state, the drift and diffusion matrices in the Fokker-Plank equation are connected by a fluctuation-dissipation like relation given by

$$\mathbf{A}\boldsymbol{\sigma} + \boldsymbol{\sigma}\mathbf{A}^T + \mathbf{B} = 0 \tag{3.3}$$

where A, B and σ are the drift or Jacobian matrix, diffusion matrix and covariance matrix respectively. The covariance matrix holds information about the variance and covariance of all the molecular species in the network. The elements in the drift matrix A are given by

$$A_{ij} = \frac{\partial}{\partial \bar{n}_i} \frac{\partial \bar{n}_i}{\partial t}$$
 3.4

Where \bar{n}_i is the average number of molecules for the *i*-th chemical species and $\frac{\partial \bar{n}_i}{\partial t}$ can be obtained from the macroscopic rate equations. The elements in the diffusion matrix \boldsymbol{B} are given by

$$B_{ij} = \sum_{k} \nu_{jk} \nu_{ik} R_k \tag{3.5}$$

Where v_{ik} and R_k are the stoichiometric coefficient of the *i*-th species in the *k*-th reaction and the rate of the *k*-th reaction, respectively.

For the three-component reaction scheme the drift and diffusion matrices are given by,

$$\mathbf{A} = \begin{bmatrix} \frac{\partial}{\partial \bar{n}_{1}} \left(\frac{\partial \bar{n}_{1}}{\partial t} \right) & \frac{\partial}{\partial \bar{n}_{2}} \left(\frac{\partial \bar{n}_{1}}{\partial t} \right) \\ \frac{\partial}{\partial \bar{n}_{1}} \left(\frac{\partial \bar{n}_{2}}{\partial t} \right) & \frac{\partial}{\partial \bar{n}_{2}} \left(\frac{\partial \bar{n}_{2}}{\partial t} \right) \end{bmatrix} = \begin{bmatrix} A_{11} & A_{12} \\ A_{21} & A_{22} \end{bmatrix}$$

$$\mathbf{B} = \begin{bmatrix} (\nu_{1} + \nu_{2} + \nu_{3} + \nu_{4}) & -(\nu_{2} + \nu_{3}) \\ -(\nu_{2} + \nu_{3}) & (\nu_{2} + \nu_{3}) \end{bmatrix}$$
3.6

Thus, the final matrix equation for the steady state covariances,

$$\begin{bmatrix} A_{11} & A_{12} & 0 \\ A_{21} & (A_{11} + A_{22}) & A_{12} \\ 0 & A_{12} & A_{22} \end{bmatrix} \begin{bmatrix} \sigma_{11} \\ \sigma_{12} \\ \sigma_{22} \end{bmatrix} = \begin{bmatrix} -(1/2)(\nu_1 + \nu_2 + \nu_{-2} + \nu_{-1}) \\ (\nu_2 + \nu_{-2}) \\ -(1/2)(\nu_2 + \nu_{-2}) \end{bmatrix}$$
3.7

Now for the mass action kinetics the drift and diffusion matrices are given by:

$$\mathbf{A} = \begin{bmatrix} -(k_1 + k_2 + k_{-1}) & (k_{-2} - k_1) \\ k_2 & -k_{-2} \end{bmatrix} \quad \mathbf{B} = \begin{bmatrix} 2(k_1 + k_{-1})\bar{n}_1 & -2k_2\bar{n}_1 \\ -2k_{-2}\bar{n}_2 & 2k_{-2}\bar{n}_2 \end{bmatrix}$$
3.8

Using the above expressions of **A** and **B** in the matrix equation (3.3) and applying the symmetry in covariance ($\sigma_{ij} = \sigma_{ji}$), the matrix equation for the steady state variances of stochastic variables obtained as,

Noise propagation in multiphosphorylation chain

$$\begin{bmatrix} \sum_{i=1}^{2} k_{i} + k_{-1} & k_{1} - k_{-2} & 0 \\ k_{2} & -\sum_{i=1}^{2} k_{i} + k_{-i} & k_{-2} - k_{1} \\ 0 & k_{2} & -k_{-2} \end{bmatrix} \begin{bmatrix} \sigma_{11} \\ \sigma_{12} \\ \sigma_{22} \end{bmatrix} = \begin{bmatrix} -(k_{2} + k_{-1})\bar{n}_{1} \\ 2k_{2}\bar{n}_{1} \\ -k_{-1}\bar{n}_{2} \end{bmatrix}$$
3.9

Solution of the above system of linear equations lead to the variances of species MP_1 and MP_2 as

$$\sigma_{11} = \frac{(k_1 k_2 + k_{-1} k_{-2}) \bar{n}_1}{k_1 k_2 + k_1 k_{-2} + k_{-1} k_{-2}}$$

$$\sigma_{22} = \frac{(k_1 k_{-2} + k_{-1} k_{-2}) \bar{n}_2}{k_1 k_2 + k_1 k_{-2} + k_{-1} k_{-2}}$$
3.10

In the special case where all the forward and backward rate constants are equal i.e., $k_1 = k_2 = k_f$ and $k_{-1} = k_{-2} = k_b$, the steady state variances can be represented as a function of equilibrium constant $(K = k_f/k_b)$ and they take simple form as,

$$\sigma_{11} = \frac{(1+K^2)\bar{n}_1}{(1+K)^2 - K}$$

$$\sigma_{22} = \frac{(1+K)\bar{n}_2}{(1+K)^2 - K}$$
3.11

Although only the variances were calculated, the covariances can also be calculated using (3.9). Further the macroscopic averages can be obtained from the deterministic dynamical equations. The general expression of the average for i^{th} phospho state is given by

$$\bar{n}_i = \frac{\left(k_f/k_b\right)^i}{\sum_{i=0}^N \left(k_f/k_b\right)^i} n_T = \frac{(K)^i}{\sum_{i=0}^N (K)^i} n_T$$
 3.12

N is the total number of phosphorylation site in the chemical species.

Similar calculations were done for three component reaction scheme with the MM kinetics, where the resulting equations are lengthy and cumbersome. The above matrix was solved using MATLAB to get the σ_{ii} values, variance of species MP₁ and MP₂. However, for the two-component phosphorylation-dephosphorylation chain the variance for the monophosphorylated species (MP₁) is found to be,

$$\sigma_{11} = \frac{\frac{k_1 E_1 (n_T - \bar{n}_1)}{K_{M1} (n_T - \bar{n}_1)} + \frac{k_{-1} E' \bar{n}_1}{K_{-M1} + \bar{n}_1}}{\frac{2k_1 E_1 K_{M1}}{[K_{M1} + (n_T - \bar{n}_1)]^2} + \frac{2k_{-1} E' K_{-M1}}{[K_{-M1} + \bar{n}_1]^2}}$$
3.13

Multiple phosphorylations of proteins in living cells provide threshold and ultrasensitive signal responses in protein activity. Additionally, it is known that a chain with more phospho states will have a sharper signal response curve and higher Hill coefficient values. In this context, similar calculations were performed for multiphosphorylation chain with four, five, and six components to study the effect of increasing phospho states on the noise of chemical species in a chain. The resulting matrix equations were therefore rather large and challenging to solve analytically. MATLAB was used in order to get the information of variances for different phosphorylated species.

3.3. Results

In Figure 3.2 presented the dependence of the average, variance, and Fano factor of the phosphorylated species on the equilibrium constant (K) of phosphorylation-dephosphorylation reactions in the three-component phosphorylation chain. This presented the findings from both the MA and the MM kinetics of reactions in order to comprehend how the rate laws affect the statistical features. Additionally, the analytical results were compared from numerical simulations carried out using Gillespie's SSA.

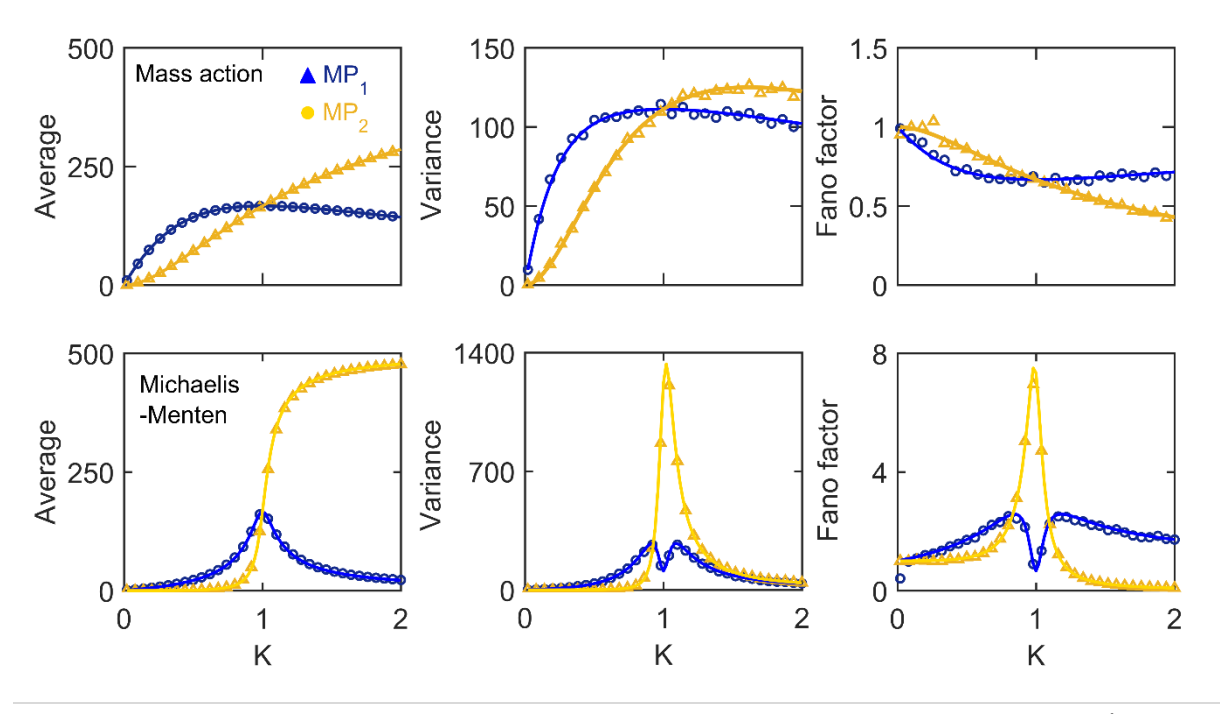


Figure 3.2: Dependency of steady state average (\bar{n}_i) , variance (σ_{ii}) and noise strength (Fano Factor=variance (σ_{ii}) /mean (\bar{n}_i)) of the phosphorylated states on the equilibrium constant of phosphorylation-dephosphorylation reactions for three component phospho chain. Solid lines and markers represent analytical and SSA simulation results, respectively. $n_T = 500$ was chosen in all the calculations. Top row: MA kinetics; bottom row: MM kinetics.

The results were provided for the situations with $k_1 = k_2$ and $k_{-1} = k_{-2}$. However, one can also obtain the dependency of statistical properties the on the individual rate constants (k_1 , k_2 , k_{-1} , and k_{-2}). For MA kinetics with the increase of K the steady state variance of the each phospho state increases and decreases steadily after going through maxima (Figure 3.2). The increase and decrease of variances are much sharper in the case of MM kinetics. For the terminally phosphorylated species (MP₂) in particular, the variance shows a sharp peak at K = 1. The ultrasensitive increase of MP₂ at K = 1 leads to the sudden rise in MP₂ variance. After K > 1, the following sharp fall in the variance is due to the decrease in the sizes of fluctuations owing to the large abundance to MP₂. Contrary to MM, in case of MA, the averages do not follow any sharp increase or decrease with increase in K, the corresponding variance do not show such sharp change. Thus, the well-known ultrasensitive switching of the terminal species drives the sharp switching behavior of steady state variance. This is supported by the variation of Fano factor which measure the strength of noise. Noted that the Fano factor value shows a deviation from 1, which dictates the non-Poissonian nature of statistics across different values of K.

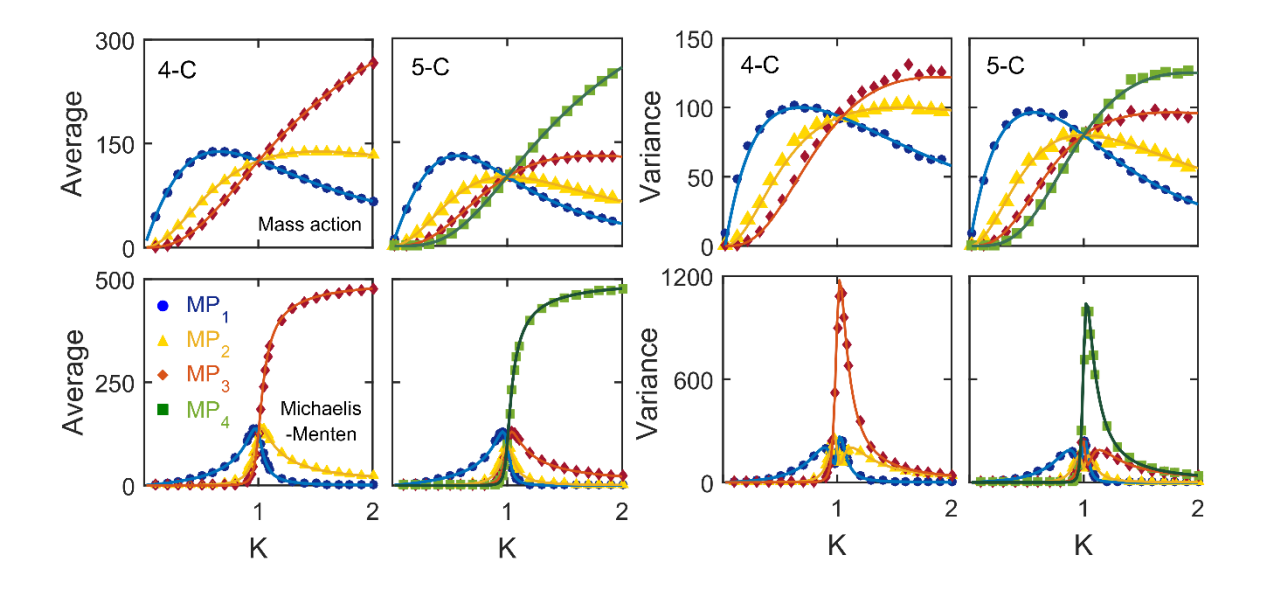


Figure 3.3: Dependency of steady state average (\bar{n}_i) , variance (σ_{ii}) of the phosphorylated states on the equilibrium constant of phosphorylation-dephosphorylation reactions for four component(4-C) and five component(5-C) phospho chain. Solid lines and markers represent analytical and SSA simulation results, respectively. To vary K, we kept k_2 (= k_{-1} = k_{-2}) fixed at 0.2 and varied k_f (= k_1 = k_2). k_M values are kept constant at 0.5, k_1 = k_2 = 50.

For four and five component chain (for equations see Appendix 1, A3.1), the steady-state averages and variances (solving the final matrix equation in Appendix 1, A3.3 and A3,4 in MATLAB), of the phosphorylated species with the equilibrium constant K are shown in Figure 3.3. Similar to the three-component chain, the MA kinetics exhibit less pronounced increase and decrease of variances than the MM kinetics. Again, due to its deterministic behaviour, the terminally phosphorylated species exhibit dramatic rises and falls in its variance in MM kinetics. Gillespie's SSA was used to perform numerical computations to further corroborate our analytical findings. In every chain, both the outcomes were remarkably consistent. It was also interesting to notice that in MA kinetics, at K = 1 the variances go through a common value.

Next our methodology was established, the impact of chain lengths or the total number of phosphorylation sites (*N*) on the variability of phosphorylated species was further investigated. To determine the noise in the chemical species, the coefficient of variation (CV=standard deviation/mean) was calculated. The CV of every phosphorylated species in chains with 3, 4, and 5 components was determined.

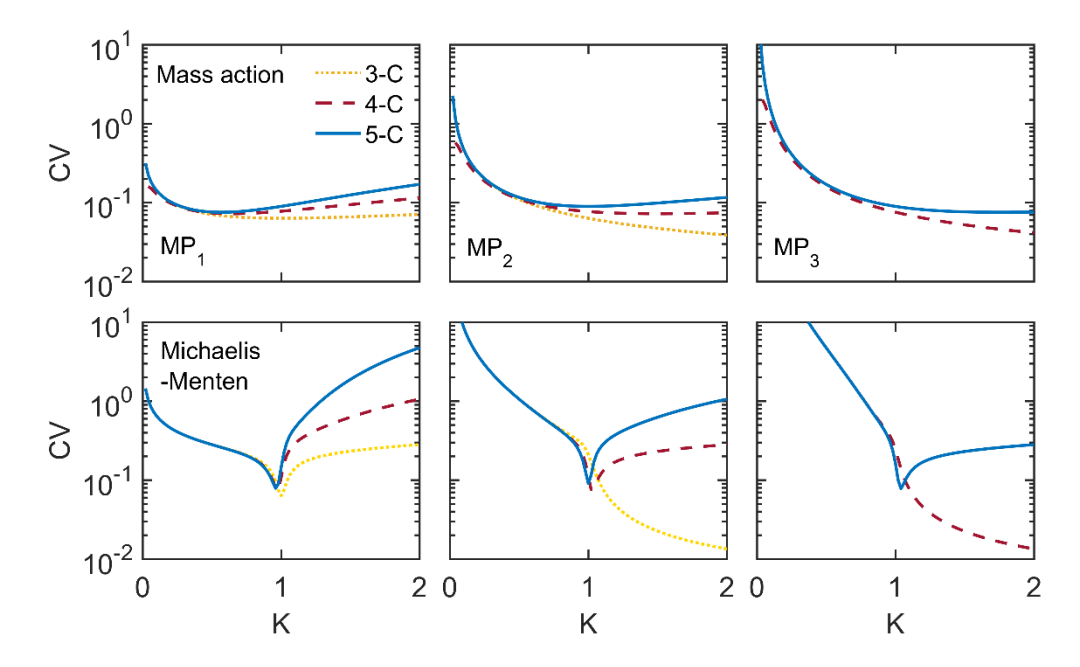


Figure 3.4: Comparison of steady noise of a specific phosphorylated species across different chain length (number of phosphorylated states in a chain). Top row: MA kinetics; bottom row: MM kinetics.

To assess the effect of the number of phosphorylation sites on the noise, the CV of a particular phosphorylated state from different chain lengths was plotted against the K (Figure 3.4). The results showed that the noise in a given phosphorylated state for MA kinetics rises with chain length. This is because the overall population is spread out among all the states, and as the chain length increases, the average abundance of a given state falls, leading to increased noise in the various phosphorylation states. However, the CV of other phosphorylated species passes through a minimum, whereas the CV of the terminally phosphorylated species in any chain demonstrate a monotonously falling pattern with the K in case of MM. The increase in average abundance with K is what causes the CV with K for terminally phosphorylated species to consistently drop. The CV of these species, however, exhibit a reversal tendency because average abundances of other phosphorylated species pass through maxima when K is increased. Again, this sharp fall of noise after K = 1 in case of MM as compared to MM is due the average dynamics. We evaluated the total variance of all the phosphorylated species and compared them for chains lengths in order to provide a more accurate estimation of the comparative noise in MA and MM kinetics (Figure 3.5). In MA kinetics, the total variance increases with K and after passing through a maximum value it decreases. Consistently, the increase and decreases are much sharper in case of MM kinetics. The total variance is found to be higher with higher

number of number of components in the chain in case of MA; whereas, in MM kinetics, the total variance of all chains is almost the same. Though the quantitative value of total variance in case of MM kinetics is significantly higher than the MA

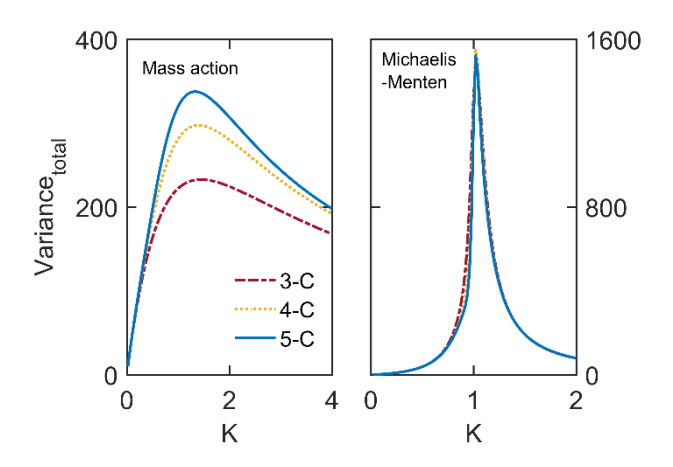


Figure3.5: Total variance ($\sum \sigma_{ii}$) of all phosphorylated species of each phosphorylated chain is plotted with equilibrium constant. Each color and line style represents different phosphorylated chains.

kinetics. Thus, it can be concluded that the non-linear rates in the chemical kinetics tends to amplify the noise. Therefore, though the non-linear reactions kinetics is the requirement for the ultrasensitive response, this comes under the cost of increased variability.

Since the discovery of gene expression noise, the propagation of chemical noise in a network of chemical reactions has attracted a lot of attention. The propagation of intrinsic noise has been studied as a function of cascade 'length' in signalling cascade networks, which has garnered particular interest^{22,23}. Therefore, it is reasonable to calculate how the noise is distributed or propagated across the different chemical species in the chain in the case of a multisite phosphorylation. It is also important to investigate how 'chain length' regulates the noise of the phosphorylated species. Additional simulations were run for higher phosphorylation chains up to 10 components to address these characteristics of noise propagation. Figure 3.6 presents the noise propagation along the various chains at K = 1.

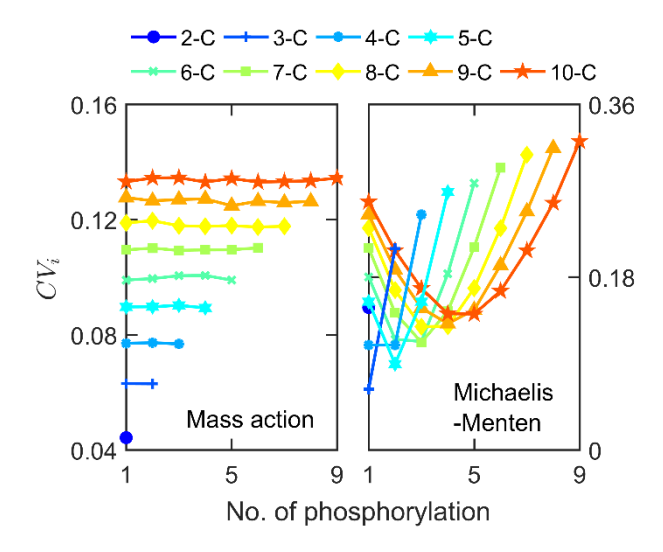


Figure 3.6: Plot for CV of the phosphorylated species of different chains with MA (left) and MM (right) kinetics. Different liner color/marker represent different 'chain length'.

The noise of all the phosphorylated species for both MA and MM kinetics for a given chain is plotted in Figure 3.6. When comparing chains using MA and MM rate laws, a striking variation in the noise propagation was discovered. For the MA kinetics, the noise of all the phosphorylated species in a given chain length were same, which reflects that the noise was more or less uniformly distributed among different species and the quantitative value of noise increases with the 'chain length'. Therefore, the extent of noise propagation is somewhat independent on the phosphorylation state. In contrast, the noise in the case of MM kinetics displayed a totally different qualitative trend. Here, the noise profile was found to be a somewhat parabolic shape in relation to the degree of phosphorylation for each species. The noise decreased along the chain and after passing through a minimum it increases with phosphorylation. As a result, compared to the terminal species, the intermediate phosphorylated species experienced lesser noise.

The dependence of CV on the average number of molecular species is one of the key features of intrinsic noise. For simple birth-death processes, the CV scales according to $CV \propto 1/\sqrt{n}$. For chains with various total numbers of phosphorylation sites, the dependency of CV on the average abundance of phosphorylated species is shown in Figure 3.7. When it comes to MA kinetics, the CV showed usual scaling with the average number of species and the CV for every phosphorylated species behaved in exactly the same way with the average. However, in case of the MM kinetics, scaling of CV was found to be complex in nature. In particular, the intermediate phosphorylated species exhibit a looplike structure.

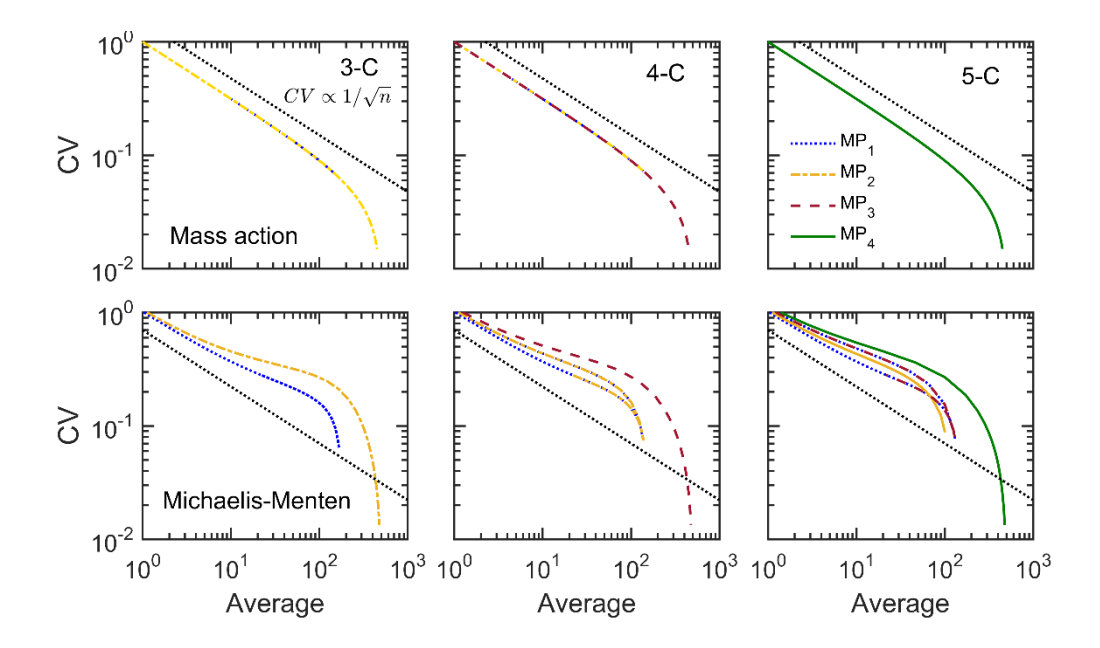


Figure 3.7: CV vs average plots for different phosphorylation states in each chain (3, 4, and 5 component). Different colors or line styles represent each phosphorylated species. The dotted line across the plot represents the $CV \propto 1/\sqrt{n}$ scaling.

3.4. Conclusion

In this chapter, the propagation of chemical noise in multisite phosphorylation chains was examined using the Linear noise approximation method. The analytical results were supplemented with numerical simulations using Gillespie's SSA. Calculations were performed using both linear (mass action) and nonlinear (Michaelis-Menten) kinetics for the enzyme activity in order to understand the role of rate laws in noise propagation. While varying the equilibrium constant of the phosphorylation-dephosphorylation reactions and the overall number of phosphorylated states in the chain, the steady-state statistical quantities such as variance, coefficient of variation, and Fano factor of phosphorylated species were determined. In case of MA kinetics, the variance of phosphorylated states steadily increased and decreased with the equilibrium constant of the phosphorylation-dephosphorylation reaction. The rise and fall of variances were far more pronounced in case of MM kinetics. Particularly, at K=1, when the reaction equilibrium is unbiased, the variance of the terminally phosphorylated species displayed a sharp peak. Additionally, variability of any phosphorylated species in case of MM kinetics is much higher than in the MA kinetics. Since the total variance in all of the phosphorylated states with MM kinetics was much higher compared to MA kinetics. This was

Noise propagation in multiphosphorylation chain

also reflected in the CV which estimates the 'noisiness' of the chemical species. These calculations show that, in contrast to MA kinetics, MM kinetics contributed to an increase in the sharpness of the signal response while also amplifying the variability of the phosphorylated states. As a result, the system made a trade-off by achieving sharp nonlinear response at the expense of more variability. The study of propagation of intrinsic noise revealed a striking difference between the chemical noise propagation along the phosphorylated species along multi phosphorylation chain for MA and MM kinetics. In case of MA kinetics, the noise propagation was found to be independent of the phosphorylated states. Whereas, the noise propagation crucially depended on the different phosphorylated states in MM kinetics. Specifically, the noise profile varied in a near parabolic manner with the phosphorylation state of species along the chain, where the terminal species in the chain were found to be more 'noisy'. Further we looked into the scaling of noise with the average abundance of species. For MA case, the system followed the usual scaling law irrespective of the phosphorylated states. On contrary, system following MM kinetics show complex scaling pattern. Further the distinct loop like profile for the CV versus average abundance plot for the intermediate phosphorylated species can be useful to determine the underlying reaction kinetics of phosphorylationdephosphorylation reactions.

3.5. References

- (1) Tyson, J. J.; Novák, B. Functional Motifs in Biochemical Reaction Networks. http://dx.doi.org/10.1146/annurev.physchem.012809.103457 2010, 61, 219–240. https://doi.org/10.1146/ANNUREV.PHYSCHEM.012809.103457.
- (2) Pedraza, J. H.; Van Oudenaarden, A. Noise Propagations in Gene Networks. *Science* (80).2005,307(5717),1965–1969. https://doi.org/10.1126/SCIENCE.1109090/SUPPL_FILE/PEDRAZA-SOM.PDF.
- (3) Brandman, O.; Ferrell, J. E.; Li, R.; Meyer, T. Interlinked Fast and Slow Positive Feedback Loops Drive Reliable Cell Decisions. *Science* (80-.). **2005**, 310 (5747), 496–498. https://doi.org/10.1126/SCIENCE.1113834.
- (4) Ghosh, B.; Karmakar, R.; Bose, I. Noise Characteristics of Feed Forward Loops. *Phys. Biol.* **2005**, *2* (1), 36. https://doi.org/10.1088/1478-3967/2/1/005.

- (5) Barik, D.; Ball, D. A.; Peccoud, J.; Tyson, J. J. A Stochastic Model of the Yeast Cell Cycle Reveals Roles for Feedback Regulation in Limiting Cellular Variability. *PLOS Comput. Biol.* **2016**, *12* (12), e1005230. https://doi.org/10.1371/JOURNAL.PCBI.1005230.
- (6) Chepyala, S. R.; Chen, Y.-C.; Yan, C.-C. S.; Lu, C.-Y. D.; Wu, Y.-C.; Hsu, C.-P. Noise Propagation with Interlinked Feed-Forward Pathways. *Sci. Rep.* **2016**, *6* (November 2015), 23607. https://doi.org/10.1038/srep23607.
- (7) Dey, A.; Barik, D. Parallel Arrangements of Positive Feedback Loops Limit Cell-to-Cell Variability in Differentiation. *PLoS One* **2017**, *12* (11), e0188623. https://doi.org/10.1371/JOURNAL.PONE.0188623.
- (8) Salazar, C.; Höfer, T. Multisite Protein Phosphorylation from Molecular Mechanisms to Kinetic Models. *FEBS J.* **2009**, *276* (12), 3177–3198. https://doi.org/10.1111/J.1742-4658.2009.07027.X.
- (9) Conradi, C.; Mincheva, M. Catalytic Constants Enable the Emergence of Bistability in Dual Phosphorylation. J. R. Soc. Interface 2014, 11 (95). https://doi.org/10.1098/RSIF.2014.0158.
- (10) Deshaies, R. J.; Ferrell, J. E. Multisite Phosphorylation and the Countdown to S Phase. *Cell* **2001**, *107* (7), 819–822. https://doi.org/10.1016/S0092-8674(01)00620-1.
- (11) Gunawardena, J. Multisite Protein Phosphorylation Makes a Good Threshold but Can Be a Poor Switch. *Proc. Natl. Acad. Sci.* **2005**, *102* (41), 14617–14622. https://doi.org/10.1073/PNAS.0507322102.
- (12) Markevich, N. I.; Hoek, J. B.; Kholodenko, B. N. Signaling Switches and Bistability Arising from Multisite Phosphorylation in Protein Kinase Cascades. *J. Cell Biol.* **2004**, *164* (3), 353–359. https://doi.org/10.1083/JCB.200308060.
- (13) Kapuy, O.; Barik, D.; Domingo Sananes, M. R.; Tyson, J. J.; Novák, B. Bistability by Multiple Phosphorylation of Regulatory Proteins. *Prog. Biophys. Mol. Biol.* 2009, 100 (1–3), 47–56. https://doi.org/10.1016/J.PBIOMOLBIO.2009.06.004.
- (14) Yao, G.; Lee, T. J.; Mori, S.; Nevins, J. R.; You, L. A Bistable Rb–E2F Switch Underlies the Restriction Point. *Nat. Cell Biol.* 2008 104 **2008**, 10 (4), 476–482. https://doi.org/10.1038/ncb1711.

- (15) Yang, L.; MacLellan, W. R.; Han, Z.; Weiss, J. N.; Qu, Z. Multisite Phosphorylation and Network Dynamics of Cyclin-Dependent Kinase Signaling in the Eukaryotic Cell Cycle. *Biophys. J.* **2004**, *86* (6), 3432–3443. https://doi.org/10.1529/BIOPHYSJ.103.036558.
- (16) Thomson, M.; Gunawardena, J. Unlimited Multistability in Multisite Phosphorylation Systems. *Nat.* 2009 4607252 **2009**, 460 (7252), 274–277. https://doi.org/10.1038/nature08102.
- (17) Ferrell, J. E.; Ha, S. H. Ultrasensitivity Part II: Multisite Phosphorylation, Stoichiometric Inhibitors, and Positive Feedback. *Trends Biochem. Sci.* **2014**, *39* (11), 556–569. https://doi.org/10.1016/j.tibs.2014.09.003.
- (18) Kampen, V. N. G. Stochastic Processes in Physics and Chemistry. *Stoch. Process. Phys. Chem.* **2007**. https://doi.org/10.1016/B978-0-444-52965-7.X5000-4.
- (19) Gillespie, D. T. Exact Stochastic Simulation of Coupled Chemical Reactions. *J. Phys. Chem.* **1977**, *81* (25), 2340–2361. https://doi.org/10.1021/J100540A008/ASSET/J100540A008.FP.PNG V03.
- (20) Paulsson, J. Models of Stochastic Gene Expression. *Phys. Life Rev.* **2005**, *2* (2), 157–175. https://doi.org/10.1016/J.PLREV.2005.03.003.
- (21) Goldbeter, A.; Koshland, D. E. An Amplified Sensitivity Arising from Covalent Modification in Biological Systems. *Proc. Natl. Acad. Sci. U. S. A.* **1981**, 78 (11 II), 6840–6844. https://doi.org/10.1073/pnas.78.11.6840.
- (22) Hooshangi, S.; Thiberge, S.; Weiss, R. Ultrasensitivity and Noise Propagation in a Synthetic Transcriptional Cascade. *Proc. Natl. Acad. Sci. U. S. A.* **2005**, *102* (10), 3581–3586. https://doi.org/10.1073/PNAS.0408507102/SUPPL_FILE/08507FIG9.PDF.
- (23) Thattai, M.; Van Oudenaarden, A. Attenuation of Noise in Ultrasensitive Signaling Cascades. *Biophys. J.* **2002**, 82 (6), 2943–2950. https://doi.org/10.1016/S0006-3495(02)75635-X.

CHAPTER 4

Pulse processing of bistable network motifs in presence of intrinsic noise

4.1 Introduction

Living cells receive plethora of external and internal signals which modifies the gene expression to perform proper cellular response against these signals¹. Signaling pathways deliver the signal information to the nucleus, where it is targeted for activation or inactivation of particular genes. The majority of the signalling networks contain a core regulatory motif that serves as the primary engine in transmitting the information downstream, despite the fact that the signalling networks can be quite complex with a sizable number of chemical components(regulators) involved in a various interconnected reaction network. Signal transducer, feed-forward loop, negative feedback loop and positive feedback loop are example of these important network motifs^{2,3}. In reaction to internal and external inputs, these networks motifs produce nontrivial dynamical and steady state responses^{4–6} For instance, the incoherent feed-forward loop and negative feedback loop are discovered to produce temporal pulses and are crucial in controlling adaptation^{7–} ⁹. Additionally, negative feedback loop is the key component for temporal oscillations seen in the cell division cycle, NF-κB pathway, and circadian oscillations ^{10–15}. Positive feedback loops are known to produce bistability, which causes a macromolecular species like genes and proteins to abruptly change its activation state or expression. Apoptosis 16,17, cellular differentiation^{18–20}, the G1 to S phase transition in mammalian cells, mitotic control in yeast²¹, and biological memory have all been linked to bistability^{22–24}.

Typically, while modelling these network motifs, the steady state dose response curves or the dynamical characteristics of the network motifs are examined along with the presence of persistent signal⁶. However, instead of persistent signal, the signals can be discrete. These signals can appear as a trail of pulses with variable amplitudes and intervals. The

signal may appear noisy since the amplitude and interval are variable²⁵. Numerous instances of pulsatile signalling causing unique gene expression patterns and cellular responses in various organisms have been documented. Proteomic analysis in Saccharomyces cerevisiae, reveals pulsatile dynamics of several transcription factors under different growth conditions²⁶, and in particular, transcription factor Msn2 has been found to exhibit dose-dependent pulsatile dynamics, under glucose starvation, controlling the expression of a number of genes based on the dynamic pattern of Msn2²⁷. Radiationinduced DNA damage causes leads to pulsatile dynamics of p53 dynamics, and depending on the characteristics of these pulses, distinct cellular fates are controlled by the p53 $dynamics^{28,29}$. Epithelial cell proliferation depends on EGF concentration-dependent modulation of ERK pulses³⁰, and Caenorhabditis elegans research has revealed that pulsatile temporal ERK activity is essential for a variety of cellular fates³¹. Temporal oscillations of expression of transcription factors Ascl1 and Hes1 are required for the proliferation and thus maintenance of multipotency in the mouse neural progenitor cells and sustained expression of Ascl1 leads to differentiation^{32,33}. Recently, a correlation between NF-κB pulses and distinct gene expression patterns has been discovered^{34,35}. As a result, it is critical to develop a systematic quantitative understanding of how different network motifs handle pulsatile signals so that the network can analyse the data as a whole while excluding signals with small amplitudes that can behave as noise.

In this chapter discussed how a bistable switch, that is produced by a positive feedback loop between two regulators, processes a pulse of signal. The pulse processing for two different bistable systems that were either generated by mutual activation (MA) or by mutual inhibition (MI) motif were investigated. In order to study the kinetics of switching from one stable steady state to another stable steady state for a population of bistable switches, three different pulse parameters were altered: amplitude, duration, and residual amplitude. Since an input pulse can cause population inversion in a bistable system, the population fractions that invert to the alternate steady state, stuck in the inverted state, then revert to the initial state were measured. In order to better understand the dynamics of pulse-induced population inversion in bistable systems, the typical time required to carry out these processes were also calculated.

4.2 Model

Bistable switches produced by two distinct mechanisms - mutual inhibition or mutual activation between two regulators to create the necessary positive feedback loop were created. A double negative feedback loop (DNFL) was produced by the mutual inhibition (MI) between to regulators, while a positive feedback loop (PFL) motif was produced by the mutual activation (MA) (Figure 4.1a-b). In order to generate ultrasensitive switch, multisite phosphorylation-dephosphorylation chain with ten phosphorylation sites was used similar to discussed in Chapter 3. The process of phosphorylation was catalysed by enzyme kinase. In case of MI the unphosphorylated protein (X_0) accelerated the degradation of kinase (K) whereas in case of MA the terminally phosphorylated species (X_{10}) , catalysed the synthesis of the kinase. Thus, the mutual antagonism between X_0 and K generated a MI loop and the mutual activation between X_{10} and K generates a MA loop. The dephosphorylation events were catalysed by the phosphatase (S). To simulate the dynamics of the chemical species present in the network, the mass action kinetics of chemical processes was employed. Implementation of mass action kinetics was done solely for the purpose of accurately capturing the effects of intrinsic noise. It was important to note that only if the kinetics of all chemical reactions adhere to the law of mass action can the wellestablished stochastic simulation algorithm developed by Gillespie accurately capture the effects of intrinsic noise³⁶.

The dynamical equations for the kinase in the DNFL was given by

$$\frac{dN_K}{dt} = k_s - k_d N_K - k_a N_{X_0} N_K \tag{4.1}$$

The dynamical equation for the Kinase in the PFL was given by

$$\frac{dN_K}{dt} = k_s + k_a N_{X_{10}} N_K - k_d N_K \tag{4.2}$$

The dynamical equations for the chemical species in the phosphorylation chain were given by

$$\frac{dN_{X_0}}{dt} = S \cdot N_{X_1} - k_p N_K N_{X_0} \tag{4.3}$$

Pulse processing of bistable network motifs in presence of intrinsic noise

$$\frac{dN_{X_j}}{dt} = S \cdot N_{X_{j+1}} + k_p N_K N_{X_{j-1}} - k_p N_K N_{X_j} - S \cdot N_{X_j}$$
 for $2 \le j \le 9$ (4.4)

$$\frac{dN_{X_{10}}}{dt} = k_p N_K N_{X_9} - S \cdot N_{X_{10}} \tag{4.5}$$

In these equations N_j represented the molecular abundance of the chemical species j. The parameters k_s , k_d , k_a and k_p are the rate constants associated with synthesis, degradation, catalytic effects of X and K, respectively. S was the phosphatase which catalysed the dephosphorylation step. The parameter values used in the calculations are listed in the table 4.1.

Table 4.1: List of parameters and their values.

Parameters	Model			
	MI	MA		
k_s	1.0	0.06		
$\overline{k_d}$	0.001	0.001		
$\overline{k_a}$	0.0002	0.01		
$\frac{1}{k_p}$	0.005	0.01		

The 1-parameter bifurcation diagram for MA and MI network were shown in Figure 4.1c and 4.1d, respectively. The phosphatase, S, was selected as the bifurcation parameter and the amount of kinase declines via bistable switch with the increase of phosphatase. The system is bistable between the two saddle-node bifurcation points S_L and S_R . In the MI network, the phosphatase, S increases the amount of X_0 which accelerated the degradation of kinase, thus increase of S resulted in decrease of kinase. In the MA network, the phosphatase decreases the availability of X_{10} that catalysed the production of the kinase thus the kinase decreases with S. To enable a fair comparison between the two networks, the models were parameterized such that it generated similar bifurcation diagrams.

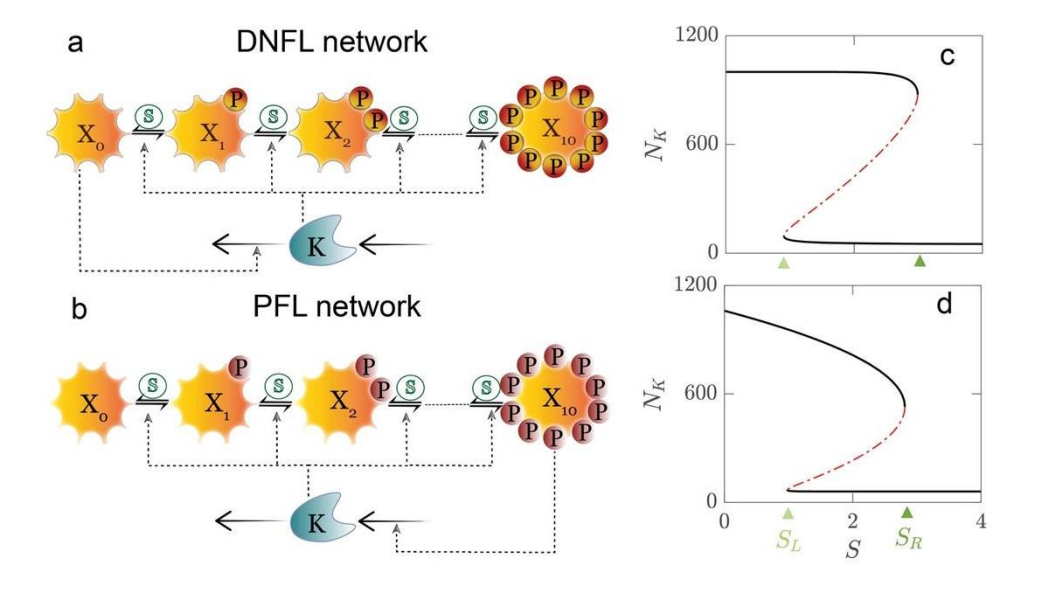


Figure 4.1: Schematic network diagrams of MI (a) and MA (b) networks, the kinase, K, catalyzes the phosphorylation of the target protein X. In return, X_0 catalyzes degradation of the kinase in the DNFL network and X_{10} catalyzes production of K in the PFL network creating net positive feedback loop. The unphosphorylated (X_0) and terminally phosphorylated (X_{10}) forms are assumed to the active forms of X in the DNFL and PFL networks, respectively. The bistable on-parameter bifurcation diagrams of the MI (c) and MA (d) are presented with the amounts of phosphatase (S) as the bifurcation parameter. The two different color triangles designate the signal values corresponding to the left (S_L) and right (S_R) saddle-node bifurcation points.

To study the stochastic realization of the dynamical equations for the MI and MA networks, Gillespie's stochastic simulation algorithm was employed. In the computational experimental setup, the system's initial phosphatase concentration was adjusted to a low level (S = 0.001) and simulated it for a long enough period of time until it reached the upper steady state (USS) of the bifurcation diagram. For a brief period of time (τ_D), a phosphatase (S) pulse of a specific amplitude (S_m) was applied, and for the remainder of the simulation, the pulse amplitude was reduced to a resting value (S_r) (Figure 4.2a). In order to study the effects of the pulse amplitude, length, and resting pulse on the transition kinetics of the bistable systems, these three parameters were altered. The pulse amplitude (S_m) was varied from starting a minimum value corresponding to the phosphatase abundance at the right saddle-node bifurcation point (S_R) and S_r was varied with a maximum value corresponding to the left saddle-node bifurcation point (S_L). Four different

outcomes were possible due to the pulse of phosphatase: the system may not at all respond to the pulse (Figure 4.2b) or the system may transiently respond to the pulse by lowering the expression of the kinase (Figure 4.2c) or the system may invert to the other steady state and remain there (Figure 4.2d) or the system may invert to the other steady state and switch back to the original state upon removal of the pulse (Figure 4.2e). Therefore, in order to predict the outcome of bistable system under the pulse, we quantified the different population fractions involved in different transitions, such as fraction of population i) inverting to the LSS, lower steady state (f_{inv}) , ii) switching back to the upper steady state after a specific pulse duration (f_{swt}) , iii) locked in the lower SS even after removal of pulse (f_{lck}) , iv) not responding the pulse (f_{nrs}) and v) responding to the pulse transiently (f_{trn}) , responded but without reaching the LSS if revert back to its original state).

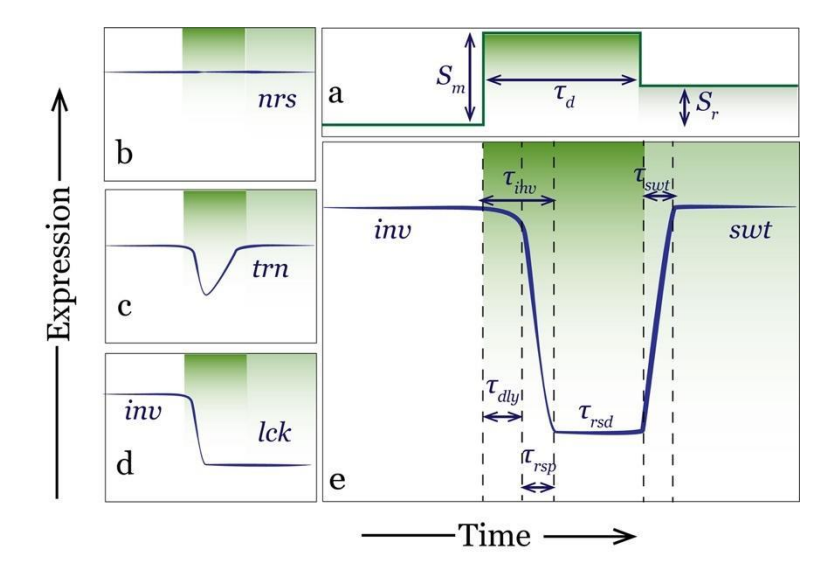


Figure 4.2: Schematic representations of the pulsatile signal (a) and various possible temporal outcomes of the kinase (b-e). The pulse amplitude (S_m) , duration of pulse (τ_d) and resting amplitude (S_r) are the three parameters that characterize the pulse of phosphatase. The four possible temporal outcomes of the kinase are: (b) non-responding trajectory (nrs), (c) transient trajectory with reduced expression without reaching the lower steady state (trn), (d) inversion (inv) of the state with permanently locked in the lower steady state (lck) and (e) inversion and subsequent switching to the upper steady state (swt). The time scales associated with the inverting into the lower steady state, residing in the lower steady state and switching into the upper steady state are represented respectively as τ_{inv} , τ_{rsd} and τ_{swt} . The inversion time was divided into an initial delay phase (τ_{dly}) and

subsequent response phase (τ_{rsp}) . The dark and light shaded regions indicate the pulse on and resting pulse regions.

Time scales associated with various transition kinetics were also quantified. Inversion time (τ_{inv}) , the time taken by the system to reach the LSS since the pulse is switched on, was estimated. The residence time (τ_{rsd}) and the switching time (τ_{swt}) were also determined which were the time the system spent in the LSS and time it took to switch back to the USS upon the removal of pulse, respectively. In order to distinguish the mechanism of inversion for MI and MA, the inversion time was divided into two phases, i.e., an initial delay in response phase (τ_{dly}) and the subsequent rapid response phase (τ_{res}) .

By setting off flags at various kinase values throughout its time course, a pulse of phosphatase was started, and the trajectory of the kinase was monitored in order to calculate the fractions of the various populations and the corresponding time scales. Since the pulse was turned on when the trajectory hit a threshold value of 100, the trajectory was counted as inverted and the inversion time(τ_{inv}) was estimated. Without reaching 100, the trajectory with unaltered expression was classified as a non-responder, and the trajectory with temporarily reduced expression was classified as a transiently responder. The threshold values of 800 and 600 was used for the MI and MA networks, respectively, to measure the initial response delay (τ_{aly}). τ_{aly} was subtracted from τ_{inv} to calculate the rapid response time, τ_{rsp} . The time taken to achieve a threshold value of 150 following the removal of the pulse, after it had reached the lower steady state, was used to estimate the residence time in the LSS (τ_{rsd}). When the system reached a threshold value of 850 and the trajectory was labelled as switched, the time required to switch back to its USS (τ_{swt}) was estimated.

4.3 Results

For the MI and MA motifs, the fraction of the population that switched to the lower steady state was presented in Figure 4.3a-b as a function of pulse dose and duration. The f_{inv} grew nonlinearly with increasing pulse dose and duration, showing that the population inversion might be achieved by a phosphatase pulse in which a strong pulse for a short duration or a weak pulse for a long duration both can alter the steady state of the bistable system. The

Pulse processing of bistable network motifs in presence of intrinsic noise

sharper curve for f_{inv} vs τ_D as compared to the sharpness in the f_{inv} vs ΔS_R suggested the critical dependence of pulse duration, this behavior was found to be more prominent in case of MA. Although the qualitative effects of the pulse on the bistable transition from MI to MA motifs were comparable, but the initial delay in the f_{inv} profile for MA network suggested that for population inversion the pulse must be exposed for a longer period of time (large τ_D) than in the case of MI. In order to support this finding, the minimum duration of pulse need to attain 1% of inverted population was calculated across various values of pulse doses (Figure 4.3c). Results showed that minimum pulse duration needed to initiate the population inversion decreased with increase in the pulse amplitude. More importantly, the minimum duration needed was higher in case of MA as compared to MI irrespective with any dose value. The flat sections $(f_{inv} = 1)$ in the surface plot drew attention to the fact that any appropriate combination of pulse dose and duration could result in a complete population inversion, implying that dose and duration played compensating roles. Additionally, the curve edge of the flat region suggested that a minimum dose and duration were needed to complete inversion of the population. The area under the pulse needed to achieve 99% population inversion was computed to identify the key factor between the dose and duration (Figure 4.3d). The area represented the exposed integrated phosphatase signal of bistable system. This implied that, in comparison to MI, MA was less responsive to the external signal. Consequently, a brief signal (or noisy signal) might not cause alteration of steady state in case of MA. Further evidence that the pulse dose had a bigger impact on population inversion than the time does on state flipping is shown by the reduction of area with increasing dose. To demonstrate that the population inversion dynamics of a bistable system are independent of the strength of the resting pulse, similar calculations were performed with various values of S_r (Appendix 2, Figure A5.1).

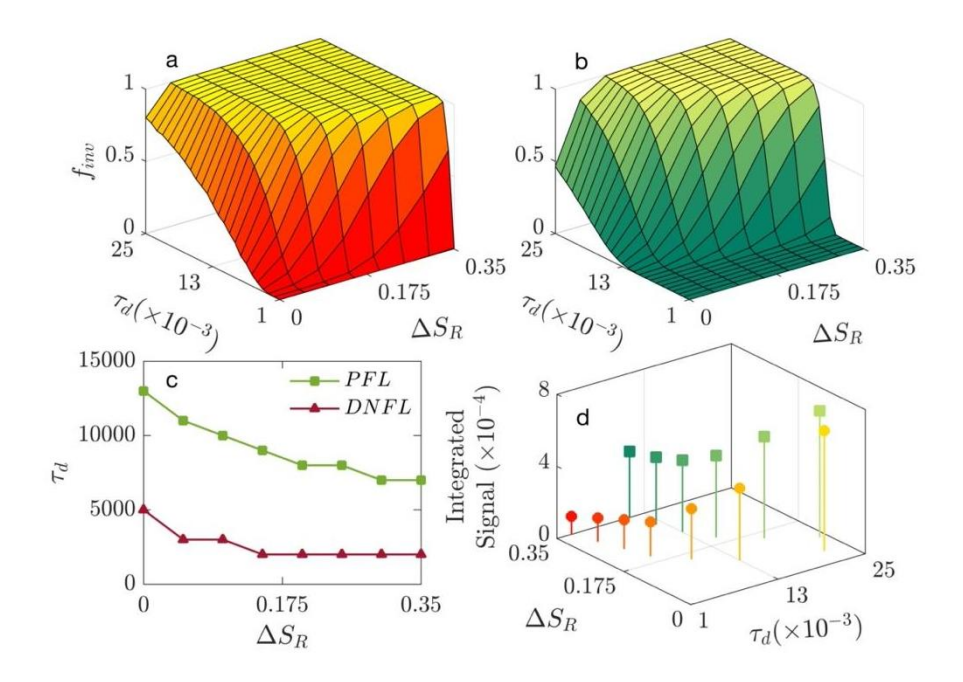


Figure 4.3: The fraction of population that inverts into the lower steady state (f_{inv}) is plotted as a function pulse duration (τ_d) and pulse dose $(\Delta S_R = S_m - S_R)$ for the MI (a) and MA (b) networks. ΔS_R represents the difference between the pulse dose and the signal corresponding to the right saddle node bifurcation point. The duration of pulse required to reach 1% population inversion is plotted as a function of ΔS_R for both the switches (c). The integrated signal required for 99% population inversion is plotted as a function of τ_d and ΔS_R for the MI (circles) and MA (squares) networks (d). The value of the resting pulse was the value of the signal corresponding to the left bifurcation point.

The transient dynamics of the DNFL and PFL networks were found to be in sharp contrast with each other. In the MI motif, f_{nrs} declined as the dose and duration increase (Figure 4.4a), while f_{trn} was quite low at all pulse doses and durations (Figure 4.4b). This suggested that the majority of trajectories eventually arrived at the LSS after the pulse induction. Contrarily, in the MA, f_{nrs} were almost zero over a range of dose and duration, indicating that regardless of the quality of pulse, the entire population responded to it (Figure 4.4c). The f_{trn} decreased with the pulse parameters in a dose-dependent manner, indicating that a large amplitude sustained pulse was necessary to flip the steady state and that a low amplitude transient pulse caused a transitory response in which the system returned to its initial state (Figure 4.4d). As a result, in the MI, the switching of the steady state in a single step process depending on the pulse parameters, whereas in the MA, this

switching decision was made later following an initial transient response. Despite the fact that a MA motif was more prone to rapid response than the MI, MA required signal for a prolonged period for state inversion. It was verified that the initial responses of the system against the pulse were independent of resting pulse (Appendix 2, Figure A5.2).

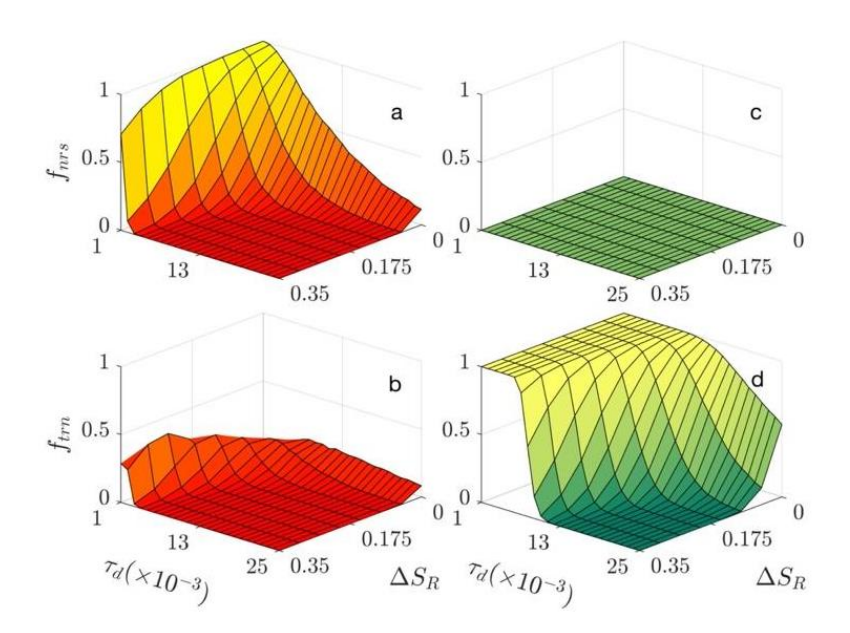


Figure 4.4: The non-responding (top row) and transiently responding (bottom row) fraction of population are plotted as a function of τ_D and ΔS_R for the MI (left) and MA (right) networks.

The duration of transition between states for bistable system was a crucial factor since it provided the information about the kinetics of inversion in the dynamical system. For each of the two bistable switches, the average amount of time it took for the switch to transition from the USS to the LSS was plotted as a function of pulse dosage and duration in Figure 4.5a-b. As the transition was facilitated by a strong pulse, the $\langle \tau_{inv} \rangle$ decreased with an increase in pulse dose. Although $\langle \tau_{inv} \rangle$ grows with τ_D for both bistable systems at low doses, its dependency on pulse duration was somewhat counterintuitive. The increase in $\langle \tau_{inv} \rangle$ with τ_D suggests that although a persistently weak signal might cause population inversion, it came as cost of time. The trajectories of the two bistable systems under the pulse were examined in order to identify the cause of this counterintuitive behaviour. These trajectories showed that in case of the MI network, system did not respond to the pulse right

away; instead, it experienced a little delay before transitioning rapidly to the LSS (Figure 4.5c). On the contrary, in the case of the MA network, all trajectories responded to the pulse right away by displaying a sluggishness in decrease of kinase level, and following this first phase, the system quickly transitioned to the LSS (Figure 4.5d). As a result, the transition period was divided into two phases: the initial delay phase (au_{dly}) and the following rapid response phase (τ_{rsp}) . In the case of MI, the average duration of the initial delay phase increased with pulse duration in the low dose regime (Figure 4.5e), while the average duration of the second phase of the response was essentially independent of dose and pulse duration (Figure 4.5g). As a result, at low doses, the increase in $<\tau_{inv}>$ with τ_D was caused by an increase in τ_{aly} . Large pulse durations enabled more trajectories to switch their states at a later period, lengthening the average time, which caused the initial delay to increase. It was important to note that, such phenomena happened when the pulse amplitude(dose) was near to the right saddle-node bifurcation point, i.e.; $\Delta S_R \sim 0$. It suggested that the critical system slowing down towards the bifurcation point was the cause of the delay in reaching a decision to flip the steady state. At a high dose, the system was far from the bifurcation point ($\Delta S_R \gg 0$), therefore there was no critical slowing downinduced delay in response, which caused the system to respond more rapidly and independently of pulse duration. The system self-propelled itself to the LSS in a pulseindependent way once the decision to make a transition was taken. As a result, the increasing delay in the first response phase in the MI system was what caused the average transition time to increase with pulse duration. The dynamics of the system were very different in the case of MA compared to the MI motif. Here, the entire population responded instantly and displayed a long-lasting gradual decay before switching to the LSS (Figure 4.5d). The time duration for the initial slow decay phase (Figure 4.5f) and the time length of the transition to LSS (Figure 4.5h) were measured. Contrary to MI, $< au_{dly}>$ was almost independent of τ_D , while $<\tau_{rsp}>$ increased with pulse duration at the low pulse dosage. Therefore, the effect of the critical slowing down was only reflected in the second phase of the switching dynamics in the MA motif. These durations were found out to be not dependent on the relative magnitude of the resting pulse (Appendix 2, Figure A5.3).

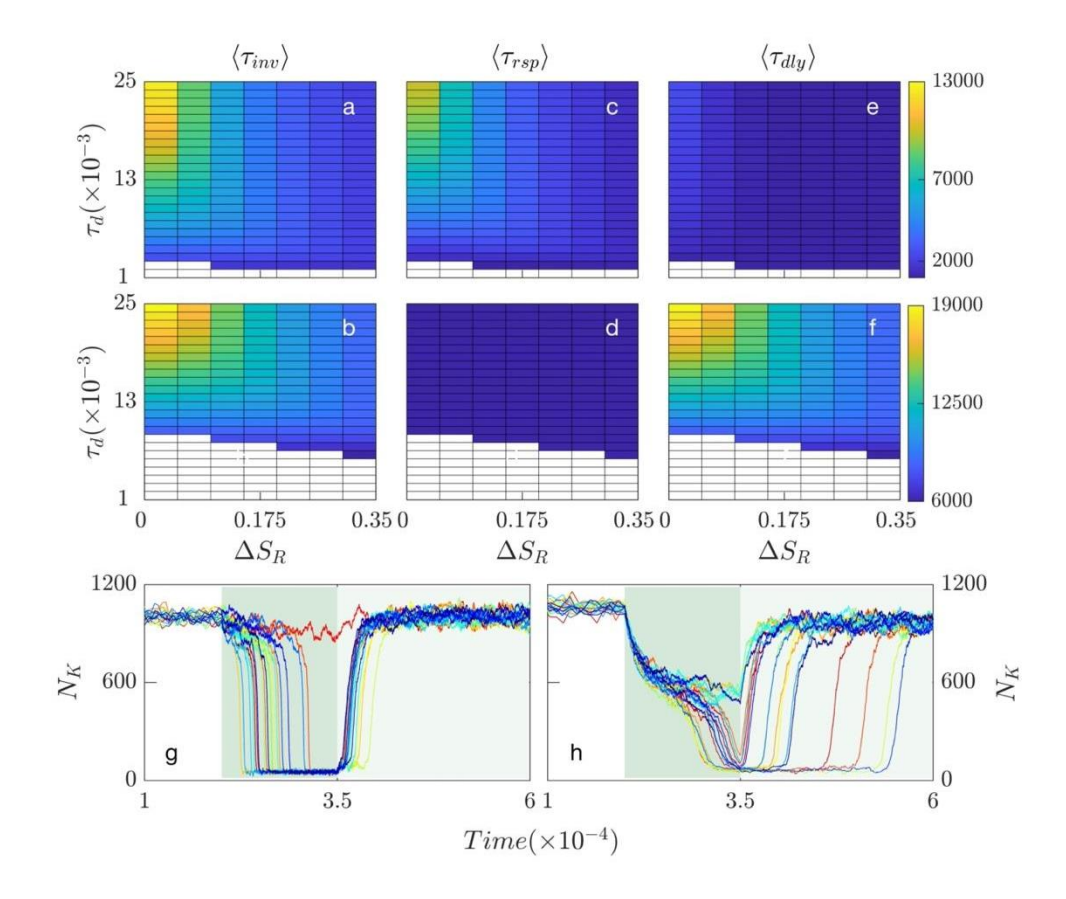


Figure 4.5: The surface plots of average inversion time $(\langle \tau_{inv} \rangle)$, average response time $(\langle \tau_{rsp} \rangle)$ and average initial delay time $(\langle \tau_{dly} \rangle)$ are presented as a function of τ_d and ΔS_R for the DNFL (top row) and PFL (middle) networks (a-f). The pulse induced temporal dynamics the kinase is shown for the DNFL (g) and PFL (h) networks. The dark and light green shaded regions indicate the pulse on state with maximum and resting amplitudes, respectively.

The fate of the flipped states was then established by calculating the percentage of cells that return to the upper steady state and the percentage that were locked in the lower steady state after the pulse had been removed. The magnitude of the resting pulse, S_r , had a significant impact on the fraction of the population that returns to the initial condition (f_{swt}) . For both bistable systems, the population returned to the upper steady state with low resting pulses (small ΔS_L), regardless of the pulse duration (Figure 4.6a-b) and amplitude (Appendix 2, Figure A5.4). However, the fraction of the population switching back dropped in a nonlinear fashion as the resting pulse (large ΔS_L) increases and as a result, the fraction of the population locked in the lower steady state increases in a complimentary manner (Appendix 2, Figure A5.5). The bistable switch of the MA motif had a lower rate of drop

of f_{swt} with increasing resting pulse as compared to the MI motif (Appendix 2, Figure A5.6). This implied that the bistable PFL motif was less prone to transition to the USS after the pulse was removed. Consistent with population results, a higher average residence duration (τ_{rsd}) at the lower steady state was caused by an increased resting pulse (Figure 5.6c-d). The longer pulse permitted the system to stay in the LSS for a longer period of time, which resulted in a little rise in τ_{rsd} . Compared to the MI, the MA had a larger effect of τ_D on τ_{rsd} . The pulse dose had no role on the system's residency and return dynamics. Although the average switching time (τ_{swt}) from the LSS to the USS increased slightly with the resting pulse, the average switching time (τ_{swt}) was mostly unaffected by the dose and pulse duration (Figure 4.6e-f).

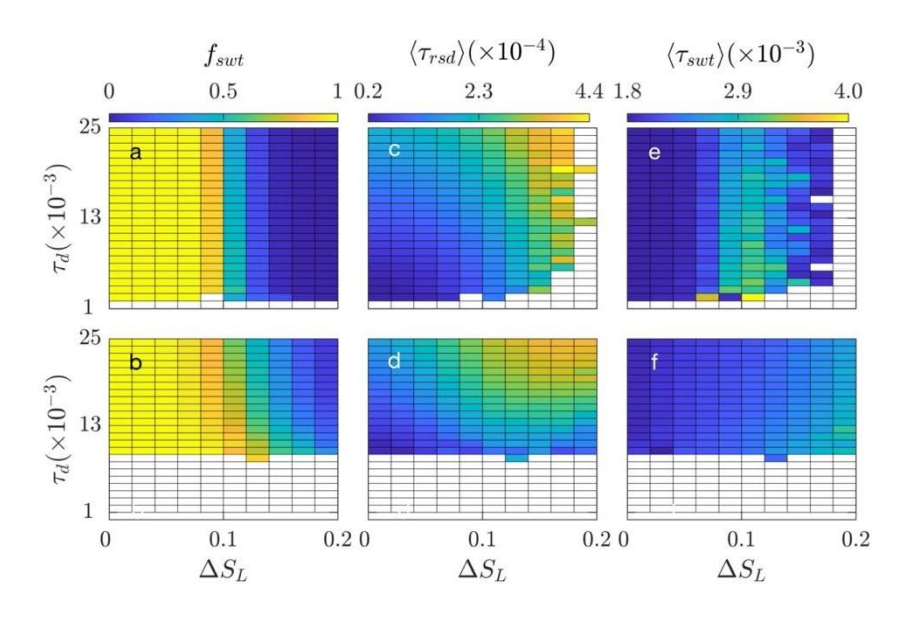


Figure 4.6: The fraction of the population that switches back to the USS (f_{swt}) , the average residence time in the LSS $(\langle \tau_{rsd} \rangle)$ and the average switching time $(\langle \tau_{swt} \rangle)$ are plotted as a function of pulse duration and resting pulse $(\Delta S_L = S_m - S_L)$ for the DNFL (top row) and PFL (bottom row) networks. ΔS_L represents the resting pulse over and above the signal value corresponding to the left saddle node bifurcation point. The value of the ΔS_R was 0.1.

The role of regulatory network was essential to reduce the chemical noise caused by fluctuations in the finite number of macromolecular species. Therefore, the coefficient of variation (Figure 4.7a–b) and average (Figure 4.c–d) duration of inversion and switching times were analysed across the MI and MA networks in order to comprehend the role of feedback loops in the regulation of chemical noise. For both networks, the noise in the

inversion time found to be increased with τ_D . This was because there was more relative time for the system to react to the pulse (= $(\tau_D - \langle \tau_{inv} \rangle)/\tau_D$) (Figure 4.7e). The relative available time quantified how much more time the system had over the typical inversion time to react to the pulse. A greater fraction of late responders could be accommodated with a longer relative available time which lead to the increased variability in τ_{inv} . When compared to the MI network, the MA network exhibited much less noisy in case both the inversion and switching time (Figure 4.7a-b). The CV and average of τ_{swt} were independent of τ_D since the switching dynamics was autonomous in nature. It was evident from these two average time durations that the MA motif required more time for the system to shift from one steady state to the other steady state of as compared to MI (Figure 4.7cd). These two findings implied that, in comparison to the bistable switch from a MI, the bistable switch from a MA was less sensitive to the external pulse. As a result, a MA motif would be less likely to undergo a stochastic transition from one state to another as a result of an external noisy signal. Thus, it could be commented that a MA would be more resistant to such perturbations by effectively removing the spurious signals. It was confirmed that greater robustness of MA was maintained across diverse pulse amplitudes by repeating similar computations for varied values of pulse amplitudes (Appendix 2, Figure A5.7).

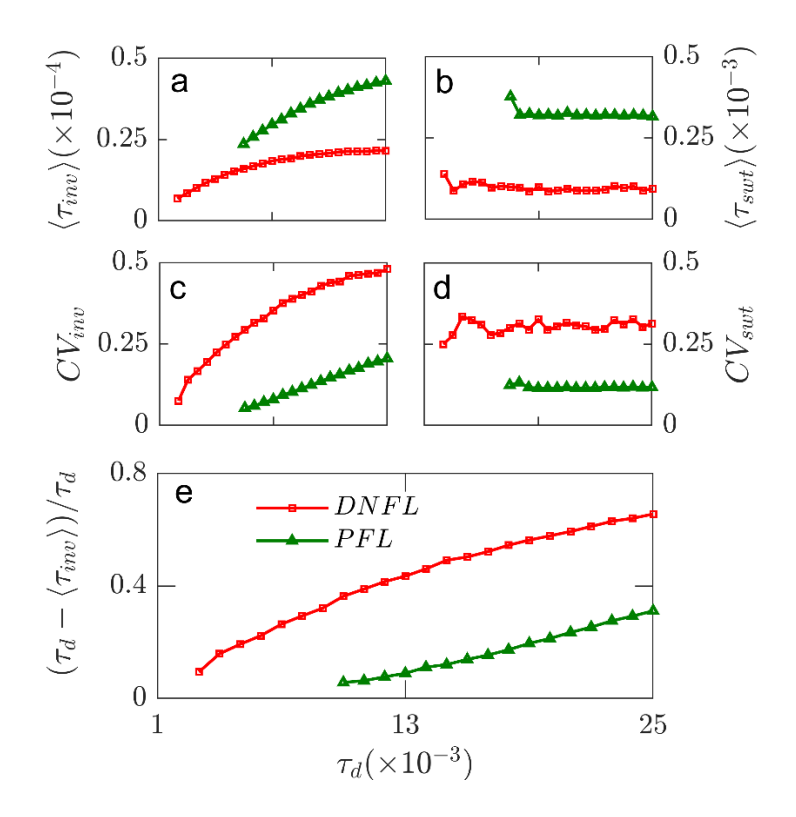


Figure 4.7: The comparison of statistical properties of inversion and switching times between the MI and MA networks (a-d). The comparison of relative available time vs. τ_d between the MI and MA networks. The values of the pulse dose and resting pulse were $\Delta S_R = 0$ and $\Delta S_R = 0$.

To determine if the history of the system influenced the future dynamics, the correlation between the inversion time and the residence time of individual trajectories for the MI motif was presented in Figure 4.8a-c. The trajectory that made an early transition to the lower steady state stayed there for a longer period of time, according to the negative correlation between these two events. The stronger the correlation coefficient, the more tightly the pulse controlled these two occurrences, or, in other words, the more predictable the system's temporal behaviour. The correlation for the MI network was stronger at higher τ_D (Figure 4.8a). This suggested that continuous exposure to a low amplitude signal may cause a delayed inversion of the steady state, however such an inversion would only last a short time. Therefore, when the inversion was caused by a low amplitude sustained signal, the dynamics of the system are more tightly controlled (or more deterministic/predictable). Because of the increasing variability of τ_{rsd} , the correlation for short pulses was weaker. On the contrary, there was a poor correlation between these two intervals at increased dose (Figure 4.8b) and resting pulse (Figure 4.8c). However, the reason behind the weaker correlations for the larger dose and resting pulse were not the same. Larger doses skewed the population toward smaller τ_{inv} without changing the switching dynamics, causing the two events to become incoherent. At a weak resting pulse, the temporal dynamics of the system correlate well with the temporal profile of the pulse and consequently, thus strong correlation between τ_{inv} and τ_{rsd} . At higher resting pulse, the temporal correlation between the pulse and the dynamics of the system was lost, resulting in a decreased correlation coefficient. A high resting pulse drove the system to be at a lower steady state with a greater $\langle \tau_{rsd} \rangle$. The qualitative effects of pulse parameters on the correlation in the case of MA are comparable to those of MI, however, the correlations were often worse than in MI across different pulse parameters (Figure 4.8d and see Appendix 2, Figure A4.8).

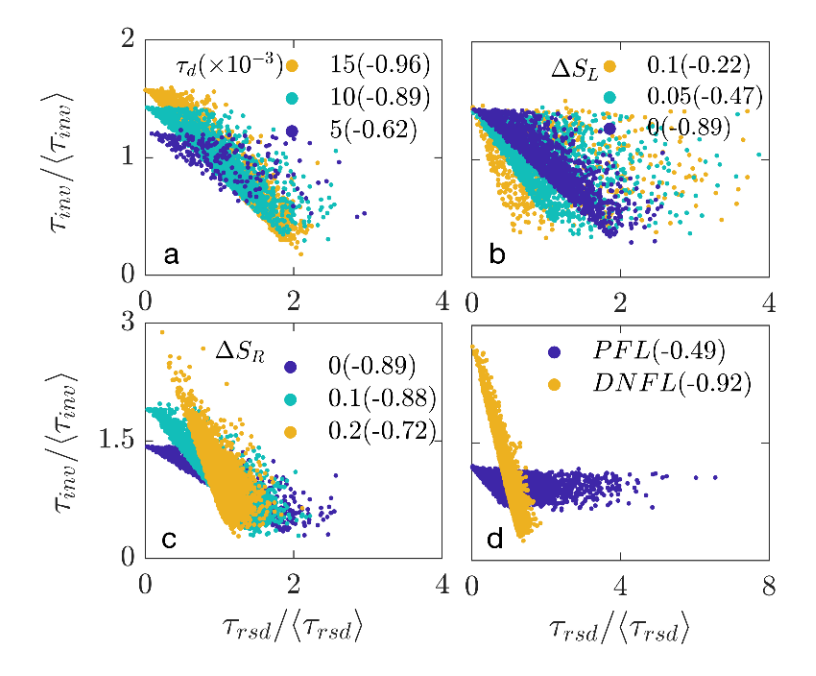


Figure 4.8: The correlation between the mean-normalized τ_{inv} and τ_{rsd} times are plotted for the indicated values of τ_d (a), resting pulse (ΔS_L , b) and pulse dose (ΔS_R , c) for the MI network. The values of correlation coefficients are indicated within the parenthesis inside each plot. In (d) the correlation between these two times is compared for the MI and MA networks.

These calculations were expanded to include networks with two merged positive feedback loops centred around the kinase K. With 10 phosphorylation sites, another protein regulator called Y was introduced. The active version of Y catalysed the synthesis or degradation of the kinase. The network diagrams for the two fused MIs and two fused MAs are shown in Figure 4.9a and 4.9b, respectively. Similar dynamical equations represented the phosphorylated chain of Y, as shown in the example of a single positive feedback loop (Eq.4.3-5). The catalytic impact of Y_0 on the kinase would add another degradation component to the equation for the kinase in the MI network. Similar to this, Y_{10} would add another synthesis term to the dynamical equation for the kinase in the MA network. In order to produce the same bifurcation diagrams as in the case of a single feedback loop, the value of k_a in this instance was decreased by a factor of two in comparison to the single loop example. Other than that, nothing had changed. Across different pulse dose and pulse length, the population fractions that invert to the other steady state in the two loops case

were consistently marginally greater (Figure 4.9c-d). The additional positive feedback loop thus facilitated pulse-induced transitions to another steady state.

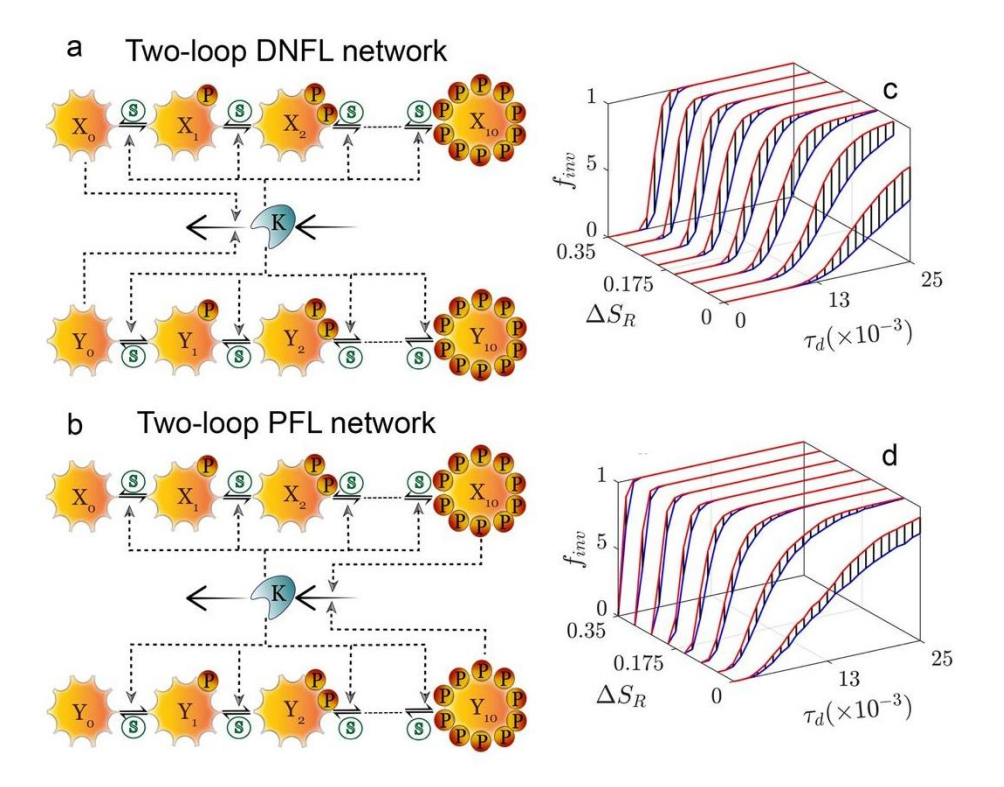


Figure 4.9: The network diagrams of two fused DNFLs (a) and two fused PFLs (b). Here, one more positive feedback loop is introduced either by mutual inhibition (a) or by mutual activation (b) between K and Y. Analogous to X, the phosphorylation and dephosphorylations of Y are catalyzed by the kinase, K, and the phosphatase, S, respectively. The plots of f_{inv} as a function of pulse dose (ΔS_R) and duration (τ_d) are compared between one-loop (blue lines) and two-loop (red lines) DNFL (c) and PFL (d) networks. The vertical black lines indicate the difference between the two lines.

4.4 Conclusion

Processing of different internal and external signals is essential for living organism to maintain a proper function of their physiology. The signal was often assumed to be in steady state while modelling the information procession by regulatory networks, where the amplitude of the signal did not change over time. But a cell may receive signals in pulsatile "packets" with changing amplitude and duration. In this chapter the fate of bistable switches was investigated produced either by mutual activation or mutual inhibition between two regulators in order to better understand how such transient signals were processed by

Pulse processing of bistable network motifs in presence of intrinsic noise

regulatory motifs. By forcing the bistable system into the other steady state, it was discovered that this kind of pulsatile signal could cause population inversion. The inversion could be induced by either a transient strong signal or a prolonged weak signal, or by a combination of both, showing that the dose or duration work compensatory with one another. It was found that the dose had a greater impact on the dynamics of the inversion than the duration of the signal. Irrespective of nature of bistable network, the pulse dose accelerated the population inversion by cutting down on average inversion time. However, the pulse duration promoted inversion by allowing late responders to switch their steady state. As a result, in the weak dose regime, the average transition time dramatically increased with pulse duration. This further demonstrated that when the signal dose was close to the saddle-node bifurcation point, the critical slowing of the trajectory had a significant impact on the dynamics. A significant distinction between how a between the processing of the pulse of mutual activation loop how a mutual inhibition loop was found. In case of mutual activation motif, the bistable system responded to the pulse instantly, and the average initial delay phase was unrelated to the duration of the pulse. Following this initial delay response, a sluggishness in the inversion process was found which was significantly influenced by the pulse duration. Whereas in case of mutual inhibition motifs, there was an initial duration dependent delay followed by a rapid inversion without exhibiting a transient response.

The percentage of the population locked in the flipped state and the average time spent in the flipped state greatly depend on the resting pulse. While the dynamics of the locked state or the switching dynamics to the original state was found to be independent of the pulse dose and pulse duration. Calculations for population inversion showed that for MA network, a prolonged duration of pulse was needed in order to population inversion. The average inversion time and the switching time were found to be higher in case of bistable switch originating from mutual activation network as compared to mutual inhibition network. Additionally, the variability in these times was smaller in case of MA network. These three results supported our conclusion that the mutual activation network is less susceptible any transient signal and therefore the mutual activation would be a better topology for a bistable switch to filter out any noisy external signal. These conclusions are consistent with previous finding that mutual activation networks are better topology in attenuating chemical noise in the context of sustained signaling ³⁷. According to correlations between inversion time and residence time, the inversion caused by the pulse and

subsequent switching to the original state were tightly regulated by weak and long duration pulses. This implied that when the inversion of steady state was achieved on by a weak signal with a longer duration, the system behaves in a deterministic or predictable manner. Thus, even if a short but strong pulse might effectively switch the steady state, the behaviour of the events that follow becomes less predictable.

4.5 References

- (1) Kholodenko, B. N. Cell-Signalling Dynamics in Time and Space. *Nat. Rev. Mol. Cell Biol.* 2006 73 **2006**, 7 (3), 165–176. https://doi.org/10.1038/nrm1838.
- (2) Ferrell, J. E. Self-Perpetuating States in Signal Transduction: Positive Feedback, Double-Negative Feedback and Bistability. *Curr. Opin. Cell Biol.* **2002**, *14* (2), 140–148. https://doi.org/10.1016/S0955-0674(02)00314-9.
- (3) Tyson, J. J.; Novák, B. Functional Motifs in Biochemical Reaction Networks. http://dx.doi.org/10.1146/annurev.physchem.012809.103457 2010, 61, 219–240. https://doi.org/10.1146/ANNUREV.PHYSCHEM.012809.103457.
- (4) Purvis, J. E.; Lahav, G. Encoding and Decoding Cellular Information through Signaling Dynamics. *Cell* **2013**, *152* (5), 945–956. https://doi.org/10.1016/j.cell.2013.02.005.
- (5) Tyson, J. J.; Novak, B. A Dynamical Paradigm for Molecular Cell Biology. *Trends Cell Biol.* **2020**, *30* (7), 504–515. https://doi.org/10.1016/j.tcb.2020.04.002.
- Tyson, J. J.; Chen, K. C.; Novak, B. Sniffers, Buzzers, Toggles and Blinkers: Dynamics of Regulatory and Signaling Pathways in the Cell. *Curr. Opin. Cell Biol.*2003, 15 (2), 221–231. https://doi.org/10.1016/S0955-0674(03)00017-6.
- (7) Ferrell, J. E. Perfect and Near-Perfect Adaptation in Cell Signaling. *Cell Syst.* **2016**, 2 (2), 62–67. https://doi.org/10.1016/j.cels.2016.02.006.
- (8) Ma, W.; Trusina, A.; El-Samad, H.; Lim, W. A.; Tang, C. Defining Network Topologies That Can Achieve Biochemical Adaptation. *Cell* **2009**, *138* (4), 760–773. https://doi.org/10.1016/j.cell.2009.06.013.
- (9) Mangan, S.; Alon, U. Structure and Function of the Feed-Forward Loop Network Motif. *Proc. Natl. Acad. Sci. U. S. A.* **2003**, *100* (21), 11980–11985.

- https://doi.org/10.1073/PNAS.2133841100/SUPPL_FILE/3841TABLE5.XLS.
- (10) Becker-Weimann, S.; Wolf, J.; Herzel, H.; Kramer, A. Modeling Feedback Loops of the Mammalian Circadian Oscillator. *Biophys. J.* **2004**, 87 (5), 3023–3034. https://doi.org/10.1529/biophysj.104.040824.
- (11) Gonze, D. Modeling Circadian Clocks: From Equations to Oscillations. *Cent. Eur. J. Biol.* **2011**, *6* (5), 699–711. https://doi.org/10.2478/S11535-011-0061-5/XML.
- (12) Kim, J. K.; Forger, D. B. A Mechanism for Robust Circadian Timekeeping via Stoichiometric Balance. *Mol. Syst. Biol.* **2012**, 8 (1), 630. https://doi.org/10.1038/MSB.2012.62.
- (13) Leloup, J. C.; Goldbeter, A. Toward a Detailed Computational Model for the Mammalian Circadian Clock. *Proc. Natl. Acad. Sci. U. S. A.* **2003**, *100* (12), 7051–7056. https://doi.org/10.1073/PNAS.1132112100/SUPPL_FILE/2112FIG8.PDF.
- (14) Ueda, H. R.; Hagiwara, M.; Kitano, H. Robust Oscillations within the Interlocked Feedback Model of Drosophila Circadian Rhythm. *J. Theor. Biol.* **2001**, *210* (4), 401–406. https://doi.org/10.1006/JTBI.2000.2226.
- (15) Hayot, F.; Jayaprakash, C. NF- κ B Oscillations and Cell-to-Cell Variability. *J. Theor. Biol.* **2006**, 240 (4), 583–591. https://doi.org/10.1016/j.jtbi.2005.10.018.
- (16) Bagci, E. Z.; Vodovotz, Y.; Billiar, T. R.; Ermentrout, G. B.; Bahar, I. Bistability in Apoptosis: Roles of Bax, Bcl-2, and Mitochondrial Permeability Transition Pores. *Biophys. J.* **2006**, *90* (5), 1546–1559. https://doi.org/10.1529/biophysj.105.068122.
- (17) Spencer, S. L.; Sorger, P. K. Measuring and Modeling Apoptosis in Single Cells. *Cell* **2011**, *144* (6), 926–939. https://doi.org/10.1016/J.CELL.2011.03.002.
- (18) Domingo-Sananes, M. R.; Szöor, B.; Ferguson, M. A. J.; Urbaniak, M. D.; Matthews, K. R. Molecular Control of Irreversible Bistability during Trypanosome Developmental Commitment. *J. Cell Biol.* **2015**, *211* (2), 455–468. https://doi.org/10.1083/jcb.201506114.
- (19) Wang, L.; Walker, B. L.; Iannaccone, S.; Bhatt, D.; Kennedy, P. J.; Tse, W. T. Bistable Switches Control Memory and Plasticity in Cellular Differentiation. *Proc. Natl. Acad. Sci. U. S. A.* 2009, 106 (16), 6638–6643. https://doi.org/10.1073/PNAS.0806137106/ASSET/84C884EC-7704-4DAB-

- BD7A-8409DE49B5DE/ASSETS/GRAPHIC/ZPQ9990975310006.JPEG.
- (20) Zhang, J.; Tian, X. J.; Zhang, H.; Teng, Y.; Li, R.; Bai, F.; Elankumaran, S.; Xing, J. TGF-β-Induced Epithelial-to-Mesenchymal Transition Proceeds through Stepwise Activation of Multiple Feedback Loops. *Sci. Signal.* 2014, 7 (345), ra91. https://doi.org/10.1126/SCISIGNAL.2005304/SUPPL_FILE/7_RA91_SM.PDF.
- (21) Pomerening, J. R.; Sontag, E. D.; Ferrell, J. E. Building a Cell Cycle Oscillator: Hysteresis and Bistability in the Activation of Cdc2. *Nat. Cell Biol.* 2003 54 2003, 5 (4), 346–351. https://doi.org/10.1038/ncb954.
- (22) Ajo-Franklin, C. M.; Drubin, D. A.; Eskin, J. A.; Gee, E. P. S.; Landgraf, D.; Phillips, I.; Silver, P. A. Rational Design of Memory in Eukaryotic Cells. *Genes Dev.* 2007, 21 (18), 2271–2276. https://doi.org/10.1101/gad.1586107.
- (23) Chang, D. E.; Leung, S.; Atkinson, M. R.; Reifler, A.; Forger, D.; Ninfa, A. J. Building Biological Memory by Linking Positive Feedback Loops. *Proc. Natl. Acad. Sci. U. S. A.* **2010**, *107* (1), 175–180. https://doi.org/10.1073/PNAS.0908314107/SUPPL_FILE/PNAS.200908314SI.PD F.
- (24) Doncic, A.; Atay, O.; Valk, E.; Grande, A.; Bush, A.; Vasen, G.; Colman-Lerner, A.; Loog, M.; Skotheim, J. M. Compartmentalization of a Bistable Switch Enables Memory to Cross a Feedback-Driven Transition. *Cell* 2015, 160 (6), 1182–1195. https://doi.org/10.1016/J.CELL.2015.02.032.
- (25) Raj, A.; van Oudenaarden, A. Nature, Nurture, or Chance: Stochastic Gene Expression and Its Consequences. *Cell* **2008**, *135* (2), 216–226. https://doi.org/10.1016/J.CELL.2008.09.050.
- (26) Dalal, C. K.; Cai, L.; Lin, Y.; Rahbar, K.; Elowitz, M. B. Pulsatile Dynamics in the Yeast Proteome. *Curr. Biol.* **2014**, 24 (18), 2189–2194. https://doi.org/10.1016/J.CUB.2014.07.076.
- (27) Hansen, A. S.; O'Shea, E. K. Encoding Four Gene Expression Programs in the Activation Dynamics of a Single Transcription Factor. *Curr. Biol.* **2016**, *26* (7), R269--R271. https://doi.org/10.1016/J.CUB.2016.02.058.
- (28) Harton, M. D.; Koh, W. S.; Bunker, A. D.; Singh, A.; Batchelor, E. P53 Pulse

- Modulation Differentially Regulates Target Gene Promoters to Regulate Cell Fate Decisions. *Mol. Syst. Biol.* **2019**, *15* (9), e8685. https://doi.org/10.15252/MSB.20188685.
- (29) Purvis, J. E.; Karhohs, K. W.; Mock, C.; Batchelor, E.; Loewer, A.; Lahav, G. P53 Dynamics Control Cell Fate. *Science* (80-.). 2012, 336 (6087), 1440–1444. https://doi.org/10.1126/SCIENCE.1218351/SUPPL_FILE/PURVIS-SOM.PDF.
- (30) Albeck, J. G.; Mills, G. B.; Brugge, J. S. Frequency-Modulated Pulses of ERK Activity Transmit Quantitative Proliferation Signals. *Mol. Cell* **2013**, *49* (2), 249–261. https://doi.org/10.1016/J.MOLCEL.2012.11.002.
- (31) de la Cova, C.; Townley, R.; Regot, S.; Greenwald, I. A Real-Time Biosensor for ERK Activity Reveals Signaling Dynamics during C. Elegans Cell Fate Specification. *Dev. Cell* **2017**, *42* (5), 542-553.e4. https://doi.org/10.1016/j.devcel.2017.07.014.
- (32) Imayoshi, I.; Isomura, A.; Harima, Y.; Kawaguchi, K.; Kori, H.; Miyachi, H.; Fujiwara, T.; Ishidate, F.; Kageyama, R. Oscillatory Control of Factors Determining Multipotency and Fate in Mouse Neural Progenitors. *Science* (80-.). 2013, 342 (6163), 1203–1208. https://doi.org/10.1126/SCIENCE.1242366/SUPPL_FILE/IMAYOSHI.SM.PDF.
- (33) Ochi, S.; Imaizumi, Y.; Shimojo, H.; Miyachi, H.; Kageyama, R. Oscillatory Expression of Hes1 Regulates Cell Proliferation and Neuronal Differentiation in the Embryonic Brain. *Dev.* **2020**, *147* (4). https://doi.org/10.1242/DEV.182204/266856/AM/OSCILLATORY-EXPRESSION-OF-HES1-REGULATES-CELL.
- (34) Lane, K.; Van Valen, D.; DeFelice, M. M.; Macklin, D. N.; Kudo, T.; Jaimovich, A.; Carr, A.; Meyer, T.; Pe'er, D.; Boutet, S. C.; Covert, M. W. Measuring Signaling and RNA-Seq in the Same Cell Links Gene Expression to Dynamic Patterns of NF-\$κ\$B Activation. *Cell Syst.* 2017, 4 (4), 458--469.e5. https://doi.org/10.1016/j.cels.2017.03.010.
- (35) Zambrano, S.; de Toma, I.; Piffer, A.; Bianchi, M. E.; Agresti, A. NF-\$κ\$B Oscillations Translate into Functionally Related Patterns of Gene Expression. *Elife* 2016, 5 (JANUARY2016). https://doi.org/10.7554/ELIFE.09100.

- (36) Gillespie, D. T. A General Method for Numerically Simulating the Stochastic Time Evolution of Coupled Chemical Reactions. *J. Comput. Phys.* **1976**, 22 (4), 403–434. https://doi.org/10.1016/0021-9991(76)90041-3.
- (37) Hornung, G.; Barkai, N. Noise Propagation and Signaling Sensitivity in Biological Networks: A Role for Positive Feedback. *PLoS Comput. Biol.* **2008**, *4* (1), 0055–0061. https://doi.org/10.1371/journal.pcbi.0040008.

CHAPTER 5

Effect of extrinsic noise on the heterogeneity of bistable responses

5.1 Introduction

Cellular physiological processes are regulated by complex networks of chemical reactions involving diverse types of biomolecules. Complexity of the regulatory networks poses a great difficulty in their characterization and understanding which are crucial in diseases context^{1,2}. Often many complex networks consist of a core regulatory unit that functions as the main regulatory engine of the physiological processes in the cell³. The core regulatory unit can be sliced into functional motifs possessing unique steady state and dynamical properties and thus functional motifs are highly relevant in understanding the behavior of the whole regulatory network (See Introduction). Signal transducer, positive feedback loop (PFL), negative feedback loop, feed-forward loop, antithetic integral feedback loop are some of the important functional motifs that have characteristic properties dictating the behavior of the regulatory network^{4,5}.

As discussed in previous chapters, PFL is well-known for its ability to generate bistable signal response curve or bistable switch. Binary decision making processes in living cells are often governed by bistable switch characterized by initial condition dependent gene expression with distinct signaling thresholds of ON and OFF states of the gene⁶. In physiological context bistability has been found to be the principal architect in regulating restriction point in the cell division cycle of mammalian cells^{7,8,9}, entry and exit from mitosis in Xenopus laevis^{10,11}, programmed cell death by apoptosis^{12–14}, mutually exclusive cell fate choice^{15–20} and cellular memory^{21,22}. Now, due to the extrinsic source of heterogeneity in isogenic populations of cells (see Introduction), the strength of regulatory interactions in similar PFL motifs may vary from one cell to another. This variability in the strength of regulatory interactions may result in

different qualitative behaviors. In a canonical bistable signal response curve, the gene expression changes from low-to-high or high-to-low through a bistable switch and a simple signal transduction of one of the genes in the PFL is sufficient to generate canonical bistability^{23–29}. When both the genes in the PFL, created either by mutual inhibition (MI) or mutual activation (MA) loop, are signaled by the same external regulator it creates a dual signaling PFL motif (Figure 5.1a). Intuitively such a network motif is expected to generate bistability. However, due to the combinatorial possibilities on the nature of dual input signals, new bistable switches may originate as emergent properties of the dual signaling PFL motif. Previous works have shown that incoherent feed-forward signaling of a self-activating gene may result mushroom and isola bistable switches³⁰. Mushroom bistability consists of two bistable switches fused in a face-to-face manner with an intervening monostable region. Isola switch on the contrary exhibits a single bistable region however with a curious feature of an island of steady states created by a stable and unstable branch^{30,31}. In both the switches the expression of the gene changes from low-to-high-to-low (or high-to-low-to-high) as opposed to a canonical switch that exhibits low-to-high (or high-to-low). This chapter discussed the robustness of such dual signaling positive feedback loop topologies attaining heterogenous bistable responses in presence of extrinsic noise. The origin of such heterogenous switches and their interconversion were also extensively studied.

5.2 Model

Figure 5.1a represented the core topology of PFL model under dual signaling where both the genes in the PFL are regulated by a common regulator. Accordance with chapter 4, the PFL was modelled with mutual inhibition (MI) and mutual activation (MA) loops between the genes. The coherent (same) or incoherent (different) nature of signaling arm towards two genes landed in a set of three networks for each for the MI and MA loops (Figure 1b). Further, due to the prevalence of fused PFLs in cellular differentiation pathways and cancer metastasis, mutual inhibition self-activation (MISA) and mutual activation self-activation (MASA) motifs was further included by introducing a self-activatory PFL in the MI and MA motifs, respectively (Figure 1c). Thus, total number of model network became of 14. Now, it is well known that depending upon the number of PFLs, networks can produce conventional bistable (Bs) and dual bistable (DBs) switches consisting of one and two bistable regions, respectively, and these switches were categorised as canonical bistable switches (Figure 1d). However,

because of certain possibility of these network generating new emergent bistable switches, a set of 12 reversible noncanonical switches consisting of one or two or three bistable regions were considered (Figure 1d). The full 1-p bifurcation diagrams of these switches were listed in the Appendix 3, Table A5.1. Isola (Is) and inverted isola (InIs) are the two noncanonical switches that consist of a single bistable region and these switches contain a disconnected stable branch and an isolated island of steady states created by connecting a stable and an unstable branch via two saddle-node (SN) bifurcation points. Mushroom (Msh), inverted mushroom (InMsh), bistable-isola (Bs-Is), bistable-inverted isola (Bs-InIs) and dual isola (DIs) are the noncanonical switches consisting of two bistable regions and four SN bifurcation points. The noncanonical switches with three bistable regions with six SN points are isola-mushroom (Is-Msh), inverted isola-mushroom (InIs-Msh), bistable-mushroom (Bs-Msh), dual bistable-isola (DBs-Is) and dual bistable-inverted isola (DBs-InIs). All of these noncanonical switches originate from the fusion of two or more canonical/noncanonical switches in various numbers, orientations and orders.

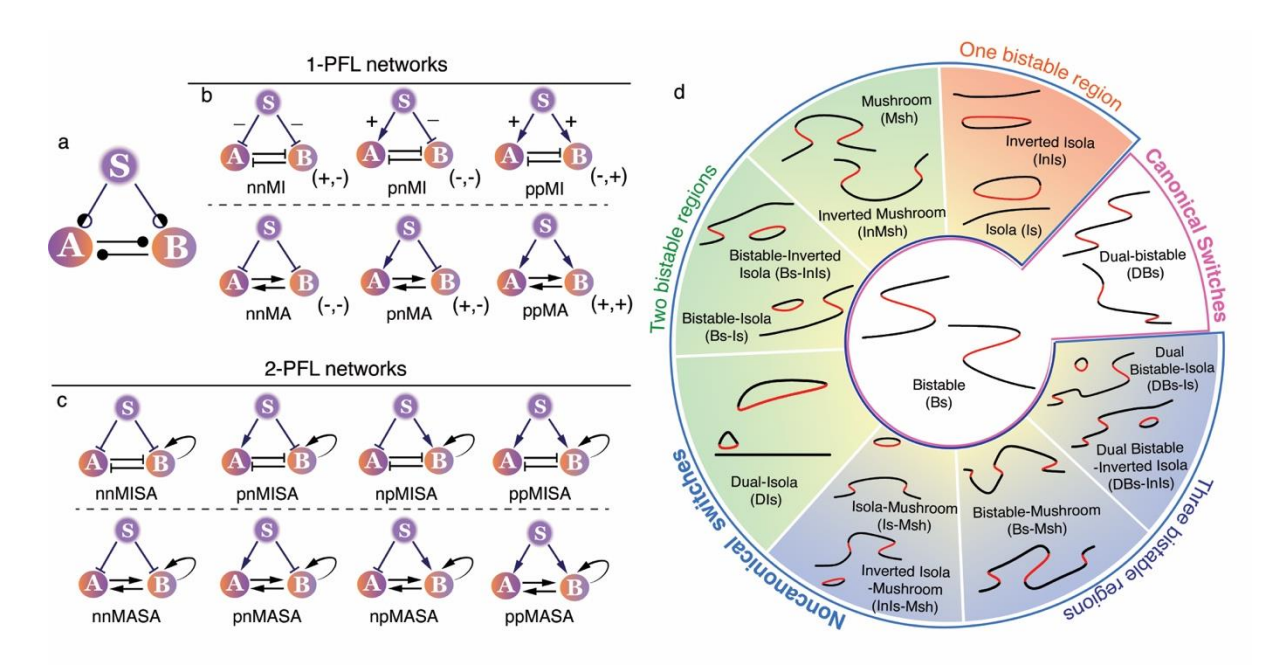


Figure 5.1: Dual signaling PFL networks and noncanonical bistable switches. The core topology of the dual signaling PFL motif consists of a regulator (S) that signals two genes (A and B) connected by a PFL (a). Arrows with partially filled circles indicate either coherent or incoherent nature of the input signals. A set of three unique networks exist both for the MI and MA loops (b). The arrow- and blunt-headed lines represent activation and inhibition, respectively. In each set, the signs of the input signal are (-,-) (+,-) and (+,+). The signs of the resultant regulation on B via the indirect and direct arms are represented beside each network.

'n' and 'p' in the network names represent inhibitory (negative) and activatory (positive) signals on the target genes, respectively. The network becomes asymmetric with the inclusion of a self-activation and a set of four networks possible both for the MISA and MASA motifs (c). The networks are categorized into 1-PFL and 2-PFL motifs based on the number of PFLs in the networks. Bistable switches are categorized into canonical and noncanonical groups and the noncanonical switches are segregated based on the number of bistable regions (d). The switches are represented by the one-parameter bifurcation diagram where the steady state of B is plotted as a function of the signal S (not shown explicitly). The black and red lines represent the stable and unstable steady states. The complete bifurcation diagrams of these switches are presented in the Appendix 3, Table A 5.1.

To investigate these noncanonical switches, the networks were modeled using nonlinear ordinary differential equations. In general, the activation of a target gene (X) by another gene (Y) is expressed by the Hill function as

$$H_{XY}^{+}(Y) = \frac{\binom{Y}{J_{XY}}^{n_{XY}}}{1 + \binom{Y}{J_{XY}}^{n_{XY}}}$$
 5.1

Where n_{XY} and J_{XY} are the Hill coefficient and activation threshold, respectively. The inhibition of the gene is represented by $H_{XY}^- = 1 - H_{XY}^+$. When a target gene is regulated by multiple regulatory signals, the functionality of the gene may need to satisfy logic gate configurations. To address this, investigation was done for both the OR- and AND-gate configurations of the gene A and B in the networks. In the OR-gate, the net regulatory influence on a target gene was represented by the summation of the individual inputs. As a representative case, the dynamical equations for the ppMI network were given as,

$$\frac{dA}{dt} = g_{A0} + g_{AS}H_{AS}^{+}(S) + g_{AB}H_{AB}^{-}(B) - \gamma_{A}A$$
 5.2

$$\frac{dB}{dt} = g_{B0} + g_{BS}H_{BS}^{+}(S) + g_{BA}H_{BA}^{-}(A) - \gamma_{B}B$$
 5.3

 g_{X0} , g_{XY} and γ_X represent the unregulated synthesis, maximal synthesis and degradation rates of X. On the contrary, the net regulatory influence on a target gene was represented by the

multiplication of the individual inputs in the AND-gate configuration. The dynamical equations for the same network were given as

$$\frac{dA}{dt} = g_{A0} + g_{A1}H_{AS}^{+}(S)H_{AB}^{-}(B) - \gamma_{A}A$$
 5.4

$$\frac{dB}{dt} = g_{B0} + g_{B1}H_{BS}^{+}(S)H_{BA}^{-}(A) - \gamma_{B}B$$
 5.5

The dynamical equations for all networks are listed in the Appendix 3, Table A 5.2. Now in order to investigate the robustness of each network towards generating heterogenous bistable responses under the influence of extrinsic noise, the steady state responses needed to be studied for variable regulatory interaction strengths. To implement this condition of variable regulatory strengths, a random parameter combination space was created. All parameters, except the activation/inhibition thresholds (J_{XY}) were sampled from independent uniform distributions having a particular range (See Appendix 3, Table A 5.3). The ranges were selected in such a way that the expression level falls in the biologically relevant range. In order to avoid bias in the threshold values, the half-functional rule was adopted to ensure that the randomly chosen values of the threshold are not biased towards activation or inhibition³⁰. The sample space for parameter combination was 900,000. Now, the conventional method of running 1-p bifurcation analysis using XPPAUT for every parameter combination for each network would have a tedious job. Thus, recently developed automated method of pseudo potential based bifurcation analysis method was deployed in order to avoid any manual intervention of these large-scale analysis (see chapter 2 for methodology). During each analysis, the types of bistable switches were also determined by exploiting the number of saddle node points (SNs) and the direction of the jump in the value of the stable steady state at the bifurcation points (see Appendix 3 Table A5.4 for jump patterns). The number of various types of switches that each network was counted in order to determine the variability of the steady state responses.

5.3 Results

Figure 5.2a showed the total count (and %) of canonical and noncanonical bistable switches for all networks under OR- and AND-gate. A group of networks were found to be generating exclusively canonical bistability without a single noncanonical response, while another group generated both the canonical and noncanonical responses. Close inspection of the networks

revealed that the noncanonical bistable switches were produced only when the input signals are coherent ((+,+) or (-,-)) for the MI loop and incoherent ((+,-) or (-,+)) for the MA loop irrespective of the number of PFLs and logic gates (Figure 2b). An alternative view of the PFL topology resulting in noncanonical responses was the resultant regulatory signs (see Figure 1b) from S to B (or S to A) via indirect and direct regulations must be dissimilar ((+,-) or (-,+)). The networks with the same resultant regulatory signs on any gene were only noncanonical switches across any parameter combination. Thus, it was concluded that the network with same resultant signs on any gene were more robust towards any variation in their regulatory strengths as it produces only canonical responses. The presence of the additional self-activation in the fused PFLs did not influence these conclusions and it only result in the increased absolute counts of bistable switches. Several additional features also emerged from these total counts. The MA loops were found to be expressing a larger number of noncanonical switches as compared to the MI loops in both the logic gates. Between OR- and AND-gate, MI loops under OR-gate were more potent in generating noncanonical responses as compared to the ANDgate. It was also quite remarkable to note that the counts or the percentage of noncanonical responses of a pair of MI networks (nnMI and ppMI or nnMISA and ppMISA) and a pair of MA networks (npMASA and pnMASA) were nearly identical.

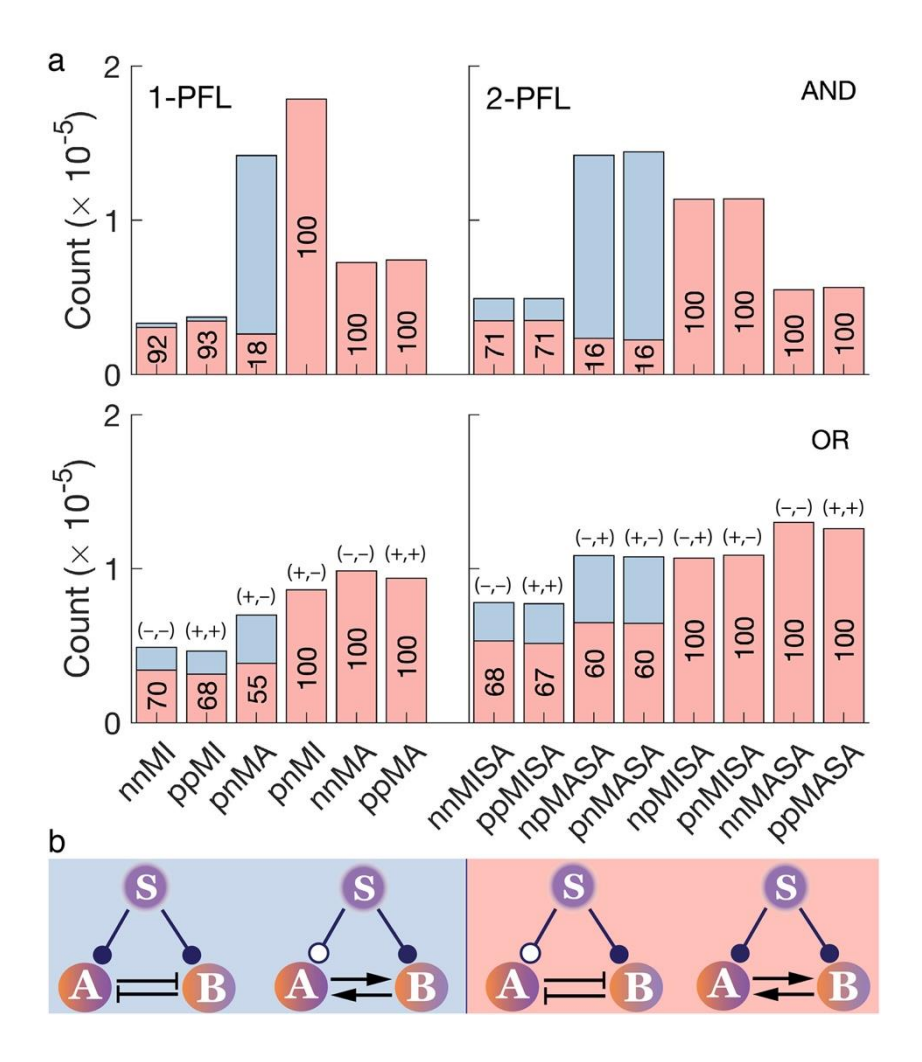


Figure 5.2: Total counts of canonical and noncanonical switches. The total count of canonical and noncanonical bistable switches from the networks under OR- (bottom row) and AND-gate (top row) (a). The percentage of canonical switches from a particular network is indicated within each bar. The signs of the two input signaling arms of each network are indicated at the top of the corresponding bar. The MI and MA loops under coherent and incoherent signaling, respectively resulted in generation of both canonical and noncanonical bistability (b, left), otherwise networks resulted in generation of only canonical response (b, right).

It was further interesting to look in to the heterogeneity of bistable switches from the counts of individual switches for the noncanonical switch producing network. The three 1-PFL networks (nnMI, ppMI and pnMA) produced a large number of canonical Bs switches and do not produce

any DBs switch (Figure 5.3a). On the contrary 2-PFL networks (nnMISA, ppMISA, npMASA and pnMASA) generated a significant number of DBs. In DBs, the expression level of B changes from low-to-intermediate-to-high (or high-to-intermediate-to-low) and thus it required two step activation (or inactivation) of the target gene. The additional PFL in the 2-PFL networks allowed such two-step activation. For comparison convenience, noncanonical switches were segregated based on the number of bistable regions and compared the counts from all the networks (Figure 5.3b-d). Both 1-PFL and 2-PFL networks produced a large number of Is and InIs switches having a single bistable region (Figure 3b). Although 1-PFL MI networks were equally capable of producing both types of isola, however the 1-PFL MA network produced an overwhelmingly larger number of InIs than the normal Is. Across all 2-PFL networks InIs is the preferred response as compared to Is. InMsh, Msh, Bs-Is and Bs-InIs were switches with two bistable regions and were generated in significant numbers by these networks (Figure 5.3c). While Msh and InMsh originated from the fusion of two canonical bistable switches, the Bs-Is and Bs-InIs result from the conglomeration of canonical Bs with noncanonical Is (Appendix Table A 5.1). Due to their complex nature, the counts of bistabilitywith-isola switches were significantly less as compared to mushroom switches. Analogous to isola switches, the counts of InMsh were significantly more than the Msh in the 1-PFL MA network and across all 2-PFL networks. It was important to note that, although 1-PFL networks did not generate a single switch consisting of two bistable regions (DBs), however, they generate various noncanonical switches consisting of two bistable regions. The counts of noncanonical switches with three bistable regions were dramatically less as compared to the two bistable regions (Figure 3d). All five noncanonical switches with three bistable regions originate from the fusion of a canonical/noncanonical switch with another noncanonical switch (Appendix 3, Table A5.1). Bs-Msh was the only noncanonical switch generated by the 1-PFL networks. However, a small number of other switches were also generated by the 2-PFL networks. Therefore, with additional fused PFL the counts of rare switches were expected to increase. In the AND-gate similar results were obatained however with shuttle differences. Overall, the heterogeneity of the noncanonical switches is less under AND-gate (Appendix 3, Figure A5.1). As opposed to OR-gate, here the Is and Msh were more as compared to their inverted counterparts. It was also intriguing to note that networks with MA loop do not generate any inverted switches (InIs or InMsh).

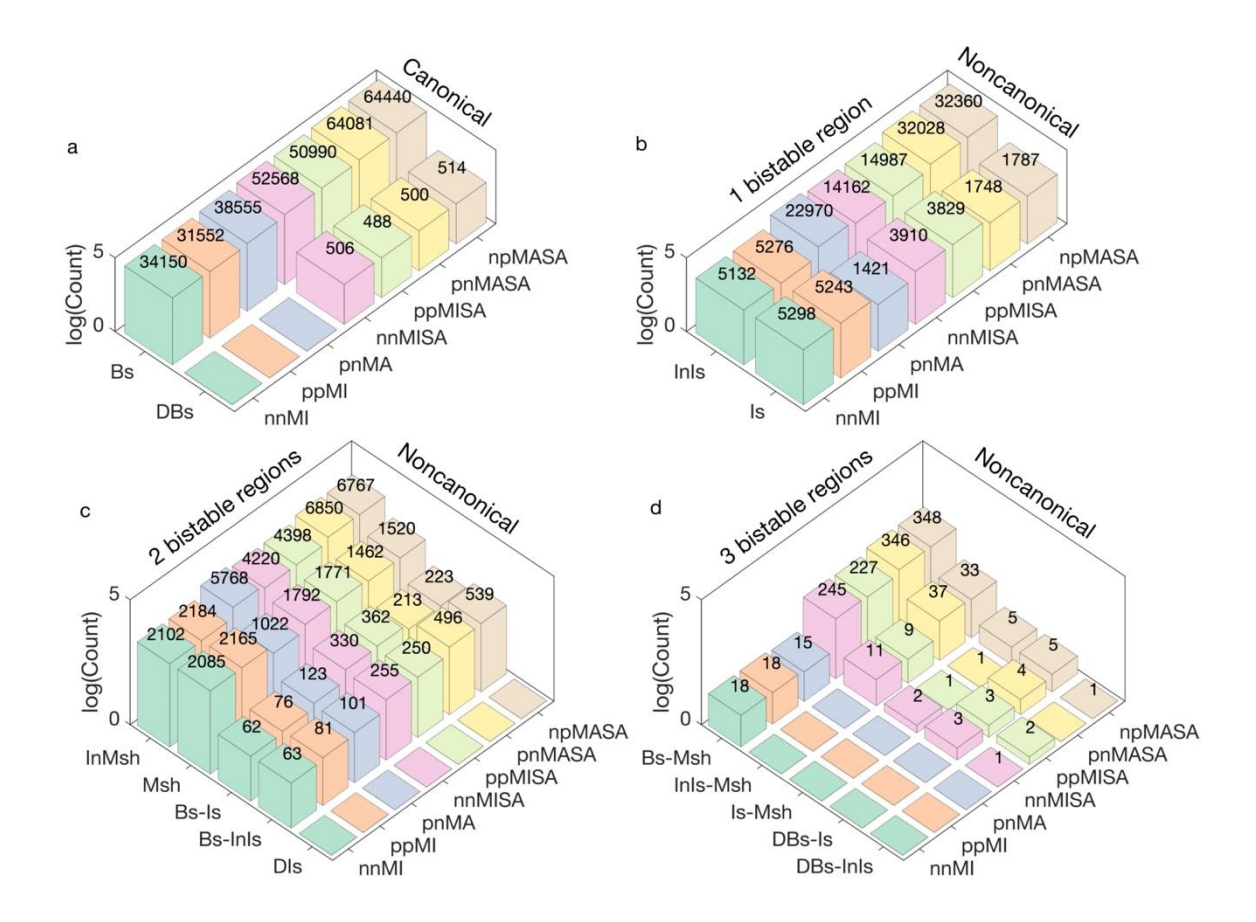


Figure 5.3: Heterogeneity of canonical and noncanonical switches. The total number of various types of canonical (a) and noncanonical (b-d) bistable switches are presented for the 1-PFL and 2-PFL networks under OR-gate configuration. The noncanonical switches are segregated into one (b), two (c) and three (d) bistable regions.

To obtain a quantitative estimation of the probability of obtaining these noncanonical switches, the percentage chance (% Chance) of noncanonical switches by normalizing their counts with the total count of all bistable switches was calculated (Figure 5.4a-b). The % Chance showed that the likelihood of obtaining some of the noncanonical switches were quite high from the dual signaling PFL networks. Among all the noncanonical switches, InIs was found to be the most likely outcome both from the MI and MA networks. In fact, there was one in three chances of obtaining an InIs in MA networks. InMsh was the second most probable noncanonical switch in MA networks. The chances of generating isola and mushroom were significant in MI networks. Probability of obtaining more complex switches involving three bistable regions were relatively less from networks with a single PFL. However, the counts 2-PFLs indicated

that complex switches are possible in fused PFL networks. The % Chance of noncanonical switches from the MI networks having (+,+) input signals correlated very well with that of the networks having (-,-) input signals (ppMISA vs. nnMISA and ppMI vs. nnMI) (Figure 5.4c). Similarly the MA network with (+,-) input signals showed a good correlation of % Chance with the MA network having (-,+) input signals (Figure 5.4d). The near perfect correlations suggest that the probability of noncanonical switch did not depend on the specific nature of the input signal pair provided the conditions of dual signaling are satisfied by the network. The % Chance for the AND-gate networks highlight the overwhelmingly high probability (~80%) of generating Is switch by the MA network (Appendix 3, Figure A5.2). Further it also showed that the MA networks under AND-gate are not all capable of producing neither inverted isola nor inverted mushroom.

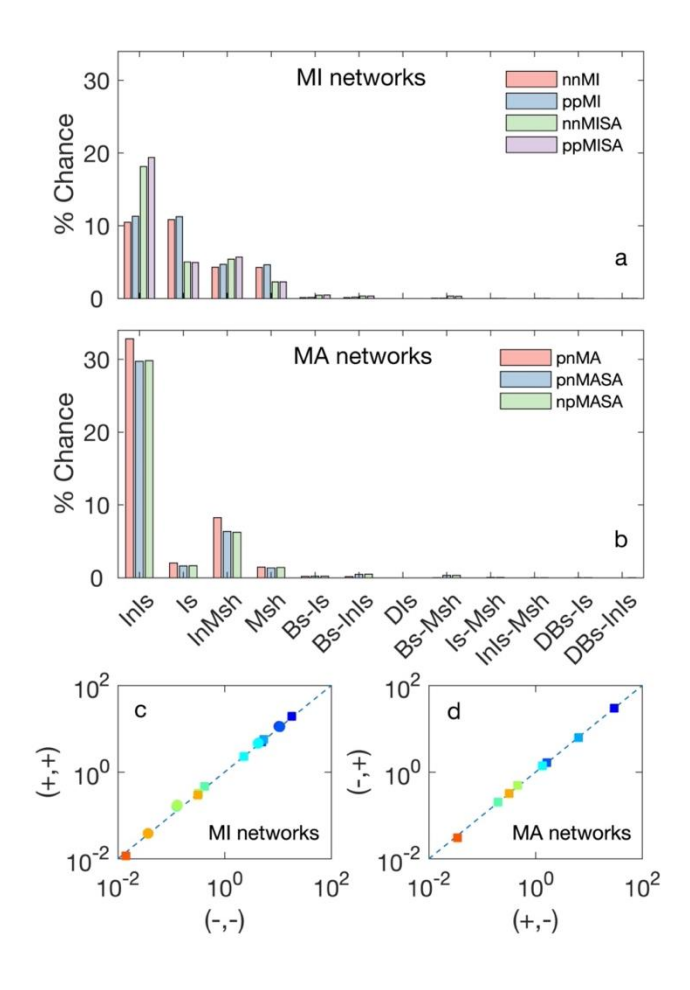


Figure 5.4: Occurrence probability of noncanonical switches. Comparison of % Chance of obtaining various types of noncanonical switches for the MI and MA networks under OR-gate configuration (a-b). The correlation of % Chance of the noncanonical switches of MI networks

(circle: 1-PFL, square: 2-PFL) under (+,+) input signal with (-,-) input signal (c). Correlation plot for the 2-PFL MA networks (d).

Next, the origin of these noncanonical switches specifically, most abundant Is and Msh was analyzed by the respective phase-plane diagrams of the dynamical systems of the ppMI network. Figure 5.5 presented the isola bifurcation diagram and its nullclines for different values of S. At small S the two nullclines intersected once leading to a stable steady state with small B. With increase of S, a new intersection of the nullclines occured at large B leading to the creation of the left SN bifurcation point (point 1) and consequently it generated a stable and an unstable node as partners. With further increase of S, the unstable node moved away from the stable partner node and thereby the separation between the stable and the unstable branches increased in the bifurcation diagram. However, with subsequent increase of S, the unstable node started moving towards the same stable partner node and consequently the gap between the stable and unstable branch decreased in the bifurcation diagram. Ultimately at large S, these two nodes annihilated each other leading to the second SN point (point 2). Strikingly both the SN points were created by the creation/annihilation of the same set of stable and unstable nodes. Consequently, the resulting stable and unstable branches were connected by two SN points creating an island of steady states in the bifurcation diagram. During this process the other stable steady node did not undergo any qualitative change and was responsible for creating the disconnected stable branch in the bifurcation diagram. In Is switch also follows similar merging characteristics of the stable and unstable nodes (Appendix 3, Figure A5.4). It was emphasized that the origin of two SN bifurcation points in isola is completely different than the origin of two SN points in the canonical bistable switch where two different sets of stable and unstable nodes were responsible for generating two SN points (Appendix 3, Figure A5.5).

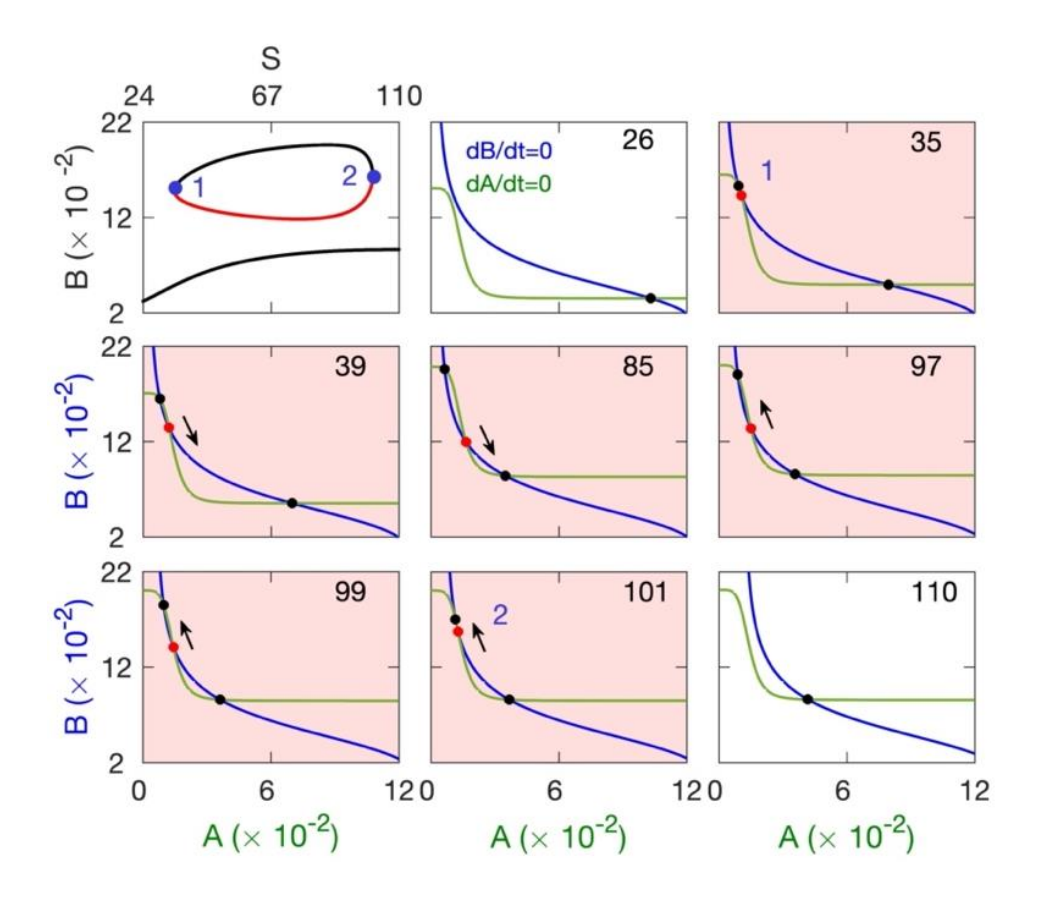


Figure 5.5: Phase-plane analysis of isola switch. The bifurcation diagram of Is switch and the corresponding phase-plane plots for the indicated values of S for the ppMI network under OR-gate. The two SN bifurcation points are indicated by the blue circles in the bifurcation diagram. The black and red circles at the intersections of two nullclines (dA/dt = 0) and dB/dt = 0 indicate the stable and unstable nodes, respectively. The parameters for the Is bifurcation are listed in the Appendix 3, Table A5.5.

The Msh bifurcation featured fusion of two canonical bistable switches in a face-to-face manner with an intervening monostable region (Figure 5.6). Phase-plane analysis indicated that a pair of new nodes appeared after the birth of the first SN point (point 1) and the system became bistable. With increasing S, the newly born unstable node moved towards the pre-existing distant stable node located at low B. The second SN point (point 2) originated from the coalescence of the unstable node with the distant stable node and beyond the second SN point the system became monostable with high B. Thus, the forward-facing Bs switch was generated and the left part of the Msh created. Subsequent increase of S lead to the birth of the third SN point (point 3) at low B and the system became bistable again. The newly born

unstable node travelled towards the pre-existing distant stable node located at high B with progressive increase of S. Finally, the merging of the unstable node with the distant stable node and the annihilation of both of them resulted in the fourth SN bifurcation point (point 4). The system became monostable beyond the fourth SN point and the backward facing Bs switch was generated as the right part of the MSh. During the entire process the expression level of B changed from low-to-high-to-low via two different bistable switches and this pattern is different than the dual bistable switch (DBs) consisting of two bistable switches where the level of B changes from low-to-intermediate-to-high (Appendix 3, Figure A5.5). The behavior of the nullclines for the InMsh were similar to Msh but the expression level of B changed from high-to-low-to-high and two bistable switches congregate in a back-to-back manner in InMsh (Appendix 3, Figure A5.5).

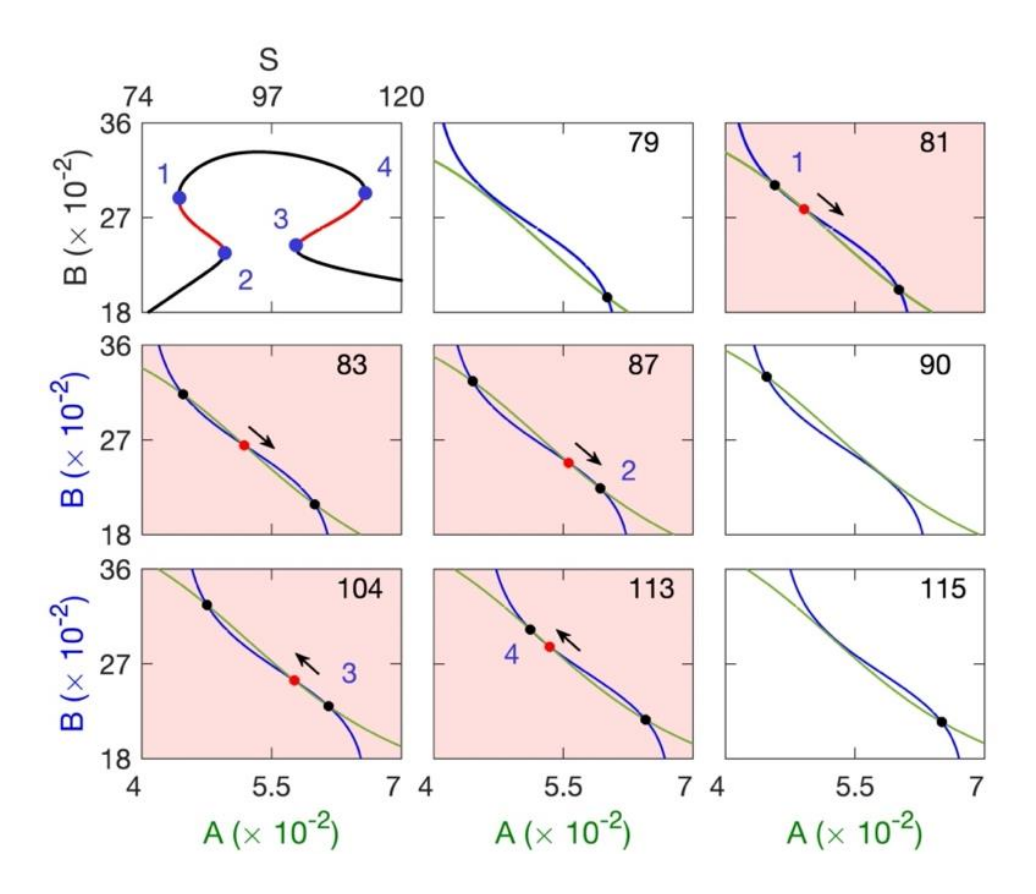


Figure 5.6: Phase-plane analysis of mushroom switch. The bifurcation diagram of Msh switch and the corresponding nullcline plots for the indicated values of S for the ppMI network under OR-gate. The parameters are listed in the Appendix 3, Table A5.5.

From the findings, that a single network topology could result in generating numerous noncanonical responses for r parameters are a key factor in determining the response in

nonlinear dynamical systems. Particularly it was envisaged that a particular type of noncanonical switch may transition into another type of switch with the modification of parameters. To determine the condition of interconversion of the various types of switches, the phase diagrams of the switches was calculated by carrying out 1-p bifurcation analysis with respect to S for varying combinations of g_{AB} and g_{BA} – the mutual regulatory strengths of gene A and B on each other. So far, a total of 14 different bistable switches were considered including two canonical switches. However, considering Bs, Is and Msh as basic building blocks, various other complex bistable switches might emerge due to the fusion of these three units in different numbers and orientations. For generating phase diagram, a total of 57 different reversible bistable switches consisting up to a maximum of three bistable regions were considered. (See the Appendix 3, Table A5.7). A bistable switch can be irreversible at the smallest (S=0) or/and at the largest (S=1000) signal values. Irreversibility means the system is bistable at S=0 or/and at S=1000. In order to account for the possibilities of the irreversible switches, an additional 69 irreversible switches were considered. Therefore, the phase diagram calculations were capable of identifying a bistable switch from a basket of 126 unique bistable switches. The switches were identified based on the number of SN points, jump pattern of stable steady state at the SN point and the location of irreversibility., Considering a switch as a particular phase, a total of 126 possible phases were taken into account in the phase diagram calculations. In phase diagram calculations, a typical phase diagram contained ~30000-40000 1-p bifurcation runs.

In Figure 5.7a the phase diagram of ppMI network starting from Is phase was plotted. The Is phase transitioned into other bistable phases with the change of feedback strengths represented by the parameters g_{AB} and g_{BA} . The canonical forward facing Bs switch occurred in the region of small g_{AB} and g_{BA} , and this phase changed into a Msh phase with increasing g_{AB} . A backward facing Bs switch appeared along with the existing forward facing Bs switch to generate Msh switch with increasing g_{AB} (Figure 5.7b). With further increase of g_{AB} , the Msh phase transformed into an Is phase where the two intermediate SN points of Msh coalesce creating an island of steady states of the Is switch (Figure 5.7c). Thus, the phase transition between Msh and Is was regulated by the regulatory interaction of gene B on gene A (g_{AB}). On the contrary, with the increase of g_{BA} the Is, Msh and Bs switches transformed into their respective irreversible switches in which the left most SN point lies before S=0 (Figure 5.7d-f). The clear phase boundaries between two phases indicated the criticality of the parameter in the transition from one switch to another. Furthermore, the size of the region indicated the

robustness of the switches with respect to modification of the parameters. In the ppMISA network with Is as an initial phase, we found a qualitatively similar phase diagram where again g_{AB} dictates the interconversion between Msh and Is (Figure 5.7g).

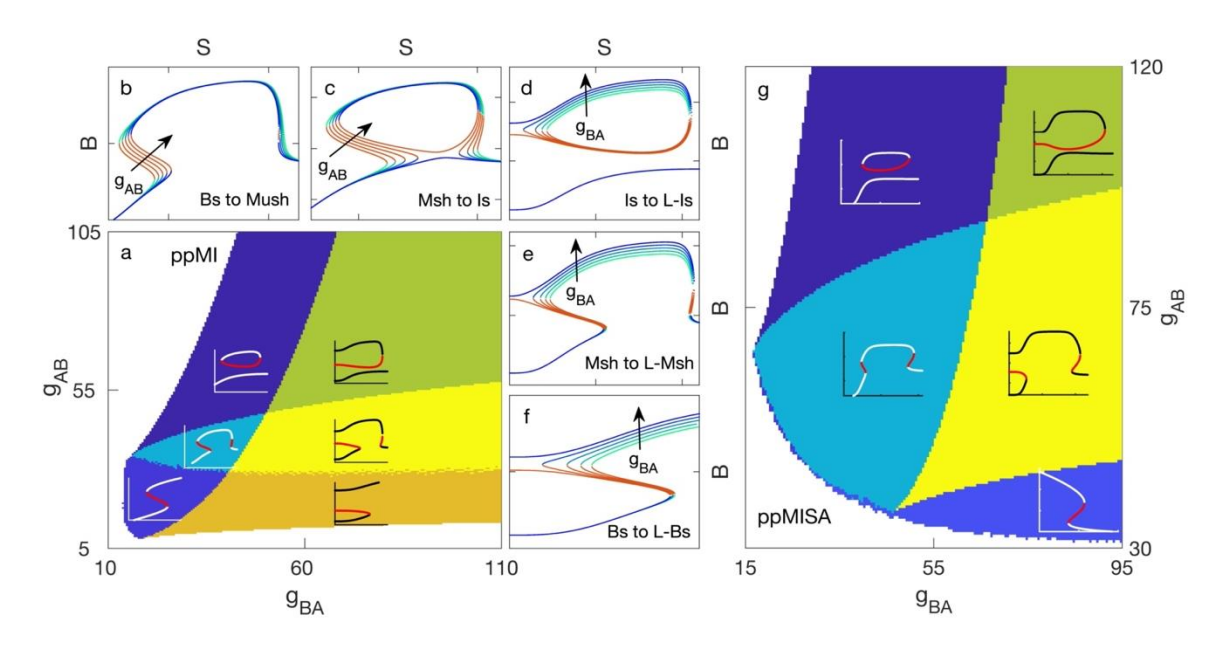


Figure 5.7: Phase diagrams of initial phase of isola. Phase diagram of Is switch (presented in the Figure 5) as initial phase in ppMI network under OR-gate (a). Bistable phases are indicated by the different colors and the representative 1-p bifurcation plots indicate the phase type (a). The white region represents monostability. 1-p bifurcation plots highlight the transition from Bs to Msh (b), Msh to Is (c), Is to L-Is (d), Msh to L-Msh (e) and Bs to L-Bs (f) with the increasing value of either g_{AB} or g_{BA} (represented by the arrow). The prefix 'L' represents irreversibility at left. Phase diagram of ppMISA network under OR-gate with Is as an initial phase (g). The parameters for the ppMISA phase diagram are listed in the Appendix 3, Table A3.8.

Similar phase diagram analysis was performed for InIs switch in ppMI network under OR-gate to uncover that various types of switches exist with the variation of g_{AB} and g_{BA} (Figure 5.8a). The forward facing Bs phase transitioned into InMsh phase with the increase of g_{BA} . With increasing g_{BA} , a new backward facing Bs switch appeared on the left of the existing forward facing Bs switch creating InMsh (Figure 8b). Subsequently with g_{BA} , the InMsh phase changed into InIs phase where the two intermediate SN points of InMsh converged to produce InIs (Figure 8c). Thus, the transitions between the InMsh and InIs switches were controlled by the regulatory strength of A on B (g_{BA}) These switches transitioned to their respective irreversible switches on the right with the increase of g_{AB} . The irreversibility on the right was

a result of the finite value of the signal (S=1000). At a large g_{AB} the InMsh becomes irreversible on the both sides. We found similar phase transition behavior of the forward facing Bs, InMsh and InIs switches in the case of ppMISA network under OR-gate (Figure 5.8d).

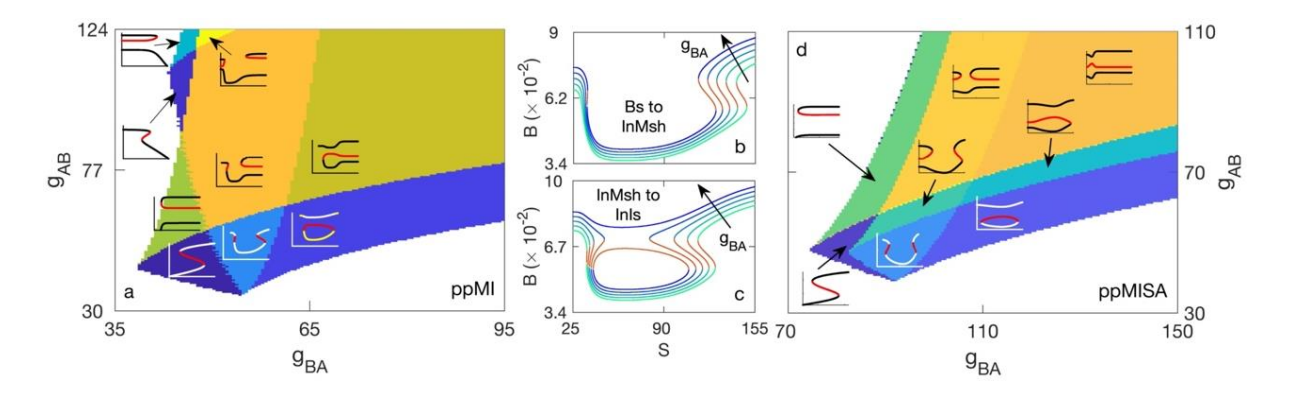


Figure 5.8: Phase diagrams of initial phase of inverted isola. Phase diagram of ppMI network in OR-gate configuration with InIs as an initial phase (a) (see the Supplementary Table S5 for the parameters). One parameter bifurcation plots highlight the transition from Bs to InMsh (b) and InMsh to InIs (c) with the variation of g_{BA} . Phase diagram of ppMISA network in OR-gate configuration with InIs as an initial phase (g). The parameters for the ppMISA network with initial InIs phase are listed in the Appendix 3, Table A5.8.

Phase transition calculations starting with mushroom phase in the same network revealed the existence of diverse types of switches with the variation of g_{AB} and g_{BA} (Figure 5.9a). Consistent with Is phase diagram, the interchangeability between Is and Msh was controlled by g_{AB} . It was curious to note that with increased g_{BA} , Msh phase changed into Bs-Msh phase consisting of three bistable regions. With increase of g_{BA} , the birth of two new SN points, on the stable branch located on the left of the Msh, created a backward facing Bs and altogether it becomes Bs-Msh (Figure 5.9b). Subsequent increase of g_{BA} lead to conversion of Bs-Msh into Bs-InIs phase where the inverted mushroom (created by the first two bistable switches) of the Bs-Msh converged to generate the InIs (Figure 5.9c). Again, the conversion of InMsh into an InIs was triggered by g_{BA} as seen in Figure 5.8. On the contrary, with increase of g_{AB} the Bs-Msh changed into a Bs-Is where the mushroom in the Bs-Msh (last two bistable regions) converged to produce the Is on the right of the first bistable switch (Figure 5.9d). This transition was again consistent with the findings of Figure 7 where the transition from Msh to Is was found to be regulated by g_{AB} . The existence of Bs-Msh, Bs-InIs and Bs-Is phases underscored

that complex switches with multiple bistable regions could be generated by a single PFL under dual signaling. These switches became irreversible on the left at higher values of g_{AB} . In case of InMsh as the initial phase, again it was found that the inter-conversion between InMsh and InIs was dictated by the g_{BA} (Figure 9e). To check the consistency, phase transition calculations of pnMA network were performed with different initial phases and again found that transition between Is and Msh is regulated by g_{AB} and transition between InIs and InMsh is regulated by g_{BA} (Appendix 3, Figure A5.6).

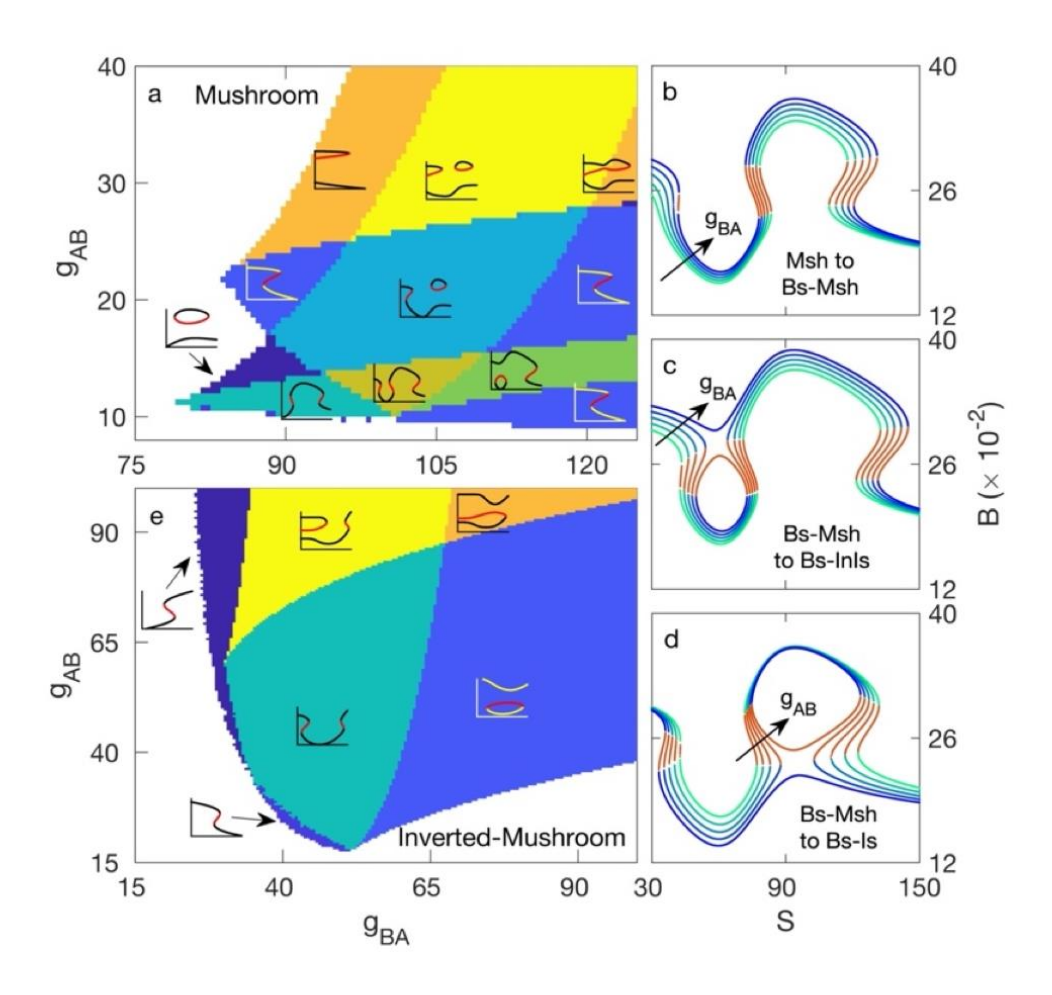


Figure 5.9: Phase diagrams of initial phase of mushroom. Phase diagrams of ppMI network under OR-gate configuration with Msh (a) and InMsh (e) as initial phases. 1-p bifurcations showcase the transition from Msh to Bs-Msh (b), Bs-Msh to Bs-InIs (c) and Bs-Msh to Bs-Is (d). The parameters for the initial phases are listed in the Appendix 3, Table A5.5.

In addition to the feedback strengths, activation (or inhibition) thresholds were key parameters as they dictate the amount of signal required to flip the state of ultrasensitive switch represented

by the Hill function. Hence, the role of signaling thresholds of the two input signaling arms, J_{AS} and J_{BS} , in generating a specific noncanonical response were investigated. From the searched parameters for the bistable switches, the logarithm of the ratio of average J_{AS} and J_{BS} was calculated to measure of dissimilarity (or similarity) of the two thresholds. Across all networks and logic gate configurations, the values of these parameters were nearly similar for the canonical Bs switch (Figure 5.10). However, for the noncanonical switches, the values of these parameters were dissimilar and followed a pattern based on the type of switch and the network. The ratios indicated that Is and Msh switches require $J_{AS} < J_{BS}$ for the nnMI, nnMISA, pnMA and pnMASA networks (Figure 5.10a). A closer inspection revealed that in these four networks, the resultant signs of the two arms from S to B is (+,-) (Figure 5.1b). Both Is and Msh switches exhibited an expression pattern of low-to-high-to-low for B and therefore B must be activated first and then deactivated later with signal. In order to satisfy this requirement, the threshold of activation arm (indirect arm; S to B via A) must be smaller than the threshold of deactivation arm (direct arm; S to B) such that B is activated and deactivated at low S and high S, respectively. Consequently, the average J_{AS} was smaller than the average J_{BS} in these four networks. On the contrary, the expression pattern of B in InIs and InMsh is high-to-low-to-high. Therefore, the deactivation and activation of B must occur at the low and high signal, respectively. In order to satisfy this the threshold of deactivation must be smaller than the threshold of activation and thus these networks showed $J_{AS} > J_{BS}$ (Figure 5.10a). These inequalities become exactly opposite for the ppMI, ppMISA and npMASA networks whose resultant signs of two signaling arms are (-,+) (Figure 10b). Due to the flipping of the regulatory signs of the signaling arms the inequalities now became opposite in these networks. The cumulative distributions of the two thresholds also show the consistent dissimilarity patterns for the noncanonical switches (Appendix 3, Figure A5.7). These networks under ANDgate followed similar inequalities (Figure 5.10c-d).

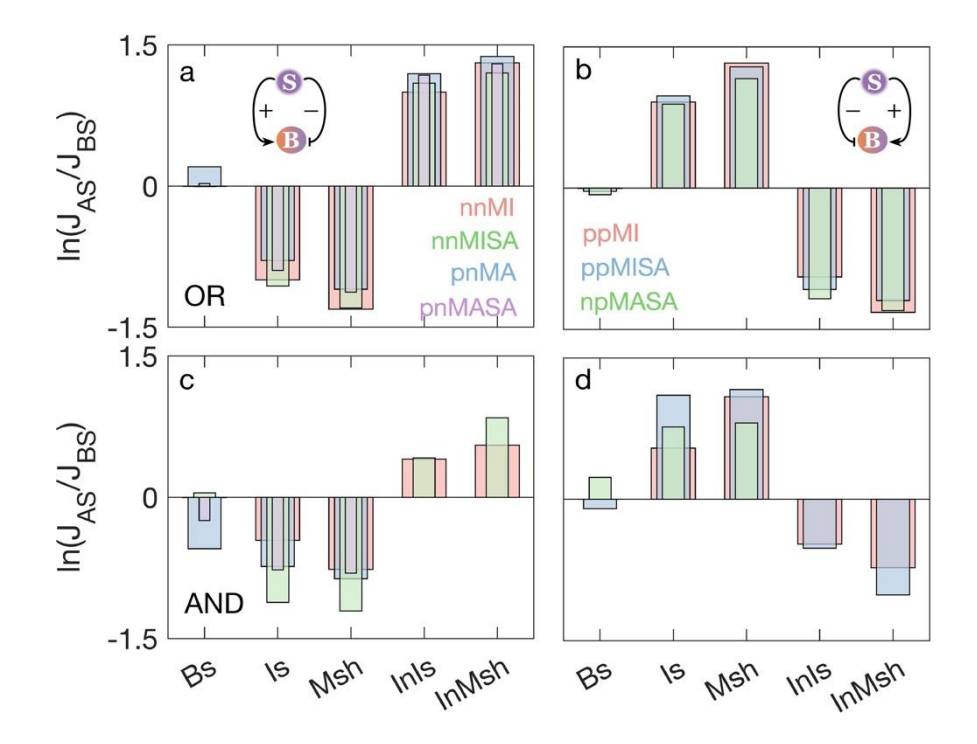


Figure 5.10: Conditions of threshold parameters. The logarithm of ratio of average J_{AS} and J_{BS} obtained from random parameter search are compared together for the networks whose resultant regulatory signs from S to B are same. In the left and right panels the resultant signs of the signal from S to B in two arms are (+,-) and (-,+), respectively. These comparisons were made both for the OR- (top panels) and AND-gate (bottom panels) configurations.

As the relative magnitudes of J_{AS} and J_{BS} were key to obtaining a particular noncanonical switch, the phase diagrams of Is, Msh, InIs and InMsh with respect to these two parameters was generated to estimate the phase separation behavior of these switches under the variation of these thresholds (Figure 5.11). A single phase was obtained in the case of Is and in case of Msh two other phases were obtained (Figure 5.11a-b). The triangular phase diagrams in these cases indicated the criticality of the ratio of the two activation thresholds. As J_{AS} increases relative to that of J_{BS} the region of Is and Msh phase increased consistent with the inequality conclusion of Figure 5.10a. On the contrary as the value of J_{BS} increases relative to J_{AS} the region of InIs and InMsh increased (Figure 11c-d). The triangular phase diagrams highlighted the importance of relative magnitudes of J_{AS} and J_{BS} .

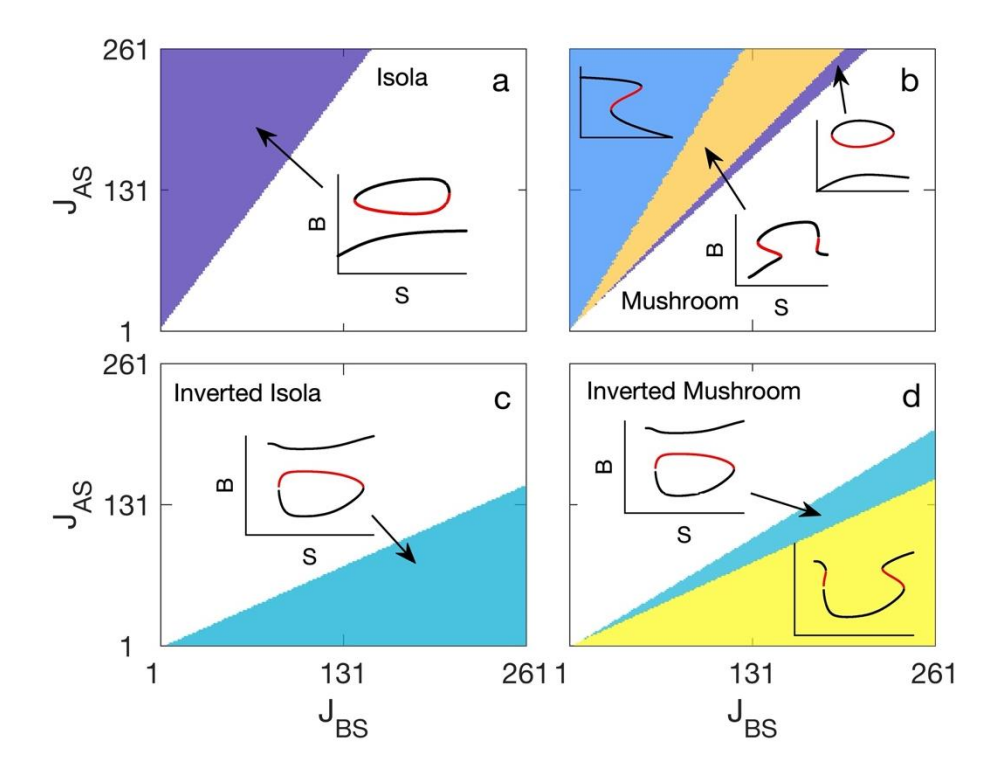


Figure 5.11: Phase diagrams under threshold parameters. Phase diagrams of Is, Msh, InIs and InMsh switches with the variation of the thresholds J_{AS} and J_{BS} for the ppMI network with ORgate configuration (parameters are listed in the Appexdix 5, table A5.5).

5.3 Conclusion

Bistability generated by PFLs has been proven to be a key mechanism in cellular decision making processes and has been investigated extensively. This chapter discussed the fate of PFLs under dual signaling where both the genes in the PFL are regulated by a common regulator in presence of extrinsic noise. The objective was to determine the robustness of network topology in generating bistable response against variation of its regulations. Further the heterogeneity of bistable responses due to fusion of canonical bistable switches in different numbers and orientations, heterogeneity of these switches and the conditions of transitions from one switch type to another type were studied. Recently developed pseudo potential energy based automated high-throughput bifurcation analysis method was carried out under random parameter variations in order to account for the effect of extrinsic noise in on the bistable responses.

As a result of random parameter variations, for dually signaled PFL with coherent signaling arm for MI and incoherent signaling arm for MA topologies only generates canonical bistable switches. Thus, it was concluded that these network topologies are more robust in presence of extrinsic variability. Otherwise, MI network with coherent and MA network with incoherent signaling arm respectively generates a variety of noncanonical switches alongside of canonical switches. These Heterogeneous types of noncanonical switches consist of one, two and three bistable regions. These conclusions were generic as it did not depend on the logic gate configurations and the number of additional PFLs in the networks. The extent of heterogeneity depends on the number of fused PFLs in the networks and logic gate configurations. Heterogeneity was found to be increased with the number of PFLs and responses from ORgate networks were more heterogeneous than the AND-gate networks. The absolute count and occurrence probability showed that isola and mushroom switches, both normal and inverted, were highly probable from simple dual signaling PFL motifs. Probability of obtaining more complex switches with more than two bistable regions were generally lower in networks with a single PFL. However, with additional fused PFL, the probability of the complex switches increased and thus inclusion of multiple PFLs in the minimal motif would increase the possibility of more complex switches. Among the group of noncanonical switches with one, two and three bistable regions, inverted isola, inverted mushroom and bistable-mushroom were the most abundant noncanonical switches, respectively. Importantly the probability of noncanonical switches did not depend on the specific nature of the input signals.

Phase-plane analyses uncovered the distinct origin of the isola switches. The island of steady states in the isola switch originated from the two SN bifurcation points where each SN point was born due to coalescence of the same pair of stable and unstable nodes. On the contrary, in canonical Bs switch a different pair of stable and unstable nodes coalesced for each SN bifurcation point. The unprecedented phase diagram calculations showed that diverse types of phases (or switches) were possible with clear phase boundaries and switching from one phase to another is triggered by the modification of mutual regulatory strengths of the two genes. Across all networks the transitions between the isola and mushroom were controlled by the regulatory strength of the terminal gene on the participating gene in the PFL and transition between the inverted isola and inverted mushroom was dictated by the regulatory strength of the participating gene on the terminal gene. The ratio of signaling thresholds of two input signaling arms were a key factor in determining the types of noncanonical response. Noncanonical switches required distinct values of the two thresholds such that multiple

conventional bistable switches could emerge sequentially in opposite orientations to emerge as noncanonical switches. We emphasized that these conclusions were general due to the random parameter searching approach of the large-scale bifurcation analysis and such analysis was only possible due to the high-throughput bifurcation analysis tool.

In another way, this work also predicted the new properties of the PFLs under dual signaling. Such motif is known to exist in several cell fate-choice regulatory networks. In the T helper (TH) and induced T regulatory (iT_{reg}/) cell fate choices, T cell receptor signaling is known coherently activate the MI loop created by T-bet/RORy3, T-bet/GATA3 and FoxP3/RORy3 in the cell fate choice between T_H1/T_H17, T_H1/T_H2 and iT_{reg}/T_H17 cells, respectively^{32,33}. TGF-\beta induced reciprocal cell fates of iT_{reg}/ T_H17 cells are regulated by mutual antagonism between FoxP3/RORy3 where both the transcription factors are coherently activated by TGF-\beta signaling³⁴. The reversible transition between the mesenchymal to amoeboid cell fates in cancer cells is regulated by the network involving a MI loop between the RhoA and Rac1 GTPases and both the GTPases are coherently inhibited by microRNA miR-34 and also separately by miR-200³⁵. Due to the less familiarity of the isola and mushroom switches, the relevance of these noncanonical switches had not been explored in these cell fate networks that satisfy the requirements of generating noncanonical switches. However mathematical modeling previously had uncovered the role of mushroom bifurcation in the fate choice of neuronal stem cell that differentiate into either glial cell or neuronal cell under the bone morphogenesis protein 2 (BMP2) signaling³⁶. A closer inspection of the network reveals the existence of incoherent BMP2 signaling on the expression of self-activating *Mash1* and results in chapter showed similar conclusion that MA motif only under incoherent dual signaling can generate mushroom or other noncanonical switches. Altogether this discovery of new emergent switches originating from a simple dual signaling PFL motif has a great potential to be relevant in the cell lineage commitment. Furthermore, the rich behavior of such a simple topology in generating complex switches can also be a new area of exploration in the field of synthetic biology. The simplicity of the design principles of network motifs enhances the feasibility of synthetic exploration of new types of bistable switches experimentally.

5.4 References

- (1) Hanahan, D.; Weinberg, R. A. Hallmarks of Cancer: The Next Generation. *Cell* **2011**, *144* (5), 646–674. https://doi.org/https://doi.org/10.1016/j.cell.2011.02.013.
- (2) Barabási, A.-L.; Gulbahce, N.; Loscalzo, J. Network Medicine: A Network-Based Approach to Human Disease. *Nat. Rev. Genet.* **2011**, *12* (1), 56–68. https://doi.org/10.1038/nrg2918.
- (3) Alon, U. Network Motifs: Theory and Experimental Approaches. *Nat. Rev. Genet.* **2007**, 8 (6), 450–461. https://doi.org/10.1038/nrg2102.
- (4) Tyson, J. J.; Novák, B. Functional Motifs in Biochemical Reaction Networks. http://dx.doi.org/10.1146/annurev.physchem.012809.103457 **2010**, 61, 219–240. https://doi.org/10.1146/ANNUREV.PHYSCHEM.012809.103457.
- (5) Khammash, M. H. Perfect Adaptation in Biology. *Cell Syst.* **2021**, *12* (6), 509–521. https://doi.org/https://doi.org/10.1016/j.cels.2021.05.020.
- (6) Ferrell, J. E. Self-Perpetuating States in Signal Transduction: Positive Feedback, Double-Negative Feedback and Bistability. *Curr. Opin. Cell Biol.* **2002**, *14* (2), 140–148. https://doi.org/10.1016/S0955-0674(02)00314-9.
- (7) Yao, G.; Lee, T. J.; Mori, S.; Nevins, J. R.; You, L. A Bistable Rb–E2F Switch Underlies the Restriction Point. *Nat. Cell Biol.* 2008 104 2008, 10 (4), 476–482. https://doi.org/10.1038/ncb1711.
- (8) Yao, G.; Tan, C.; West, M.; Nevins, J. R.; You, L. Origin of Bistability Underlying Mammalian Cell Cycle Entry. *Mol. Syst. Biol.* 2011, 7 (1), 485. https://doi.org/10.1038/MSB.2011.19.
- (9) Heldt, F. S.; Barr, A. R.; Cooper, S.; Bakal, C.; Novák, B. A Comprehensive Model for the Proliferation–Quiescence Decision in Response to Endogenous DNA Damage in Human Cells. *Proc. Natl. Acad. Sci.* 2018, 115 (10), 2532–2537. https://doi.org/doi:10.1073/pnas.1715345115.
- (10) Sha, W.; Moore, J.; Chen, K.; Lassaletta, A. D.; Yi, C.-S.; Tyson, J. J.; Sible, J. C. Hysteresis Drives Cell-Cycle Transitions in Xenopus Laevis Egg Extracts. https://doi.org/10.1073/PNAS.0235349100.

- (11) Pomerening, J. R.; Sontag, E. D.; Ferrell, J. E. Building a Cell Cycle Oscillator: Hysteresis and Bistability in the Activation of Cdc2. *Nat. Cell Biol.* 2003 54 **2003**, 5 (4), 346–351. https://doi.org/10.1038/ncb954.
- (12) Spencer, S. L.; Sorger, P. K. Measuring and Modeling Apoptosis in Single Cells. *Cell* 2011, 144 (6), 926–939. https://doi.org/10.1016/J.CELL.2011.03.002.
- (13) McKenna, S.; García-Gutiérrez, L.; Matallanas, D.; Fey, D. BAX and SMAC Regulate Bistable Properties of the Apoptotic Caspase System. *Sci. Rep.* 2021, 11 (1), 3272. https://doi.org/10.1038/s41598-021-82215-2.
- (14) Ballweg, R.; Paek, A. L.; Zhang, T. A Dynamical Framework for Complex Fractional Killing. *Sci. Rep.* **2017**, *7* (1), 8002. https://doi.org/10.1038/s41598-017-07422-2.
- (15) Graham, T. G. W.; Tabei, S. M. A.; Dinner, A. R.; Rebay, I. Modeling Bistable Cell-Fate Choices in the Drosophila Eye: Qualitative and Quantitative Perspectives.

 *Development 2010, 137 (14), 2265–2278. https://doi.org/10.1242/dev.044826.
- (16) Bednarz, M.; Halliday, J. A.; Herman, C.; Golding, I. Revisiting Bistability in the Lysis/Lysogeny Circuit of Bacteriophage Lambda. *PLoS One* **2014**, *9* (6), e100876. https://doi.org/10.1371/journal.pone.0100876.
- (17) Jukam, D.; Xie, B.; Rister, J.; Terrell, D.; Charlton-Perkins, M.; Pistillo, D.; Gebelein, B.; Desplan, C.; Cook, T. Opposite Feedbacks in the Hippo Pathway for Growth Control and Neural Fate. *Science* (80-.). 2013, 342 (6155), 1238016. https://doi.org/doi:10.1126/science.1238016.
- (18) Bouldin, C. M.; Manning, A. J.; Peng, Y.-H.; Farr Gist H., I. I. I.; Hung, K. L.; Dong, A.; Kimelman, D. Wnt Signaling and Tbx16 Form a Bistable Switch to Commit Bipotential Progenitors to Mesoderm. *Development* 2015, *142* (14), 2499–2507. https://doi.org/10.1242/dev.124024.
- (19) Schröter, C.; Rué, P.; Mackenzie, J. P.; Martinez Arias, A. FGF/MAPK Signaling Sets the Switching Threshold of a Bistable Circuit Controlling Cell Fate Decisions in Embryonic Stem Cells. *Development* **2015**, *142* (24), 4205–4216. https://doi.org/10.1242/dev.127530.
- (20) Fang, X.; Liu, Q.; Bohrer, C.; Hensel, Z.; Han, W.; Wang, J.; Xiao, J. Cell Fate Potentials and Switching Kinetics Uncovered in a Classic Bistable Genetic Switch.

- *Nat. Commun.* **2018**, 9 (1), 2787. https://doi.org/10.1038/s41467-018-05071-1.
- (21) Xiong, W.; Ferrell, J. E. A Positive-Feedback-Based Bistable / memory Module/' That Governs a Cell Fate Decision. *Nature* **2003**, *426* (6965), 460–465.
- (22) Wang, L.; Walker, B. L.; Iannaccone, S.; Bhatt, D.; Kennedy, P. J.; Tse, W. T. Bistable Switches Control Memory and Plasticity in Cellular Differentiation. *Proc. Natl. Acad. Sci. U. S. A.* 2009, 106 (16), 6638–6643. https://doi.org/10.1073/PNAS.0806137106/ASSET/84C884EC-7704-4DAB-BD7A-8409DE49B5DE/ASSETS/GRAPHIC/ZPQ9990975310006.JPEG.
- (23) Gardner, T. S.; Cantor, C. R.; Collins, J. J. Construction of a Genetic Toggle Switch in Escherichia Coli. *Nature* **2000**, *403* (6767), 339–342. https://doi.org/http://www.nature.com/nature/journal/v403/n6767/suppinfo/403339a0_S1.html.
- (24) Lebar, T.; Bezeljak, U.; Golob, A.; Jerala, M.; Kadunc, L.; Pirš, B.; Stražar, M.; Vučko, D.; Zupančič, U.; Benčina, M.; Forstnerič, V.; Gaber, R.; Lonzarić, J.; Majerle, A.; Oblak, A.; Smole, A.; Jerala, R. A Bistable Genetic Switch Based on Designable DNA-Binding Domains. *Nat. Commun.* 2014, 5 (1), 5007. https://doi.org/10.1038/ncomms6007.
- (25) Santos-Moreno, J.; Tasiudi, E.; Stelling, J.; Schaerli, Y. Multistable and Dynamic CRISPRi-Based Synthetic Circuits. *Nat. Commun.* **2020**, *11* (1), 2746. https://doi.org/10.1038/s41467-020-16574-1.
- (26) Benenson, Y. Biomolecular Computing Systems: Principles, Progress and Potential. *Nat. Rev. Genet.* **2012**, *13* (7), 455–468. https://doi.org/10.1038/nrg3197.
- (27) Ajo-Franklin, C. M.; Drubin, D. A.; Eskin, J. A.; Gee, E. P. S.; Landgraf, D.; Phillips, I.; Silver, P. A. Rational Design of Memory in Eukaryotic Cells. *Genes Dev.* 2007, 21 (18), 2271–2276. https://doi.org/10.1101/gad.1586107.
- (28) Zhu, R.; del Rio-Salgado, J. M.; Garcia-Ojalvo, J.; Elowitz, M. B. Synthetic Multistability in Mammalian Cells. *Science* (80-.). **2022**, 375 (6578), eabg9765. https://doi.org/doi:10.1126/science.abg9765.
- (29) Wu, F.; Su, R.-Q.; Lai, Y.-C.; Wang, X. Engineering of a Synthetic Quadrastable Gene Network to Approach Waddington Landscape and Cell Fate Determination. *Elife* **2017**,

- 6, e23702. https://doi.org/10.7554/eLife.23702.
- (30) Dey, A.; Barik, D. Emergent Bistable Switches from the Incoherent Feed-Forward Signaling of a Positive Feedback Loop. *ACS Synth. Biol.* **2021**, *10* (11), 3117–3128. https://doi.org/10.1021/ACSSYNBIO.1C00373/ASSET/IMAGES/LARGE/SB1C0037 3 0008.JPEG.
- (31) Song, H.; Smolen, P.; Av-Ron, E.; Baxter, D. A.; Byrne, J. H. Bifurcation and Singularity Analysis of a Molecular Network for the Induction of Long-Term Memory. *Biophys. J.* **2006**, *90* (7), 2309–2325. https://doi.org/https://doi.org/10.1529/biophysj.105.074500.
- (32) Hong, T.; Xing, J.; Li, L.; Tyson, J. J. A Simple Theoretical Framework for Understanding Heterogeneous Differentiation of CD4+ T Cells. *BMC Syst. Biol.* **2012**, 6 (1), 66. https://doi.org/10.1186/1752-0509-6-66.
- (33) Zhu, J.; Yamane, H.; Paul, W. E. Differentiation of Effector CD4 T Cell Populations. *Annu. Rev. Immunol.* **2010**, 28 (1), 445–489. https://doi.org/10.1146/annurevimmunol-030409-101212.
- (34) Hong, T.; Xing, J.; Li, L.; Tyson, J. J. A Mathematical Model for the Reciprocal Differentiation of T Helper 17 Cells and Induced Regulatory T Cells. *PLOS Comput. Biol.* **2011**, *7* (7), e1002122. https://doi.org/10.1371/journal.pcbi.1002122.
- (35) Hong, T.; Watanabe, K.; Ta, C. H.; Villarreal-Ponce, A.; Nie, Q.; Dai, X. An Ovol2-Zeb1 Mutual Inhibitory Circuit Governs Bidirectional and Multi-Step Transition between Epithelial and Mesenchymal States. *PLOS Comput. Biol.* **2015**, *11* (11), e1004569. https://doi.org/10.1371/JOURNAL.PCBI.1004569.
- (36) Sengupta, D.; Kar, S. Unraveling the Differential Dynamics of Developmental Fate in Central and Peripheral Nervous Systems. *Sci. Rep.* **2016**, *6* (1), 36397. https://doi.org/10.1038/srep36397.

CHAPTER 6

Control of chemical noise in general network topology

6.1 Introduction

Living things must be reliable and robust in order to respond appropriately to different internal and external stimuli and to ensure their long-term existence. These two crucial characteristics of biological systems may be hindered by the stochasticity of chemical processes emanating from both internal and external causes. Therefore, a lot of work has gone into understanding how living systems control the stochasticity that eventually leads to population heterogeneity - an inevitable outcome for a population of genetically identical cells grown in homogenous environments^{1,2}. Fluctuations caused by limited number of macromolecules of species in a tiny volume of cell land in generating stochastic trajectories of chemical reactions. Thus, chemical reactions inside a cell are intrinsically affected by the 'finite number effect'. As a result, the expression of gene is bound to be noisy and termed as 'gene expression noise' 3-6. The mechanism of gene expression noise has been well understood by statistical mechanical models of a single gene or a few genes in a cascade^{7–13}. These models have deciphered the importance of translation and transcription rate, lifetimes of protein and mRNA in the noise of gene expression. Further works were done to understand how feedback controls might either attenuate or exacerbate biochemical noise^{7,14–16}.

Although the propagation of chemical noise in biological reaction networks has been extensively studied in the literature, but examination of stochasticity in a generalised network is sparse. It is particularly important to keep in mind that living cells' system level response depends on the coordinated expression of many genes that are interacted to one

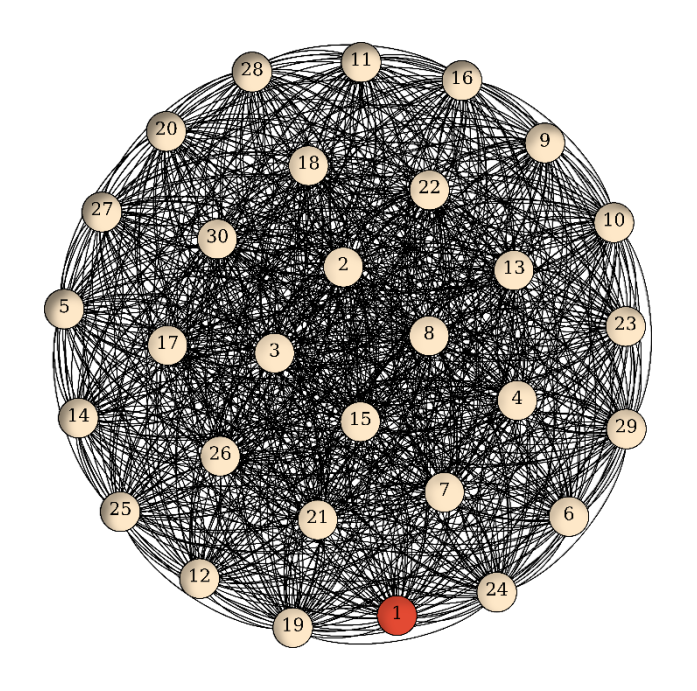
Chemical noise in generalised network

another. The global network topology of these gene regulation networks is an intriguing feature ^{17–19}. According to recent literature, these organisations of these networks frequently resemble either a democratic architecture²⁰, in which each gene is controlled by other genes (or gene products) in the network or autocratic architecture ^{18–23} where multiple regulators are present in each rung of the hierarchical organisation of the transcription factors.

This chapter discusses the variability due to intrinsic noise in generalized chemical reaction architecture. The main objective was to study the correlation between the intrinsic variability and the qualitative (inhibitory or activatory) and quantitative (strength) nature of interactions in the networks.

Part A

Chemical noise propagation in democratic network topology



S Das and D Barik, *Phys. Rev. E* 101, 042407 (2020)

6.A.1 Model

The democratic network model consists of nodes and the edges. The edges represent the nature of the relationship between the two connected nodes, whereas the nodes serve as representatives of any macromolecular species such as proteins, genes, transcripts, or metabolites inside a living cell. The regulatory interactions between two nodes can be positive (activatory) or negative (inhibitory). A specific number of incoming and outgoing edges, represented by different types of arrowhead, are present at each node in the network (Figure.6A.1). While outgoing arrows represent the effect of the source node on the recipient nodes in the network, the incoming arrows represent the influence of other nodes on the recipient node. We assumed that each node in the fully connected democratic network, experiences the same number of incoming and outgoing interactions. This implies that each node in the network receives inhibitory or activatory signals from every other node. Therefore, the total number of interactions (m_{tot}) on each node in the network of $d_{\it N}$ nodes would be $d_N - 1$. In addition to these interactions, every node engages engages in uncontrolled synthesis and degradation on its own. The mean field dynamics of the nodes can be described by a collection of coupled ordinary linear differential equations, assuming the mass action rate laws of chemical reactions:

$$\frac{d\bar{n}_i}{dt} = k_i - \gamma_i \bar{n}_i + \sum_{i \neq j}^{d_N} a_{i,j} \bar{n}_i \bar{n}_j$$

$$6A.1$$

The average molecular abundance of the node i is represented by \bar{n}_i in the equation above. The i^{th} node's unregulated synthesis and degradation are represented by the first and second terms on the right-hand side of the equation, respectively. The rate constants for the synthesis and degradation reactions are k_i and γ_i respectively. Mutual interactions between nodes i and j are represented by the final term. $a_{i,j}$ is the strength of mutual interactions and the sign of $a_{i,j}$ reflects the qualitative nature of interaction. Inhibitory and activatory interactions are denoted by $a_{i,j} < 0$ and $a_{i,j} > 0$ respectively. It is possible to create many networks by altering the proportion of negative (m_i^-) and positive (m_i^+) interactions on each node. The total number of interactions on every node is fixed at m_{tot} (= $m_i^- + m_i^+$). Hence, a democratic network consisting d_N nodes will experience d_N $(d_N - 1)$ number of regulatory interactions.

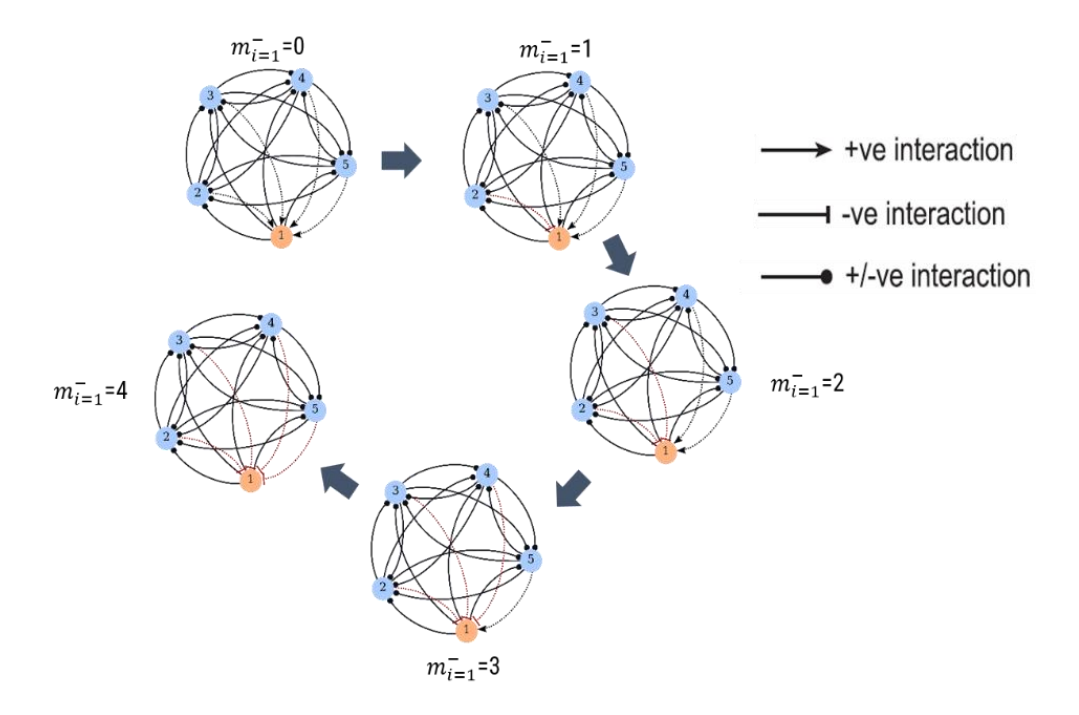


Figure 6A.1. Schematic diagram of democratic network consisting 5 nodes ($d_N = 5$). The labelled circles and curved arrows represent the nodes and mutual regulations respectively. Different types of arrowheads represent different type of interactions (mentioned in the figure). Node 1 was chosen as the representative node for estimating the statistical properties of the network. Starting with all positive interactions on node $1(m_{i=1}^- = 0)$, the number of incoming negative interactions ($m_{i=1}^-$) were systematically varied to determine the effect of the quality of interactions on the statistical properties of the target node.

The basal synthesis rate constant ($k_i = 1.0$) and the degradation rate constant($\gamma_i = 0.01$) was set to a fixed value for each node in the network. However, different values of the mutual interaction strength ($a_{i,j}$) was chosen for each pair of interacting nodes. The $a_{i,j}$ values wer picked from log-normal distributions with average values of a^- (for negative interactions) and a^+ (for positive interactions), with a coefficient of variation of 0.3 in both cases, in order to introduce an asymmetry in the strength of interactions. It is crucial to remember that the values of the interaction parameters can be selected from any distribution that can be plausibly connected to the reaction networks. However, the selection of the distribution for $a_{i,j}$ must not bias the results. With the use of the Gaussian distribution for $a_{i,j}$ in this context, it was confirmed that the conclusions of our

investigations remain unchanged. As there were that many binary interactions accessible in the network, the sample size for the distribution of was d_N ($d_N - 1$). Thus, an asymmetric network in terms of interaction strength was produced by using a lognormal distribution for interaction strengths. To find out how the strength of interactions affected the network's statistical characteristics, we repeatedly changed a^- and a^+ .

The main aim was to investigate the impact of both positive and negative interactions on the chemical species' steady-state variability in democratic networks. In order to achieve this, networks with varying numbers of positive and negative interactions were looked upon. Because of the network's democratic structure, any node can be selected to analyse the network's statistical features, including mean, noise (coefficient of variation), and noise strength (Fano factor). Here, node 1 was our choice of investigation. The number of negative interactions on node 1 $(m_{i=1}^-)$ was gradually increased, and in each case, the steady-state statistical properties of both node 1 and all other nodes in the network were quantified. This allowed to assess the impact of negative interactions on noise. The number of interactions toward all other nodes, both positive $(m_{i\neq 1}^+)$ and negative $(m_{i\neq 1}^-)$, remained constant throughout these analyses. Now, to find out the role of the nature of interaction on the rest of the nodes $(i \neq 1)$ on the statistical properties of node 1, our similar simulations were repeated by systematically varying the $m_{i\neq 1}^-$.

6.A.2 Results

Gillespie's SSA²⁴ was used to investigate the inherent stochastic kinetics of chemical reactions originating from the intrinsic noise. To achieve the exact solutions of the stochastic kinetics, it was assumed that the reactions follow mass action kinetics and the corresponding set of mean field dynamical equations were presented in 6A.1. For a network with d_N number of nodes, there are d_N number of both synthesis and degradation reactions and total number of mutual regulations is $d_N(d_N-1)$. As a result total number of reactions turned out to be $d_N(d_N+1)$. To assure the trajectories reached their steady states, the simulations were run for sufficiently long time and repeated for 5000 realisation in order to estimate the ensemble average. The simulation time increased steeply with increasing network size (d_N) and larger rate constants. In order to cut down the simulation time and to ignore the trajectories that increases asymptotically, a cut-off rule of 10,000 molecules/node was implemented. According to this rule, a simulation would stop when

the abundance of any of the nodes crosses beyond this threshold value. This setting of cutoff was completely reasonable as the noise associated with high abundance will be very low as based on the $1/\sqrt{\overline{n}_1}$ rule of fluctuations.

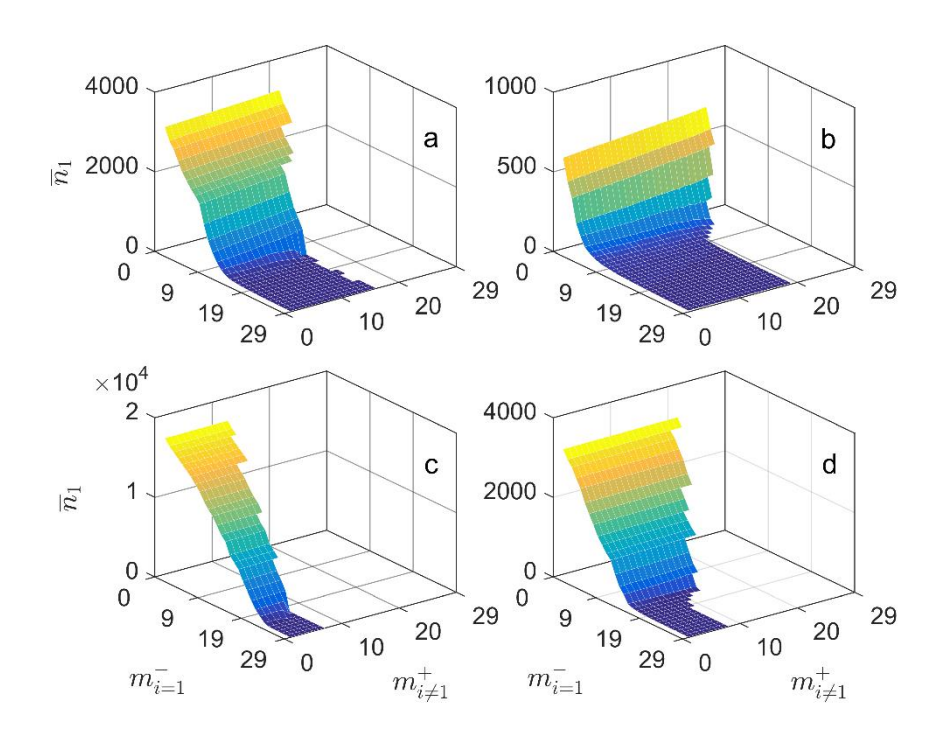


Figure 6A.2. Surface plot of the average abundance of node 1 (\bar{n}_1) as a function of the number of negative interactions on node 1 (m_1^-) and the number of positive interactions on other nodes $(m_{i\neq 1}^+)$ for different combination of average positive and negative interaction strengths (\bar{a}_-, \bar{a}_+) . (a) (0.001, 0.001), (b) (0.005, 0.001), (c) (0.001, 0.005), and (d) (0.005, 0.005).

Firstly, the average behavior of the system with varying number of negative interactions on node 1 $(m_{i=1}^-)$ and the number of positive interactions on all other nodes $(m_{i\neq 1}^+)$ was determined. Variation of average abundance of node 1 (\bar{n}_1) with different $m_{i=1}^-$ and $m_{i\neq 1}^+$ is shown in Figure. 6A. 2(a) keeping the average strengths of the positive and negative interactions remains constant. As expected, the average abundance of node 1 decreased with $m_{i=1}^-$ for a given value of $m_{i\neq 1}^+$. The quantitative and qualitative behavior of \bar{n}_1 did not change with the increasing values of $m_{i\neq 1}^+$, we got comparable qualitative behaviour of \bar{n}_1 . Notably, there is any bare change in the \bar{n}_1 with the increase in $m_{i\neq 1}^+$. Nevertheless, at higher value of $m_{i\neq 1}^+(>15)$ the system diverged, because of the imposed cut off condition, there was no data point of \bar{n}_1 in the surface plot. Thus, it can be concluded that

the qualitative and the quantitative behaviour of \bar{n}_1 was regulated by the nature of regulations on the node of interest and the nature of interactions on the other nodes did not have any influence. It is to be noted that for the sake of ease in implementation, the number of negative interactions on node 1 was increased in a specific order. Incoming interaction starting from node 2 and following numerical order, the positive interactions were replaced with negative interactions in order to increase the number of negative interactions. Similar order was followed for implementation of $m_{i\neq 1}^+$. However, similar calculations were carried where the implementation was done in arbitrary manner and the results found out to be independent of any specific ordering.

Calculations were repeated with different average strength of positive and negative interactions in order to investigate for the dependency of the strength of interactions on average property. Figure 6A.2b-d presented the results for 5X increase in negative, positive and both the interactions strength respectively. As expected, with increased value of \bar{a}_{-} alone, the \bar{n}_{1} value decreases (Figure 6A.2b). In addition, fewer negative interactions $(m_{i=1}^{-})$ were required to "shut down" the node 1. On the other hand, as the value of \bar{a}_{+} alone increased, \bar{n}_{1} increased considerably and more negative interactions were required to halt the production of node 1 (Figure 6A.2c). Additionally, the divergence of abundance took place at a considerably at smaller number of $m_{i\neq 1}^{+}$. Finally, just a small change in \bar{n}_{1} was seen when both strengths were increased by the same factor (Figure 6A.2d).

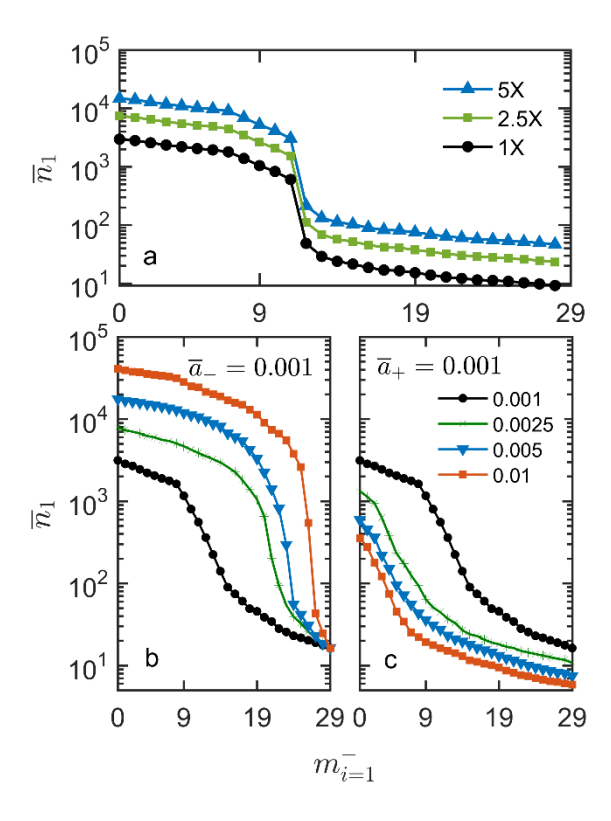


Figure 6A.3. Dependence of the ultrasensitivity of node 1 on the scaling factors that systematically modifies that average abundance of all the nodes in the network. The values of \bar{a}_+ and \bar{a}_- were 0.001 and 0.001, respectively. (b) Dependence of the ultrasensitivity on the average strength of positive interactions keeping the \bar{a}_- fixed. (c) Dependence of the ultrasensitivity on the \bar{a}_- keeping the \bar{a}_+ fixed.

From Figure 6A.3a, it appeared that after a certain threshold of $m_{i=1}^-$, the average of node 1 (\bar{n}_1) was abruptly decreased from high to low. Thus, the qualitative variation of \bar{n}_1 with $m_{i=1}^-$ behaved as an ultrasensitive switch of protein abundance. It is important to note that the inherent nonlinearity of the underlying chemical reactions often contributes to ultrasensitivity in biochemical systems. The relevance of ultrasensitivity in producing nonlinear responses like bistability and oscillations makes it crucial for biochemical reaction networks. Although the democratic network here lacks nonlinear chemical reaction rates yet it exhibited a weak ultrasensitivity. As a result, the conditions regarding ultrasensitive switching of node 1 were further investigated. The abundance of the nodes was progressively increased by 2.5X and 5.0X to answer the query of whether the switchlike behaviour of node 1 was caused by the extremely few molecules at high

 $m_{i=1}^-$ (Figure. 6A.3a). The zero- and second-order rate constants were multiplied and divided respectively by the necessary scaling factor in order to scale up the abundance. Even with a higher population abundance, node 1's ultrasensitive switching remained unaffected, suggesting that the ultrasensitivity is inherent to the democratic network. The stiffness of the switch was found to be dependent on the average strength of the positive interactions, according to simulations using varying average strengths of positive and negative interactions. However, the transition threshold of $m_{i=1}^-$ appeared to be controlled by the strength of the negative interaction (Figure. 6A.3b-c).

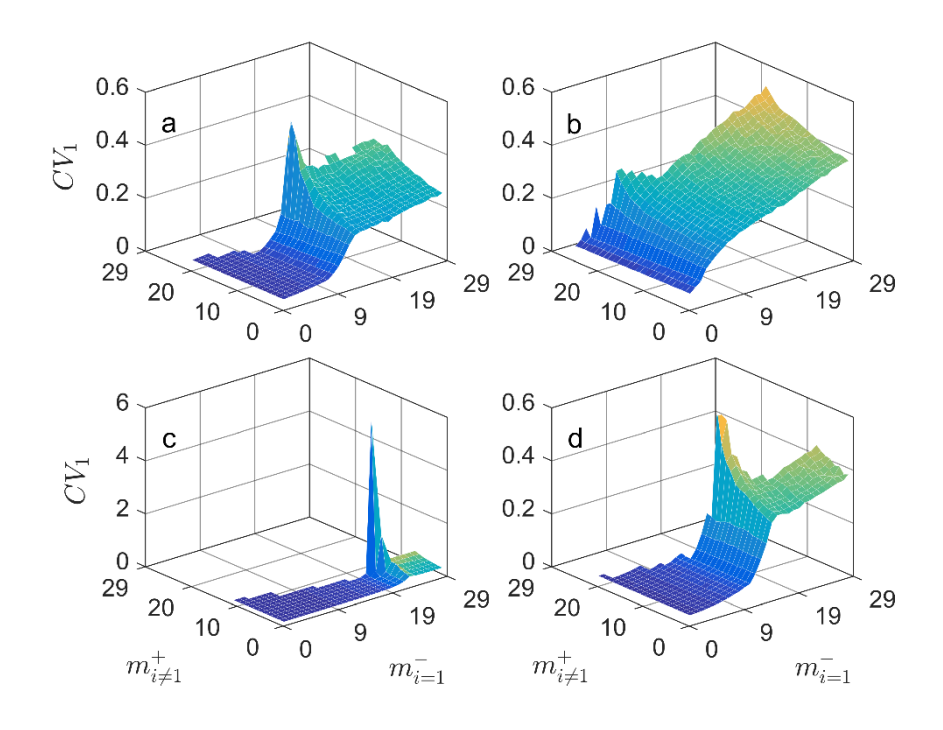


Figure 6A.4. Surface plot for the coefficient of variation of node 1 (*CV*) as function of $m_{i=1}^-$. The average strength of negative and positive interaction was (a) (0.001, 0.001), (b) (0.005, 0.001), (c) (0.001, 0.005), and (d) (0.005, 0.005).

Next, the effect of negative interactions on the noise in node 1 was further examined. The steady state noise was measured by quantifying the coefficient of variation $(CV_i = {}^{\sigma_i}/{\bar{n}_i})$, where σ_i is the standard deviation of i^{th} node). The noise in node 1 (CV_1) displayed a switchlike behaviour as a function of $m_{i=1}^-$, when the strengths of the positive and negative interactions were equal (Figure. 6A.4a). In particular, CV nearly saturated at a greater

number of $m_{i=1}^-$, and it stayed very low for a smaller number of $m_{i=1}^-$ (high \bar{n}_1). This qualitative feature of noise was maintained for an increasing number of positive interactions on the other nodes, $m_{i\neq 1}^+$, quantitatively the noise appeared to increase steadily with an increase in $m_{i\neq 1}^+$ on other nodes particularly in the high-noise regime (large $m_{i=1}^-$). Overall, the direct negative interactions on node 1 result in a non-monotonous change in noise, whereas the indirect positive interactions results in only small increase in noise. Similar calculations were repeated with various average strengths of both interactions $(\bar{a}_{-}$ and $\bar{a}_{+})$ to determine how these qualitative noise characteristics depends on the strength of interactions. The transition from low to high noise occurred at a much lower value $m_{i=1}^-$ (Figure 6A.4b) with an increased value of \bar{a}_{-} alone. In contrast to smaller \bar{a}_{-} (Figure 6A.4a), the variability in this instance, increased significantly. This was as a result of a lower average, intensifying the 'finite number effect' with high \bar{a}_{-} . Furthermore, at high values of $m_{i=1}^-$, the effect of $m_{i\neq 1}^+$ on CV was more predominant. The change from low to high noise occurred at a substantially higher value of $m_{i=1}^-$ with an increasing value of \bar{a}_+ alone (Figure 6A.4c). The noise grew considerably across different values of $m_{i=1}^-$ and $m_{i\neq 1}^+$ (Figure 6A.4d) where both interaction strengths were increased by the same factor. This was most likely due to the efficient noise propagation in the network.

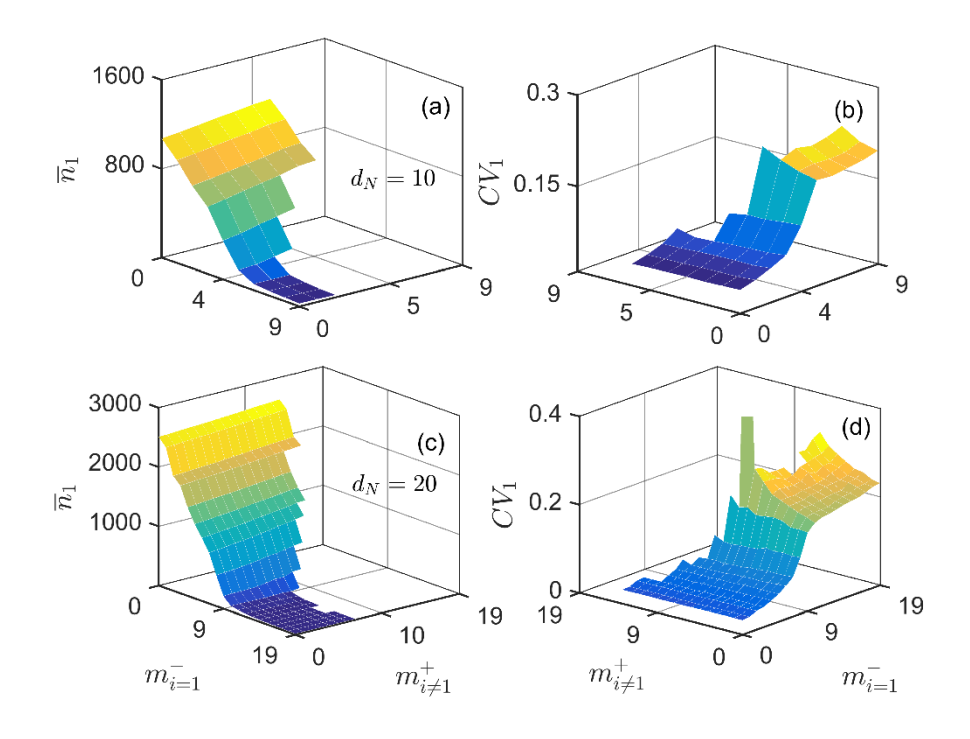


Figure 6A.5. Surface plots of the average abundance and CV of node 1 for the networks with 10 (top row) and 20 (bottom row) nodes as a function of $m_{i=1}^-$. The values of \bar{a}_- and \bar{a}_+ , were 0.001 and 0.001, respectively.

To ascertain the generality of the qualitative character of noise with $m_{i=1}^-$, similar simulations were run for democratic networks of various sizes. The simulation results from networks with 10 and 20 nodes are shown in Figure 6A.5. Similar qualitative behavior of noise and average abundance was found for both network sizes. The CV_1 vs $m_{i=1}^-$ of three different network sizes ($d_N = 10, 20, \text{ and } 30$) in Figure 6A.6a, where the number of positive interactions on every other node was kept constant at 0 ($m_{i\neq 1}^+ = 0$). The comparison demonstrates that the abrupt change in noise from a low to a high number is consistent across all network sizes. With growing network size, we also see a systematic shift of the curves towards lower $m_{i=1}^-$. Their individual normalised averages were compared in Figure. 6A.6b to observe the sharp decline of the corresponding averages with $m_{i=1}^-$.

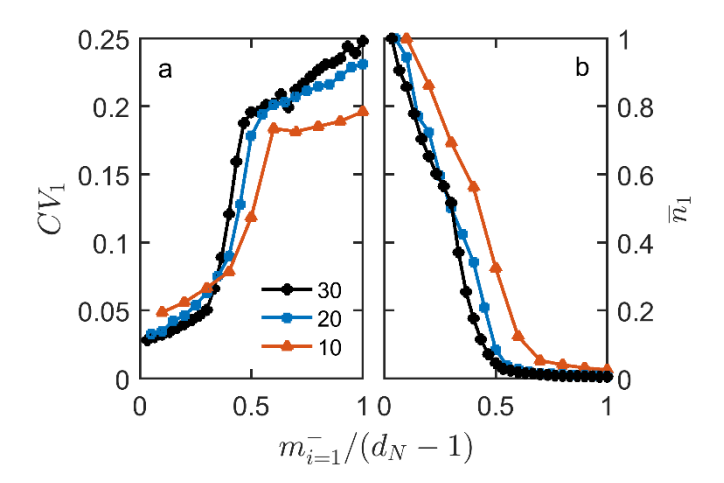


Figure 6A.6. Variation of CV (a) and normalized average (b) of node 1 as a function normalized $m_{i=1}^-$, $(m_{i=1}^-/(d_N-1))$ for the indicated sizes of networks with $m_{i\neq 1}^+=0$. The average was normalised by dividing by the maximum average value \bar{n}_1 in each case. The values of \bar{a}_- and \bar{a}_+ were same in Figure 5A.5.

It has been important to measure the scaling characteristic of noise with the average abundance in case of the stochastic calculations of coupled chemical reaction systems. To address this issue, in Figure 6A.7a CV_1 with \bar{n}_1 for various values of $m_{i\neq 1}^+$ was plotted. Two separate power-law scalings (piecewise power-law, $CV \propto \bar{n}^{\alpha}$) with two different scaling exponents, α_1 and α_2 , best suited the dependency of noise on the average, such scaling is considerably different from $CV \propto 1/\sqrt{\bar{n}}$ scaling. The linear regions of individual

lines were fitted (in the log-log plot) and determined the average and standard deviation of the scaling exponents. The scaling exponent was $\alpha_1=0.2\pm0.02$ in the low to intermediate abundance regime and $\alpha_2=0.9\pm0.03$ in the intermediate to high abundance zone. By determining the R^2 (goodness of fit) values for each fit, the accuracy of the fits was evaluated. For α_1 and α_2 , the average R^2 values were 0.908 ± 0.05 and 0.996 ± 0.002 , respectively. The scaling of noise for node 15, a candidate node in the network whose average was not immediately affected by the systematic alteration of $m_{i=1}^-$, was then calculated. It was discovered that this node displayed the well-known scaling of $CV \propto 1/\sqrt{n}$ across the various values of $m_{i\neq 1}^+$ (Figure 6A.7a). It implied that a node whose average was directly influenced by negative regulations obeys the biphasic scaling of noise, but a node, whose average was indirectly modified by negative regulations, follows the conventional scaling of noise. It is evident from Figure. 6A.7 that the average abundance range for node 1 was far wider than the abundance range for any other node in the network.

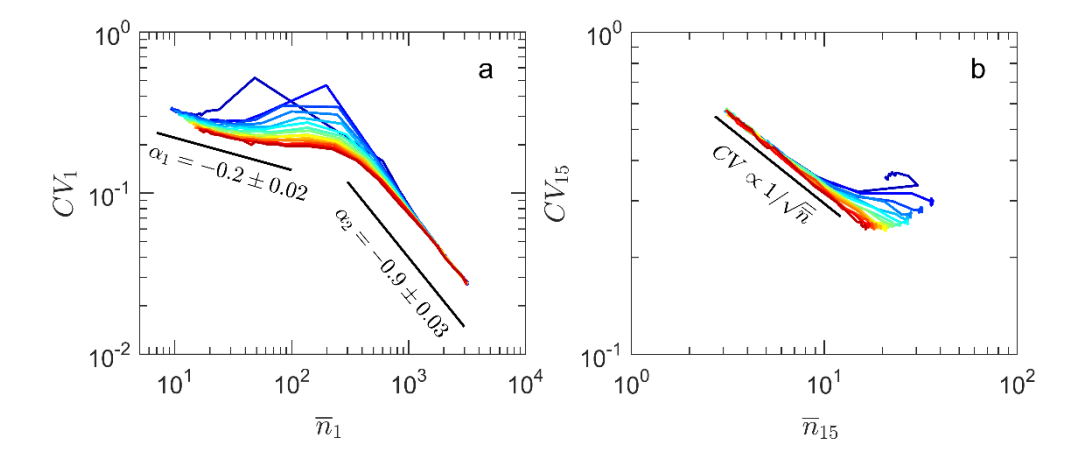


Figure 6A.7. Dependence of CV vs average of node 1 (a) and node 15 (b). Different lines represent different values of $m_{i\neq 1}^+$: from red $(m_{i\neq 1}^+=0)$ to blue $(m_{i\neq 1}^+=16)$ the value of $m_{i\neq 1}^+$ increases by 1. The scaling exponents from power-law fitting $(CV \propto \bar{n}^{\alpha})$ of the data segment are indicated inside the plots.

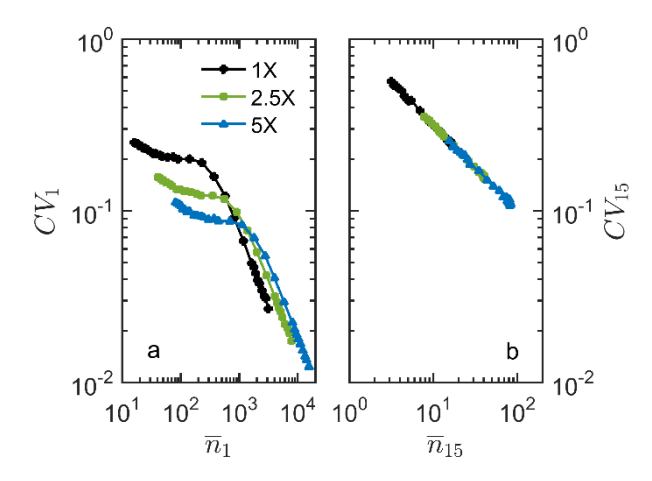


Figure 6A.8. Variation of biphasic behavior of noise in node 1 (left) and monophasic behavior of noise in node 15 (right) with the indicated values of scaling factors in the overall abundance.

This begged the obvious question of whether the disparate scaling behaviours were caused by the distinct regimes of abundance they experienced. The node 1 was directly influenced by the changes in $m_{i=1}^-$ while all other nodes in the network were indirectly impacted, thus the ranges of node 1 and other nodes were different. Further simulations were performed with various scaling factors that progressively increased the abundance of each node. For the networks with $m_{i\neq 1}^+ = 0$, Figure 6A.8 showed the CV against \bar{n} plots for node 1 and 15 with various scaling factors. The universality of the scaling law of node 1 and the other nodes in the democratic network was demonstrated by the shifting of entire scaling curves to the higher abundance regime. The universality of scaling principles was further demonstrated to be independent of $m_{i\neq 1}^+$. (Figure 6A.9).

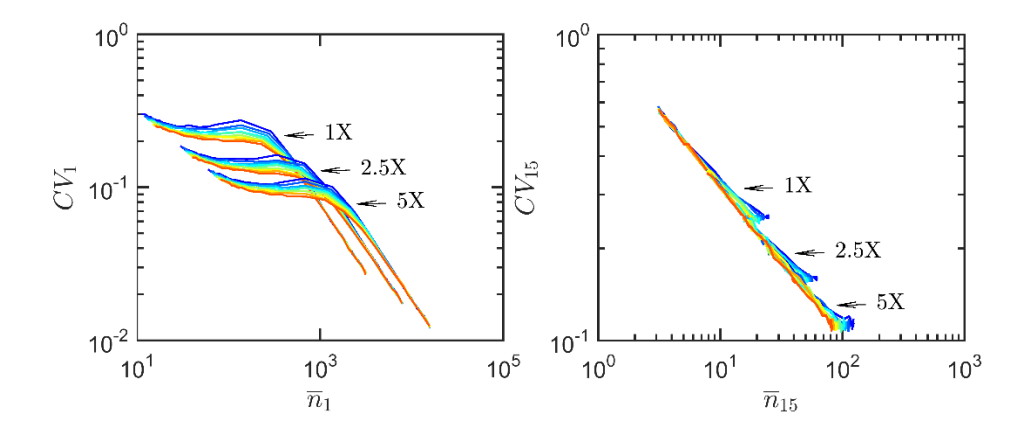


Fig 6A. 9. Plots similar to those in Figure 6A.8 with different values of $m_{i\neq 1}^+$ for different total abundance.

In order to determine the effect of strengths of positive and negative interactions on the scaling exponents, for a variety of values of \bar{a}_{-} and \bar{a}_{+} the exponents were calculated. Regardless of the values of \bar{a}_{+} , there was a systematic increase in both exponents with higher negative interaction strength (Figure 6A.10). It implied that the effect of negative interaction on noise is stronger for its higher strength. On the other hand, regardless of the value of \bar{a}_{-} , the values of both exponents decreased as the \bar{a}_{+} was increased. As a result, in contrast to positive interactions, negative interactions strongly regulate the noise in a democratic network.

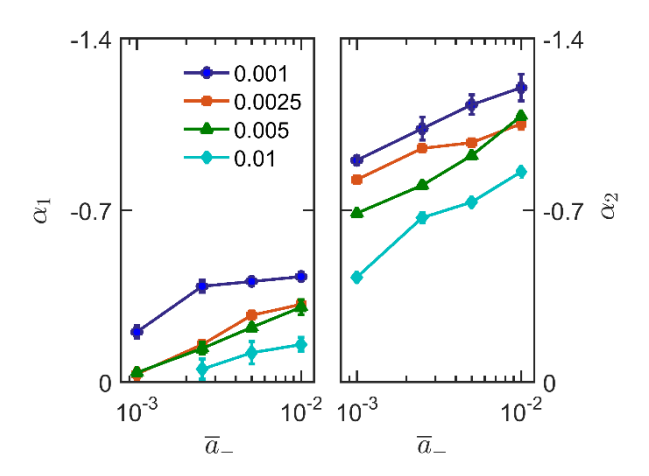


Figure 6A.10. Variation of scaling exponents α_1 and α_2 with the \bar{a}_- for the indicated values of \bar{a}_+ .

The role of negative regulation in attenuating noise has previously been investigated in the context of small gene regulatory networks. It has been discovered that it dampens the intrinsic noise, whereas positive regulations were found to exacerbate the noise. Later studies, notably in the context of feedback-regulated systems, however, demonstrated that positive regulations can also reduce noise. The impact of negative interactions on the noise strength (quantified as Fano factor, $FF = \frac{\sigma_i^2}{n_i}$) was further investigated in order to address this problem within the framework of democratic network. Irrespective value of $m_{i\neq 1}^+$, noise strength passed through a maximum with average, showing that at the intermediate average (i.e., intermediate number of $m_{i=1}^-$), it produced the largest noise strength (Figure 5A. 11a). The peak noise strength also increases with higher value of $m_{i\neq 1}^+$. While the network displayed similar qualitative behaviour of noise strength over a range of

 \bar{a}_{-} values, higher \bar{a}_{-} values led to a reduction in overall noise strength (Figures 5A. 11a-c).

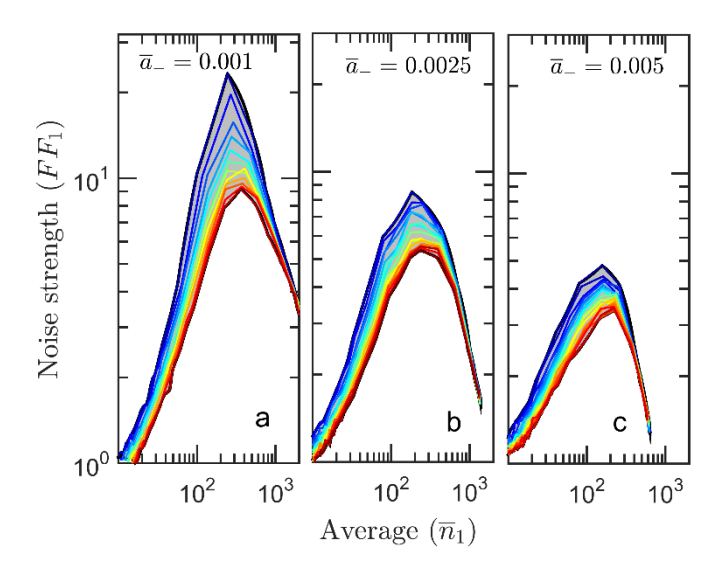


Figure 6A.11. Variation on noise strength (quantified as Fano factor) as function of \bar{n}_1 . In all three panels the value of \bar{a}_+ was kept fixed to 0.001.

Figure 6A. 12a presented the maximum value of noise strength (max_{FF}) of node 1 as a function of \bar{a}_- in the network with $m_{i\neq 1}^+=0$ to comprehend the impact of both \bar{a}_- and $m_{i=1}^-$, on the noise strength. These figures showed that, regardless of the strength of the positive interaction, the maximum noise strength decreases with increasing strength of negative interaction. The noise attenuation capability of negative restrictions is indicated by the decreasing of noise intensity with \bar{a}_- . However, the maximum noise strength constantly increased with increased strength of positive interaction, demonstrating that the positive interaction amplifies the noise strength. The conclusion that the negative interactions attenuate intrinsic noise was further supported by the plot of the number of negative interactions on node 1 that corresponded to the maximum noise strength $(max_{m_{i=1}^-})$ with \bar{a}_- (Figure 6A. 12b). Additionally, the anticorrelation between $max_{m_{i=1}^-}$ and \bar{a}_- showed that either a large number of weak negative interactions or a small number of strong negative interactions can limit noise.

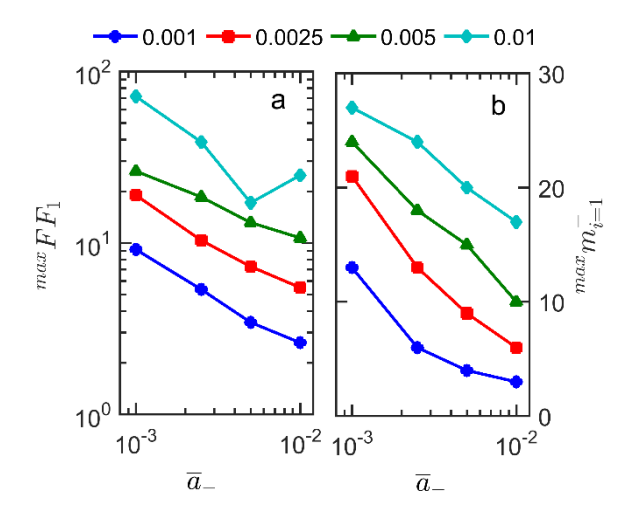


Figure 6A.12. a) Dependence of maximum noise strength (max_{FF}) (obtained from Figure. 6A.11) with \bar{a}_{-} for $m_{i\neq 1}^{+}=0$.b) Variation of $max_{m_{i=1}^{-}}$, the number of negative interactions where corresponding to maximum noise strength with \bar{a}_{-} . Different lines represent different value of \bar{a}_{+} .

A fully connected democratic network, in which every node connects with every other node in the network, served as the foundation for all of our calculations. But in reality, the networks may be sparse, where a node may not be connected to all other nodes. Thus, the number of mutual connections were lowered by randomly removing a fixed number of interactions while leaving the interaction between node 1 and all other nodes intact $(a(1,j) \neq 0)$ and $a(i,1) \neq 0$ in order to examine the attributes of similar networks with lower connectivity. As with fully connected networks, these modified networks showed similar qualitative average and intrinsic noise behaviour (Figure 6A.13).

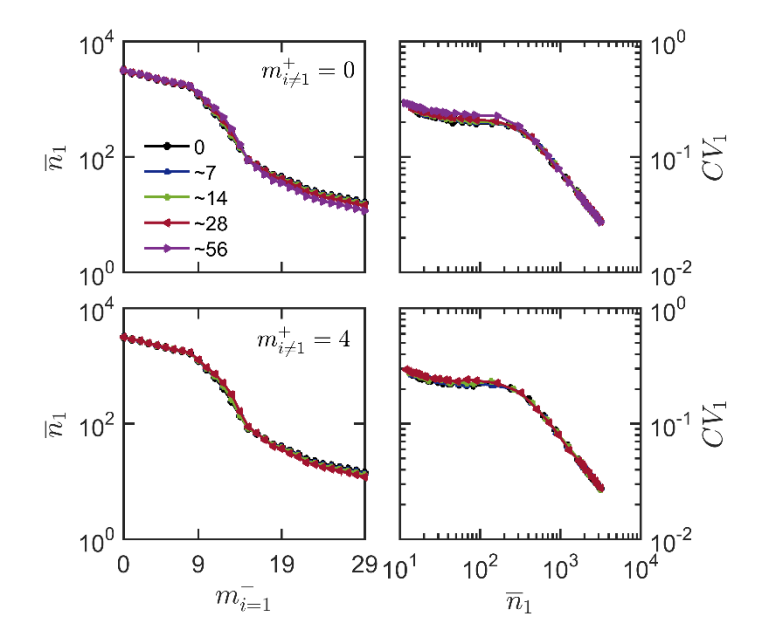


Figure 6A.13. Ultrasensitivity (left) and biphasic scaling (right) of node 1 in networks with removed interactions. The percentage reduction of mutual interactions on all other nodes is indicated inside the plot. Top row: $m_{i\neq 1}^+ = 0$ and bottom row: $m_{i\neq 1}^+ = 4$.

6.A.3 Conclusion

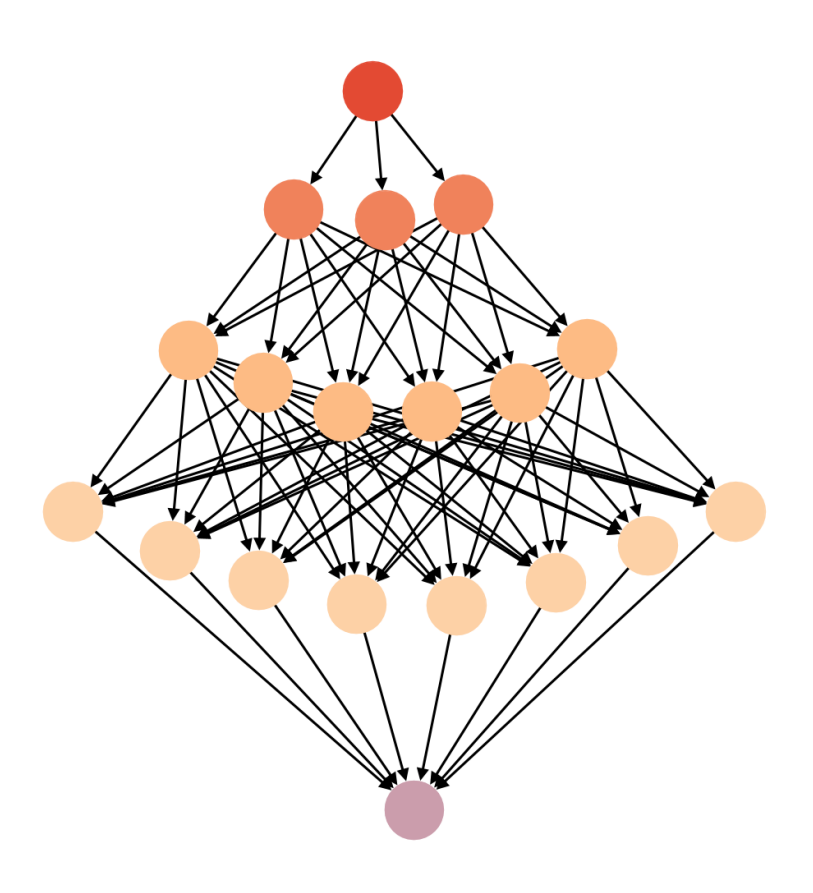
The experimental observations of cellular heterogeneity in single- and multi-cellular organisms are a result of both variations in external stimuli and fluctuations in the molecular abundance of a finite number of macromolecular species inside a living cell. Statistical mechanical models of gene expression noise have been demonstrated the ability to quantitatively explain observed protein abundance variability. Additional models have investigated the functions of feedback controls in noise propagation, whether in single genes or gene networks. Positive feedback loops and the average lifetime of molecular species have been identified as key components in attenuating chemical noise in system-level models of cellular physiology, such as the cell cycle. To the best of our knowledge, no research has yet been done on how chemical noise in a generalised chemical reaction network is controlled. One must accept that a specific cellular function results from the well-coordinated effort of a variety of interrelated genes, especially in the context of organisms' response to external cues. In this context, in chapter discusses how noise propagates within a democratic chemical network, where each node is connected to the others via either positive or negative interactions. Here, the main goal was to ascertain how

the qualitative and quantitative characteristics of interactions dictates the variability of the chemical species in the network.

A democratic chemical network with 30 interconnected nodes using the mass action rate laws of chemical reactions was developed. It is discovered that when the number of negative interactions on the target node increased, the noise, as measured by the coefficient of variation, sharply increased from low to high. It is significant to note that the qualitative behavior of the noise was largely unrelated to the qualitative nature of interactions on the other nodes in the network. It is concluded that the weak ultrasensitive switching of the average results in switching behavior of noise. Further investigation supported the conclusion that a democratic network with linear kinetics can also behave in an ultrasensitive manner. Analyses of noise showed that noise scales with average in according to a biphasic power-law with two different scaling exponents. The quantitative value of the mutual interactions had a significant impact on the values of these two exponents. According to the results of our simulation, the strength of the negative interactions led to decrease in the noise level, but the strength of the positive interactions amplifies it. Therefore, it is reasonable to draw the conclusion that positive interactions amplify the noise and negative interactions attenuate its effect.

Part B

Chemical noise propagation in autocratic network topology



S Das and D Barik, *Phys. Rev. E* **2021**, *103* (4), 042403 (2021)

In an autocratic network organisation, the nodes(genes/protein) are arranged in layers. In addition to controlling the nodes in other levels, the nodes in one layer may also interact with one another. Furthermore, there appears to be a common pattern of organisation for regulators in terms of abundance, lifetime and variability.²⁵ These studies demonstrated that the network designs included both pyramidal²² and nonpyramidal²⁵ architecture. Protein interaction networks, such as the kinase-phosphatase network in yeast, contain similar hierarchical networks²³. In an autocratic network, one or more layers of intermediary genes allow a group of master genes to control the regulation of a vast number of downstream genes.

6.B.1 Model

This chapter discussed how intrinsic noise is controlled in an autocratic reaction network, which consists of an input node and an output node coupled by three intermediate layers of nodes (Figure 6B.1). A node controls the expression of a node in the layer below, resulting in a unidirectional flow of information and the network is devoid of any feedback regulations. The network shown in Figure 6B.1 is made up of nodes grouped in layers (or hierarchy), where nodes in one layer control nodes in the next-level layer below it. Here, the nodes in a given layer do not interact with one another, and the nodes in the lower level do not affect the nodes in the upper level. The nodes at the highest and lowest levels, are referred respectively, as input and output nodes. The top, core, and terminal layers are the three node levels that lie in between the input and output nodes. The nodes in the autocratic network are connected either by activatory or inhibitory regulatory interactions. Direct and indirect regulations on the output node were classified as proximal and nonproximal regulations, respectively, based on the proximity. The nonproximal interactions were divided into two categories here: near-nonproximal and far-nonproximal interactions. The regulations on the top layer and core are collectively referred to as the far-nonproximal group, while the edges on the terminal layer are referred to as the near-nonproximal group.

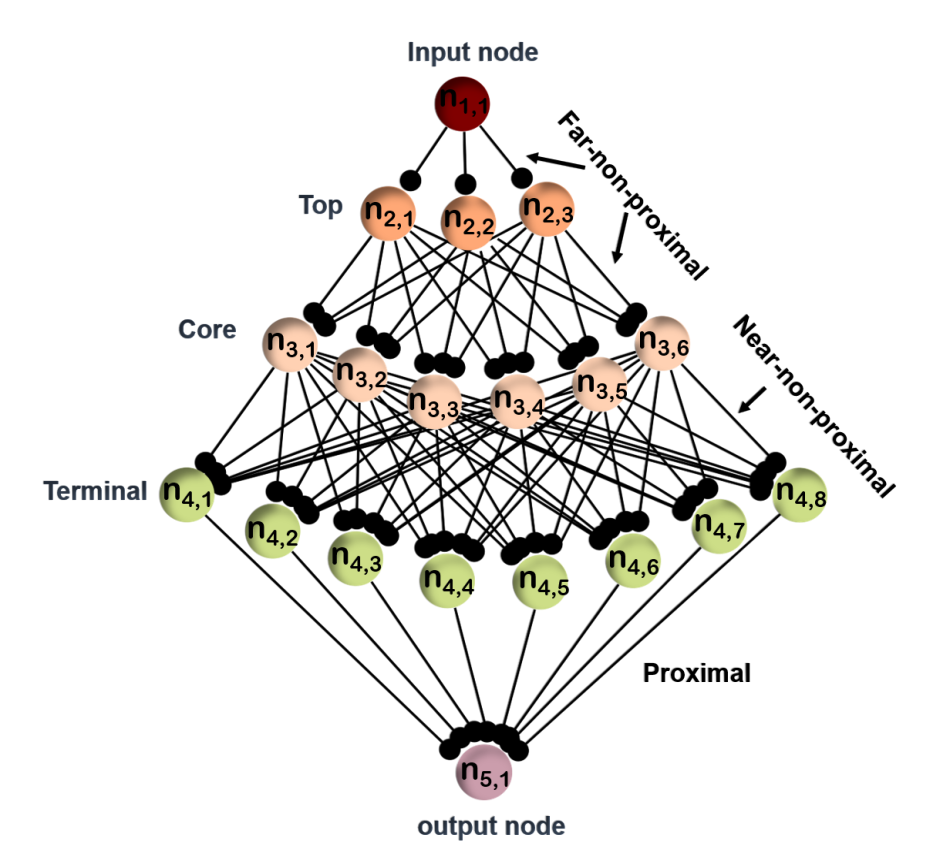


Figure 6B.1. Schematic representation of the autocratic network model. Colored circles are nodes typically served as a representative of chemical species found inside live cells, such as genes, proteins, transcripts, or metabolites. The lines with a circle at the other end represent the regulatory interactions from one node to the next, and in our autocratic network model, all of these circles point in the same direction.

Networks of different sizes can be created by varying the number of nodes in each layer, N_i ($d_N = \sum_i N_i$). Here, the total number of nodes presented in the layer above it ($m_{i,j} = N_{i-1}$) determined the total number of interactions on the jth node in the ith layer ($m_{i,j}$). Additionally, because a regulatory interaction could be either inhibitory or activatory, we varied the number of inhibitory ($m_{i,j}^-$) and activatory ($m_{i,j}^+$) interactions using the conservation relation $m_{i,j}^- + m_{i,j}^+ = m_{i,j}$, in order to study how these interactions effect in chemical noise propagation in our autocratic network model. The total number of the inhibitory regulations across all nodes in a particular layer is defined as, $M_j^- = \sum_j m_{i,j}^-$.

Each node also has its own uncontrolled production and degradation/dilution processes in addition to the regulatory interactions. The input, top, core, terminal, and output layers in this work will each contain the following number of nodes: $N_1 = 1$, $N_2 = 3$, $N_3 = 6$, $N_4 = 1$

8, and $N_5 = 1$. As a result, 1, 3, 6, and 8 respectively represent the number of regulatory interactions on each node in the top, core, terminal, and output layers. The mean field dynamics of the nodes we defined as the following set of coupled ordinary differential equations,

$$\frac{d\bar{n}_{i,j}}{dt} = \Omega \kappa_{i,j} - \gamma_{i,j} \bar{n}_{i,j} + \frac{1}{\Omega} \sum_{k=1}^{N_{i-1}} a_{i,k} \, \bar{n}_{i-1} \bar{n}_{i,j}$$
 6B.1

The equation represents the time evolution of the average molecular abundance $(\bar{n}_{i,j})$ of the jth node in the ith layer. The first two terms in the right hand side of equation represents, respectively, gain and loss resulting from production and degradation/dilution. The associated rate constants for these two reactions are $\kappa_{i,j}$ and $\gamma_{i,j}$. Then final term represents the bimolecular regulatory interaction from kth node in the (i-1)th layer. The magnitude and sign of $a_{i,k}$ respectively, indicate the regulation's strength and kind. Inhibitory and activatory regulations are represented by $a_{i,k} < 0$ and $a_{i,k} > 0$ respectively. $m_{i,j}^-$ and $m_{i,j}^+$ represent the number of inhibitory and activating interactions on the jth node. The total number of regulatory interactions, $M = \sum_{i=2}^{N_{i-1}N_i} N_i$ shared across d_N number of nodes. We maintained a fixed value of $\kappa_{i,j}$ =0.012 and $\gamma_{i,j}$ =0.02 for the production and the degradation rate constants, respectively. For regulatory interactions, a^+ and a^- were chosen to be equal to ± 0.003 , respectively for activation and inhibition. We parametrize our model such that the system must attain a stationary state within a finite simulation time and that the quantity of molecules per node must be within the realistic range often found in a live cell. Because timescales can vary greatly from one organism to another, it is important to note that we have not specified the units of the rate constants, particularly for the time, to make the model applicable to networks representing various organisms. The half-life of ~35 time units, which is the most typical half-life for many proteins in budding yeast ²⁶(in min) and mammalian²⁷(in hour) systems, is represented by the chosen value of the degradation constant, $\gamma_{i,j}$. The scaling factor, Ω increases the population abundance of the interconnected nodes while preserving the system's dynamics. We have used $\Omega = 100$ throughout the entire work, unless otherwise stated. Using Gillespie's stochastic simulation algorithm²⁸, we simulated the chemical reactions associated with our model (Eqn 5B.1) in order to ascertain the impact of finite numbers in autocratic networks. We calculated the effect of intrinsic noise accurately thanks to the linearity of the reaction rate laws in our model. There are $2d_N + M$ number of reactions in an autocratic network of size d_N that

correspond to d_N production, d_N degradation, and M regulatory interaction. We conducted an ensemble of 10,000 trajectories for a very long time to acquire reliable steady state statistics (50,000 time units). When the propensity of chemical reactions increases due to the involvement of a large number of molecular species and/or significant rate constants of the chemical processes, the runtime for stochastic simulation can become quite long. In order to prevent this, we implemented a cut off rule of 100,000 molecules/node to stop the calculation, where the simulation becomes substantially slower with huge population abundance. This calculation is left out of the analysis. Given that the finite number effect will be very insignificant given the huge abundance, this choice of cut-off criterion is quite reasonable.

The goal in this study was to investigate how the qualitative and quantitative nature of the proximal and nonproximal regulatory interactions regulate intrinsic chemical noise in the output node. The nature of the proximal and nonproximal interactions on the output node, as well as the variation of average and noise in it, were systematically explored.

6B.2 Results

For a specific number of inhibitory near-nonproximal $(m_{nnp}^- = \sum_{j=1}^{N_4} m_{4,j}^-)$ and far-nonproximal interactions $(m_{fnp}^- = \sum_{j=1}^{N_2} m_{2,j}^- + \sum_{j=1}^{N_3} m_{3,j}^-)$ on the nodes in different layers, the average abundance of the output node $(\bar{n}_{5,1})$ decreased with increasing proximal inhibitory interactions (m_p^-) (Figure 6B.2).

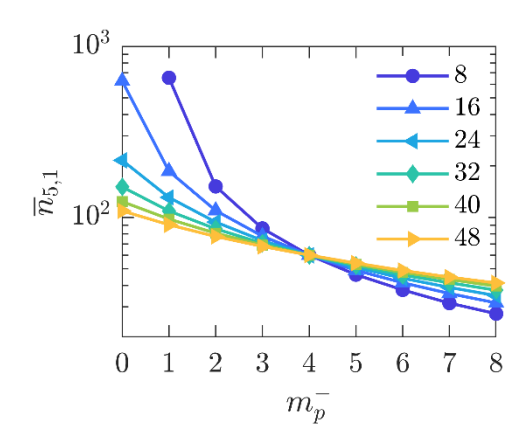


Figure 6B.2. Dependency of average abundance of output node ($\overline{n}_{5,1}$) on the number

negative proximal interactions (m_p^-) for indicated number of near-nonproximal negative interactions (m_{nnp}^-) . The value of m_{fnp}^- kept at 6.

In order to increase m_{nnp}^- , one more inhibitory regulation towards each node in the terminal layer were added. A certain order was followed to allocate the inhibitory interactions on a particular node in the terminal layer from the nodes in the core layer in order to make implementation of easier. Particularly, the inhibitory interactions originate from the left nodes in the core layer. For example, to implement $m_{nnp}^- = 8$ ($m_{4,1}^- = 1$) and $m_{nnp}^- = 16$ ($m_{4,1}^- = 2$), in first only the node $n_{3,1}$ and in second case both $n_{3,1}$ and $n_{3,2}$ inhibits all the nodes in the terminal layer respectively. A similar approach was used to modify m_{fnp}^- . Across various values of m_{nnp}^- , $\bar{n}_{5,1}$ falls as m_p^- increases (Figure 6B.2).

However, a greater number of near-nonproximal inhibitory regulations contributed to the abundance of the output node when the proximal inhibitory regulations were proportionately more than the activatory regulations ($m_p^->4$). As a result, both near-nonproximal and proximal interactions controlled the output node's abundance. Next, $\bar{n}_{5,1}$ against m_p^- for various numbers of m_{fnp}^- for a fixed number of m_{nnp}^- was plotted to ascertain how the far-nonproximal interactions in the top and core layer control the abundance of the output node (Figure 6B.3). Across a range of m_{nnp}^- values, the influence of the far-nonproximal inhibitory interactions on the output node is quite minimal. Therefore, the proximity of the regulatory interactions was found crucial in determining the level of regulation in an autocratic network.

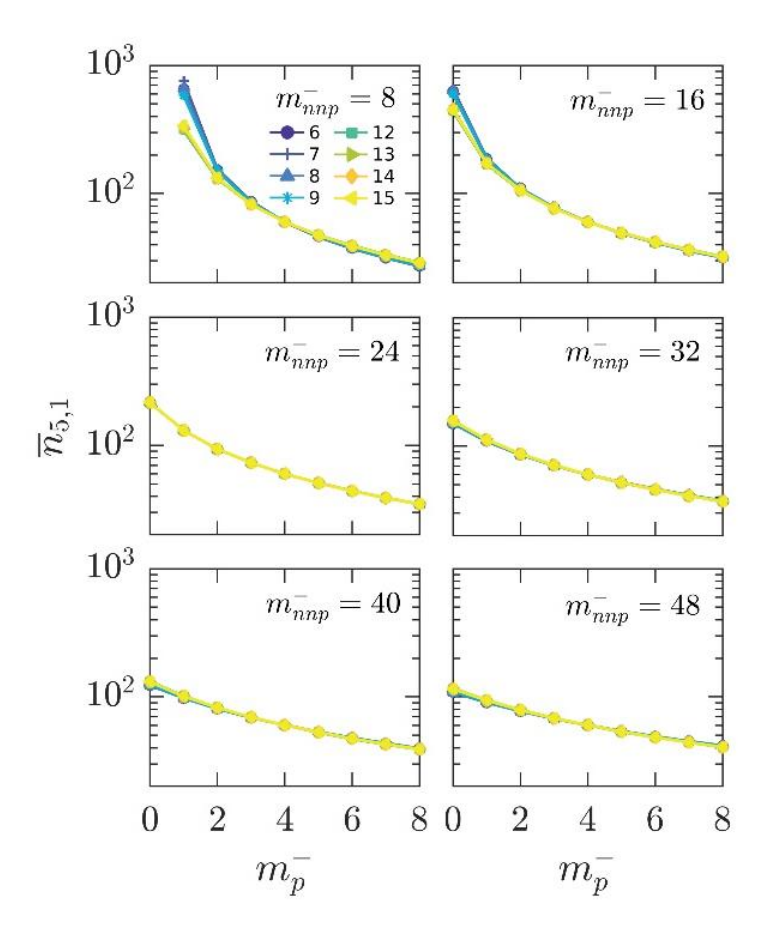


Figure 6B.3. Plot of $\bar{n}_{5,1}$ with m_p^- for a different number of far-nonproximal inhibitory interactions (m_{fnp}^-) with a particular value of m_{nnp}^- . Each line type corresponds to a particular value of m_{nnp}^- as indicated.

An essential aspect of noise regulation in biological reaction networks is the scaling of the noise with average, which is determined from the coefficient of variation (CV) with the average abundance. In Figure 6B.4a, the CV of the output node at steady state was plotted against average abundance. The average abundance was altered by modifying the number of proximal inhibitory contacts (m_p^-) on the output node. It was found that the near-nonproximal interactions played a crucial role in determining the qualitative behaviour of noise with the average. The noise decreased with the increase in average for higher values of m_{nnp}^- , which is predicted behaviour from 'the finite number effect'. However, for low values of m_{nnp}^- , the CV first reduces with increasing average for smaller values of m_p^- , but then increases after passing through a minimum (Figure 6B.4a). The 'finite number effect' of the stochastic chemical kinetics predicts that noise would decrease as abundance increases. However, the increase in noise with increased average is counterintuitive by its very nature, making it a nontrivial or unexpected result for the autocratic system. This non-

trivial scaling holds for only low number of near-nonproximal interactions. These computations were repeated by scaling all the rate constants systematically such that the abundance of all the nodes increases in a consistent manner ($\Omega = 500$) in order to ascertain the universality of the scaling behaviour. It was found that noise scaling behaviour (Figure 6B.4b) is qualitatively comparable to that shown in Figure 6B.4a with $\Omega = 100$. It was noted that the CV values were now lower and that the greater average abundance marked the turning point of CV.

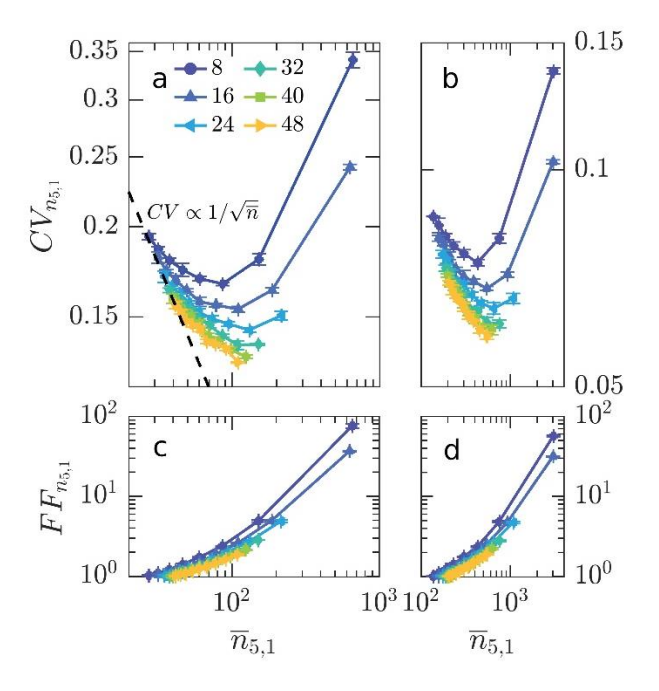


Figure 6B.4. a) Plot for CV with the average abundance of the output node for different values of $m_{\rm nnp}^-$ with a fixed value of $m_{fnp}^- = 6$. The dashed line corresponding to the conventional $CV \propto 1/\sqrt{n}$ scaling. b) Similar plot for network with 5X increased abundance ($\Omega = 500$).

Thus, these findings suggested that the unusual scaling of noise is a fundamental characteristic of the autocratic network and that it was influenced by the quantity of inhibiting interactions on the terminal layer (m_{nnp}^-) . The comparison of the CV for the various values of m_{nnp}^- also showed that the output node's variability was decreased by a significant number of inhibitory interactions on the upstream layer. Plots of the Fano factor (FF) and the average (Figures 6B.4c-d) showed that the noise strength increased as the number of proximal inhibitory regulations decreases. Therefore, the direct activatory

Chemical noise in generalised network

controls are to reason for the increased intrinsic noise. Next, the effect of far-nonproximal interactions on noise scaling was determined. It was found that for a given value of m_{nnp}^- , the number of far-nonproximal inhibitory interactions had little effect on the scaling of noise (Figue 6B.5). As a result, the near-nonproximal interactions on the terminal layer, rather than the far-nonproximal interactions originating at the top and core layers, dictated the qualitative nature of the scaling of noise in the output node.

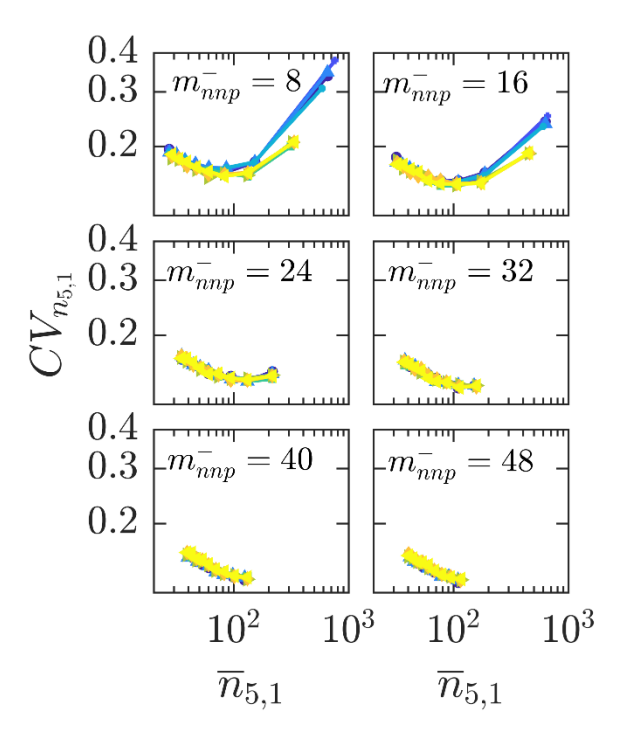


Figure 6B.5. Plot of $CV_{5,1}$ with m_p^- for a different number of far-nonproximal inhibitory interactions (m_{fnp}^-) with a particular value of m_{nnp}^- . Each line type corresponds to a particular value of m_{nnp}^- as indicated in Figure 6B.3.

The striking feature in stochasticity for the autocratic network is the rise in noise at high abundance region. One reason of this high noise at abundance could be the steady state population splitting. But the model network did not have any nonlinearity or any feedback regulation, the splitting of population options was ruled out. Thus, to determine the reason for this high noise at high abundance region, steady state distributions of the output node population abundance was plotted in Figure 6B.6a with an increasing number of proximal inhibitory interactions.

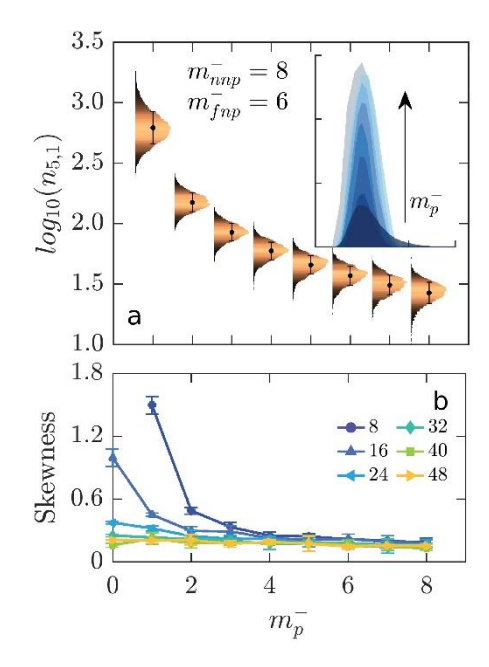


Figure 6B.6: Plot for steady state population distribution of the output node for different m_p^- values. Comparison of distributions centered at the abundance corresponding to the peak of the distribution (inset). (b) Plot of skewness of the steady state population distributions as a function of m_p^- . Diffferent color lines represent different values of m_{nnp}^- .

These distributions made it abundantly evident that the multimodality of the steady state distributions was not the cause of the increased noise. These distribution widths in the high and low abundance regimes (low m_p^- and high m_p^-)were wider than the distribution for intermediate abundance. To see how the shapes changed as m_p^- increased, these distributions were further compared, centred at the peak (Figure 6B.6(a) inset). In comparison to the high value of m_p^- , the distribution associated with a low value of m_p^- is positively skewed towards a high of $\overline{n}_{5,1}$. Furthermore, the skewness vs. m_p^- plot (Figure 6B.6b) demonstrated that the skewness of these distribution decreased with higher m_p^- values across different values of m_{nnp}^- . Thus, the increase tail of the distribution at large abundance regime is responsible for high noise.

To examine further, the trajectories of output node for various values of m_p^- were looked into (Figure 6B.7). The stochastic trajectory displayed a fluctuation pattern resembling bursty gene expression kinetics in the large abundance limit with $m_p^- = 1$. Particularly, the system becomes highly noisy and the steady state distribution became positively skewed as a result of the large and irregular fluctuations. The stochasticity in the time courses

Chemical noise in generalised network

appeared to be more regular and free of any significant deviation from the mean value in the low abundance limit with increasing values of m_p^- . The phase space of the trajectories were plotted by correlating the time course of the output node against the time course of a representative node $(n_{4,8})$ in the terminal layer (Figure 6B.7). The bursty nature of the output node was evident from the phase space plot for $m_p^- = 1$, which spanned a bigger area than the phase space for the larger values of m_p^- .

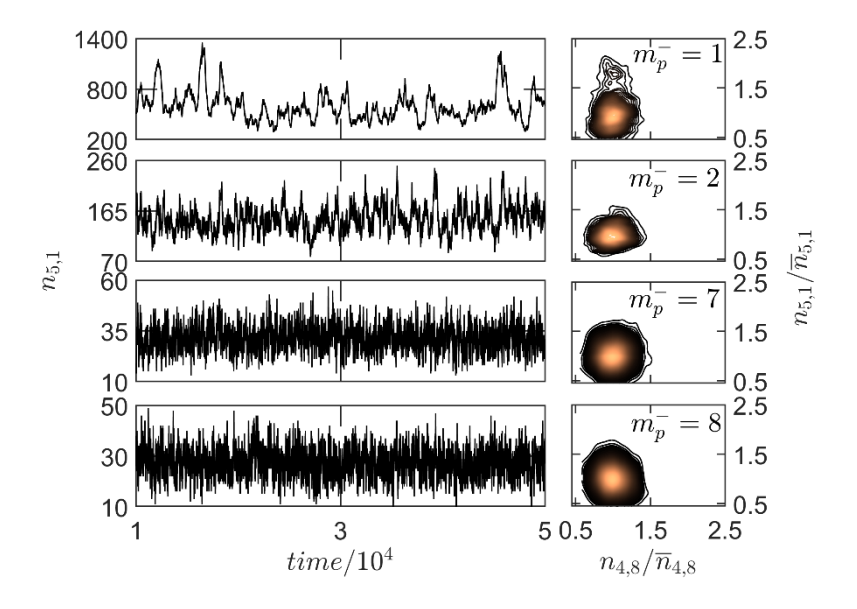


Figure 6B.7: The time course trajectories (left) and the phase space plots (right) of the network with $m_{nnp}^- = 8$ and $m_{fnp}^- = 6$. In the phase space plot of output node, $n_{5,1}(t)$ is plotted as a function of $n_{4,8}(t)$, a node in the terminal layer.

For $m_p^-=1$, the output node receives only one inhibitory and seven activatory input signals from the nodes in the terminal layer. The production of the output node was accelerated as a result of the higher quantity of activatory interactions, which cannot be countered by the smaller number of inhibitory interactions. The bursty kinetics of output node represented the end outcome of these two antagonistic interactions. An increase in the inhibitory input interaction which counters the production by accelerating the degradation of output node, leads to disappearance of the excitable nature of the output node.

Due to higher number of inhibitory interactions from the nodes in the terminal layer to the output node, the variation of m_p^- changed the average abundance on the output node. However, it was interesting to study the explicit role of m_p^- on the noise without the

variation in the average abundance. In order to maintain the same average abundance while changing m_p^- , the synthesis rate $(\kappa_{5,1})$ was scaled. The average abundance remained constant as we varied m_p^- in this scenario (inset of Figure 6B.8). It was found that when m_p^- increases, the noise in the output node decreases. This was consistent behaviour for various m_{nnp}^- values. However, similar to the findings in Figures 6B.4a-b, the effect of m_p^- was more pronounced for smaller values of m_{nnp}^- . These findings once more showed that a high number of activatory interactions (small m_p^-) on the output node contributed to the increased variability.

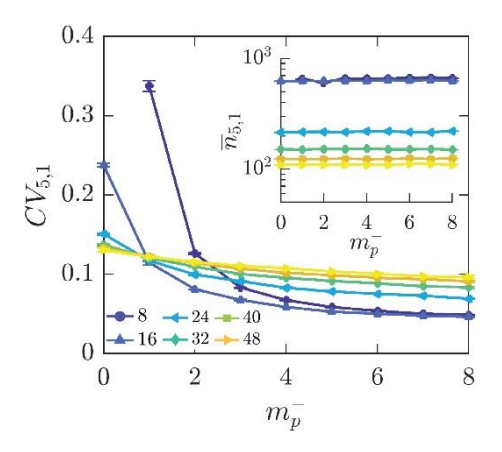


Figure 6B.8: Plot of $CV_{5,1}$ with m_p^- for different value of m_{nnp}^- and $m_{fnp}^- = 6$. While modifying the m_p^- , the synthesis rate of the output node $\kappa_{5,1}$ was adjusted such that the average remains unchanged (inset). The different color and marker type are for different values of m_{nnp}^- as indicated in Figure 6B.4.

So far, the number of proximal and nonproximal interactions were only altered while maintaining the strength of the activatory and inhibitory regulations (a^+ and a^-). To determine the effect of strength of these interactions on the scaling of the intrinsic noise, next the rate constants of the activatory and inhibitory interactions were varied. The rate constants ratio was adjusted by a factor of 2.

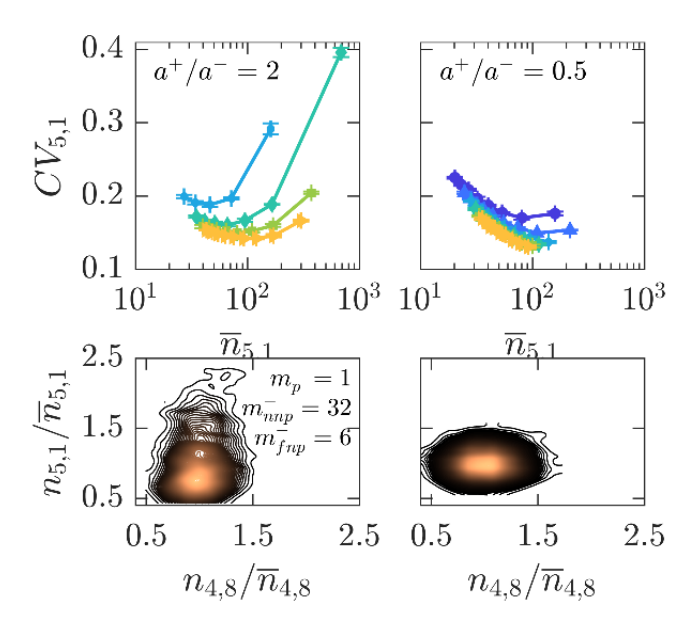


Figure 6B.9: Plot of $CV_{5,1}$ with m_p^- where a) $a^+/a^- = 2$ and b) $a^+/a^- = 0.5$. c) and d) are the phase space plot for the same. The different color and marker type are for different values of m_{nnp}^- as indicated in Figure 6B.4.

In Figures 6B.9a-b the scaling of the noise for $a^+/a^- = 2$ and $a^+/a^- = 0.5$ was plotted respectively. The nontrivial scaling of noise became more pronounced across the various numbers of near-nonproximal interactions when the strength of activatory interactions were more than the strengths of negative interactions (Figure 6B.9a). In contrast, the network appeared to show typical scaling the stronger negative interactions (Figure 9b). Similar bursty nature of output node confirmed from the phase space plots in the case $a^+/a^-=2$ (Figure 9c) as compared to $a^+/a^- = 0.5$ (Figure 9d). Thus, higher strength of a^+ supported the argument of bursty kinetics further by promoting the non-trivial scaling. The scaling of noise was also considered when the interaction strengths were varied at each layer. To investigate the layer-specific regulatory function of the interaction strengths on the scaling of the noise, simulations were ran using various interaction strengths in each layer. Two sets of calculations were performed, increasing the strength of the interaction from the input to the output layer in one set (Figure 6B.10a) and decreasing it in the other set (Figure 6B.10b). We have selected the values of interactions as $a_{2,j}^{+/-} = 0.003$, $a_{3,j}^{+/-} = 0.004$, $a_{4,j}^{+/-} = 0.004$ = 0.005, and $a_{5,i}^{+/-}$ = 0.006 for the interaction between input/top, top/core, core/terminal, and terminal/output layers, respectively, in the situation of increasing strength from the input

to the output layer. For the decrease in interaction strengths from the input to the output layers, the reverse order was employed. It was found that the scaling of noise with the average was comparable in both the situations. However, when the strength of interactions was stronger in the terminal layer, the high noise in the high abundance nature of noise was more obvious across different values of m_{nnp}^- .

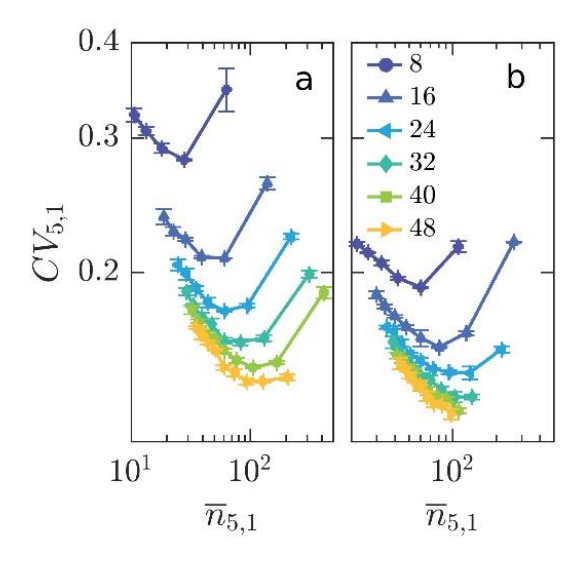


Figure 6B.10: Plot of $CV_{5,1}$ vs $\overline{n}_{5,1}$ with an increasing order of interaction strength from a) top to bottom and b) bottom to top layer of the network. The different color lines and marker represents different value of m_{nnp}^- as indicated.

Every node in the network model was connected to every other node in the layer above it and below it, making the autocratic network fully connected. In real scenario, networks may not be entirely interconnected²⁹. Therefore, a random number of regulatory interactions were deleted from the network across all layers except the output layer in order to assess the noise in such sorts of autocratic networks. The values of $a_{i,j}$ were arbitrarily chosen to be 0 in order to remove a certain number of interactions from the network's top, core, and terminal layers. For instance, we set 1, 6, and 8 numbers of randomly selected $a_{i,j}$ from the top, core, and terminal layers, respectively, to exclude 20% of interactions. Notably, there are 69 interactions overall in these three tiers in the completely connected network. In the instance of 40%, we multiplied these amounts by two. It was found that removing 20% and 40% of the regulatory interactions from the network did not change the scaling of the noise (Figure 6B.11), indicating the universality of the scaling behavior in the autocratic network.

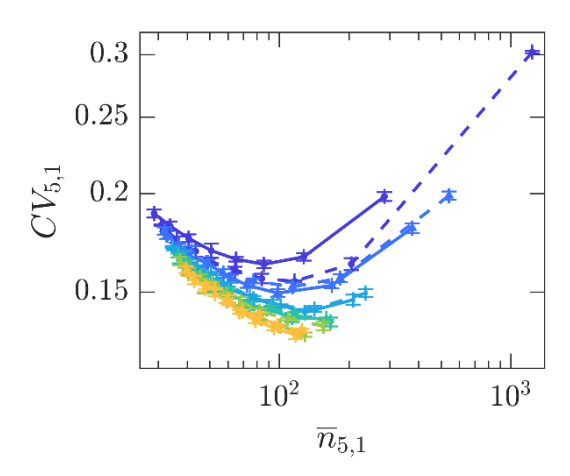


Figure 6B.11: Comparison of the scaling of $CV_{5,1}$ vs $\bar{n}_{5,1}$, with ~20% (solid lines) and ~40% (dashed lines) reduction of interactions, at random, in the top, core and terminal layers of the network. The different color lines represent different value of m_{nnp}^- as indicated in Figure 6B.10.

In order to establish a network with a certain number of inhibitory near-nonproximal and far-nonproximal connections, we chosen these regulatory interactions in a specific manner for the autocratic network. A given number of m_{nnp}^- and m_{fnp}^- , the numbers could be satisfied by a variety of mutual combinations of interactions, leading to the creation of multiple equivalent networks (microstates). Five such comparable networks were created where the regulatory interactions were all randomly chosen and had the same values of m_{nnp}^- and m_{fnp}^- to test whether the findings were affected by the particular mutual interactions (i,j) chosen. Figures 6B.12a-c demonstrated that the nature of the scaling was independent of the particular mutual interactions that are chosen.

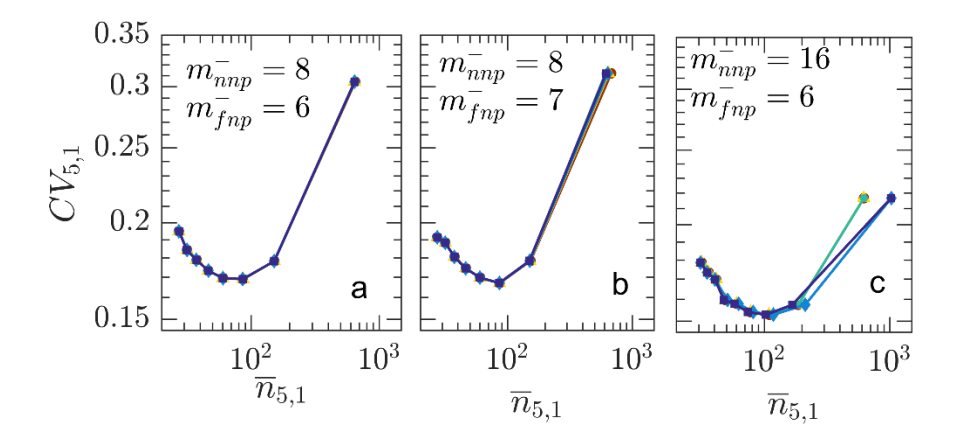


Figure 6B.12: Scaling of $CV_{5,1}$ vs $\bar{n}_{5,1}$ for the indicated values of m_{nnp}^- and m_{fnp}^- . For each combination of m_{nnp}^- and m_{fnp}^- five different networks having randomly chosen mutual interactions were presented.

Finally, investigation of the scaling of noise was carried out in a mixed network with nodes in a certain hierarchical layer were connected to each other to create a democratic architecture. As a result, the nodes in the top, core, and terminal layers controlled one another, creating an internally democratic subnetwork. As a result, the resulting network becomes a conglomeration of democratic and autocratic network (Figure 6B.13a). The scaling of intrinsic noise with the average was found to be unaffected by the democratic mutual interactions in the three layers (Figure 6B.13b). The hybrid network exhibited considerable noise in both the low and high abundance regimes, strictly following the scaling of noise behavior in an autocratic network.

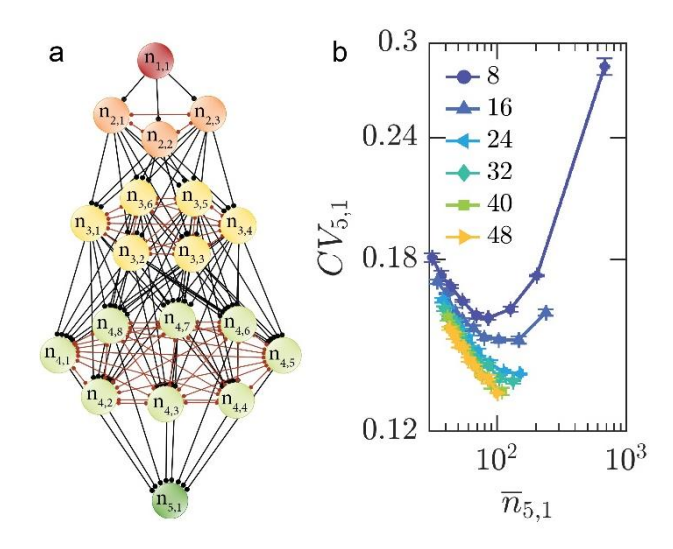


Figure 6B.13.Schematic representation of the mixed network. The nodes in the top, core, and terminal layers form democratic subnetworks within themselves. The mutual

Chemical noise in generalised network

interactions within a democratic subnetwork are represented by the edges with filled circles at both ends (red lines). (b) The scaling of noise in the output node with its average. The values of a^+ and a^- were chosen as +0.0025 and -0.0025 respectively. In the democratic subnetworks activatory and inhibitory interactions were equally distributed with strength of 0.001 for both interactions.

6B.3 Conclusion

This chapter focussed on how chemical noise propagates in an autocratic network, where nodes in one layer regulates nodes in another layer. The goal was to determine how the qualitative (activatory/inhibitory) and quantitative (strength) interactions of regulatory interactions influence the variability in the autocratic network. In order to employ the stochastic simulation algorithm to precisely estimate the intrinsic chemical noise in the network, the mass action rate law of chemical reaction was applied to represent the network. The qualitative nature of the proximal (direct) and near-nonproximal (indirect) interactions were found to strongly regulate the steady state statistical properties of the output node. Whereas the far-nonproximal rules had no impact on such attributes. In particular, when the network contained more activating near-nonproximal regulations than inhibiting near-nonproximal regulations, calculations showed that the noise passed through a minimum as a function of average abundance. This kind of scaling resulted in increased variability of output node in both the low and high abundance regimes. The system exhibited greater variability despite having a large average, such scaling of noise with the average was new and nontrivial. It was demonstrated that the system's bursty kinetics, which were regulated by a significant number of direct activatory regulations from the nodes in the neighbouring layer, were the cause of the nontrivial scaling of noise with the average. The higher strength of activatory regulation enhanced the nontrivial scaling of the variability by altering the strengths of the activatory and inhibitory interactions. The activatory regulations, either in high number or in higher strength compared to the inhibitory regulations, increased the system variability by generating bursty trajectories. Even with the addition of democratic mutual interactions between nodes in a specific layer, the qualitative aspect of scaling remains unaltered.

As conclusion, in a network that is entirely democratic the intrinsic noise showed a biphasic scaling and showed weak ultrasensitivity in the average. Whereas the autocratic or mixed networks, both showed a nontrivial scaling of noise in which the downstream node becomes noisy in both the low abundance and high abundance regimes.

6.2 References:

- (1) Raj, A.; van Oudenaarden, A. Nature, Nurture, or Chance: Stochastic Gene Expression and Its Consequences. *Cell* **2008**, *135* (2), 216–226. https://doi.org/10.1016/J.CELL.2008.09.050.
- (2) Sanchez, A.; Choubey, S.; Kondev, J. Regulation of Noise in Gene Expression. http://dx.doi.org/10.1146/annurev-biophys-083012-130401 2013, 42 (1), 469–491. https://doi.org/10.1146/ANNUREV-BIOPHYS-083012-130401.
- (3) Ozbudak, E. M.; Thattai, M.; Kurtser, I.; Grossman, A. D.; Van Oudenaarden, A. Regulation of Noise in the Expression of a Single Gene. *Nat. Genet.* 2002 311 2002, 31 (1), 69–73. https://doi.org/10.1038/ng869.
- (4) Elowitz, M. B.; Levine, A. J.; Siggia, E. D.; Swain, P. S. Stochastic Gene Expression in a Single Cell. *Science* (80-.). **2002**, 297 (5584), 1183–1186. https://doi.org/10.1126/SCIENCE.1070919/SUPPL_FILE/ELOWITZSOM.PDF.
- (5) Blake, W. J.; Kærn, M.; Cantor, C. R.; Collins, J. J. Noise in Eukaryotic Gene Expression. *Nat.* 2003 4226932 2003, 422 (6932), 633–637. https://doi.org/10.1038/nature01546.
- (6) Raser, J. M.; O'Shea, E. K. Control of Stochasticity in Eukaryotic Gene Expression. *Science* (80-.). **2004**, 304 (5678), 1811–1814. https://doi.org/10.1126/SCIENCE.1098641/SUPPL_FILE/RASER.SOM.PDF.
- (7) Thattai, M.; Van Oudenaarden, A. Intrinsic Noise in Gene Regulatory Networks. *Proc. Natl. Acad. Sci. U. S. A.* **2001**, 98 (15), 8614–8619.
 https://doi.org/10.1073/PNAS.151588598/ASSET/296583DD-83EE-408D-8B96-34237EE6E852/ASSETS/GRAPHIC/PQ1515885005.JPEG.
- (8) Pedraza, J. H.; Van Oudenaarden, A. Noise Propagations in Gene Networks. *Science* (80-.). **2005**, 307 (5717), 1965–1969. https://doi.org/10.1126/SCIENCE.1109090/SUPPL_FILE/PEDRAZA-SOM.PDF.

- (9) Paulsson, J. Summing up the Noise in Gene Networks. *Nat.* 2004 4276973 2004,427 (6973), 415–418. https://doi.org/10.1038/nature02257.
- (10) Friedman, N.; Cai, L.; Xie, X. S. Linking Stochastic Dynamics to Population Distribution: An Analytical Framework of Gene Expression. *Phys. Rev. Lett.* 2006, 97 (16), 168302. https://doi.org/10.1103/PHYSREVLETT.97.168302/FIGURES/3/MEDIUM.
- (11) Shahrezaei, V.; Swain, P. S. Analytical Distributions for Stochastic Gene Expression. *Proc. Natl. Acad. Sci. U. S. A.* **2008**, *105* (45), 17256–17261. https://doi.org/10.1073/PNAS.0803850105/SUPPL_FILE/APPENDIX_PDF.PDF.
- (12) Pedraza, J. M.; Paulsson, J. Effects of Molecular Memory and Bursting on Fluctuations in Gene Expression. *Science* (80-.). **2008**, 319 (5861), 339–343. https://doi.org/10.1126/science.1144331.
- (13) Jia, T.; Kulkarni, R. V. Intrinsic Noise in Stochastic Models of Gene Expression with Molecular Memory and Bursting. *Phys. Rev. Lett.* **2011**, *106* (5), 58102. https://doi.org/10.1103/PHYSREVLETT.106.058102/FIGURES/2/MEDIUM.
- (14) Becskel, A.; Serrano, L. Engineering Stability in Gene Networks by Autoregulation. *Nat.* 2000 4056786 **2000**, 405 (6786), 590–593. https://doi.org/10.1038/35014651.
- (15) Bruggeman, F. J.; Blüthgen, N.; Westerhoff, H. V. Noise Management by Molecular Networks. *PLoS Comput. Biol.* **2009**, *5* (9), e1000506. https://doi.org/10.1371/JOURNAL.PCBI.1000506.
- (16) Hinczewski, M.; Thirumalai, D. Noise Control in Gene Regulatory Networks with Negative Feedback. J. Phys. Chem. B 2016, 120 (26), 6166–6177. https://doi.org/10.1021/ACS.JPCB.6B02093/SUPPL_FILE/JP6B02093_SI_001.P DF.
- (17) Chalancon, G.; Ravarani, C. N. J.; Balaji, S.; Martinez-Arias, A.; Aravind, L.; Jothi, R.; Babu, M. M. Interplay between Gene Expression Noise and Regulatory Network Architecture. *Trends Genet.* **2012**, 28 (5), 221–232. https://doi.org/10.1016/J.TIG.2012.01.006.
- (18) Bhardwaj, N.; Yan, K. K.; Gerstein, M. B. Analysis of Diverse Regulatory Networks in a Hierarchical Context Shows Consistent Tendencies for Collaboration in the

- Middle Levels. *Proc. Natl. Acad. Sci. U. S. A.* **2010**, *107* (15), 6841–6846. https://doi.org/10.1073/PNAS.0910867107/SUPPL_FILE/PNAS.0910867107_SI.P DF.
- (19) Jothi, R.; Balaji, S.; Wuster, A.; Grochow, J. A.; Gsponer, J.; Przytycka, T. M.; Aravind, L.; Babu, M. M. Genomic Analysis Reveals a Tight Link between Transcription Factor Dynamics and Regulatory Network Architecture. *Mol. Syst. Biol.* **2009**, *5* (1), 294. https://doi.org/10.1038/MSB.2009.52.
- (20) Bar-Yam, Y.; Harmon, D.; De Bivort, B. Systems Biology: Attractors and Democratic Dynamics. *Science* (80-.). **2009**, 323 (5917), 1016–1017. https://doi.org/10.1126/SCIENCE.1163225/SUPPL_FILE/BARYAM-SOM-REV.PDF.
- (21) Ma, H. W.; Buer, J.; Zeng, A. P. Hierarchical Structure and Modules in the Escherichia Coli Transcriptional Regulatory Network Revealed by a New Top-down Approach. *BMC Bioinformatics* **2004**, *5* (1), 1–10. https://doi.org/10.1186/1471-2105-5-199/TABLES/2.
- (22) Yu, H.; Gerstein, M. Genomic Analysis of the Hierarchical Structure of Regulatory Networks. *Proc. Natl. Acad. Sci. U. S. A.* **2006**, *103* (40), 14724–14731. https://doi.org/10.1073/PNAS.0508637103/SUPPL_FILE/08637FIG12.PDF.
- (23) Abd-Rabbo, D.; Michnick, S. W. Delineating Functional Principles of the Bow Tie Structure of a Kinase-Phosphatase Network in the Budding Yeast. *BMC Syst. Biol.* **2017**, *11* (1), 1–14. https://doi.org/10.1186/S12918-017-0418-0/FIGURES/7.
- (24) Gillespie, D. T. A General Method for Numerically Simulating the Stochastic Time Evolution of Coupled Chemical Reactions. *J. Comput. Phys.* **1976**, 22 (4), 403–434. https://doi.org/10.1016/0021-9991(76)90041-3.
- (25) Jothi, R.; Balaji, S.; Wuster, A.; Grochow, J. A.; Gsponer, J.; Przytycka, T. M.; Aravind, L.; Babu, M. M. Genomic Analysis Reveals a Tight Link between Transcription Factor Dynamics and Regulatory Network Architecture. *Mol. Syst. Biol.* **2009**, *5* (1), 294. https://doi.org/10.1038/MSB.2009.52.
- (26) Belle, A.; Tanay, A.; Bitincka, L.; Shamir, R.; O'Shea, E. K. Quantification of Protein Half-Lives in the Budding Yeast Proteome. *Proc. Natl. Acad. Sci. U. S. A.*

- **2006**, *103* (35), 13004–13009. https://doi.org/10.1073/PNAS.0605420103/SUPPL_FILE/SUPPDATASET.TXT.
- (27) Cambridge, S. B.; Gnad, F.; Nguyen, C.; Bermejo, J. L.; Krüger, M.; Mann, M. Systems-Wide Proteomic Analysis in Mammalian Cells Reveals Conserved, Functional Protein Turnover. *J. Proteome Res.* **2011**, *10* (12), 5275–5284. https://doi.org/10.1021/PR101183K/SUPPL_FILE/PR101183K_SI_002.XLS.
- (28) Gillespie, D. T. Exact Stochastic Simulation of Coupled Chemical Reactions. *J. Phys. Chem.* **1977**, *81* (25), 2340–2361. https://doi.org/10.1021/J100540A008/ASSET/J100540A008.FP.PNG_V03.
- (29) Martin, O. C.; Krzywicki, A.; Zagorski, M. Drivers of Structural Features in Gene Regulatory Networks: From Biophysical Constraints to Biological Function. *Phys. Life Rev.* **2016**, *17*, 124–158. https://doi.org/10.1016/J.PLREV.2016.06.002.

CHAPTER 7

Future scope

The thesis work dealt with the investigation of noise propagation across different network motifs and how the noisy behavior influences the functionality of such networks. Various non-trivial scaling of chemical noise for different network architectures and reaction kinetics has been established. Further the effects of extrinsic noise on the heterogeneity in the bistable responses is investigated. In this chapter the future scope of the work is discussed.

A single pulsatile signal had been used to investigate the difference in the transition kinetics for a bistable system originating from two different network topologies, mutual inhibition and mutual activation in chapter 4. However, cells may experience trail of pulsatile signals or input signals in the form of decaying oscillations. Additional to conventional bistable switch, such positive feedback loop network types with slight tweaking in their architecture can lead to various non canonical responses as mentioned in chapter 5. In future, this work can be extended further with other types of input signals and network topologies with noncanonical responses.

Chapter 5 discussed the effect of extrinsic noise on the heterogeneity of bistable switches. However, in case of cellular differentiation, a growing number of studies have highlighted the possibility of a mixed state which can be explained by tristable switches. In this regard, further investigation can be carried out for similar network topologies with an additional positive feedback loops using the same automated method. New types of complex tristable switches can be expected.

In chapter 6, to simulate the generalized networks, the mass action rate law was used to model the chemical reactions involved. However, in both protein interaction and gene regulatory networks, nonlinear rate laws like the Hill function and Michaelis-Menten kinetics are frequently used to compare the mathematical predictions to the experimental

Future Scope

findings. The use of mass action kinetics allowed to accurately estimate intrinsic chemical noise by using Gillespie's SSA. Additionally, it discarded the other possibilities of nonlinear phenomena, such as multistability and oscillations. Protein interaction network modeling based on mass-action kinetics has grown significantly because of its higher accuracy to predict how intrinsic chemical noise would affect the reaction networks. In future, it will be interesting to examine how noise propagates in networks with nonlinear rate laws using approximate simulation techniques like the chemical Langevin equation.

CHAPTER 7

Future scope

The thesis work dealt with the investigation of noise propagation across different network motifs and how the noisy behavior influences the functionality of such networks. Various non-trivial scaling of chemical noise for different network architectures and reaction kinetics has been established. Further the effects of extrinsic noise on the heterogeneity in the bistable responses is investigated. In this chapter the future scope of the work is discussed.

A single pulsatile signal had been used to investigate the difference in the transition kinetics for a bistable system originating from two different network topologies, mutual inhibition and mutual activation in chapter 4. However, cells may experience trail of pulsatile signals or input signals in the form of decaying oscillations. Additional to conventional bistable switch, such positive feedback loop network types with slight tweaking in their architecture can lead to various non canonical responses as mentioned in chapter 5. In future, this work can be extended further with other types of input signals and network topologies with noncanonical responses.

Chapter 5 discussed the effect of extrinsic noise on the heterogeneity of bistable switches. However, in case of cellular differentiation, a growing number of studies have highlighted the possibility of a mixed state which can be explained by tristable switches. In this regard, further investigation can be carried out for similar network topologies with an additional positive feedback loops using the same automated method. New types of complex tristable switches can be expected.

In chapter 6, to simulate the generalized networks, the mass action rate law was used to model the chemical reactions involved. However, in both protein interaction and gene regulatory networks, nonlinear rate laws like the Hill function and Michaelis-Menten kinetics are frequently used to compare the mathematical predictions to the experimental

Future Scope

findings. The use of mass action kinetics allowed to accurately estimate intrinsic chemical noise by using Gillespie's SSA. Additionally, it discarded the other possibilities of nonlinear phenomena, such as multistability and oscillations. Protein interaction network modeling based on mass-action kinetics has grown significantly because of its higher accuracy to predict how intrinsic chemical noise would affect the reaction networks. In future, it will be interesting to examine how noise propagates in networks with nonlinear rate laws using approximate simulation techniques like the chemical Langevin equation.

Appendix

Appendix 1 (Chapter 3)

General form for the dynamical equations for the phosphorylated species involved in multi-phospho chain with N number of phospho states:

For non-terminal species
$$\frac{\partial \bar{n}_i}{\partial t} = \left(\nu_i + \nu_{-(i+1)}\right) - \left(\nu_{i+1} + \nu_{-i}\right)$$
For terminal species
$$\frac{\partial \bar{n}_N}{\partial t} = \left(\nu_N - \nu_{-N}\right)$$
A3.1

Where, v_i and v_{-i} are the phosphorylation and dephosphorylation rate of the i^{th} species.

Mass action	Michaelis Menten			
$v_i = k_i n_{i-1}$	$v_i = \frac{k_i E(n_{i-1}/K_{M_i})}{1 + \sum_{i=1}^{N} n_{i-1}/K_{M_i}}$			
$\nu_{-i} = k_{-i} n_i$	$\nu_{-i} = \frac{k_{-i}E'(n_i/K_{-M_i})}{1 + \sum_{i=0}^{N-1} n_{i+1}/K_{-M_i}}$			

Final covariance matrix equation for 4-component chain,

$$\begin{bmatrix} A_{11} & A_{12} & A_{13} & 0 & 0 & 0 \\ A_{21} & (A_{11} + A_{22}) & A_{23} & A_{12} & A_{13} & 0 \\ A_{31} & A_{32} & (A_{11} + A_{33}) & 0 & A_{12} & A_{13} \\ 0 & A_{21} & 0 & A_{22} & A_{23} & 0 \\ 0 & 0 & A_{31} & 0 & A_{32} & A_{32} \end{bmatrix} \begin{bmatrix} \sigma_{11} \\ \sigma_{12} \\ \sigma_{13} \\ \sigma_{22} \\ \sigma_{23} \\ \sigma_{33} \end{bmatrix} = \begin{bmatrix} -\frac{1}{2}(\nu_1 + \nu_2 + \nu_{-1} + \nu_{-2}) \\ (\nu_2 + \nu_{-2}) \\ 0 \\ -\frac{1}{2}(\nu_2 + \nu_3 + \nu_{-2} + \nu_{-3}) \\ (\nu_3 + \nu_{-3}) \\ -\frac{1}{2}(\nu_3 + \nu_{-3}) \end{bmatrix}$$

$$A3.3$$

Where,
$$A_{11} = \frac{\partial (\nu_1 + \nu_{-2}) - (\nu_2 + \nu_{-1})}{\partial \bar{n}_1}$$
, $A_{12} = \frac{\partial (\nu_1 + \nu_{-2}) - (\nu_2 + \nu_{-1})}{\partial \bar{n}_2}$, $A_{13} = \frac{\partial (\nu_1 + \nu_{-2}) - (\nu_2 + \nu_{-1})}{\partial \bar{n}_3}$, $A_{21} = \frac{\partial (\nu_2 + \nu_{-3}) - (\nu_3 + \nu_{-2})}{\partial \bar{n}_1}$, $A_{22} = \frac{\partial (\nu_2 + \nu_{-3}) - (\nu_3 + \nu_{-2})}{\partial \bar{n}_2}$, $A_{23} = \frac{\partial (\nu_2 + \nu_{-3}) - (\nu_3 + \nu_{-2})}{\partial \bar{n}_3}$, $A_{31} = \frac{\partial (\nu_3 + \nu_{-3})}{\partial \bar{n}_1}$, $A_{32} = \frac{\partial (\nu_3 + \nu_{-3})}{\partial \bar{n}_2}$, and $A_{33} = \frac{\partial (\nu_3 + \nu_{-3})}{\partial \bar{n}_3}$

A3.4

$-\frac{1}{2}(\nu_1+\nu_2+\nu_{-1}+\nu_{-2})$	(, , + , ,)	0	0	1	$-\frac{1}{2}(v_2+v_3+v_{-2}+v_{-3})$	$(\nu_3+\nu_{-3})$	0	$\begin{bmatrix} 1 \\(v_2 + v_3 + v_4) \end{bmatrix}$	2 (3 74 7 3 7 4	$(\nu_4 + \nu_{-4})$	$\left[\begin{array}{cc} -rac{1}{2}(u_4+ u_{-4}) \end{array} ight]$
	_	7 6	1 00	4	2	ا «	4	3	4	4٦	
	$1_{r\sigma_1}$	$0 \frac{\sigma_{11}}{\sigma_{12}}$	σ_1	σ_1	σ_2	σ_2	$\frac{\sigma_2}{\sigma_2}$	<i>σ</i> ³	3]L0 ₄	
	0	0	0	A_{14}	0	0	A_{24}	0	A_{34}	A_{44}	
	0	0	A_{14}	A_{13}	0	A_{24}	A_{23}	A_{34}	$(A_{33} + A_{44})$	A_{43}	
	0	0	A_{13}	0	0	A_{23}	0	A_{33}	A_{43}	0	
	0	A_{14}	0			A_{34}	$\overline{}$				
	0	A_{13}	A_{12}	0	A_{23}	$_{2}$ $(A_{22} + A_{33})$	A_{43}	A_{32}	A_{42}	0	
	0	A_{12}	0	0	A_{22}	A_{32}	A_{42}	0	0	0	
	A_{14}	A_{24}	A_{34}	$(A_{11} + A_{44})$	0	0	A_{21}	0	A_{31}	A_{41}	
	A_{13}	A_{23}	$(A_{11} + A_{33})$	A_{43}	0	A_{21}	0	A_{31}	A_{41}	0	
	A_{12}	$(A_{11} + A_{22})$	A_{32}	A_{42}	A_{21}	A_{31}	A_{41}	0	0	0	

 A_{11} A_{21} A_{31} A_{41} 0 0 0 0 0 0 0

Final covariance matrix equation for 5-component chain,

 $A_{22} = \frac{\partial(v_2 + v_{-3}) - (v_3 + v_{-2})}{\partial n_2}, A_{23} = \frac{\partial(v_2 + v_{-3}) - (v_3 + v_{-2})}{\partial n_2}, A_{24} = \frac{\partial(v_2 + v_{-3}) - (v_3 + v_{-2})}{\partial n_3}, A_{31} = \frac{\partial(v_3 + v_{-4}) - (v_4 + v_{-3})}{\partial n_2}, A_{32} = \frac{\partial(v_3 + v_{-4}) - (v_4 + v_{-3})}{\partial n_3}, A_{33} = \frac{\partial(v_3 + v_{-4}) - (v_4 + v_{-3})}{\partial n_3}, A_{34} = \frac{\partial(v_3 + v_{-4}) - (v_4 + v_{-3})}{\partial n_3}, A_{34} = \frac{\partial(v_3 + v_{-4}) - (v_4 + v_{-3})}{\partial n_3}, A_{34} = \frac{\partial(v_3 + v_{-4}) - (v_4 + v_{-3})}{\partial n_3}, A_{34} = \frac{\partial(v_3 + v_{-4}) - (v_4 + v_{-3})}{\partial n_3}, A_{34} = \frac{\partial(v_3 + v_{-4}) - (v_4 + v_{-3})}{\partial n_3}, A_{34} = \frac{\partial(v_3 + v_{-4}) - (v_4 + v_{-3})}{\partial n_3}, A_{34} = \frac{\partial(v_3 + v_{-4}) - (v_4 + v_{-3})}{\partial n_3}, A_{34} = \frac{\partial(v_3 + v_{-4}) - (v_4 + v_{-3})}{\partial n_3}, A_{34} = \frac{\partial(v_3 + v_{-4}) - (v_4 + v_{-3})}{\partial n_3}, A_{34} = \frac{\partial(v_3 + v_{-4}) - (v_4 + v_{-3})}{\partial n_3}, A_{34} = \frac{\partial(v_3 + v_{-4}) - (v_4 + v_{-3})}{\partial n_3}, A_{34} = \frac{\partial(v_3 + v_{-4}) - (v_4 + v_{-3})}{\partial n_3}, A_{34} = \frac{\partial(v_3 + v_{-4}) - (v_4 + v_{-3})}{\partial n_3}, A_{34} = \frac{\partial(v_3 + v_{-4}) - (v_4 + v_{-3})}{\partial n_3}, A_{34} = \frac{\partial(v_3 + v_{-4}) - (v_4 + v_{-3})}{\partial n_3}, A_{34} = \frac{\partial(v_3 + v_{-4}) - (v_4 + v_{-3})}{\partial n_3}, A_{34} = \frac{\partial(v_3 + v_{-4}) - (v_4 + v_{-3})}{\partial n_3}, A_{34} = \frac{\partial(v_3 + v_{-4}) - (v_4 + v_{-3})}{\partial n_3}, A_{34} = \frac{\partial(v_3 + v_{-4}) - (v_4 + v_{-3})}{\partial n_3}, A_{34} = \frac{\partial(v_3 + v_{-4}) - (v_4 + v_{-4})}{\partial n_3}, A_{34} = \frac{\partial(v_3 + v_{-4}) - (v_4 + v_{-4})}{\partial n_3}, A_{34} = \frac{\partial(v_3 + v_{-4}) - (v_4 + v_{-4})}{\partial n_3}, A_{34} = \frac{\partial(v_3 + v_{-4}) - (v_4 + v_{-4})}{\partial n_3}, A_{34} = \frac{\partial(v_3 + v_{-4}) - (v_4 + v_{-4})}{\partial n_3}, A_{34} = \frac{\partial(v_3 + v_{-4}) - (v_4 + v_{-4})}{\partial n_3}, A_{34} = \frac{\partial(v_3 + v_{-4}) - (v_4 + v_{-4})}{\partial n_3}, A_{34} = \frac{\partial(v_3 + v_{-4}) - (v_4 + v_{-4})}{\partial n_3}, A_{34} = \frac{\partial(v_3 + v_{-4}) - (v_4 + v_{-4})}{\partial n_3}, A_{34} = \frac{\partial(v_3 + v_{-4}) - (v_4 + v_{-4})}{\partial n_3}, A_{34} = \frac{\partial(v_3 + v_{-4}) - (v_4 + v_{-4})}{\partial n_3}, A_{34} = \frac{\partial(v_3 + v_{-4}) - (v_4 + v_{-4})}{\partial n_3}, A_{34} = \frac{\partial(v_3 + v_{-4}) - (v_4 + v_{-4})}{\partial n_3}, A_{34} = \frac{\partial(v_3 + v_{-4}) - ($ Where, $A_{11} = \frac{\partial (v_1 + v_{-2}) - (v_2 + v_{-1})}{\partial \overline{n}_1}$, $A_{12} = \frac{\partial (v_1 + v_{-2}) - (v_2 + v_{-1})}{\partial \overline{n}_2}$, $A_{13} = \frac{\partial (v_1 + v_{-2}) - (v_2 + v_{-1})}{\partial \overline{n}_2}$, $A_{14} = \frac{\partial (v_1 + v_{-2}) - (v_2 + v_{-1})}{\partial \overline{n}_1}$, $A_{21} = \frac{\partial (v_2 + v_{-3}) - (v_3 + v_{-2})}{\partial \overline{n}_2}$, $\frac{-22}{\partial (v_3 + v_4) - (v_4 + v_{-3})}, \quad A_{34} = \frac{\partial (v_3 + v_{-4}) - (v_4 + v_{-3})}{\partial \bar{n}_4}, \quad A_{41} = \frac{\partial (v_4 - v_{-4})}{\partial \bar{n}_1}, \quad A_{42} = \frac{\partial (v_4 - v_{-4})}{\partial \bar{n}_2}, \quad A_{43} = \frac{\partial (v_4 - v_{-4})}{\partial \bar{n}_3}, \quad A_{44} = \frac{\partial (v_4 - v_{-4})}{\partial \bar{n}_4}, \quad A_{45} = \frac{\partial (v_4 - v_{-4})}{\partial \bar{n}_3}, \quad A_{44} = \frac{\partial (v_4 - v_{-4})}{\partial \bar{n}_4}$

Appendix 2 (Chapter 4)

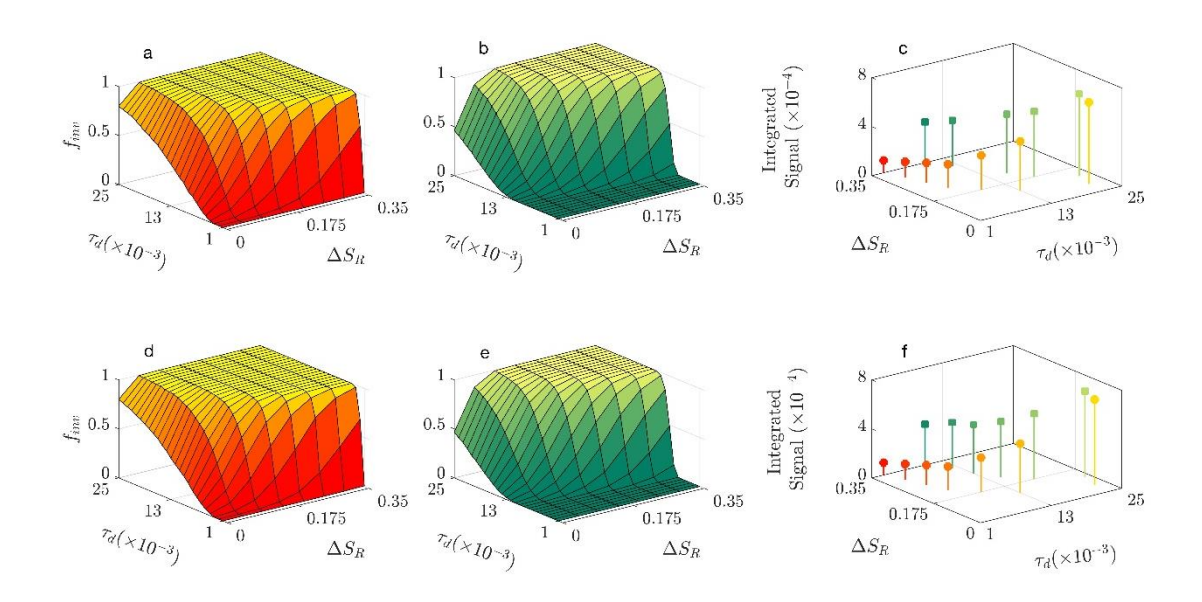


Figure A4.1: Effect of resting pulse on the population inversion. The plot of f_{inv} as a function pulse duration (τ_d) and pulse dose (ΔS_R) for the MI (first column) and MA (second column) networks for two different doses of resting pulse ($\Delta S_L = 0.05$ top row, and $\Delta S_L = 0.1$, bottom row). The integrated signal required for 99% population inversion is plotted as a function of τ_d and ΔS_R for two different values of resting pulse (c & f) in the MI (circles) and MA (squares) networks.

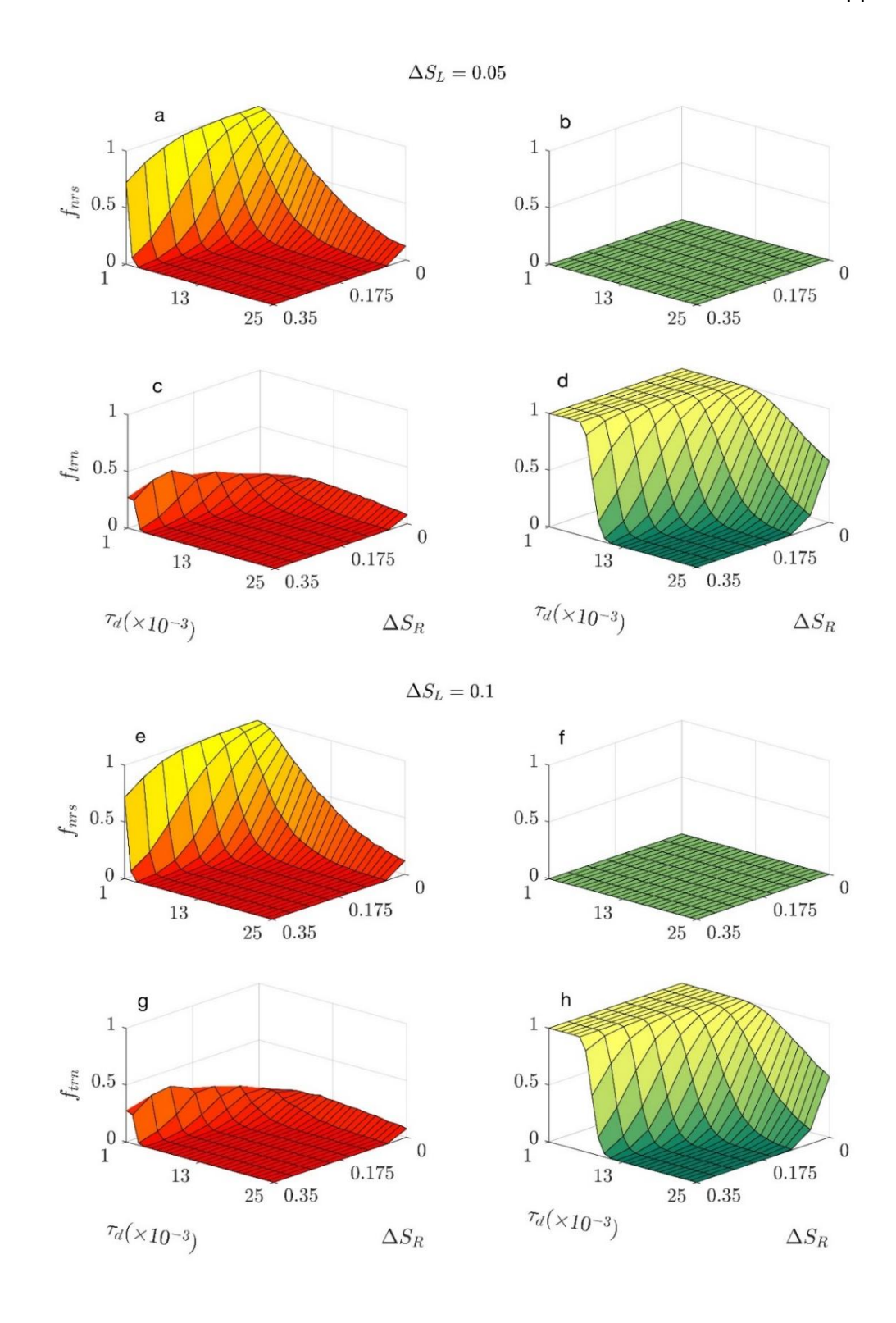


Figure A4.2: Effect of resting pulse on the transient dynamics. f_{nrs} and f_{trn} are plotted as a function of τ_d and ΔS_R for the MI (a, c, e and f) and MA (b, d, f and h) networks for different values of resting pulse, $\Delta S_L = 0.05$ (a-d) and $\Delta S_L = 0.1$ (e-h).

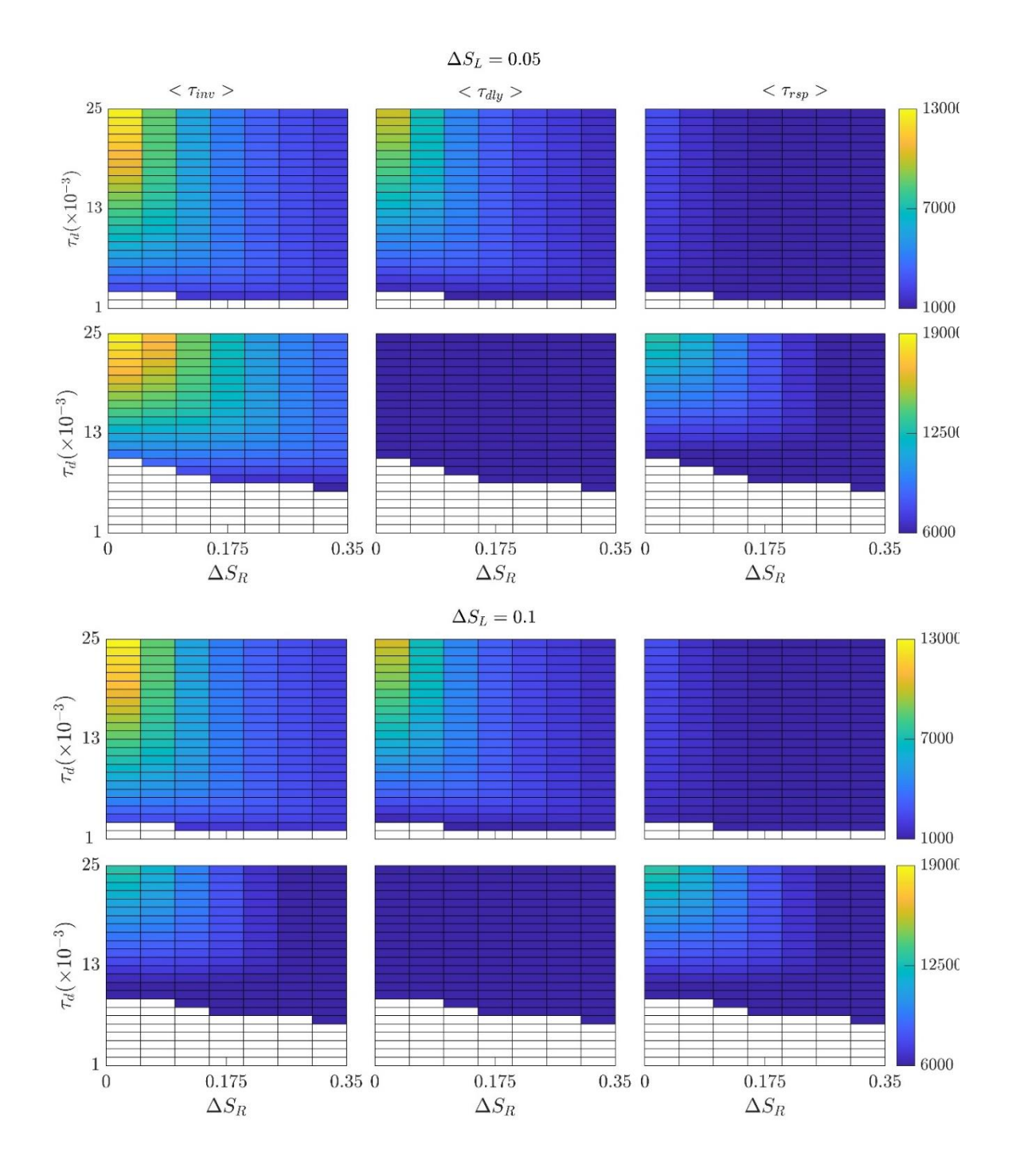


Figure A4.3: Effect of resting pulse on the time scales of population inversion. The surface plots of average inversion time $(\langle \tau_{inv} \rangle)$, average response time $(\langle \tau_{rsp} \rangle)$ and average initial delay time $(\langle \tau_{aly} \rangle)$ are presented as a function of τ_d and ΔS_R for the MI (1st and 3rd rows) and MA (2nd and 4th rows) networks at two different values of ΔS_L .

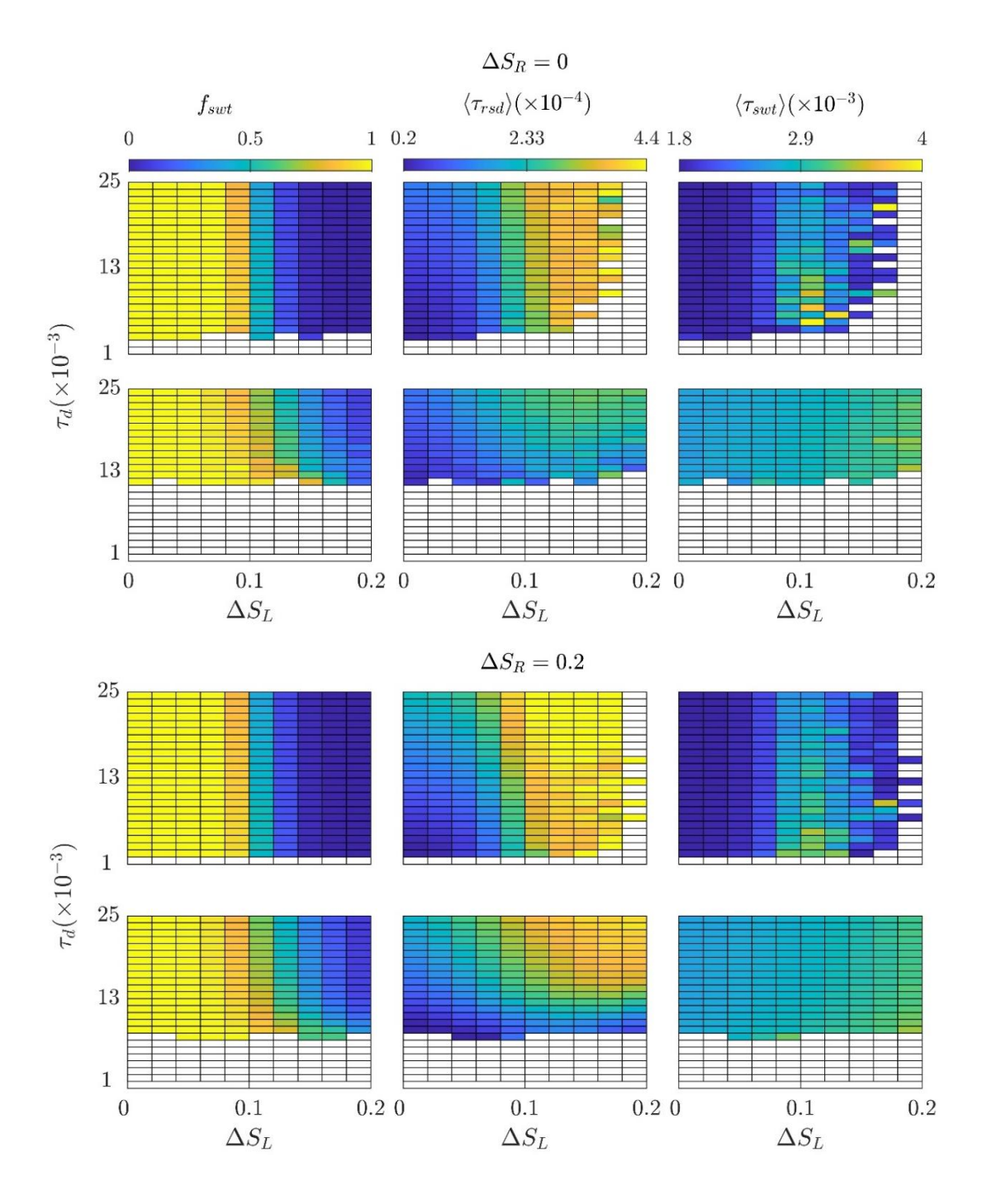


Figure A4.4: Effect of pulse amplitude on residence and switching times. The fraction of the population that switches back to the upper steady state (f_{swt}) , the average residence time in the lower steady state $(\langle \tau_{rsd} \rangle)$ and the average switching time $(\langle \tau_{swt} \rangle)$ are plotted as a function of pulse duration (τ_d) and resting pulse (ΔS_L) for the MI $(1^{st}$ and 3^{rd} rows) and MA $(2^{nd}$ and 4^{th} rows) networks. The values of the ΔS_R were 0.0 and 0.2.

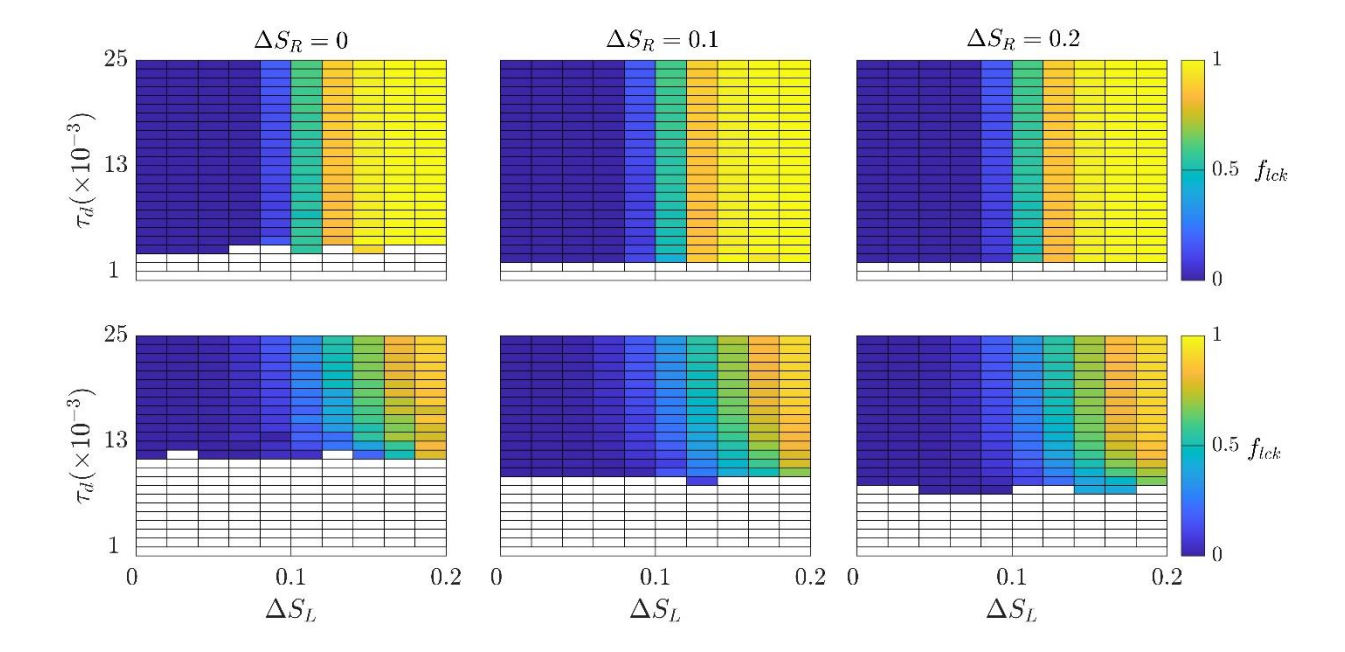


Figure A4.5: The effect of pulse amplitude on the population locked in the inverted state. Fraction of cells locked at lower steady state, f_{lck} is plotted as a function of pulse duration (τ_d) and resting pulse (ΔS_L) for the MI (top row) and MA (bottom row) networks for the indicated values of pulse amplitude.

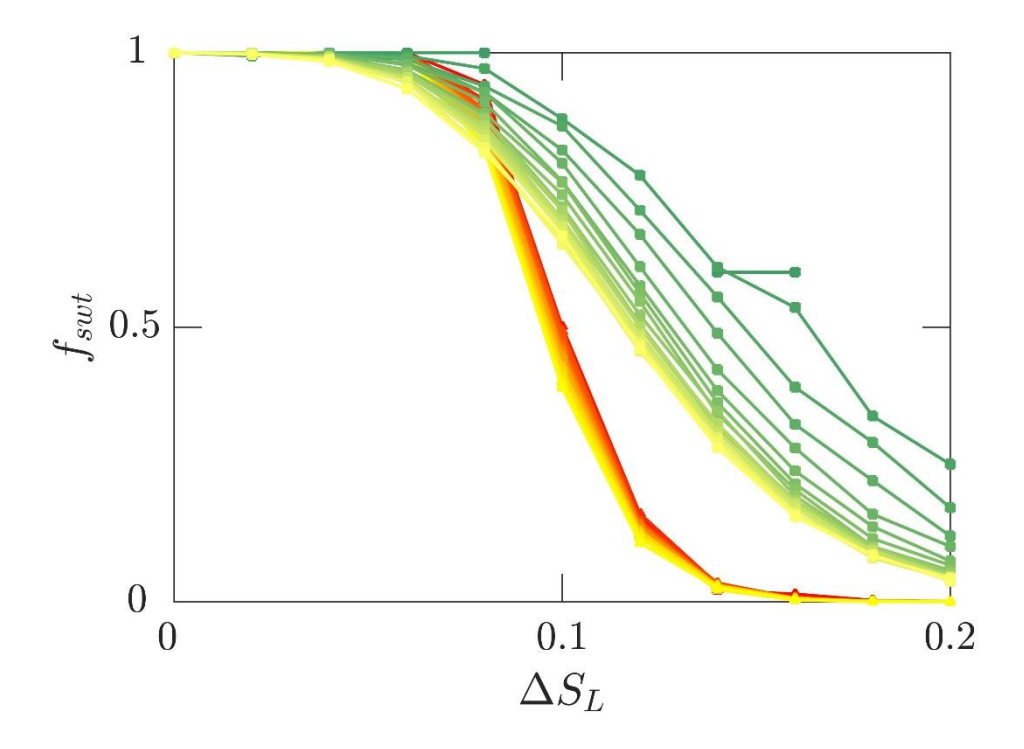


Figure A4.6. The fraction of the population that switches back to the upper steady state (f_{swt}) is plotted as a function of resting pulse (ΔS_L) for increasing values of pulse duration, τ_d , in case of MI (red to yellow) and MA (green to yellow) networks. The value of the ΔS_R was 0.2.

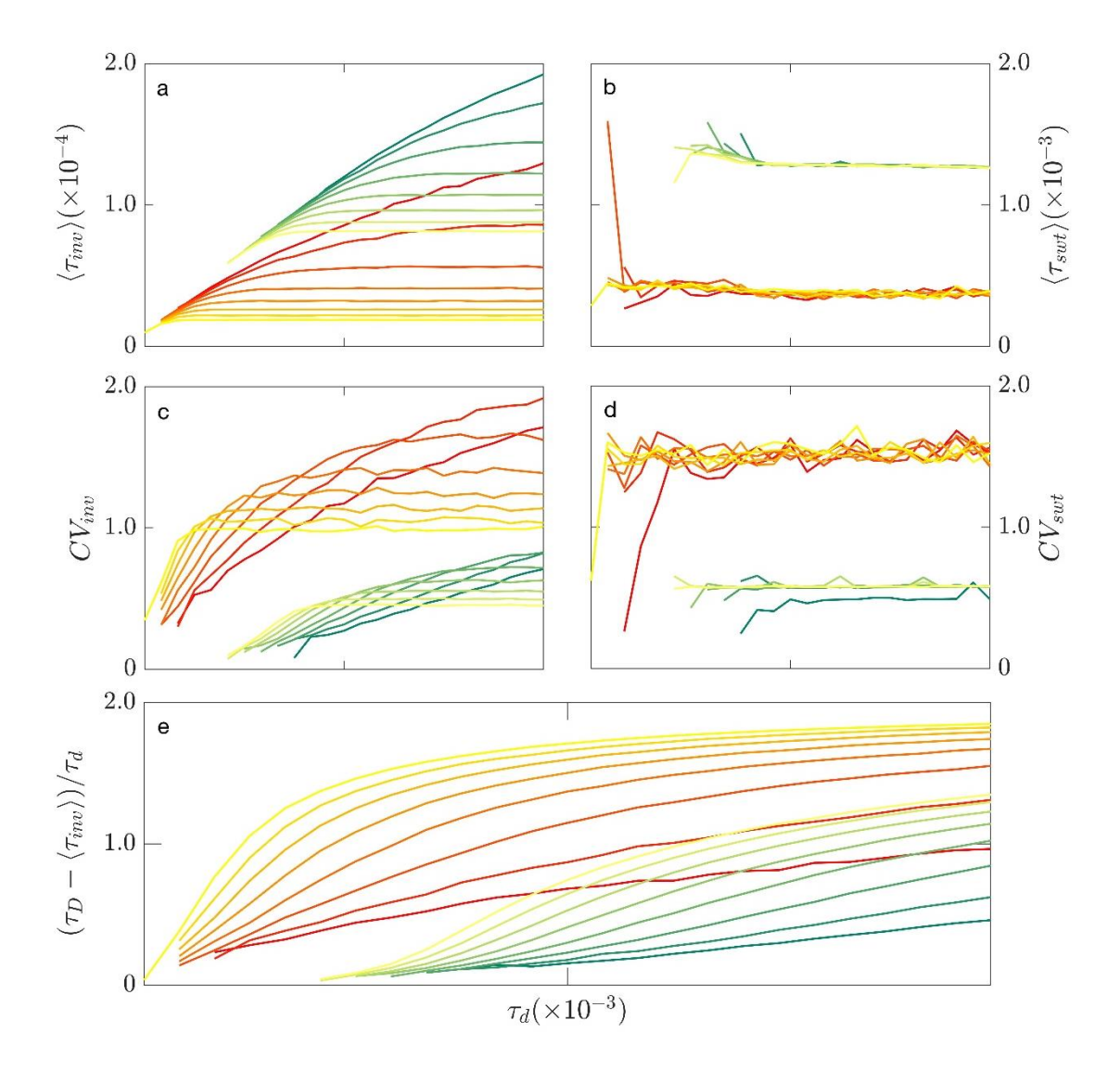


Figure A4.7: The comparison of statistical properties of inversion and switching times between the MI and MA networks for different values of pulse dose (a-d). The comparison of relative available time vs. τ_d between the MI and MA networks. Different colors represent different value of dose (ΔS_R) following an increasing trend of red to yellow for the MI and green to yellow for the MA.

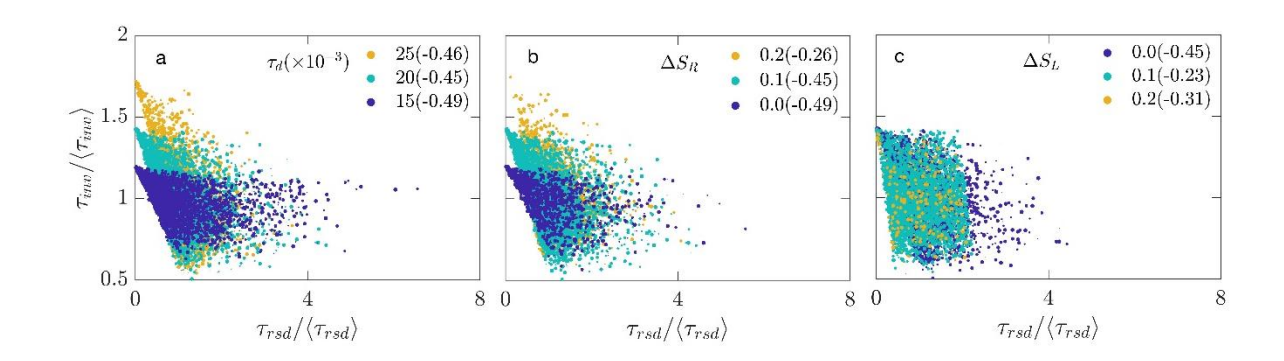


Figure A4.8: The correlation between the mean-normalized τ_{inv} and τ_{rsd} times are plotted for the indicated values of pulse duration (a), pulse dose (b) and resting pulse (c) for the MA network. The values of correlation coefficients are indicated within the parenthesis inside each plot.

Appendix 3 (Chapter 5)

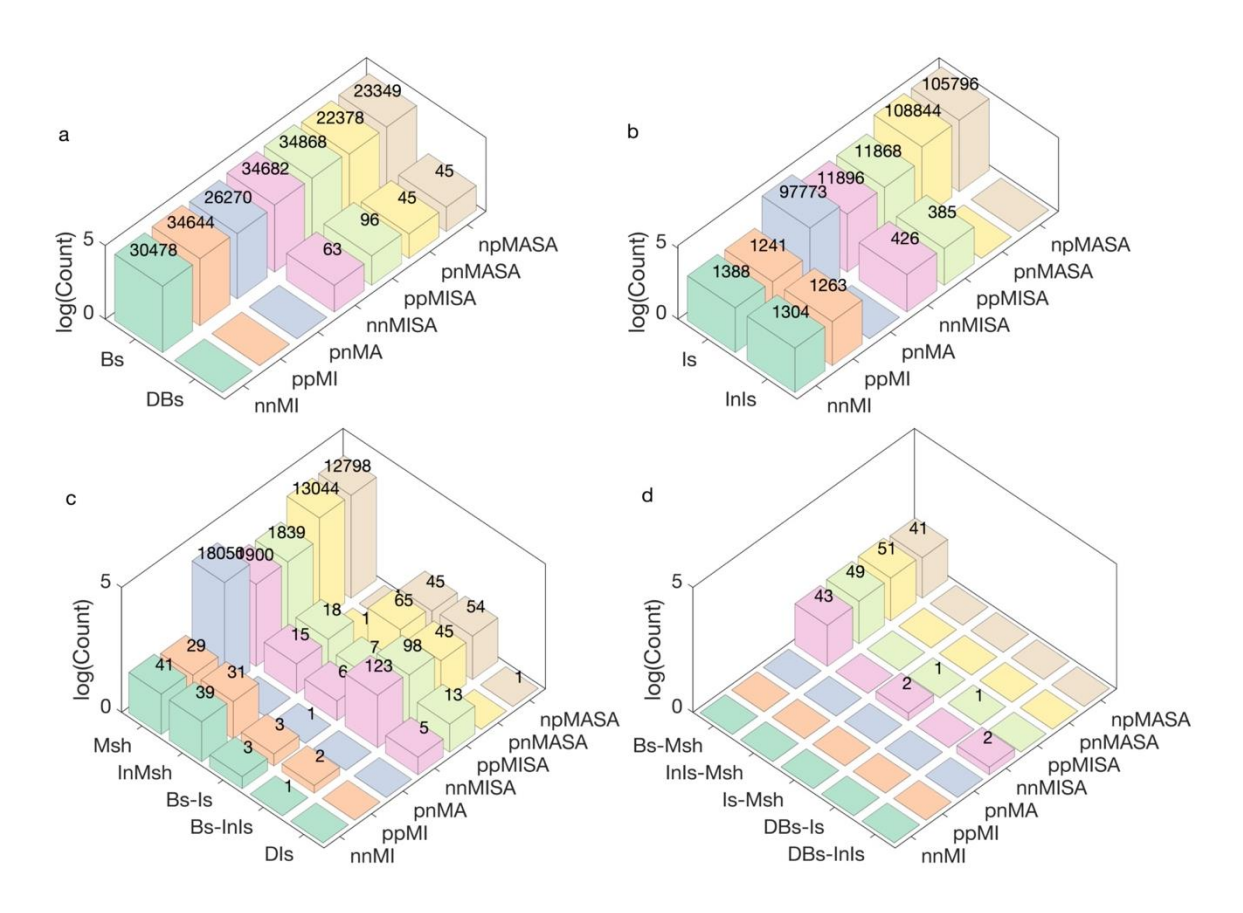


Figure A5.1: The total number of various types of canonical (a) and noncanonical (b-d) bistable switches are presented for the 1-PFL and 2-PFL networks under AND-gate configuration. The noncanonical switches are segregated into one (b), two (c) and three (d) bistable regions.

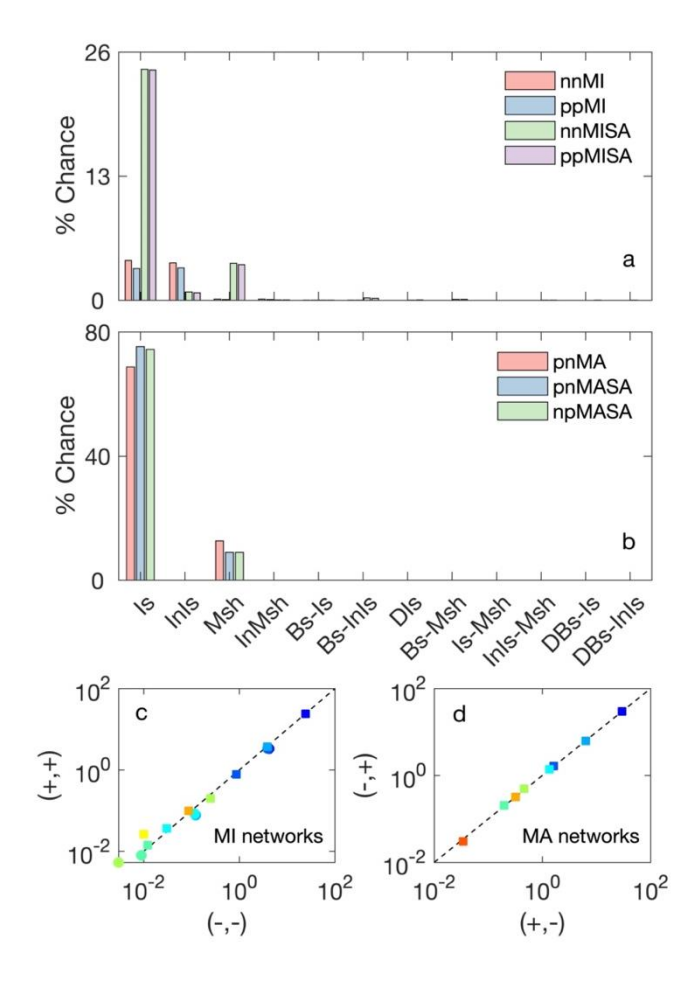


Figure A5.2: Percentage chance (% Chance) of obtaining various types of noncanonical bistable switches are compared for the MI (a) and MA (b) networks under AND-gate configuration. The correlation of % Chance of noncanonical switches of MI networks (circle: 1-MA, square: 2-MA) under (+,+) input signal with (-,-) input signal (c). Similar correlation for the 2-MA MA networks (d).

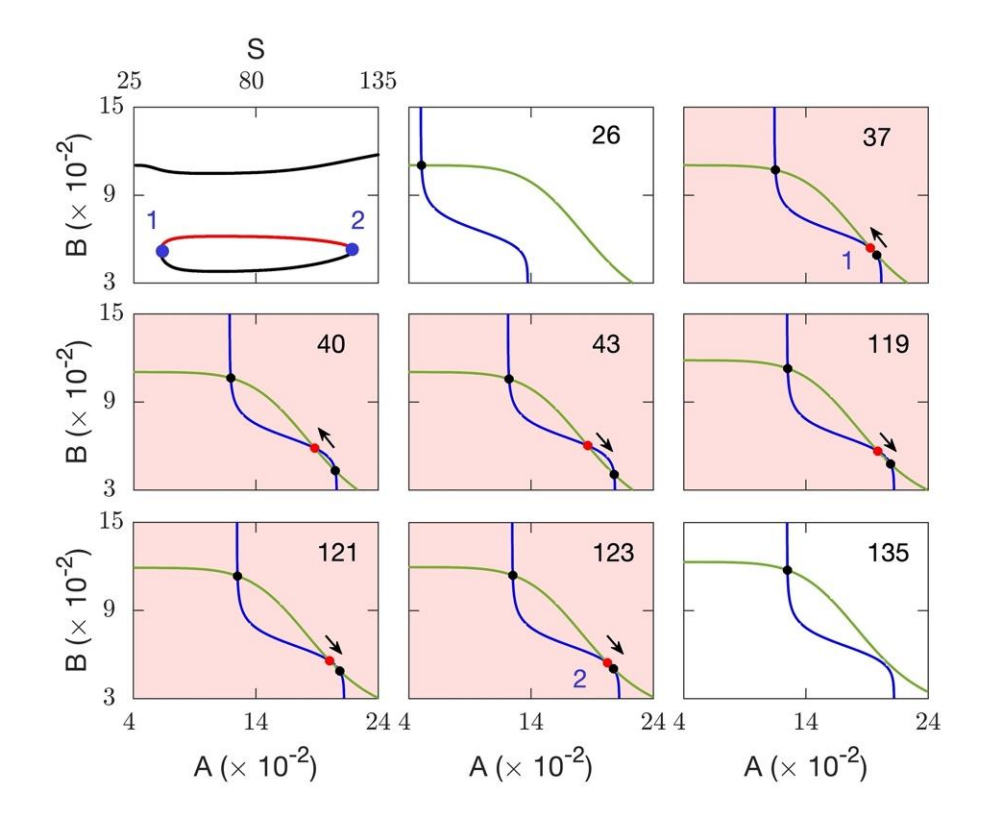


Figure A5.3: The inverted isola bifurcation and its phase-plane plots for the indicated values of S for the ppMI network under OR-gate. The two SN bifurcation points are indicated by the filled blue circles. The black and red circles at the intersections of two nullclines indicate the stable and unstable nodes, respectively. Parameters for the InIs switch are listed in Table the S5.

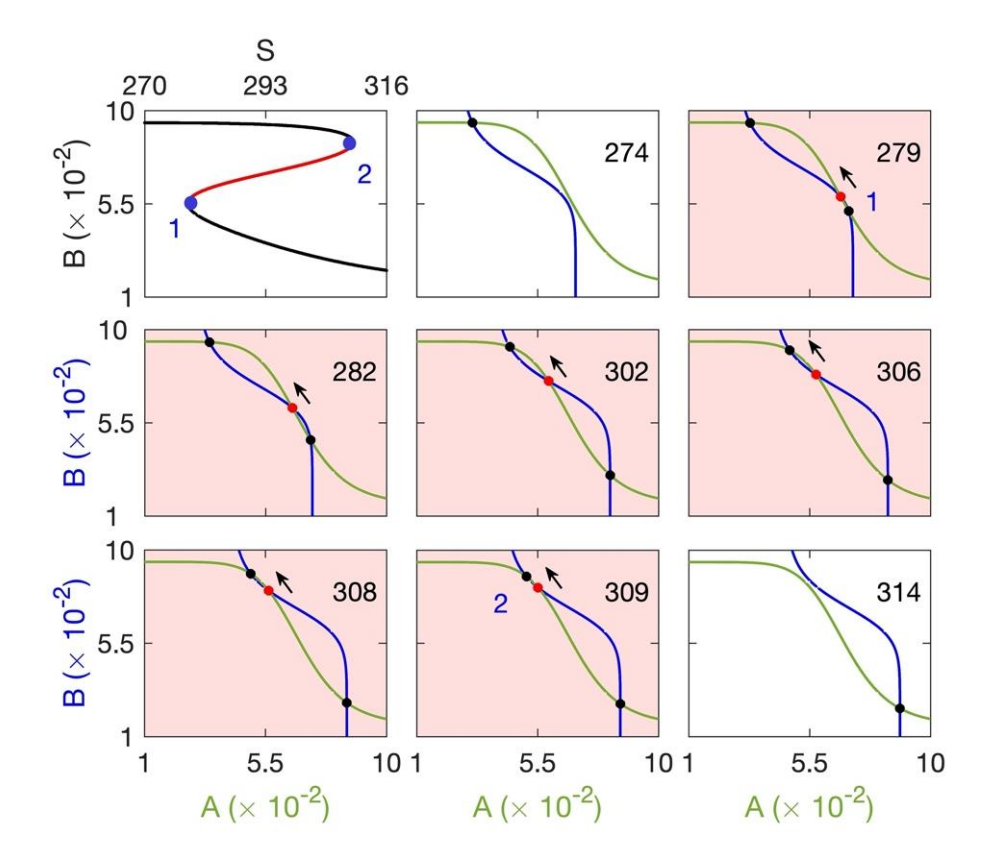


Figure A5.4: The bifurcation diagram of canonical bistable switch and its phase-plane plots for the indicated values of S for the ppMI network under OR-gate. The unstable node (red dot) originates with one stable node (black dot) and merges with another stable node leading to two SN bifurcation points. Parameters are listed in the Table S5.

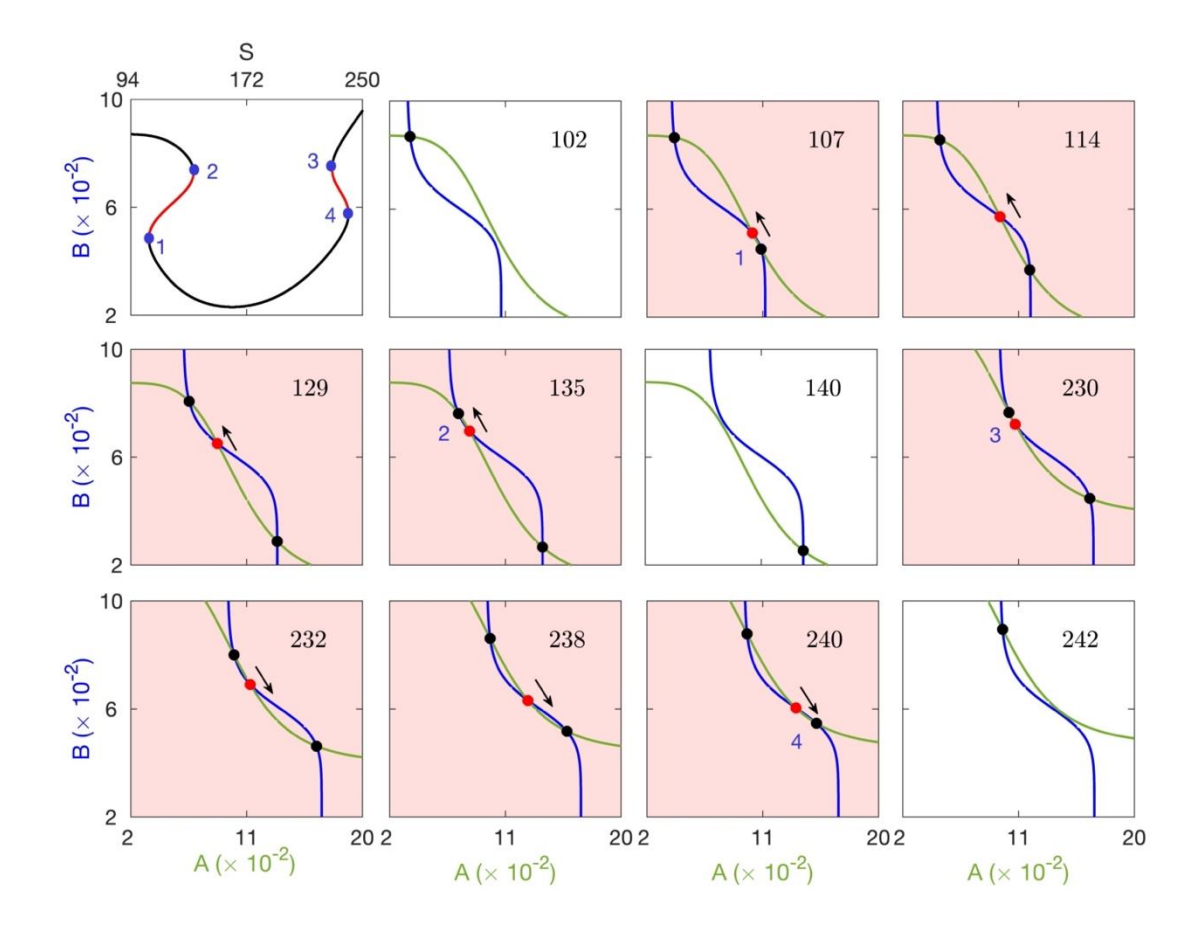


Figure A5.5: The inverted mushroom bifurcation and phase-plane plots for the indicated values of S for the ppMI network with OR-gate configuration. Parameters are listed in the Table S5.

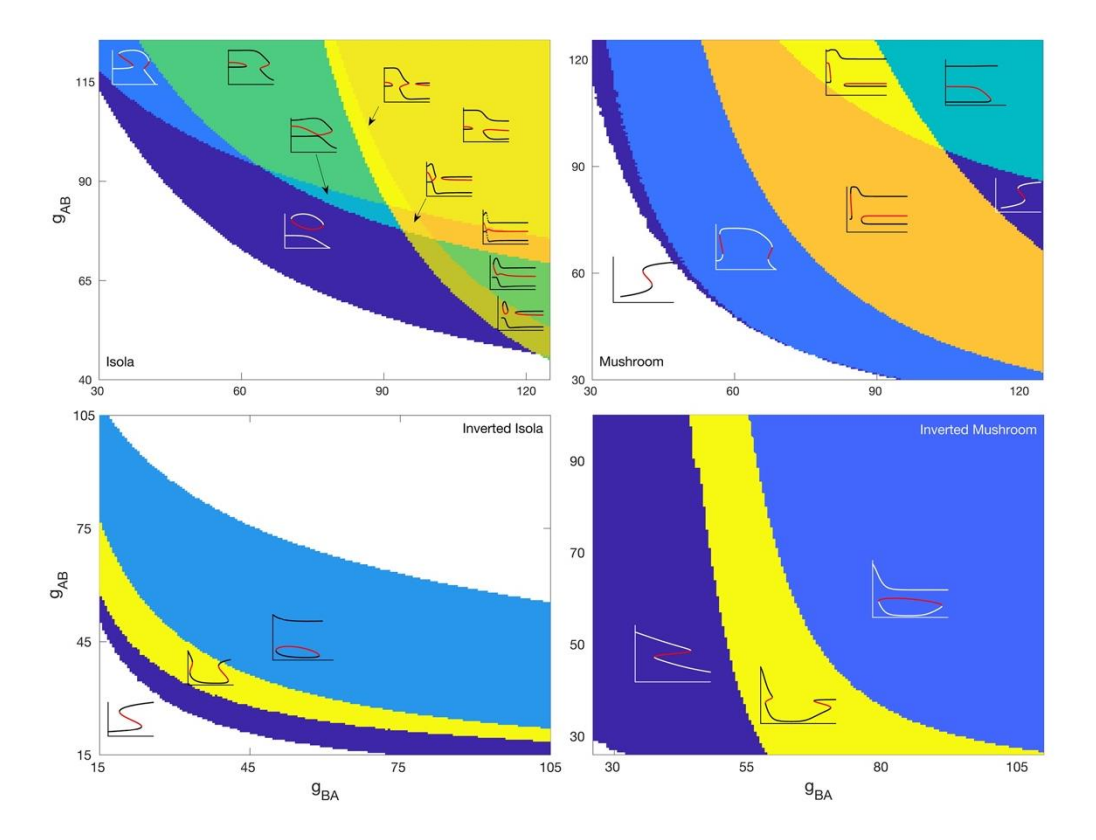


Figure A5.6: Phase diagrams in the pnMA network under OR-gate configuration. The initial phases are indicated within each phase diagrams. The parameters for the initial phases are listed in the Table S9.

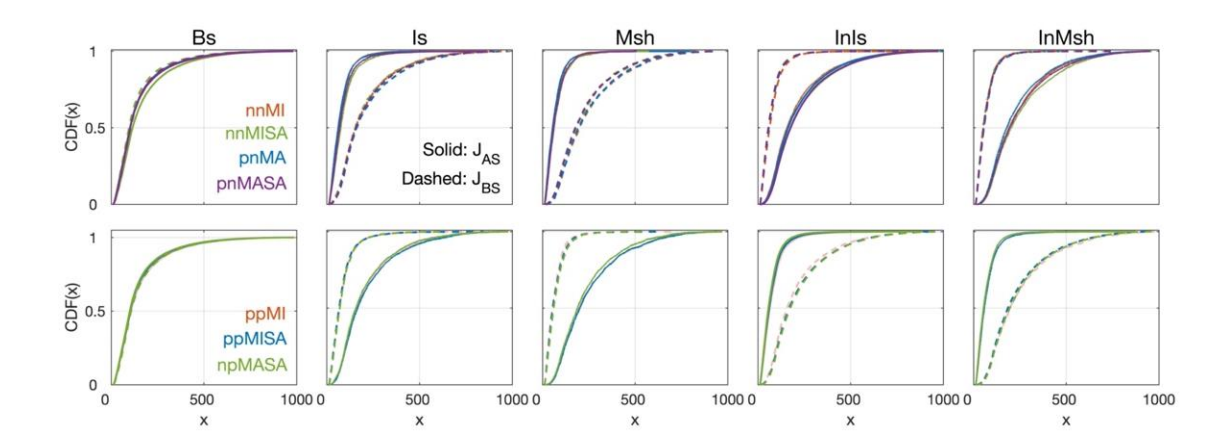
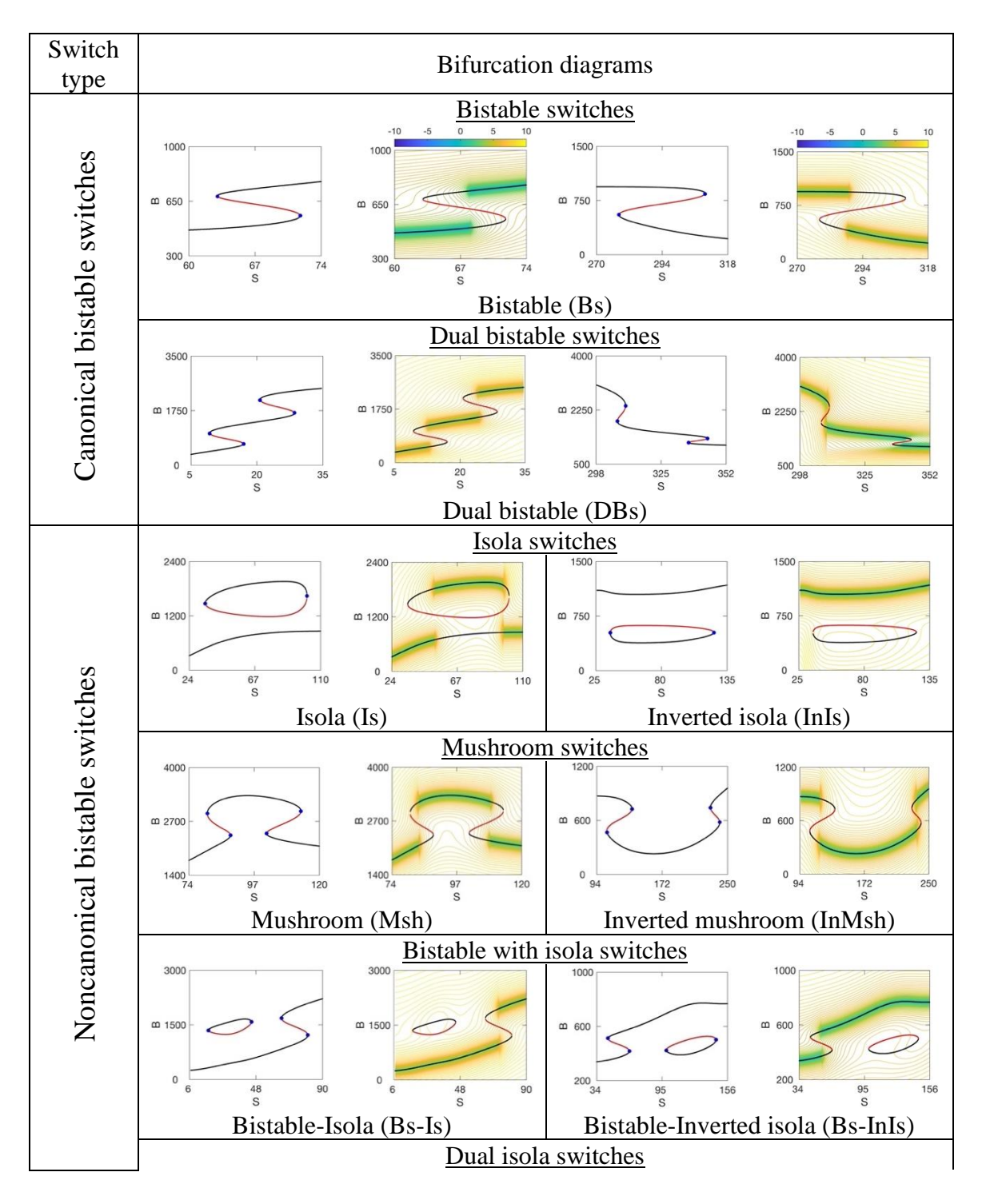


Figure A5.7: Cumulative distribution function (CDF) plots of the parameters J_{AS} and J_{BS} for different switches obtained from various networks. The resultant regulatory signs of S to B for the networks in the top and bottom rows are (+,-) and (-,+), respectively.

Table A5.1: One-parameter bifurcation diagrams of canonical and noncanonical bistable switches. In the bifurcation diagrams the stable and unstable branches are indicated by the black and red lines, respectively. The solid circles indicate the saddle-node bifurcation point. The overlaid plot of the potential energy contours and bifurcation diagram is presented adjacent to the respective bifurcation diagram. The potential energy was obtained by integrating the effective force (for example Eq.(8) for the ppMI network) and the bifurcation diagrams were generated from the potential energy. These bifurcation diagrams were obtained from the ppMI and ppMISA networks and the parameters are listed in the Table S5 and Table S6.



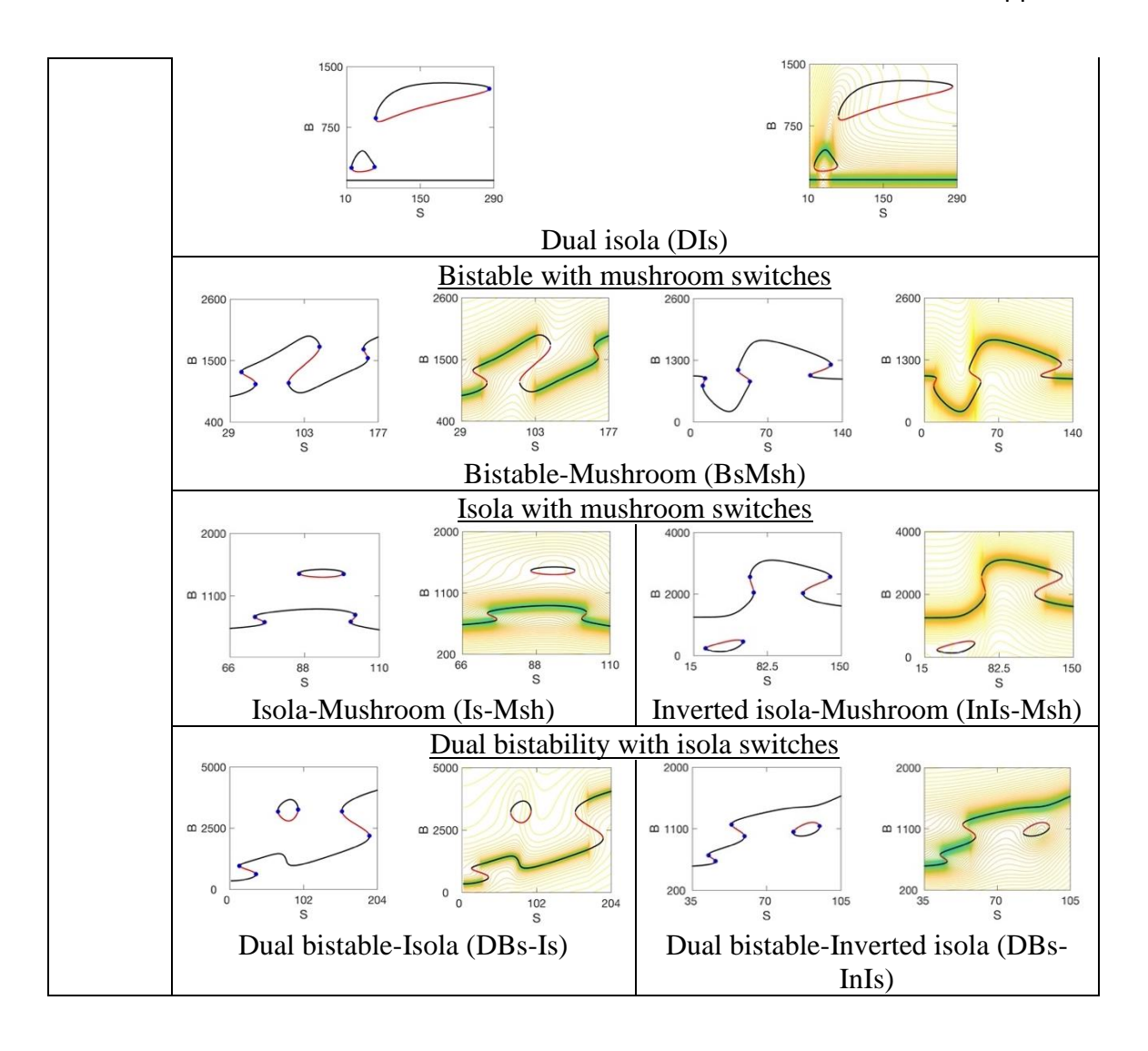


Table A5.2: The dynamical equations for all the networks in OR- and AND-gate configurations.

Network	OR-gate	AND-gate
nnMI	dA	41
	$\frac{dH}{dt} = g_{A0} + g_{AS}H_{AS}^{-} + g_{AB}H_{AB}^{-} - \gamma_A A$	$\begin{vmatrix} \frac{dA}{dt} = g_{A0} + g_{A1}H_{AS}^-H_{AB}^ \gamma_A A \\ dB \end{vmatrix}$
	$\frac{dB}{dt} = g_{B0} + g_{BS}H_{BS}^{-} + g_{BA}H_{BA}^{-} - \gamma_{b}B$	$\frac{dB}{dt} = g_{B0} + g_{B1}H_{BS}^{-}H_{BA}^{-} - \gamma_{b}B$
	$dt = g_{B0} + g_{BS} + g_{BA} + g_{BA} + g_{BA}$	ut
pnMI	dA	$\frac{dA}{dt} = g_{A0} + g_{A1}H_{AS}^{+}H_{AB}^{-} - \gamma_{A}A$
	$\frac{dA}{dt} = g_{A0} + g_{AS}H_{AS}^{+} + g_{AB}H_{AB}^{-} - \gamma_{A}A$	AD.
	$\left \frac{dB}{dt} \right = g_{B0} + g_{BS}H_{BS}^{-} + g_{BA}H_{BA}^{-} - \gamma_b B$	$\frac{dB}{dt} = g_{B0} + g_{B1}H_{BS}^{-}H_{BA}^{-} - \gamma_{b}B$
MI	at	44
ppMI	$\frac{dA}{dA} = a \cdot \cdot + a \cdot \cdot H^{+} + a \cdot \cdot H^{-} = v \cdot A$	$\frac{dA}{dt} = g_{A0} + g_{A1}H_{AS}^{+}H_{AB}^{-} - \gamma_{A}A$
	$\frac{dH}{dt} = g_{A0} + g_{AS}H_{AS}^{+} + g_{AB}H_{AB}^{-} - \gamma_{A}A$ dB	AD.
	$\frac{dB}{dt} = g_{B0} + g_{BS}H_{BS}^{+} + g_{BA}H_{BA}^{-} - \gamma_{b}B$	$\frac{dB}{dt} = g_{B0} + g_{B1}H_{BS}^{+}H_{BA}^{-} - \gamma_b B$
nnMA		dA
	$\left \frac{dA}{dt} = g_{A0} + g_{AS}H_{AS}^{-} + g_{AB}H_{AB}^{+} - \gamma_{A}A \right $	$\frac{dA}{dt} = g_{A0} + g_{A1}H_{AS}^-H_{AB}^+ - \gamma_A A$
	дR	$\frac{dB}{dt} = g_{B0} + g_{B1}H_{BS}^{-}H_{BA}^{+} - \gamma_b B$
	$\frac{dB}{dt} = g_{B0} + g_{BS}H_{BS}^{-} + g_{BA}H_{BA}^{+} - \gamma_{b}B$	dt dt db db bi bi bi
pnMA	dA	$\frac{dA}{dt} = g_{A0} + g_{A1}H_{AS}^{+}H_{AB}^{+} - \gamma_{A}A$
	$\frac{dA}{dt} = g_{A0} + g_{AS}H_{AS}^{+} + g_{AB}H_{AB}^{+} - \gamma_{A}A$	dR
	$\left \frac{dB}{dt} \right = g_{B0} + g_{BS}H_{BS}^{-} + g_{BA}H_{BA}^{+} - \gamma_{b}B$	$\frac{dB}{dt} = g_{A0} + g_{B1}H_{BS}^{-}H_{BA}^{+} - \gamma_{b}B$
ppMA	$\frac{dA}{dt} = g_{A0} + g_{AS}H_{AS}^{+} + g_{AB}H_{AB}^{+} - \gamma_{A}A$	$\frac{dA}{dt} = g_{A0} + g_{A1}H_{AS}^{+}H_{AB}^{+} - \gamma_{A}A$
	d D	1 J D
) ATC A	$\frac{dB}{dt} = g_{B0} + g_{bs}H_{BS}^{+} + g_{BA}H_{BA}^{+} - \gamma_b B$	$\frac{dB}{dt} = g_{B0} + g_{B1}H_{BS}^{+}H_{BA}^{+} - \gamma_b B$
nnMISA	$\frac{dA}{dA} = a \cdot a + a \cdot a + a \cdot b + $	$\frac{dA}{dt} = g_{A0} + g_{A1}H_{AS}^{-}H_{AB}^{-} - \gamma_{A}A$
	$\frac{dt}{dt} = g_{A0} + g_{AS}H_{AS}^{-} + g_{AB}H_{AB}^{-} - \gamma_A A$ dB	1 dB
	$\frac{dB}{dt} = g_{B0} + g_{BS}H_{BS}^{-} + g_{BA}H_{BA}^{-}$	$\frac{dS}{dt} = g_{B0} + g_{B1}H_{BS}^{-}H_{BA}^{-}H_{BB}^{+}$
	$+ g_{BB}H_{BB}^+ - \gamma_b B$	$-\gamma_b B$
pnMISA	dA .	$\frac{dA}{dt} = g_{A0} + g_{A1}H_{AS}^{+}H_{AB}^{-} - \gamma_{A}A$
	$\frac{dH}{dt} = g_{A0} + g_{AS}H_{AS}^{+} + g_{AB}H_{AB}^{-} - \gamma_{A}A$	$ dt = \frac{-y_{A0} + y_{A1} + y_{A1}}{dR} $
	$\left \frac{dB}{dt} \right = g_{B0} + g_{BS}H_{BS}^{-} + g_{BA}H_{BA}^{-}$	$\frac{dB}{dt} = g_{B0} + g_{B1}H_{BS}^{-}H_{BA}^{-}H_{BB}^{+}$
	$ \begin{vmatrix} dt & g_{BB} & g_{BB} & g_{BB} \\ + g_{BB} H_{BB}^+ - \gamma_b B \end{vmatrix} $	$-\gamma_b B$
npMISA	d A	dA
припол	$\frac{dA}{dt} = g_{A0} + g_{AS}H_{AS}^{-} + g_{AB}H_{AB}^{-} - \gamma_{A}A$	$\frac{1}{dt} = g_{A0} + g_{A1}H_{AS}^{-}H_{AB}^{-} - \gamma_A A$
	$\frac{dB}{dt} = g_{B0} + g_{BS}H_{BS}^{+} + g_{BA}H_{BA}^{-}$	$\frac{dB}{dt} = g_{B0} + g_{B1}H_{BS}^{+}H_{BA}^{-}H_{BB}^{+}$
	$ dt + g_{BB}H_{BB}^+ - \gamma_b B $	$\begin{array}{c c} dt & {}^{g_{B0}} \cdot {}^{g_{B1}} \cdot {}^{g_{B3}} \cdot {}^{g_{B4}} \cdot {}^{g_{B4}} \\ & - \gamma_b B \end{array}$
<u> </u>	. <u>ARR., RR 10 p</u>	100

ppMISA	$\frac{dA}{dt} = g_{A0} + g_{AS}H_{AS}^{+} + g_{AB}H_{AB}^{-} - \gamma_{A}A$ $\frac{dB}{dt} = g_{B0} + g_{BS}H_{BS}^{+} + g_{BA}H_{BA}^{-}$ $+ g_{BB}H_{BB}^{+} - \gamma_{b}B$	$\frac{dA}{dt} = g_{A0} + g_{A1}H_{AS}^{+}H_{AB}^{-} - \gamma_{A}A$ $\frac{dB}{dt} = g_{B0} + g_{B1}H_{BS}^{+}H_{BA}^{-}H_{BB}^{+}$ $-\gamma_{b}B$
nnMASA	$\frac{dA}{dt} = g_{A0} + g_{AS}H_{AS}^{-} + g_{AB}H_{AB}^{+} - \gamma_{A}A$ $\frac{dB}{dt} = g_{B0} + g_{BS}H_{BS}^{-} + g_{BA}H_{BA}^{+}$ $+ g_{BB}H_{BB}^{+} - \gamma_{b}B$	$\frac{dA}{dt} = g_{A0} + g_{A1}H_{AS}^{-}H_{AB}^{+} - \gamma_{A}A$ $\frac{dB}{dt} = g_{B0} + g_{B1}H_{BS}^{-}H_{BA}^{+}H_{BB}^{+}$ $-\gamma_{b}B$
pnMASA	$\frac{dA}{dt} = g_{A0} + g_{AS}H_{AS}^{+} + g_{AB}H_{AB}^{+} - \gamma_{A}A$ $\frac{dB}{dt} = g_{B0} + g_{BS}H_{BS}^{-} + g_{BA}H_{BA}^{+}$ $+ g_{BB}H_{BB}^{+} - \gamma_{b}B$	$\frac{dA}{dt} = g_{A0} + g_{A1}H_{AS}^{+}H_{AB}^{+} - \gamma_{A}A$ $\frac{dB}{dt} = g_{B0} + g_{B1}H_{BS}^{-}H_{BA}^{+}H_{BB}^{+}$ $-\gamma_{b}B$
npMASA	$\frac{dA}{dt} = g_{A0} + g_{AS}H_{AS}^{-} + g_{AB}H_{AB}^{+} - \gamma_{A}A$ $\frac{dB}{dt} = g_{B0} + g_{BS}H_{BS}^{+} + g_{BA}H_{BA}^{+}$ $+ g_{BB}H_{BB}^{+} - \gamma_{b}B$	$\frac{dA}{dt} = g_{A0} + g_{A1}H_{AS}^{-}H_{AB}^{+} - \gamma_{A}A$ $\frac{dB}{dt} = g_{B0} + g_{B1}H_{BS}^{+}H_{BA}^{+}H_{BB}^{+}$ $-\gamma_{b}B$
ppMASA	$\frac{dA}{dt} = g_{A0} + g_{AS}H_{AS}^{+} + g_{AB}H_{AB}^{+} - \gamma_{A}A$ $\frac{dB}{dt} = g_{B0} + g_{BS}H_{BS}^{+} + g_{BA}H_{BA}^{+}$ $+ g_{BB}H_{BB}^{+} - \gamma_{b}B$	$\frac{dA}{dt} = g_{A0} + g_{A1}H_{AS}^{+}H_{AB}^{+} - \gamma_{A}A$ $\frac{dB}{dt} = g_{B0} + g_{B1}H_{BS}^{+}H_{BA}^{+}H_{BB}^{+}$ $-\gamma_{b}B$

Table A5.3: Parameters and their chosen ranges. Parameters were sampled from independent uniform distributions with the mentioned ranges.

Parameters	Parameter types	Range		
$g_{ m A0}$ and $g_{ m B0}$	Basal synthesis rates	1-10		
$g_{\mathrm{AS}}, g_{\mathrm{BS}}, g_{\mathrm{AB}}, g_{\mathrm{BA}}, g_{\mathrm{BB}}$	Maximal synthesis rates	1-100		
1 1 1 1	Thresholds of			
$J_{AS}, J_{BS}, J_{AB}, J_{BA}, J_{BB}$	activation/inhibition	Using half-functional rule		
$n_{\mathrm{AS}}, n_{\mathrm{BS}}, n_{\mathrm{AB}}, n_{\mathrm{BA}}, n_{\mathrm{BB}}$	$n_{\rm AS}, n_{\rm BS}, n_{\rm AB}, n_{\rm BA}, n_{\rm BB}$ Hill coefficients			
$\gamma_{ m A}$ and $\gamma_{ m B}$	Degradation rates	0.01-0.1		

Table A5.4: Jump pattern of the stable branch at the bifurcation points of reversible canonical and noncanonical switches. The upward and downward jumps are represented by + and - sings, respectively.

Switch type	Number of Saddle node points (N)	Number of Jumps (J)	Bistable switches					
witches	N=2	J=1	Pc (1)	Po ()				
Canonical Switches	N=4	J=2	Bs (+) DBs (+,+)	Bs (-) DBs (-,-)				
	N=2	J=0		[s				
	N=2	J=2	InIs (-,+)					
al Switches		J=2	Msh (+,-)	InMsh (-,+)				
Noncanonical Switches	N_4	J=1		(s (+)				
	N=4	J=3						
		J=0	Bs-InIs (+,-,+) DIs					

		J=2	Is-Msh (+,-)				
	N=6	J=4	InIs-InMsh (-,-,+,+)				
		J=3	51 7 7				
		J=2	Bs-Msh (+,-,+) Bs-Msh (-,+,-) DBs-Is (+,+)				
		J=4	DBs-Is (+,+,-,+)				

Table A5.5: Parameters for different switches from the ppMI network under OR-gate. These parameters are relevant for the representative bifurcation diagrams in the Figure 1d and Table A5.1; phase-plane analysis in Figure 5.5-6 and A5.3-5 Figures; phase diagrams in Figure 5.7a, Figure 5.8a, Figure 5.9a, Figure 5.9e and Figure 5.11.

Parameters	Bistable (left diagram)	Bistable (right diagram)	Isola	Inverted Isola	Mushroom	Inverted Mushroom	Bistable- isola	Bistable- Inverted isola	Bistable- Mushroom (left diagram)	Bistable- Mushroom (right diagram)
g_{A0}	5.40796	2.30238	1.16189	3.91086	5.61338	2.14577	2.82458	8.00958	4.94922	3.38580
g_{AS}	98.5099	62.7262	60.1037	82.2862	39.7386	67.0659	38.8018	94.5969	51.3682	94.6726
$g_{\scriptscriptstyle AB}$	72.9167	16.2866	58.7307	60.5229	12.4514	51.2801	99.7156	87.5328	50.9559	44.9678
g_{B0}	3.33803	3.24908	6.08283	3.90089	5.41966	7.51982	4.44888	3.90556	9.61109	1.87407
g_{BS}	67.1020	10.6801	25.6386	16.1169	43.8093	58.4625	94.4743	65.3754	59.7813	83.4666
$g_{\scriptscriptstyle BA}$	37.8199	73.9437	41.3745	78.2889	87.6818	46.7369	62.4992	42.0374	41.5308	93.6896
J_{AS}	180.884	379.859	141.549	27.7697	101.614	118.419	42.3847	121.927	102.359	81.5759
J_{BS}	118.768	68.4776	37.1898	128.319	75.1887	259.318	86.4997	148.646	115.949	46.7086
J_{AB}	763.437	739.303	595.305	670.519	2677.69	615.182	1237.12	535.278	1418.68	985.783
J_{BA}	1243.46	682.014	141.538	1888.71	550.999	1036.18	737.882	1047.30	2254.29	2564.77
n_{AS}	5	6	10	8	1	5	7	6	10	1
n_{BS}	6	9	3	7	10	8	2	3	3	10
n_{AB}	7	9	3	10	9	10	5	9	10	9
n_{Ba}	6	8	5	7	6	5	5	5	8	8
γ_A	0.06515	0.03809	0.04834	0.06916	0.05790	0.07023	0.09215	0.09676	0.02535	0.02448
γ_B	0.05701	0.09326	0.03587	0.07449	0.03365	0.06225	0.04864	0.08721	0.03913	0.09828

Table A5.6: Parameters for different switches reported in the Figure 1d and Table S1 from the ppMISA network.

			OR-gate				AND-gate	
Parameters	Dual bistable (left diagram)	Dual bistable (right diagram)	Isola- Mushroom	Inverted Isola- Mushroom	Dual bistable- Isola	Dual bistable- Inverted isola	Parameters	Dual isola
g_{A0}	5.17627	3.55117	8.25783	1.55466	5.39796	9.15053	g_{A0}	9.03108
g_{AS}	27.3560	72.7125	48.0782	49.7661	57.1797	43.6249	g_{A1}	24.3663
g_{AB}	95.8391	46.2017	22.2070	63.7841	65.2393	90.5569	g_{B0}	5.40892
g_{B0}	5.24728	5.48261	4.19034	5.90409	9.59969	9.73973	g_{B1}	82.7562
g_{BS}	74.8802	31.0285	12.3761	56.6088	81.1651	69.9967	J_{AS}	85.3933
g_{BA}	71.1375	99.8927	77.8168	80.2127	29.0245	64.5581	J_{BS}	40.1371
g_{BB}	80.1445	23.0812	62.7681	96.4198	82.9614	21.9119	J_{AB}	782.615
J_{AS}	143.634	246.624	132.961	54.7708	99.5336	86.8653	J_{BA}	219.425
J_{BS}	34.7550	170.819	85.8930	65.5468	162.465	107.753	J_{BB}	215.229
J_{AB}	759.522	1747.82	770.557	529.507	805.504	1245.86	n_{AS}	1
J_{BA}	982.583	1048.99	456.526	2196.10	840.440	4334.88	n_{BS}	2
J_{BB}	1932.44	1286.44	1301.06	2369.74	2813.66	670.013	n_{AB}	3
n_{AS}	3	3	8	3	5	10	n_{BA}	7
n_{BS}	1	9	7	8	2	5	n_{BB}	8
n_{AB}	5	4	10	3	2	6	γ_A	0.07038
n_{BA}	2	8	2	9	6	4	γ_B	0.05600
n_{BB}	9	8	10	8	6	8		
γ_A	0.04370	0.05459	0.08468	0.02396	0.04630	0.02092		
γ_B	0.07497	0.03899	0.09009	0.06929	0.03340	0.07324		

Table A5.7: Schematic bifurcation diagrams of reversible and irreversible bistable switches with a maximum of three bistable regions. The reversible switches are presented in the 2^{nd} column and irreversible switches on the left (S=0), right (S=1000) and both sides of a particular switch are presented on the 4^{th} , 6^{th} and 8^{th} column, respectively. The 'L' and 'R' prefix and suffix represents the irreversibility on the left and right, respectively. The shaded box represents the repetition of the bifurcation represented by the number serial number of the bifurcation. The irreversible switches that were not considered are represented by the empty boxes. Forward and backward facing switches are represented by 'F' and 'B' letters in the names of the switch.

SI No	Reversible bistable switch	Sl No	Irreversible bistable switch on left (S=0)	Sl No	Irreversible bistable switch on right (S=1000)	Sl No	Irreversible bistable switch on both sides
1		58		82		10 6	
	Isola (Is)		L-BsB		BsF-R		L-Bs-R
2	Bistable Forward (BsF)	59	L-BsF		82		106
3	Bistable Backward (BsB)		58	83	BsB-R		106
4	Inverted isola (InIs)		59		83		106
5	Dual isola (DIs)	60	L-DIs	84	R-DIs	10 7	L-DIs-R
6	Dual inverted isola (DInIs)	61	L-DInIs	85	DInIs-R	10 8	L-DInIs-R
7	Dual bistable forward (DBsF)	62	L-DBsF	86	DBsF-R	10 9	L-DBsF-R
8	Dual bistable backward (DBsB)	63	L-DBsB	87	DBsB-R	11 0	L-DBsB-R

9	Mushroom (Msh)	64	L-Msh	88	Msh-R		108
10	Inverted mushroom (InMsh)	65	L-InMsh	89	InMsh-R		107
11	Is-BsF		65		84		107
12	BsF-Is	66	L-BsF-Is		86		109
13	InIs-BsF		62	90	InIs-BsF-R		109
14	BsF-InIs		61		88		108
15	Is-BsB		63	91	Is-BsB-R		110
16	InIs-BsB		64		85		108
17	BsB-Is		60		89		107
18	BsB-InIs	67	L-BsB-InIs		87		110
19	TBsF			92	TBsF-R	11 1	L-TBsF-R
20	TBsB	68	L-TBsB			11 2	L-TBsB-R

21	Is-DBsF	69	L-Is-DBsF	93	Is-DBsF-R	11 3	L-Is-DBsF-R
22	BsF-Is-BsF	70	L-BsF-Is-BsF	94	BsF-Is-BsF-R	11 4	L-BsF-Is- BsF-R
23	DBsF-Is	71	L-DBsF-Is		92		111
24	InIs-DBsF						111
25	BsF-InIs- BsF					11 5	L-BsF-InIs- BsF-R
26	DBsF-InIs					11 6	L-DBsF- InIs-R
27	Is-DBsB		68	95	Is-DBsB-R		112
28	BsB-Is-BsB	72	L-BsB-Is- BsB	96	BsB-Is-BsB-R	11 7	L-BsB-Is- BsB-R
29	DBsB-Is	73	L-DBsB-Is	97	DBsB-Is-R	11 8	L-DBsB-Is-R
30	InIs-DBsB					11 9	L-InIs- DBsB-R
31	700					12 0	

	BsB-InIs- BsB						L-BsB-InIs- BsB-R
32	DBsB-InIs						112
33	00	74	20	98	000	12 1	20
	DIs-BsF		L- Dis-BsF		DIs-BsF-R		L- DIs-BsF- R
34	Is-BsF-Is	75	L-Is-BsF-Is		93		113
35	BsF-DIs	76	L-BsF-DIs		94		114
36	DIs-BsB		72	99	Dis-BsB-R		117
37	Is-BsB-Is		73	10 0	Is-BsB-Is-R		118
38	BsB-DIs	77	L-BsB-DIs	10 1	BsB-DIs-R		121
39	Is-Msh	78	L-Is-Msh	10 2	Is-Msh-R	12 2	L- Is-Msh-R
40	BsF-Is-BsB	79	L-BsF-Is-BsB	10 3	BsF-Is-BsB-R	12	C L-BsF-Is-
41	Msh-Is	80	L-Msh-Is	10 4	Msh-Is-R	12 4	BsB-R L-Msh-Is-R
42	InIs-Msh						116

	ı			1		1	
43						12 5	> <
	BsF-InIs- BsB						L- BsF-InIs- BsB-R
44	5						119
	Msh-InIs						
45		81			100		118
	Is-InMsh		L-Is-InMsh				
46			74		101		121
	BsB-Is-BsF						
47	250		75	10 5	25		113
	InMsh-Is				InMsh-Is-R		
48							124
	InIs-InMsh						
49						12 6	V)0
	BsB-InIs- BsF						L-BsB-InIs- BsF-R
50	250						122
	InMsh-InIs						
51	55				104		124
	Msh-BsF						
52	52						119
	Msh-BsB						
53	InMsh-BsF		69		105		113
	IIIIvisii-DSF						
54	5 6						116
	BsF-Msh						

55	757	78		122
	InMsh-BsB			
56	ا ر	81	97	118
	BsB-InMsh			
57	000	77	98	121
	Tripple isola (Tis)			

Table A5.8: Parameters for the phase diagram calculations with isola and inverted isola initial phases in the ppMISA network under OR-gate (for the Figure 7g and Figure 8d in the main text).

Parameters	Isola phase (Figure 7g)	Inverted isola phase (Figure 8d)
g_{A0}	9.26266	8.53582
g_{AS}	53.9575	15.2853
$g_{\scriptscriptstyle AB}$	Varied	Varied
g_{B0}	9.92193	2.57871
g_{BS}	39.8924	22.3152
$g_{\scriptscriptstyle BA}$	Varied	Varied
g_{BB}	38.0415	28.6408
J_{AS}	101.757	70.0372
J_{BS}	24.9417	160.348
J_{AB}	2624.14	1111.90
J_{BA}	545.969	4851.50
J_{BB}	238.052	4190.46
n_{AS}	6	3
n_{BS}	6	10
n_{AB}	9	6
n_{BA}	7	3
n_{BB}	3	1
γ_A	0.08210	0.01237
γ_B	0.03667	0.07217

Table A5.9: Parameters for the phase diagram calculations of the pnMA network under OR-gate (for the **Figure A5.6**).

Parameters	Isola phase	Inverted isola phase	Mushroom phase	Inverted mushroom phase
g_{A0}	8.62687	6.40066	3.79978	7.90062
g_{AS}	39.2674	94.9022	45.2186	23.3619
g_{AB}	Varied	Varied	Varied	Varied
g_{B0}	7.37762	2.05024	9.93726	4.46789
g_{BS}	62.3360	77.9861	25.2221	93.2656
g_{BA}	Varied	Varied	Varied	Varied
J_{AS}	76.3361	726.918	69.3061	140.891
J_{BS}	96.1479	123.081	210.264	49.9116
J_{AB}	2040.48	1105.94	1006.39	1087.82
J_{BA}	641.550	914.359	633.213	2307.20
n_{AS}	3	5	8	6
n_{BS}	9	6	10	8
n_{AB}	4	1	3	7
n_{Ba}	8	9	9	7
γ_A	0.09738	0.01660	0.09803	0.01216
γ_B	0.04797	0.08282	0.08474	0.05817

Investigation of chemical noise propagation and its consequence in simple regulatory motifs and complex networks

by Soutrick Das

Submission date: 27-Dec-2022 10:18AM (UTC+0530)

Submission ID: 1986826878

File name: consequence_in_simple_regulatory_motifs_and_complex_networks.pdf (9.69M)

Word count: 37950

Character count: 194024

Investigation of chemical noise propagation and its consequence in simple regulatory motifs and complex networks

ORIGINA	LITY REPORT				
SIMILA	% RITY INDEX	4% INTERNET SOURCES	7% PUBLICATIONS	3% STUDENT PAP	PERS
PRIMARY	/ SOURCES		1		
1	signaling distinct activation	Das, Debashis g of bistable swinature of pulse on and mutual in retical Biology, 2	itches reveal processing be nhibition loop	the y mutual	2 % source of the sh
2	eprints-	phd.biblio.unitn	Dr. As	Debashis Barik sociate Professor shool of Chemistry ersity of Hyderabad abad-500 046, India.	1%
3	Submitt Student Pape	ed to University	of Sydney		1%
4	wikimili. Internet Source				1 %
5	mcb.ber	keley.edu			1 %
6	Chemica	i, Tudor. "Nume al Master Equat ne, 2012.			<1%

quan dictat	rick Das, Debashis Barik. "Qualitative and titative nature of mutual interactions te chemical noise in a democratic tion network", Physical Review E, 2020	<1%
Bistal Forwa	bam Dey, Debashis Barik. "Emergent ble Switches from the Incoherent Feed- ard Signaling of a Positive Feedback ", ACS Synthetic Biology, 2021	<1%
intrin	rick Das, Debashis Barik. "Scaling of asic noise in an autocratic reaction ork", Physical Review E, 2021	<1%
Lands	oam Dey, Debashis Barik. "Potential scapes, Bifurcations, and Robustness of able Networks", ACS Synthetic Biology,	<1%
	nitted to Cardiff and Vale College [Coleg Hafren], Cardiff	<1%
12 WWW.	.bandim.org Source	<1%
13 WWW.	.scribd.com Source	<1%

quan dictat	rick Das, Debashis Barik. "Qualitative and titative nature of mutual interactions te chemical noise in a democratic tion network", Physical Review E, 2020	<1%
Bistal Forwa	bam Dey, Debashis Barik. "Emergent ble Switches from the Incoherent Feed- ard Signaling of a Positive Feedback ", ACS Synthetic Biology, 2021	<1%
intrin	rick Das, Debashis Barik. "Scaling of asic noise in an autocratic reaction ork", Physical Review E, 2021	<1%
Lands	oam Dey, Debashis Barik. "Potential scapes, Bifurcations, and Robustness of able Networks", ACS Synthetic Biology,	<1%
	nitted to Cardiff and Vale College [Coleg Hafren], Cardiff	<1%
12 WWW.	.bandim.org Source	<1%
13 WWW.	.scribd.com Source	<1%

14	Biology", Springer Science and Business Media LLC, 2021 Publication	<1%
15	C. P. Bhunu. "Tuberculosis Transmission Model with Chemoprophylaxis and Treatment", Bulletin of Mathematical Biology, 05/2008 Publication	<1%
16	documents.mx Internet Source	<1%
17	Rekia Meriem Ahmed Bacha, Abdellatif El Badia, Ahmad El Hajj, Stephane Mottelet. "Identification of physical parameters in pressing of rapeseeds from the oil flux measurements", Mathematical Methods in the Applied Sciences, 2020 Publication	<1%
18	Katica (Stevanović) Hedrih. "Energy transfer in double plate system dynamics", Acta Mechanica Sinica, 06/2008 Publication	<1%
19	H VWESTERHOFF. "The methodologies of systems biology", Systems Biology, 2007 Publication	<1%
20	Marco Del Giudice, Stefano Bo, Silvia Grigolon, Carla Bosia. "On the role of extrinsic noise in	<1%

microRNA-mediated bimodal gene expression", PLOS Computational Biology, 2018

Publication

Wei-Yin Chen. "Stochasticity and noiseinduced transition of genetic toggle switch", Journal of Uncertainty Analysis and Applications, 2014

<1%

- Publication
- Submitted to Hochschule Bremen Student Paper

<1%

Soutrick Das, Debashis Barik. "Investigation of chemical noise in multisite phosphorylation chain using linear noise approximation", Physical Review E, 2019

< 1 %

Publication

Exclude quotes

Exclude bibliography

On

Exclude matches

< 14 words